Rainfall estimation for hydrology using volumetric weather radar

Pieter Hazenberg

Thesis committee

Promotor
Prof. dr. ir. R. Uijlenhoet
Professor of Hydrology and Quantitative Water Management
Wageningen University

Co-promotors
Dr. ir. H. Leijnse
Senior researcher,
Royal Netherlands Meteorological Institute, De Bilt,
The Netherlands

Dr. G. Delrieu
Senior researcher,
Laboratoire d'étude des Transferts en Hydrologie et
Environnement, Grenoble, France

Other members:
Prof. dr. A. P. Barros, Duke University, Durham, USA
Prof. dr. ir. N. van de Giesen, Delft University of Technology
Prof. dr. W. Hazeleger, Wageningen University
Prof. dr. ir. P. A. Troch, University of Arizona, Tucson, USA

This research was conducted under the auspices of the Graduate School SENSE.

Rainfall estimation for hydrology using volumetric weather radar

Pieter Hazenberg

Thesis
submitted in fulfilment of the requirements for the degree of doctor
at Wageningen University
by the authority of the Rector Magnificus
Prof. dr. M.J. Kropff,
in the presence of the
Thesis Committee appointed by the Academic Board
to be defended in public
on Monday 24 June 2013
at 4 p.m. in the Aula.

Hazenberg, P.

Rainfall estimation for hydrology using volumetric weather radar,
xviii+234 pages.

Ph.D. thesis, Wageningen University, NL (2013)
With references, with summaries in Dutch and English

ISBN 978-94-6173-630-7

Abstract

Radars are known for their ability to obtain a wealth of information about the spatial and temporal characteristics of rainfall fields. Unfortunately, precipitation estimates obtained by weather radar are affected by multiple sources of error, which have to be corrected for in order to provide realistic rainfall estimates. This thesis specifically focuses on the correction of weather radar data for its dominant sources of error, so its product becomes directly applicable for hydrological purposes.

In general, weather radar measurement errors can be split into two main groups: 1) errors related to reflectivity measurements of the radar, and 2) errors related to the conversion of the measured reflectivity values into a rainfall intensity. The former type of errors result from the characteristics of the radar (e.g. radar calibration), the surrounding environment (e.g. blockage, clutter, signal attenuation), or from the interpretation of reflectivity measurements (e.g. vertical profile of reflectivity, VPR). Errors related to the latter originate from continuous spatial and temporal changes of the particle size distribution of the hydrometeors, in case of rainfall the so-called drop size distribution (DSD). The relation between the radar reflectivity and rainfall rate is usually described by a power law. Since both radar reflectivity and rainfall intensity are related to the DSD, their effective relation changes continuously. This gives rise to the problem that similar radar reflectivity values can result from different raindrop size distributions with different rainfall intensities.

This thesis focuses specifically on weather radar rainfall measurements in stratiform precipitation. In North-Western Europe this type of

precipitation is most dominant in winter and leads to the largest hydrological response of catchments. Unfortunately, the quality of uncorrected radar rainfall estimates starts decreasing at relatively close range from the radar for this type of precipitation. Therefore, as a first approach, a number of previously proposed radar error correction algorithms were applied in this thesis. The implementation of these methods shows a positive impact on the quality of the obtained precipitation measurements as compared to rain gauges. However, the traditional approach of applying a uniform Eulerian based algorithm for the entire radar umbrella to correct for VPR, limits its impact to improve the corrected weather radar precipitation measurements.

In order to obtain further improvements in the quality of weather radar correction mechanisms, contrary to previous implementations, a Lagrangian approach is proposed in this thesis. This is expected to be highly beneficial, because precipitation fields are continuously changing in space and time. For this purpose, the Rotational Carpenter Square Cluster Algorithm (RoCaSCA) was developed to identify and discriminate between precipitation regions, which are then followed over time. Within each precipitation region, using previously developed methods, the type of precipitation is identified for each pixel discriminating between convective, stratiform and non-convective/non-stratiform precipitation. The latter two types of precipitation are then corrected for the impact of VPR using a newly developed approach. After combining this Lagrangian correction approach with previously proposed radar correction algorithms, radar reflectivity values are converted into rainfall rates using a precipitation type dependent relationship.

For the winter half-year of study, results show that the newly proposed procedure leads to a large improvement in the quality of weather radar rainfall estimates up to distances of 150 km. After accounting for all dominant error sources, radar precipitation estimates have a similar quality as those obtained from in situ rain gauge measurements. Therefore, contrary to traditional operational correction algorithms, there is no need to perform a final bias correction using rain gauge data to generate reliable rainfall estimates.

It is recognized that after correcting for errors considerable differences between the measurements of both devices remain, either originating from unaccounted error sources, small-scale precipitation variability, or from scale issues when comparing weather radar and rain gauge measurements. However, instead of applying a bias correction procedure to account for these differences, in this thesis the amount of uncertainty as-

sociated with the weather radar rainfall measurement is identified. For this purpose, two conceptual approaches were developed. Using the volumetric weather radar data, the first approach is able to estimate the amount of uncertainty originating from spatial and temporal variability of the VPR. As a second procedure, the uncertainty originating from the applied relation between radar reflectivity and rainfall rate is estimated using a statistical technique, which assumes the two parameters of the log-transformed relation follow a bivariate log-normal distributions. This assumption of log-normality was derived from the analysis of a long-term DSD dataset obtained from disdrometer measurements in the South of France. For stratiform precipitation, these two types of uncertainty are assumed to have the most dominant impact on the quality of radar rainfall measurements. Results confirm this hypothesis and show that once either type of uncertainty is taken into account, a large part of the difference between weather radar and rain gauge measurements can be accounted for.

As a last aspect of this thesis, the hydrological impact of error-corrected weather radar rainfall measurements is assessed by simulating the rainfall-runoff response of the medium-sized Ourthe catchment. This basin is situated within the Belgian Ardennes region, a hilly environment consisting of shallow sloping soils that give rise to a relatively fast hydrological response to rainfall. Since this basin is one of the major tributaries of the river Meuse before it enters The Netherlands, understanding and simulating its response to rainfall is important for operational flood forecasting. Using the corrected weather radar data in a lumped hydrological model, discharge simulations have a similar quality as those based on in situ rain gauge data. However, using the latter type of data results in a serious underestimate of the largest flood peak observed during the period of simulation. In case the weather radar data are used, including information on the uncertainty originating from both considered sources, much better simulations of the observed flood peak are obtained. This shows the benefit of using weather radar data in rainfall-runoff applications. Since the resolution of operational hydrological models increases and the quality of radar rainfall estimates is expected to improve even further as a result of new technology (polarimetry), it is anticipated that the possibilities of applying weather radar information in hydrology will only increase further in the near future.

Voorwoord/Preface

Indien men mij tien jaar geleden gezegd zou hebben dat dit proefschrift het resultaat zou zijn van een door mij uitgevoerd promotieonderzoek, zou ik diegene niet hebben geloofd. Zowel tijdens mijn Bachelor Bodem, Water en Atmosfeer als gedurende een groot deel van mijn Master Hydrology and Water Quality in Wageningen heb ik nooit stilgestaan bij een wetenschappelijke carrière. Ik wilde consultant worden, en dan bij voorkeur bij één of ander prestigieus kantoor aan de Amsterdamse Zuidas, London of New York. Om mijn kans op het krijgen van een dergelijke topbaan te bevorderen verbreedde ik mijn studiepakket met een jaar lang economische vakken en werd ik actief in het studentenleven. Het enige dat aan het eind van mijn studie nog aan mijn CV ontbrak was internationale ervaring. Maar aangezien het mijn droom was om stage te lopen in de Verenigde Staten, het land van de onbegrensde mogelijkheden, kon ik ook aan deze eis voldoen. Zo was ik destijds overtuigd.

Vanaf augustus 2006 liep ik stage in de onderzoeksgroep van Peter Troch aan de University of Arizona voor een periode van 7 maanden. Mijn onderzoekswerkzaamheden waren erg afwisselend en varieerden tussen veldwerk, afvoermodelering, sneeuwhydrologie, neerslagmetingen en flash floods. Met name deze laatste twee onderwerpen boeiden mij enorm. Hoe gaaf was het om in het ruige landschap van Arizona (waarin ik als een cowboy rondliep) onderzoek te doen naar hevige zomerse onweersbuien die in de bergen extreme afvoeren kunnen veroorzaken. Tegelijkertijd was het erg frustrerend dat de interne klokken van een groot aantal regenmeters onregelmatige tijdsprongen maakten waardoor

het nagenoeg onmogelijk was om de exacte periode van een bui te bepalen. Achteraf gezien is deze stage van grote invloed geweest op mijn latere keuzes. Ik kwam erachter dat de hydrologische wetenschap toch wel erg interessant was!

Hoewel ik na het afronden van mijn studie allereerst nog op zoek ben gegaan naar die zo fel begeerde topbaan, ben ik hiermee vrij snel gestopt. Voor mijn gevoel was ik nog niet klaar met studeren en het idee van een promotieonderzoek trok inmiddels meer dan een baan in het bedrijfsleven. In het voorjaar van 2007 had ik hierover een zeer goed gesprek met Remko Uijlenhoet, die net was aangesteld als nieuwe hoogleraar Hydrologie en Kwantitatief Waterbeheer in Wageningen. Hij was betrokken bij het Europese project Hydrate, dat zich richte op het analyseren en voorspellen van extreme neerslag die kan leiden tot flash floods. Weerradarmetingen speelden hierbij een essentiële rol. Gegeven mijn ervaring in Arizona en de wetenschap slechts in beperkte mate gebruik te hoeven maken van foutieve regenmeterdata, leek mij dit een geweldig promotie onderzoek. Weerradarmetingen hadden minder last van dergelijke fouten was mijn onschuldige overtuiging destijds ☺.

Zeer gemotiveerd startte ik in september 2007 mijn promotieonderzoek, waarbij we in eerste instantie weerradarinformatie voornamelijk wilden gebruiken voor het verkrijgen van ruimtelijke neerslag. Hierbij poogden we ruimtelijke variaties aan druppelgrootteverdelingen gemeten aan de grond te koppelen aan de weerradarmetingen. Vervolgens zou deze informatie dan gebruikt kunnen worden in een hoge resolutie neerslag-afvoermodel waarbij expliciet individuele hellingen werden gemodelleerd. Na dit geïmplementeerd te hebben zouden we dan eventueel kunnen kijken naar ruimtelijke variaties in reistijdenverdelingen. Hoewel een hoog ambitieniveau nooit verkeerd is, realiseer ik mij inmiddels dat het nagenoeg onmogelijk is dit in een tijdsperiode van vier jaar af te ronden.

Uiteindelijk heb ik mij de afgelopen jaren voornamelijk gefocused op het verkrijgen van nauwkeurige neerslaginformatie uit weerradarda-ta en de invloed van ruimtelijke variaties in druppelgrootteverdelingen. Dit blijkt toch niet zo eenvoudig te zijn, zoals u in dit proefschrift kunt lezen. Weerradarmetingen bevatten vele fouten. In plaats van met standaardmethodes weerradargegevens te corrigeren met regenmeterdata (deze kunnen nog steeds leiden tot een hoop onzekerheid en worden helaas nog te vaak toegepast!) ben ik in samenwerking met Remko en postdoc Hidde Leijnse correcties gaan toepassen gebasseerd op onze fysische kennis van de radar en de neerslag. De weerradar geeft iedere 5 minuten

een enorme hoeveelheid informatie over het ruimtelijk neerslagveld. De grote uitdaging hierbij is deze informatie efficiënt te verwerken. Gelukkig had ik tijdens het afstudeervak van mijn Master bij Paul Torfs de lagere programmeertaal C++ geleerd, iets waar ik tot de dag van vandaag profijt van heb. Het eerste jaar van mijn promotie hebben we met name reeds bekende correctiemethodes geïmplementeerd, wat leidde tot hoofdstuk 2 van dit proefschrift. Aan de hand van deze ervaring ontstonden vele nieuwe ideeën tot het verder verbeteren van de kwaliteit van weerradarmetingen, die worden besproken in de hoofdstukken 4, 5 en 6 van dit proefschrift.

Since the topic of my PhD was initially focused on flash floods, I got the opportunity to stay for 5 months in the research group of Guy Delrieu at the Laboratoire d'étude des Transferts en Hydrologie et Environnement in Grenoble from October 2008 to February 2009. This institute is world-famous for its physical approach to correct volumetric weather radar data. Together with Nan Yu, a Chinese PhD student in Grenoble, and under the supervision of Guy, Remko and postdoc Brice Boudevillain, I kept myself busy with precipitation scaling-law theory and its impact on the applied radar reflectivity - rainfall intensity relationship. The work done during this period directly lead to Chapter 3 of this thesis and is the foundation of some of the ideas presented in later chapters.

Vanaf 2011 ben ik intensief gaan samenwerken met Marjolein van Huijgevoort, die haar promotieonderzoek richtte op droogte in globale hydrologische modellen. Onderzoeksresultaten op basis van deze modelgegevens hebben een grote maatschappelijk impact. Helaas biedt de kwaliteit van veel modellen ruimte voor verdere verbetering, waar ik graag aan wilde werken. Toen ik bij toeval (hoewel ik mij dat soms afvraag) aan het einde van mijn promotie een vacature voor een postdoc positie voor het opzetten van een nieuw globaal hydrologisch model in de groep van Xubin Zeng aan de University of Arizona tegenkwam, heb ik hier op gesolliciteerd. Deze positie bood de ideale mogelijkheid mijzelf de komende jaren te verbreden en door te ontwikkelen in de wetenschap.

Eind maart 2012, toen ik afreisde naar Arizona, was mijn proefschrift nog niet af. Hoewel Remko en ik er van overtuigd waren dat dit in de eerste maanden in Tucson zou gebeuren, heeft dit toch wat langer op zich laten wachten. De combinatie van een nieuwe baan met een nieuw onderwerp, zonnige temperaturen en een zwembad in de tuin bood hierbij teveel afleiding.

Het moge duidelijk zijn dat er een hoop mensen een rol hebben

gespeeld in mijn ontwikkeling de afgelopen jaren. Allereerst wil ik mijn promotor en dagelijks begeleider Remko Uijlenhoet bedanken voor zijn tijd, inzet maar bovenal de gezelligheid in de afgelopen jaren. Remko, ik weet dat ik je een hoop vrijdagmiddagen van je weekend heb afgehouden tijdens langdurige besprekingen. Daarnaast blijven mij een hoop interessante en gezellige Europese projectbesprekingen en conferenties bij, waar ik met heel veel plezier op terug kijk. Dank voor je enthousiasme en het delen van je kennis en ervaringen op alle momenten van de dag!

Vervolgens bedank ik mijn co-promotor Hidde Leijnse, die na de eerste 2 jaar in Wageningen weerradaronderzoeker werd bij het Koninklijk Nederlands Meteorologisch Instituut (KNMI). Hidde, wij hadden de afgelopen jaren een hoop interessante discussies over mogelijke verbeteringen in de weerradarmetingen. De positiviteit en het enthousiase die jij hierbij uitstraalde werken erg motiverend. Dank hiervoor!

I would also like to thank my second co-promotor Guy Delrieu for allowing me to work in his research group in Grenoble. Guy, your critical assessment has always motivated me to come up with better solutions and answers. Many thanks for this! When it comes to my stay in Grenoble I also wish to thank Brice Boudevillain and Nan Yu for many interesting discussions.

Verder wens ik Paul Torfs te bedanken die mijn begeleider was tijdens zowel mijn Bachelor als Master afstudeervak. Paul, je interesse voor numerieke problemen, lagere programmeertalen en computertoepassingen in het algemeen hebben mij erg geholpen bij het tot stand komen van dit proefschrift zowel als mijn huidige positie. Dank hiervoor! Verder wil ik Patrick Bogaart, Ruud Hurkmans, Ype van der Velde, Olda Rakovec, Ryan Teuling, Henny van Lanen en Piet Warmerdam bedanken voor interessante discussies de afgelopen jaren. Deze hebben mij zeker hydrologisch gevormd. With respect to this latter aspect I also want to thank Peter Troch and Steve Lyon for the interesting work and discussions, which resulted in my decision to pursue a PhD.

Een persoon die ik absoluut niet mag vergeten te noemen is Joris Eekhout, mijn kamergenoot in Wageningen. Joris, het delen van een kamer met jou heb ik als zeer prettig ervaren. Ik denk dat wij uitstekend in staat waren op de juiste wijze onze frustraties op het gebied promoveren, wetenschap, het universitaire bedrijf, zowel als politiek en maatschappij te delen. Hierbij zetten de “Louis van Gaal Klassieker” op youtube en het “Had je een probleem” op dumpert vaak de juiste toon. Ik kijk dan ook met veel plezier terug op deze periode! Verder wens ik de overige collega’s van de leerstoel Hydrologie en Kwantitatief Waterbe-

heer en van de voormalige leerstoel Bodemnatuurkunde, Ecohydrologie en Grondwaterbeheer te bedanken!

Tijdens mijn promotieperiode heb ik de nodige studenten begeleid tijdens hun Bachelor en Master thesis. Ondanks dat veel van de onderwerpen niet direct van toepassing waren op mijn huidige onderzoek heb ik het begeleiden van studenten als zeer prettig en interessant ervaren. Boudewijn, Kay, Karlijn, Erik, Tjeerd, Deen, Katie, Marjolein, Jouke, Sihine en Tung, bedankt voor deze samenwerking!

Dit onderzoek had nooit kunnen plaatsvinden als ik geen gebruik had kunnen maken van data uit België. Daarom wil ik Laurent Delobbe van het Koninklijk Meteorologisch Instituut in België bedanken voor het verstrekken van de ruwe volumetrische radardata en zijn interesse voor mijn vorderingen. Next to that, I wish to thank Philippe Dierickx for providing lots of information on raingauge and discharge measurements taken by the Hydrological Service of the Walloon Region of Belgium (METSETHY). Ook wil ik Albrecht Weerts en Paolo Reggiani van Deltares in Delft bedanken voor het verstrekking van het hydrologische model gebruikt in hoofdstuk 2.

Tenslotte will ik nog een aantal mensen in de privé-sfeer bedanken. Allereerst mijn beiden paranimfen Gertjan Dijkstra en Anton van den Broek. Gertjan, wij kennen elkaar al sinds de middelbare school. Dank voor alle gezelligheid de afgelopen 1,5 decennia. Anton, ook jij bedankt voor al je gezelligheid, inclusief je no nonsense houding en realisme met betrekking tot mijn wetenschappelijke vorderingen en de impact hiervan!

Mijn ouders en zusje Renate voor hun onvoorwaardelijke steun, liefde en motivatie die ze mij gaven om mijzelf te blijven ontwikkelen. Uit de grond van mijn hart, dank hiervoor! Last I wish to thank my fiancée Karen Casas, whom I met last year at the beginning of Summer in Tucson. This last year in Tucson has been an amazing experience mainly due to your pressence. Our love brought the final piece of this thesis, the cover photo. This photo was taken while visiting your family in Colombia this winter. I am looking forward getting married to you three days after my PhD defense!

Pieter Hazenberg,
Tucson, May 2013

Contents

CHAPTER 1

Introduction

1.1 Background

Weather radars are able to obtain a wealth of information on the spatio-temporal properties of precipitation (*Zawadzki*, 1975; *Joss and Lee*, 1995; *Smith et al.*, 2001). RADAR, which is an acronym for **Ra**dio **D**etection **A**nd **R**anging, was developed before and during World War 2 to detect enemy objects using reflected radio waves. A radar transmits a short pulse of electromagnetic radiation into the atmosphere, which is then reflected by particles in the atmosphere (e.g. airplanes, birds, insects, rain drops) or the surrounding environment (e.g. mountains, trees, ocean waves). Part of the reflected signal is transferred back to the radar where its intensity (and in case of coherent or Doppler radars also its phase) is measured. From the intensity of the observed reflected signal it is possible to make an estimate of the occurrence and strength of the precipitation field.

Because of its ability to detect precipitation, meteorologists have used these images for over half a century to identify precipitation and issue warnings/forecasts in case heavy rainfall is observed. Nowadays, however, professional meteorologists are not the only ones interested in radar images to issue precipitation 'forecasts'. Widely available weather radar imagery, presented on the Internet and on mobile Apps, is influencing many people's daily decisions. By assessing and extrapolating these images, we have turned the weather radar into our own personal virtual

weatherman, whom we consult for questions like: 1) What should/can I wear?, 2) When will I leave/go home/to work?, 3) Should I take an umbrella today?, etc. As such, weather radars have become an important part of our lives.

Besides the meteorological community, hydrologists have also become interested in the ability of weather radars to provide estimates of surface precipitation. Especially the detailed information on the spatial variation of precipitation intensities is very appealing to hydrologists. Historically, rain gauges were used for to measure surface precipitation amounts. However, their small size, limited spatial representativity, and relatively high maintenance cost, together with the much more detailed information provided by weather radars makes weather radars very attractive for hydrological use. Nowadays, more and more operational centers are starting to use radar information to monitor the hydrological system. In case (extreme) precipitation is observed, warnings/forecasts on the occurrence of possibly local (flash)floods can be issued (*Collier and Knowles*, 1986; *Joss and Waldvogel*, 1990; *Carpenter et al.*, 2001; *Vivoni et al.*, 2006).

Unfortunately, radar precipitation estimates are far from perfect as they are affected by multiple sources of error. This makes it difficult to use weather radar information directly for hydrological purposes. Historically, rain gauge information was used to adjust the weather radar data for bias errors and hence to improve the quality of radar rainfall estimates. Unfortunately, this procedure has a number of limitations. Firstly, many of the errors arise from the reflection of the radar signal off the surrounding landscape, known as clutter. Although these ground clutter returns have different signal properties than precipitation, it is difficult to distinguish and remove them in case artifacts are embedded within a larger precipitation system. Secondly, since the spatial density of many operational gauge networks is rather course compared to the typical spatial variability of precipitation fields (*Berne et al.*, 2004a) and most types of radar error are spatially variable as well, correcting for bias errors can still lead to errors in precipitation estimates. Thirdly, up to recently, much of the rain gauge information was not available in real-time. This made it impossible to adjust radar data for bias errors until rain gauge measurements became available (typically after several hours). Therefore, to improve the hydrological potential of weather radar measurements, many efforts have been devoted to automatically correcting these precipitation estimates for the most dominant sources of error. In general, these can be divided into two main categories: 1)

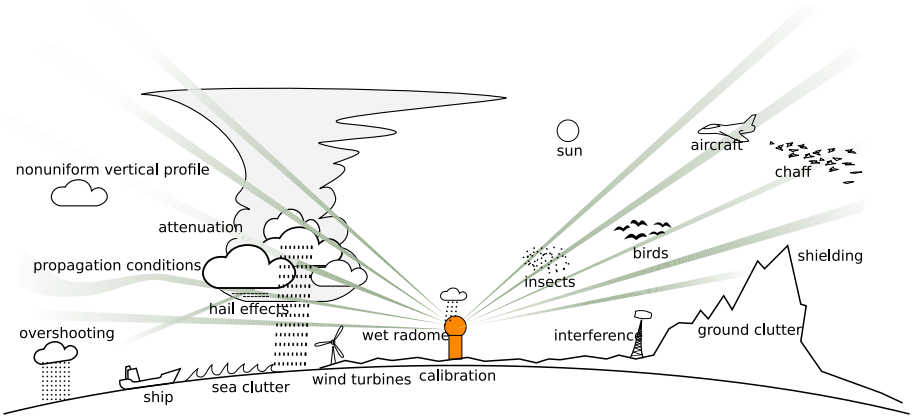

Figure 1.1: Overview of possible sources of error affecting weather radar measurements. Source: M. Peura, Finnish Meteorological Institute.

radar reflectivity measurement errors (Section 1.2) and 2) errors related to converting the radar reflectivity aloft to precipitation intensity on the ground (Section 1.3) (*Jordan et al.*, 2000; *Chumchean et al.*, 2008). Both types of error sources need to be addressed before the true hydrological potential of weather radar can be exploited.

1.2 Reflectivity measurement errors

As explained in the previous section, radar reflectivity measurements are affected by multiple sources of error. An overview of the different possible sources of error is presented in Fig. 1.1. In general, radar reflectivity measurement errors can be subdivided into three main groups, related to 1) the characteristics of the radar, 2) the surrounding environment and 3) interpretation of reflectivity measurements.

An error related to the characteristics of the radar is:

1. *Radar calibration* – The intensity of the returned signal measured by a radar depends on both the amount of transmitted power and on the conversion from the power entering the antenna feed to digital values by the radar receiver. Erroneous calibration of the radar will result in an under- or overestimation of the true reflectivity values (*Ulbrich and Lee*, 1999; *Atlas*, 2002).

The errors related to the surrounding environment comprise:

1. *Beam blockage* – In case the radar is located in a mountainous environment or close to tall buildings, signal interaction with these objects can result in (partial) beam blockage. This results in an underestimation of the atmospheric reflectivity value (e.g. *Delrieu et al.*, 1995; *Germann and Joss*, 2002; *Germann et al.*, 2006).

2. *Clutter* – Fixed objects such as mountains, trees, buildings, or wind turbines that are close to the radar can cause spurious echoes, even if these objects are not in the main radar beam. This results in an overestimation of the atmospheric reflectivity value (e.g. *Delrieu et al.*, 1995; *Gabella and Perona*, 1998; *Dinku et al.*, 2002).

3. *Anomalous propagation* – While propagating through the atmosphere the microwave signal encounters gradients in the refractive index of air perpendicular to the propagation direction. This causes the beam to bend. At radio frequencies, the refractive index of air depends mainly on pressure, temperature, and humidity. Therefore, vertical profiles of these variables determine to what degree the radar beam is bent towards or away from the earth surface. Usually, standard atmospheric profiles are used to obtain an estimate of the measurement height at a given distance from the radar. However, due to temporal changes in the vertical profile of the index of refraction, the actual height changes over time. Significant deviation of the true propagation path from that resulting from a standard atmosphere is called anomalous propagation (AP). Strong bending of the beam towards the earth's surface can cause severe ground clutter. If the opposite occurs, overshooting of precipitation can take place and atmospheric reflectivity values are underestimated (e.g. *Fabry et al.*, 1997; *Steiner and Smith*, 2002).

4. *Wet radome attenuation* – In case intense precipitation occurs directly on top of the radar, a film of water is able to form on the radome. This film attenuates the microwave signal leaving and entering the radome. This results in an underestimation of the atmospheric reflectivity value (*Germann*, 1999).

5. *Path-integrated attenuation* – Operational weather radars commonly transmit at three possible frequencies or wavelengths to measure precipitation, i.e. X-band (8-12 GHz or ~3 cm), C-band (4-8 GHz or ~5 cm), and S-band (2-4 GHz or ~10 cm). Lower frequency radars require larger antennas to have beam widths similar

to those operating at higher frequencies. Higher frequencies suffer more from signal attenuation, especially for X-band radar, but also for C-band during intense precipitation (*Delrieu et al.*, 1991, 2000). An attenuated signal leads to a decrease of the measured reflectivity value, and in extreme cases or at long ranges can cause total signal loss, leading to radar 'blindness'. On the other hand, radars operating at lower frequencies have a lower weather signal-to-clutter ratio. The effect of clutter is hence larger than for radars operating at higher frequencies.

The errors related to the interpretation of reflectivity measurements comprise:

1. *Vertical profile of reflectivity (and associated range effects)* – Based on the vertical wind field, precipitation events can usually be divided into convective and non-convective, where for the former vertical wind speeds typically exceed 1 to 3 m s^{-1}. The core of a convective precipitation system is usually formed aloft, before descending towards the earth's surface while simultaneously moving in the direction of the dominant horizontal wind field. Therefore, convective systems usually exhibit a complicated 3-dimensional reflectivity structure. Radar reflectivity measured at a given elevation does not necessarily correspond to the reflectivity at the surface (*Yuter and Houze Jr.*, 1995a; *Steiner et al.*, 1995). Non-convective precipitation can be subdivided into stratiform and non-stratiform precipitation. The former is characterized by a strong vertical stratification of the atmosphere. Stratiform precipitation is generally formed well above the freezing level, resulting in snow and ice particles. Because ice reflects radio waves much less efficiently than liquid water, radar reflectivities measured above the freezing level are generally lower than those well below it. Just below the zero-degree isotherm melting of snow gives rise to relatively large, water-coated particles, which lead to larger reflectivities than well below the freezing level. This is known as the bright band (BB). Non-stratiform precipitation is usually observed in the transition from convective to stratiform precipitation within meso-scale convective systems. For this type of precipitation, the vertical variation of the precipitation field contains characteristics of both convective and stratiform precipitation (*Houze Jr.*, 1997). This variation of the vertical profile of

reflectivity (VPR) coupled with the dependence of the radar beam height and size on range can lead to misinterpretation of radar reflectivity measurements (e.g. *Fabry and Zawadzki*, 1995; *Smyth and Illingworth*, 1998; *Cluckie et al.*, 2000).

2. *Temporal sampling effects* – Volumetric weather radars scan the atmosphere at multiple elevation angles to obtain detailed 3-D information on precipitation. Using a larger number of elevation angles will result in a more detailed representation. However, this also leads to a decrease in the temporal scanning frequency at a given radar elevation. Since precipitation properties are constantly changing in space and time, the scanning strategy has an influence on errors caused by unobserved changes in the precipitation field in both space and time.

1.3 Rainfall estimation by radar

The second source of error that influences the quality of the radar precipitation estimates is related to the conversion of the measured radar reflectivity Z [mm^6 m^{-3}] to rainfall intensity R [mm h^{-1}]. Usually, a power-law relationship is assumed to exist between both variables (*Marshall et al.*, 1955; *Battan*, 1973):

$$Z = AR^b. \tag{1.1}$$

Both radar reflectivity and rain rate are moments of the drop size distribution (DSD). Therefore, the parameters A and b also depend on the DSD. More specifically, by assuming that the drop sizes are exponentially (*Marshall and Palmer*, 1948), gamma (*Ulbrich*, 1983), or lognormally (*Feingold and Levin*, 1986) distributed, it can be shown that the possible range of the Z-R exponent is constrained (*Sekhon and Srivastava*, 1971; *Smith and Krajewski*, 1993; *Steiner et al.*, 2004). For a lognormal DSD, *Smith and Krajewski* (1993) found b to vary between 1 and 3.125, while for the gamma distribution *Steiner et al.* (2004) obtained values between 1 and 1.63.

Given the fact that conventional weather radars are unable to measure raindrop size distributions, non-polarimetric estimates of A and b cannot be obtained from these radars (and would not be necessary because R could be directly derived from the DSD otherwise). An estimate of their values can in principle be obtained from disdrometer information (*Tokay and Short*, 1996; *Atlas et al.*, 1999; *Uijlenhoet et al.*, 2003b).

Another option is to combine radar and rain gauge measurements of Z and R, respectively. However, differences in sampling characteristics limit the representativity of these results (*Kitchen and Blackall*, 1992; *Steiner and Smith*, 2004).

Instead, operational weather radars generally use a single fixed Z–R relation that is representative of the dominant type of precipitation (*Battan*, 1973). On average, these relations make optimal use of the information on average drop size distributions (*Zhang et al.*, 2011). However, given the fact that the actual DSD is variable in space and time, the assumption of a fixed Z–R-relation will lead to errors in the retrieved precipitation intensity.

1.4 Error correction and rainfall estimation

During the past decades different techniques have been developed to correct for the errors described in Sections 1.2 and 1.3, resulting in a serious improvement in the quality of radar precipitation estimates (e.g. *Kitchen and Jackson*, 1993; *Andrieu et al.*, 1997; *Ciach et al.*, 1997; *Sánchez-Diezma et al.*, 2000; *Tabary*, 2007; *Gourley et al.*, 2009). *Joss and Lee* (1995) implemented a stepwise algorithm identifying clutter, correcting for beam occultation, radar calibration errors and VPR effects using either a climatological or real-time profile estimate. *Anagnostou and Krajewski* (1999a,b) developed a similar system for an environment where topography causes no serious problems. *Delrieu et al.* (2009) implemented a more elaborate error correction algorithm for a series of extreme precipitation events in a mountainous environment in the southern part of France. Besides correcting for the errors mentioned above, the type of precipitation (convective vs. stratiform) was identified as well. This resulted in a radar product of which the quality is comparable to that of dense rain gauge measurements available.

However, many of these studies made use of rain gauge measurements to correct for any remaining bias in the weather radar precipitation estimates. Most studies on the quality of radar error correction have focused predominantly on convective precipitation in thunderstorms or in mesoscale convective systems. If these events are slow-moving, long-duration high-intensity precipitation can lead to severe (flash) flooding, especially in mountainous environments. Long-term investigations of the influence of different correction mechanisms for stratiform situations have been presented in some papers (*Vignal and Krajewski*, 2001; *Borga*, 2002; *Germann et al.*, 2006; *Bellon et al.*, 2007). Unfortunately, these studies

did not attempt to verify the quality of the adjusted radar precipitation estimates by using them as an input to a hydrological model.

1.5 Radar measurements and hydrology

The hydrological potential of weather radar has been investigated for individual precipitation events (e.g. *Hossain et al.*, 2004; *Berne et al.*, 2005; *Vieux and Bedient*, 1998; *Ogden et al.*, 2000; *Berenguer et al.*, 2005; *Smith et al.*, 2007) as well as on a longer term basis (*Borga*, 2002; *Neary et al.*, 2004). Most of these studies identify the main benefit of using radar to be the ability to obtain precipitation information at a high resolution in both space and time. Unfortunately, only few of them corrected for all significant sources of error, which makes it difficult to assess to true potential of weather radar for hydrology. Given the challenging nature of measuring precipitation amounts, together with the difficulty of modeling the resulting catchment behavior, the uncertainties in the resulting model output will be significant. This has triggered the recent interest in the use of ensemble stream flow simulations for flood forecasting (e.g. *Carpenter and Georgakakos*, 2006; *Cloke and Pappenberger*, 2009; *Germann et al.*, 2009; *Rossa et al.*, 2011).

Because volumetric weather radars provide a wealth of information on the characteristics of the precipitation field at a much higher spatial resolution than typical networks of rain gauges (*Joss and Waldvogel*, 1990), these instruments are interesting for hydrology. However, if radar precipitation estimates are not corrected for all dominant sources of error, these errors can propagate through the hydrological model, resulting in erroneous discharge simulations (*Vivoni et al.*, 2007; *Collier*, 2009).

Even if weather radar data are corrected for the most dominant sources of error, considerable uncertainty around the estimated precipitation values remains. This uncertainty is caused by uncorrected error sources or by unknown properties of the precipitation field. Therefore, to improve the quality of operational rainfall-runoff forecasts using radar data, this uncertainty needs to be accounted for (*Villarini and Krajewski*, 2010). During the last decade, a number of approaches has been developed to account for these uncertainties using specialized multiplicative and additive statistical error models based on the spatial correlation structure of the precipitation field (e.g. *Ciach et al.*, 2007; *Germann et al.*, 2009; *AghaKouchak et al.*, 2010; *Seo and Krajewski*, 2011). However, in order to apply these data-intensive methods, long term precipi-

tation data from different storm types observed in different seasons are needed. Recently, a limited number of such long data sets has become available (e.g. *Overeem et al.*, 2009; *Boudevillain et al.*, 2011; *Wright et al.*, 2012; *Smith et al.*, 2012), but this is certainly not sufficient for large-scale operational application. Therefore, there is a need to estimate the uncertainty in weather radar precipitation estimates using volumetric weather radar data alone.

1.6 Areas of interest

In the current thesis, the different aspects of weather radar correction and its potential for hydrology are assessed using data obtained from two different regions within Europe. The main region of study is the Ourthe region in Belgium, while an increased understanding on the different aspects of drop size distributions and Z–R relations was obtained using data from the Cévennes-Vivarais region, France.

1.6.1 The Ourthe region, Belgium

The hilly plateaus of the Ardennes, part of the Meuse basin, are situated in the eastern part of Belgium (see Fig. 1.2) and display maximum elevations of around 650 m ASL. The hydrologic response can be classified as rain-fed with some snow in winter. This results in a runoff regime that can be classified as highly variable, giving rise to low discharges in summer and high discharges in winter (*Leander et al.*, 2005).

Within the Ardennes region a weather radar is situated from which the volumetric information is available at a five-minute resolution for the winter period October 1, 2002 until March 31, 2003. During this winter half-year most storms had a stratiform character, for which bright bands could already be observed within 1000 m from the surface.

Directly to the North of the radar lies the ~1600 km^2 Ourthe catchment, which has been the focus of previous studies (*Berne et al.*, 2005; *Driessen et al.*, 2010). Its outlet is situated in the North near Tabreux, at approximately 60 km from the radar. Rain gauge information in the region is available for 69 rain gauges, of which 10 are situated inside the watershed.

1.6.2 The Cévennes-Vivarais region, France

The results presented Chapter 3 were based on data collected within the Cévennes-Vivarais region in the South of France. This region is prone

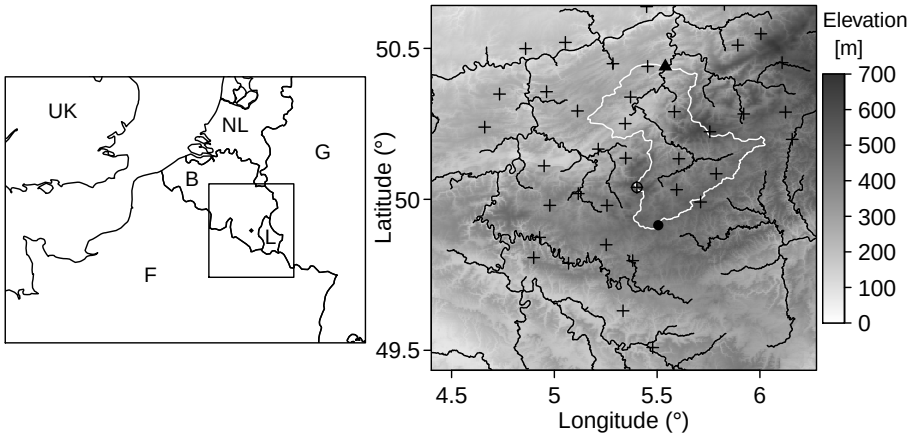

Figure 1.2: The left panel shows the location of the Ourthe region, with a 200 by 200 km box indicating the area shown in the right panel. The right panel shows a topographic map of the Belgian Ardennes, where the solid lines represent the channel network. The white line indicates the Ourthe catchment (1600 km^2). Also shown are the position of the radar (•), catchment outlet (▲), the meteorological station (∘), and the position of the rain gauges (+) (*Hazenberg et al.*, 2011a).

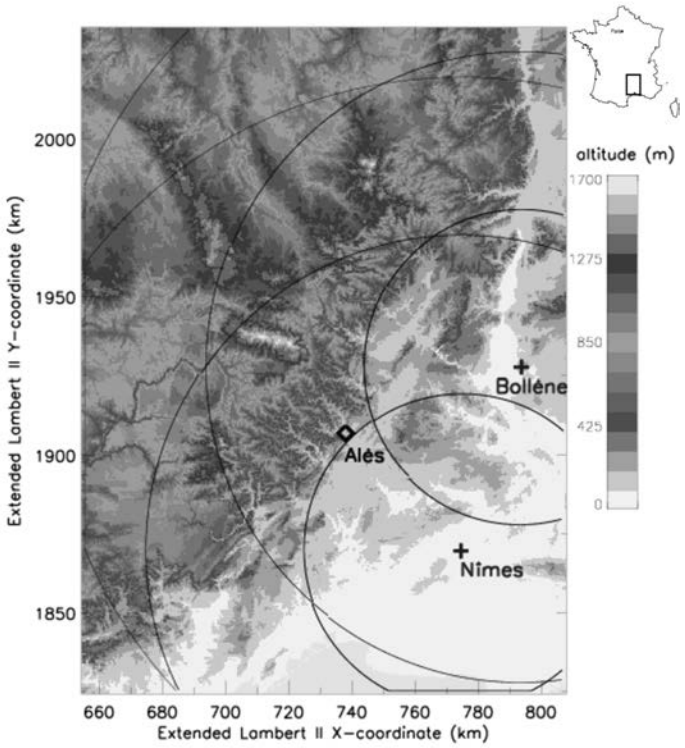

Figure 1.3: Overview of the Cévennes-Vivarais Mediterranean Hydro-meteorological Observatory (OHMCV) in the South of France, which is the region of focus in Chapter 3.

to heavy and long-lasting rainfall events that occasionally lead to severe flash floods. As part of the Cévennes-Vivarais Mediterranean Hydrometeorological Observatory (OHMCV, www.ohmcv.fr), near the city of Alès data were available from an optical OTT/Parsivel disdrometer as well as a tipping bucket raingauge. In addition, data from two Meteo France S-band radars situated near Nîmes and Bollène, at distances of about 48 and 57 km from Alès, respectively, have been applied. An overview of this region is presented in Fig. 1.3.

1.7 Research questions and thesis outline

This thesis deals with the potential of using weather radar data for hydrological purposes. More specifically, the research presented in this

thesis mainly deals with the quality of radar precipitation estimates during a winter period. In Western Europe and many other temperate regions of the world, precipitation is usually of stratiform type in the winter period. A dominant source of error affecting radar rainfall estimation for this type of precipitation is the vertical profile of reflectivity (VPR) (e.g. *Battan*, 1973; *Smith*, 1986; *Joss and Pittini*, 1991). In order to improve the quality of weather radar surface precipitation estimates, data have to be corrected for VPR effects. So far, this has not been straightforward (*Kirstetter et al.*, 2010a).

From a hydrological perspective, the largest flood peaks are usually observed during the winter period in Western Europe. In order to learn more about the complex processes that govern the response of a catchment to precipitation, it is vital to have accurate and robust measurements of this precipitation as well as a clear understanding of the associated uncertainties.

These considerations lead to the following research questions, which will be addressed in this thesis:

1. What are the most dominant sources of error in radar precipitation estimation and what is the best way to correct for them (Chapters 2 and 5)?

2. How are the parameters of the Z–R relation related to the characteristics of the DSD, and how do these parameters relate to each other (Chapter 2)?

3. Is it possible to develop a method that is efficiently able to discriminate between regions with different precipitation types (Chapters 4 and 5)?

4. For a given precipitation region, is it possible to improve the radar estimates of the vertical profile of reflectivity, and to provide uncertainties of these estimates (Chapter 5)?

5. How well can the response of a catchment be modelled using corrected radar precipitation estimates (Chapter6)?

6. What are the contributions to the uncertainties in hydrologic model output of VPR (Chapter 5) and DSD/Z–R (Chapter 3) uncertainties relative to hydrologic model parameter uncertainties (Chapter 6)?

CHAPTER 2

Measuring rainfall using weather radar

2.1 Introduction

Weather radars have long been recognized for their ability to obtain spatio-temporal information about storm fields at a much higher resolution than conventional rain gauge networks (*Zawadzki*, 1975; *Joss and Lee*, 1995; *Smith et al.*, 2001; *Berne et al.*, 2004a). Therefore, large-scale implementation of these systems during the last decades would in principle make this instrument an important tool for rainfall monitoring in the framework of hydrological applications such as (flash)flood forecasting (*Collier and Knowles*, 1986; *Joss and Waldvogel*, 1990; *Carpenter et al.*, 2001; *Vivoni et al.*, 2006).

Unfortunately, data obtained by weather radars are known to be affected by multiple sources of error. Interaction with the nearby environment can result in (partial) beam blockage and backscatter, which especially play a dominant role in mountainous regions. This results either in an under- or overestimation of the amount of precipitation (e.g. *Delrieu et al.*, 1995; *Gabella and Perona*, 1998; *Germann and Joss*, 2002; *Germann et al.*, 2006; *Dinku et al.*, 2002). Other sources of error are

This chapter is a slightly modified version of: Hazenberg, P., H. Leijnse, and R. Uijlenhoet (2011), Radar rainfall estimation of stratiform winter precipitation in the Belgian Ardennes, *Water Resour. Res.*, *47*, W02507, doi:10.1029/2010WR009068.

related to temporal changes of the index of refraction (e.g. *Fabry et al.*, 1997; *Steiner and Smith*, 2002), variability of the drop size distribution (e.g. *Waldvogel*, 1974; *Berenguer and Zawadzki*, 2008), and variability of the vertical profile of reflectivity (VPR) (e.g. *Fabry and Zawadzki*, 1995; *Smyth and Illingworth*, 1998; *Cluckie et al.*, 2000).

During the past decades different techniques have been developed to correct for these types of errors, resulting in a serious improvement in the radar data quality (e.g. *Kitchen and Jackson*, 1993; *Ciach et al.*, 1997; *Pellarin et al.*, 2002; *Gourley et al.*, 2009). *Joss and Lee* (1995) implemented a stepwise algorithm identifying clutter, and correcting for beam occultation, radar calibration errors and VPR effects using either a climatological or real-time profile estimate. *Anagnostou and Krajewski* (1999a,b) developed a similar system for an environment where topography causes no serious problems. In all of these studies rain gauge measurements were used to correct for any final bias. A different approach was taken by *Delrieu et al.* (2009) for a series of extreme precipitation events within a mountainous environment in the southern part of France. Besides correcting for the errors mentioned above, the type of precipitation (convective vs. stratiform) was identified as well. This resulted in a radar product of which the quality is comparable to that of rain gauge measurements.

The impact of radar correction steps for stratiform precipitation systems occurring within a winter period has received less attention. During such situations, the upper part of the atmosphere consists of snow and ice particles. The melting of these particles results in a stronger return signal, known as the bright band, and causes the amount of precipitation to be overestimated by the weather radar. For the snow/ice region above the bright band a significant decrease in the returned reflectivity signal can be observed. Especially at further ranges, reflectivity samples originate from these two regions, which has a detrimental impact on the quality of the radar product (*Fabry et al.*, 1992; *Kitchen and Jackson*, 1993; *Bellon et al.*, 2005). Long-term investigations of the influence of different correction mechanisms for such stratiform situations have been presented in some papers (*Vignal and Krajewski*, 2001; *Borga*, 2002; *Germann et al.*, 2006; *Bellon et al.*, 2007). Unfortunately, these studies did not attempt to verify the quality of the adjusted radar product by using it as an input to a hydrological model.

The hydrological potential of weather radar has been investigated for both individual precipitation events (e.g. *Hossain et al.*, 2004; *Berne et al.*, 2005; *Vieux and Bedient*, 1998; *Ogden et al.*, 2000; *Smith et al.*,

2007) or on a longer term basis (*Borga*, 2002; *Neary et al.*, 2004). Most of these studies identify the benefits of using radar (i.e., the ability to obtain spatial-temporal properties of the precipitation field at a high resolution). Unfortunately, only few of them corrected for all significant types of measurement errors. As a consequence, obtained results using weather radar rainfall information as an input to a hydrological model are highly dependent on the quality of the data and the environment of application.

This chapter addresses the importance of correcting volumetric radar reflectivity data, and the applicability of these correction steps for long-term real-time hydrological purposes. The region studied is situated in the Belgian Ardennes mountain range and focuses on a winter half-year during which most of the precipitation has a stratiform character. Volumetric radar data is corrected for errors associated with attenuation, ground clutter and anomalous propagation conditions, VPR, and advection. It was decided not to correct for the remaining final bias between the amount of precipitation estimated by the radar and a rain gauge network. This to get a better understanding of the quality of the radar and because of inherent scale problems between both devices (e.g. *Austin*, 1987; *Kitchen and Blackall*, 1992; *Steiner et al.*, 1999; *Ciach and Krajewski*, 1999a; *Morin et al.*, 2003).

The chapter is organized as follows. Section 2.2 will give an overview of the study area and data availability. Section 2.3 focuses on the different radar correction steps that have been implemented, followed by a comparison with rain gauge measurements for a series of events (Section 2.4). Next, a whole winter period is analyzed (Section 2.5). The different implementations are discussed in Section 2.6, in which we will also present an application to real-time hydrological modeling at the catchment scale.

2.2 Study area and data availability

The hilly plateaus of the Ardennes, part of the Meuse basin, are situated in the eastern part of Belgium (see Fig. 2.1) and display maximum elevations of around 650 m ASL. The hydrologic response can be classified as rain-fed with some snow in winter. This results in a runoff regime that can be classified as highly variable, giving rise to low discharges in summer and high discharges in winter (*Leander et al.*, 2005).

In 2001 a C-band Doppler radar was installed at an elevation of 600 m ASL near the village of Wideumont, close to the border with

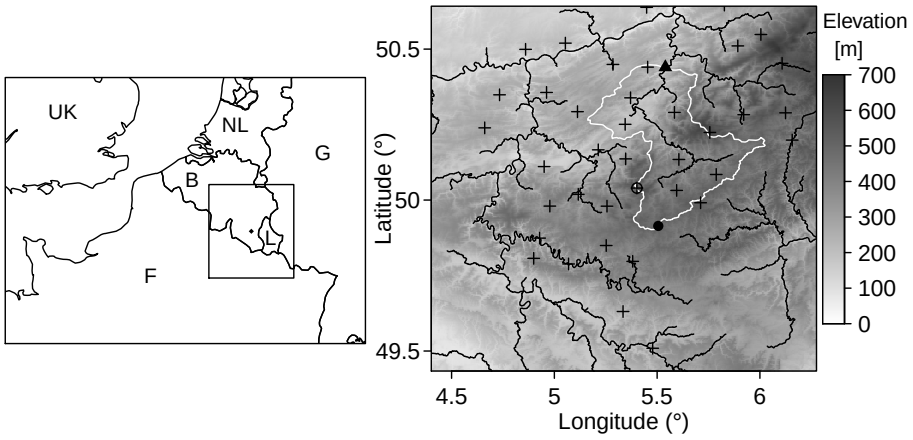

Figure 2.1: The left panel shows the location of the study area, with a 200 by 200 km box indicating the area shown in the right panel. The right panel shows a topographic map of the Belgian Ardennes, where the solid lines represent the channel network. The white line indicates the Ourthe catchment (1600 km^2). Also shown are the position of the radar (•), catchment outlet (▲), the meteorological station (∘), and the position of the rain gauges (+).

Luxembourg. The radar has two scan sequences; one every five minutes at five different elevations and a second scan at another ten elevations every fifteen minutes. In this study the five-minute data were used to obtain areal information about the precipitation field. The reflectivity data from the second scan serves only to obtain an initial estimate of the VPR. A summary of the characteristics of the weather radar is presented in Table 2.1.

Directly to the North of the radar lies the ~1600 km^2 Ourthe catchment, which has been the focus of previous studies (*Berne et al.*, 2005; *Driessen et al.*, 2010). Its outlet is situated in the North near Tabreux, at approximately 60 km from the radar. Rain gauge information in the region is available for 42 rain gauges, of which 10 are directly situated inside the watershed. Besides that, hourly temperature and potential evaporation data are available from the weather station near St. Hubert (see Fig. 1.2).

This study analyzes the spatial and temporal characteristics of rainstorms and the resulting catchment response of the Ourthe for the period from October 1, 2002 until March 31, 2003. During this winter half-year most storms had a stratiform character, for which bright bands could

Table 2.1: Characteristics of the C-band Doppler radar at Wideumont used in this study.

Parameter	Value
Coordinates lat/lon [°]	49.91, 5.51
Height [m ASL]	600
Frequency [GHz]	5.64
PRF [Hz]	600
Beam width [°]	1
Antenna diameter [m]	4.2
Maximum range [km]	240
Scanning sequences	2
Pulse length [m]	250 (scan 1)
	500 (scan 2)
Recurrence interval [min]	5 (scan 1)
	15 (scan 2)
Elevations [°]	0.3, 0.9, 1.8, 3.3, 6.0 (scan 1)
	0.5, 1.2, 1.9, 2.6, 3.3,
	4.0, 4.9, 6.5, 9.4, 17.5 (scan 2)

already be observed within 1000 m from the surface. Radar data are not available for the second week of November and for one day at the end of March. These periods are left out of the analysis. For the hydrological analysis they are substituted by rain gauge data.

2.3 Radar reflectivity analysis

The general measurement equation of the radar can be stated as follows:

$$P(r) = \frac{CZ_m(r)}{r^2} \tag{2.1}$$

where $P(r)$ is the received power [W] for a given elevation at a range r [m] from the radar, C [$\mathrm{W\,m^5\,mm^{-6}}$] is the radar constant and $Z_m(r)$ is the measured reflectivity [$\mathrm{mm^6\,m^{-3}}$]. Both the radar reflectivity and rainfall intensity R [$\mathrm{mm\ h^{-1}}$] are dependent on the raindrop size distribution. The relationship between both parameters is generally assumed to follow a power law (*Marshall and Palmer*, 1948; *Marshall et al.*, 1955; *Battan*, 1973)

$$Z = aR^b, \tag{2.2}$$

where the parameters a and b are a function of the raindrop size distribution and vary with precipitation type (*Ulbrich*, 1983). Before radar data can be used for hydrological purposes, errors related to the environment and spatio-temporal atmospheric variations should be accounted for (*Andrieu et al.*, 1997). Based on the characteristics of the weather radar (see Table 2.1) and the Ardennes mountain range, it was therefore decided to correct the data for losses due to attenuation, artifacts due to clutter, range effects due to VPR, and potential errors due to finite sampling of rainfall. Although the radar data may be affected by other types of errors (e.g. radome attenuation, radar calibration, partial beam filling, blockage and overshooting), these four are considered to be the main sources of error for the environment under study. The following sections present an in-depth overview of the different steps taken to correct for these four sources of errors.

2.3.1 Signal attenuation

Signal attenuation can become a source of error for operational C-band weather radars, especially during high rainfall intensities, and depends on both the raindrop size distribution and temperature (e.g. *Delrieu et al.*, 1991, 1997; *Berenguer et al.*, 2002). One method to correct for attenuation was developed by *Hitschfeld and Bordan* (1954) (HB algorithm). The measured radar reflectivity is the product of two terms

$$Z_m(r) = Z_a(r)A(r), \tag{2.3}$$

where $Z_a(r)$ [$\mathrm{mm^6\,m^{-3}}$] is the apparent reflectivity at a given height not subject to any attenuation. In this study, it is assumed that the radar is well-calibrated and there are no signal losses due to wet radome effects. Then, the amount of two-way path-integrated attenuation (PIA) [dB] is given by

$$A(r) = \exp\left[-\frac{2\ln 10}{10}\int_0^r k(s)ds\right]. \tag{2.4}$$

In this last equation $k(s)$ [$\mathrm{dB\,km^{-1}}$] is the specific attenuation at a distance s [km]. The relation between the reflectivity and specific attenuation can also be stated as a power law

$$Z = ck^d. \tag{2.5}$$

On the basis of Eqs. (2.3), (2.4) and (2.5), the apparent reflectivity can be expressed as

$$Z_a(r) = \frac{Z_m(r)}{\left[1 - \frac{2\ln 10}{10d} \int_0^r \left(\frac{Z_m(s)}{c}\right)^{1/d} ds\right]^d}. \quad (2.6)$$

In case of severe attenuation the denominator of Eq. 2.5 becomes small, causing the HB algorithm to become unstable. Another algorithm (originally developed for space-borne radar, see *Marzoug and Amayenc*, 1994), which is not prone to this source of error, makes use of a mountain reference (*Delrieu et al.*, 1997; *Bouilloud et al.*, 2009). Unfortunately, in the current study mountainous returns are limited to a region close to the radar and cannot be applied for attenuation correction. Although it can be expected that the amount of PIA is limited for the stratiform precipitation encountered during a winter period (*Delrieu et al.*, 1999, 2000; *Uijlenhoet and Berne*, 2008), the maximum amount of PIA was set to 10 dB to prevent the algorithm from becoming unstable. The parameter values of the Z–k relation (Eq. 2.5) were estimated based on drop size distributions sampled in the Netherlands (*Uijlenhoet*, 2008), with c=7.34×10^5 and d = 1.344. These were assumed to originate from similar storm systems as those observed in the Ardennes region.

2.3.2 Anomalous propagation and clutter identification

Radar data in mountainous environments can be contaminated by ground clutter (GC) due to side lobe reflections from and/or (partial) blockage by topography (e.g. *Delrieu et al.*, 1995; *Gabella and Perona*, 1998; *Pellarin et al.*, 2002). Anomalous propagation (AP) occurs in situations where the vertical gradient of refractivity is large in the lower part of the atmosphere, causing the radar signal to bend down towards the surface, resulting in ground echoes (e.g. *Alberoni et al.*, 2001; *Steiner and Smith*, 2002; *Cho et al.*, 2006; *Berenguer et al.*, 2006). Especially at longer ranges, AP-induced GC can result in serious overestimates of the amount of precipitation (*Andrieu et al.*, 1997).

In literature, multiple GC identification techniques have been proposed, using either pulse to pulse reflectivity fluctuations (*Wessels and Beekhuis*, 1994), radial Doppler velocity information (*Joss and Lee*, 1995), spatial reflectivity information (*Alberoni et al.*, 2001), or dual polarization data (*Giuli et al.*, 1991). Other sources of data have also been used to identify GC, such as a digital elevation models (DEM), temperature, or satellite information (e.g. *Delrieu et al.*, 1995; *Michelson and Sunhede*, 2004; *Fornasiero et al.*, 2006). Nowadays, most GC

identification algorithms make use of a classification scheme using multiple information criteria (e.g. *Joss and Pittini*, 1991; *Joss and Lee*, 1995; *Steiner and Smith*, 2002; *Grecu and Krajewski*, 2000; *Berenguer et al.*, 2006; *Cho et al.*, 2006). In the framework of this study it was decided to use the identification tree as proposed by *Steiner and Smith* (2002), because no radial velocity information was available. The original algorithm was extended to all elevations to also identify GC pixels for the higher radar elevations as well. In the first step, a polar pixel is identified as GC if it has a minimum vertical extent less then 500 m. Next, radar pixels for which spatial variability and vertical variability both exceed a threshold value are identified as clutter. Further details of this method can be found in *Steiner and Smith* (2002). Within mountainous environments beam occultation causes a decrease in the total beam power, resulting in an underestimation by the radar (*Delrieu et al.*, 1995). For this type of error no corrections were implemented because the Wideumont radar is situated at a relatively high altitude within the region. It is assumed that most of the observed GC is caused by side lobe interception instead of direct blockage of the main beam, and that therefore no beam occultation occurs.

2.3.3 Identification of the vertical profile of reflectivity

As explained in the introduction, variation in the vertical structure of the precipitation field can be a serious source of error, especially for stratiform precipitation (*Andrieu et al.*, 1997; *Seo et al.*, 2000). *Kitchen et al.* (1994) applied a correction method which updates the shape of a theoretical stratiform VPR using local meteorological characteristics. Results showed significant improvement in the estimated amount of precipitation. *Germann and Joss* (2002) estimate a spatially variable apparent VPR based on measured volumetric weather radar data for regions up to 70 km from the radar (the meso-β scale). What these investigators and others (e.g. *Dinku et al.*, 2002; *Jordan et al.*, 2003) did not consider is the fact that the radar sampling volume increases with range.

A method which does take this aspect into account is the inverse VPR identification technique of *Andrieu and Creutin* (1995), which was extended for volumetric radar data by *Vignal et al.* (1999). The main assumptions behind this method are a spatially uniform VPR over a certain region and the decomposition of the spatial variation of the apparent reflectivity $Z_a(r)$ (Eq. (2.3)) into a horizontal and vertical component

$$Z_a(r) = Z_{REF}(x) z_a(y). \tag{2.7}$$

Here $Z_{REF}(x)$ is the reflectivity at a certain reference level at distance x from the radar, $z_a(y)$ is the apparent vertical profile of reflectivity, which is influenced by the increase of the radar beam volume as a function of range. This latter effect can be written in a simplified way as

$$z_a(y) = \int f^2(\theta_0, y) z(y) dy, \tag{2.8}$$

where f is the power distribution of the radar signal, θ_0 is the radar beam width and $z(y)$ represents the actual average vertical reflectivity signal. The numerical solution discretizes $z(y)$ into finite intervals of a few hundred meters. For each of these increments at a given range from the radar, its contribution to the total power distribution of the transmitted signal is calculated. In order to estimate the discretized profile of $z(y)$, two types of information are needed. First, an initial estimate of the VPR, for which either a climatological profile or one estimated from the sampled volumetric data can be used. The second type of information needed are the so-called ratio functions, which represent the ratio of one of the higher elevations with respect to the bottom one as a function of distance. Theoretical ratio functions are also calculated for the initial VPR using the characteristics of the radar. Then, using an inverse optimization scheme (*Menke*, 1989) the initial VPR is adjusted in such a way as to minimize the difference between the theoretical and measured ratio functions.

This inverse method is well able to identify VPRs for stratiform situations with low level bright bands (*Borga et al.*, 1997). Therefore, in this study this technique is applied to obtain a VPR estimate. During winter, most of the storm systems passing over the Ardennes have an echotop well below 6 km. The estimates of the VPR are therefore performed up to a height of 6 km at 250 m increments in the current study. The power distribution at a given distance from the radar for the different intervals was calculated based on the radar characteristics. It is decided to use only the information within a fifteen-minute window to diminish the effect of temporal changes in the VPR (*Fabry et al.*, 1992; *Bellon et al.*, 2005; *Joss et al.*, 2006). The initial VPR estimate is obtained by combining all volumetric data of both scanning sequences (see Section 2.2) within a fifteen-minute window for distances between 10 to 50 km from the radar. Next, based on the fifteen-minute interval volumetric data for the first scanning sequence the ratio profiles are estimated up to a distance of 100 km. This is done by calculating the ratios of the measured reflectivity values for the four higher elevations (2-5) with respect to the bottom elevation reflectivity values. These are

subsequently averaged over all polar radar cells at a given range. Once both the initial VPR estimate and the four sampled ratio profiles are obtained, the inverse optimization method is applied from which a final spatially averaged VPR is obtained.

Although different studies have shown improved radar rainfall estimates when this method is applied (*Andrieu et al.*, 1995; *Anagnostou and Krajewski*, 1999b; *Vignal et al.*, 1999), a critical aspect is the assumption of a spatially uniform profile. *Vignal et al.* (2000) therefore identified the VPR for regions of 20×20 km. *Delrieu et al.* (2009) proposed first to select the type of precipitation system (convective, stratiform and undefined) and then estimate the VPR for each type separately. To analyze the option of using a local VPR, in this study a profile is also estimated based on the polar reflectivity data sampled over the Ourthe catchment only. In this manner, a catchment-scale VPR is obtained, which also improves the consistency between the spatial and temporal meteorological scales (*Germann and Joss*, 2002). No precipitation identification has been performed because in general, during the period of interest, most precipitation originates from stratiform systems only.

2.3.4 Beam integration and grid conversion

After correcting for the three mentioned types of error (associated with attenuation, ground clutter and VPR, respectively), the final step is to obtain a 2D-corrected polar reflectivity field. Similar to other radar correction algorithms operating in a mountainous environment (e.g. *Joss and Lee*, 1995; *Germann and Joss*, 2002; *Delrieu et al.*, 2009), a weighted average was taken over the different radar elevations up to a height of 2500 m. Polar cells which were identified as GC are not taken into account. Each elevation at each point was weighted using $1/(h+1)$, where h is the height [m] of the measurement, because of the assumption that lower elevations give a better estimate of the true reflectivity at the surface. The maximum measurement elevation of 2500 m was identified because most precipitation systems in this region for the period of interest have a small vertical extent. This maximum is similar to the study of *Anagnostou and Krajewski* (1999b). After this aggregation step, all polar points are converted to a Cartesian grid by averaging those corresponding to a given Cartesian grid cell. In case a Cartesian cell does not contain at least three corresponding polar points, interpolation with respect to the three nearest points is performed.

2.3.5 Storm field advection and Z–R conversion

Because of the temporal scanning strategy of the radar it is necessary to take the advection velocity of the precipitation field into account (e.g. *Fabry et al.*, 1994; *Jordan et al.*, 2000). To correct for this source of error a correlation-based technique is applied (e.g. *Rinehart and Garvey*, 1978; *Tuttle and Foote*, 1990; *Anagnostou and Krajewski*, 1999a). The Cartesian grid is subdivided into 20×20 km grid blocks. For each of these, the advection direction and velocity are calculated by maximizing the correlation between two consecutive reflectivity (dBZ) fields. It is known that in case of a spatially homogeneous precipitation field, or due to the influence of residual GC, the obtained advection direction and velocity could differ from the actual ones when calculated in this manner (*Tuttle and Foote*, 1990; *Li et al.*, 1995). In order to minimize this possibility, advection directions are averaged over 40×40 km grid blocks removing those values with correlation < 0.7. Using the resulting advection field, the radar data are then interpolated in time at 30-second intervals. Growth and decay of the storm field are not considered here.

To convert the obtained radar reflectivity to an equivalent rainfall rate (Eq. (2.2)), the Marshall-Palmer relationship $Z = 200R^{1.6}$ is applied (*Marshall et al.*, 1955). This relationship is generally assumed to be representative for stratiform situations (*Battan*, 1973). Radar data are then avaraged into hourly intervals.

One problem not accounted for in the current algorithm implementation is related to possible temporal changes in the transmitted power of the weather radar in Eq. 2.1 (*Ulbrich and Lee*, 1999). Steady clutter points could be used to get an indication of such changes. Results based on a few steady polar GC points for the Wideumont radar indeed showed a non-constant backscatter. Unfortunately, it is difficult to isolate such variations from apparent changes in the refractivity or from temporal changes in vegetation and the occurrence of snow at the surface (*Delrieu et al.*, 1995). It was therefore decided not to take this aspect into account.

In many studies an additional step is performed to remove any residual bias with respect to rain gauge measurements (e.g. *Krajewski et al.*, 1996; *Smith and Krajewski*, 1991; *Ciach and Krajewski*, 1999a; *Seo and Breidenbach*, 2002; *Goudenhoofdt and Delobbe*, 2009). Such a final step is not implemented here, because we feel that by correcting the data based on the volumetric measurements only, the full hydrological potential of weather radar in a hilly environment can be analyzed.

2.4 The importance of the different correction steps

In this section the influence of the correction steps is analyzed by comparing 42 hourly radar-rain gauge pairs for three rainfall events typical to the region for a winter period. In order to reduce the effect of sampling differences between radar and rain gauge measurements (*Joss and Lee*, 1995), hourly rainfall accumulations are compared.

2.4.1 Event 1: A stratiform system

The first event selected was a fast moving stratiform system which started at around 20:00 UTC and lasted for about 9 hours. Average reflectivities in the range 30-43 dBZ were observed, as well as a clear bright band at around 1800 m above the radar.

In the upper part of Fig. 2.2 the total event accumulation for the uncorrected (a) and corrected radar data (b) are presented. Comparison of both plots immediately shows the impact of both the clutter correction and advection algorithm. Not taking the former into account leads to an overestimation of the amount of precipitation. While for the latter the observed small-scale pattern in (a) do not represent reality.

For each time step, at a given polar radar pixel at a 10-50 km distance, the reflectivity values sampled at one of the higher radar elevations were normalized with the lowest elevation by taking the ratio. Based on these ratios for each 250 m interval up to a height of 6 km a frequency plot was created. This frequency is indicated by the gray shading in Fig. 2.2c. Such a frequency diagram is similar to the CFAD profile by *Yuter and Houze Jr.* (1995b) or the meso-γ profile by *Germann and Joss* (2002). Besides the occurrence of a bright band, it can also be observed that the distribution of VPRs is very broad.

The average VPR calculated from the frequency distribution is indicated by the dotted line. As explained in Section 2, beam broadening was not taken into account for this profile. Together with the measured reflectivity ratios in Fig. 2.2d (dashed lines), it serves as the initial VPR estimate. Using the inverse identification method of *Andrieu and Creutin* (1995) the final VPR was estimated, which is used to correct radar data for VPR effects. This profile is indicated by the black line in Fig. 2.2c. Compared to the initial VPR obtained from the radar data, it can be observed that especially the bright band is more intense for the final profile. In order to indicate how well this final profile is able to represent a spatially averaged VPR, the characteristics of the radar

were used to estimate the theoretical ratio functions. When compared to the observed ratio functions, it can be observed that they show a good correspondence. The differences that do occur are related to the spatial non-uniformity of the VPR as represented by the spread in gray shading areas in Fig. 2.2c.

The correspondence between the corrected radar rainfall estimates and the different rain gauges is shown in Fig. 2.3. Hourly precipitation depths are well correlated in (a), although overall radar rainfall estimates are lower than those from the rain gauges. This is also confirmed by the storm accumulations in (b). Linear regression without intercept between the different radar-rain gauge pairs (gray line) confirms the underestimation by the radar. At the hourly and total event scale the regression-based underestimation was about 29% and 34%, respectively. Such large differences are not uncommon for radar-rain gauge comparisons, especially for stratiform systems.

To investigate whether the observed errors can be related to range effects, the lower panel of Fig. 2.3 shows the event accumulation ratios and Nash-Sutcliffe (NS) coefficients (*Nash and Sutcliffe*, 1970) of the different radar-rain gauge pairs as a function of distance from the radar. A Radar/Gauge ratio less than one (c) indicates an underestimation by the radar. In both (c) and (d) a range effect can be observed. Up to about 60 km the behavior is rather constant. At greater distances the difference between both instruments increases. It is expected that this is due to the usage of a global VPR. The estimated profile in Fig. 2.2c generally tends to give more weight to the reflectivity values close to the radar. For the current event, storm cells observed further away from the radar had a slightly different average VPR than presented in Fig. 2.2c, and were therefore not always properly VPR-corrected. This reveals a drawback of estimating one single VPR profile for the entire radar umbrella (*Vignal et al.*, 1999).

Table 2.2 presents the influence of the different correction steps on the radar-rain gauge comparison statistics. Uncorrected (raw) radar data are well able to capture the dynamic pattern of the storm system as indicated by the large coefficient of determination (ρ^2). However, the correspondence between these radar rainfall estimates and those from the raingauge is poor, containing an overall positive bias and very small Nash-Suthcliffe statistic. A large improvement in the quality of the data is obtained when correcting for clutter (as could be observed from Figs. 2.2a and b). Correcting for attenuation leads to a bias improvement. The implementation of the VPR correction method on average does not

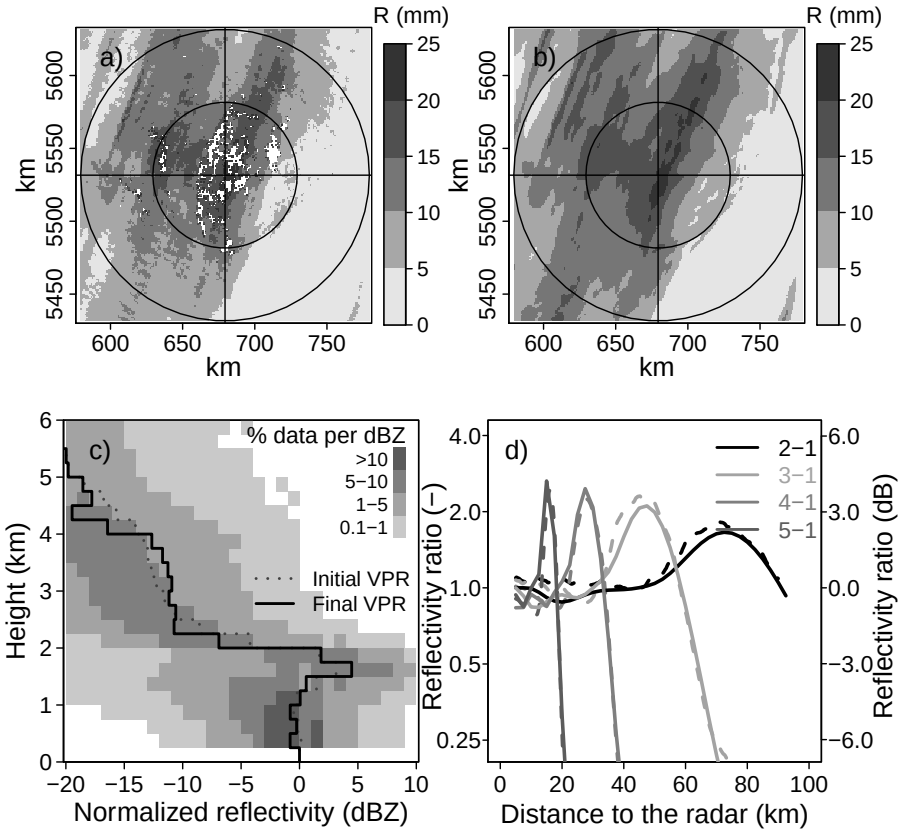

Figure 2.2: Upper panels show the total storm accumulation for uncorrected (a) and fully corrected (b) radar data for the event on October 22-23, 2002. White areas correspond to severe ground clutter leading to an overestimation. Panel c) shows the initial estimate of the VPR, the final VPR obtained using the inverse method, and a frequency plot of the measured normalized VPR (similar to the CFAD of *Yuter and Houze Jr.* (1995b)). Panel d) shows the measured reflectivity and simulated reflectivity ratios using the obtained final VPR. Different colors represent the ratio between a given elevation and the lowest one. The data for panels c) and d) correspond to a fifteen-minute time window sampled around 11:00 PM UTC on October 22.

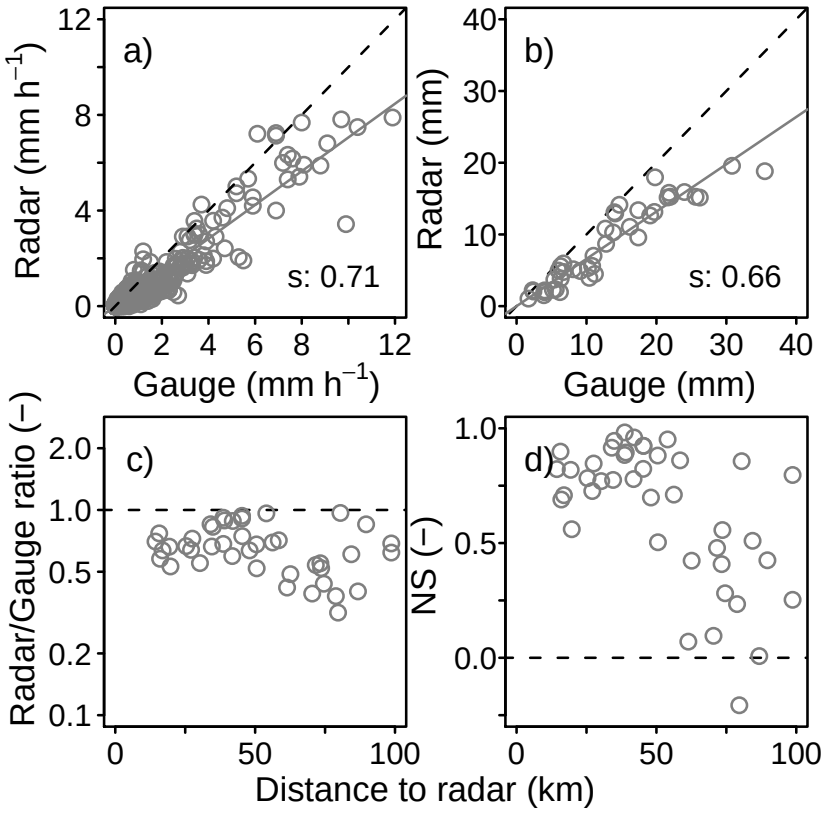

Figure 2.3: Comparison of rainfall intensities and accumulations from 42 rain gauges and the corresponding radar pixels for the event on October 22-23, 2002. The upper panels show scatter plots of the hourly a) and total event b) rainfall accumulation for the 42 pairs. The gray lines correspond to the linear regression between the two, of which the slope is given by s. The bottom panels show the quality of the radar measurement as a function of range from the radar, where radar/gauge ratio was defined as $\sum \text{Radarrainfall} / \sum \text{Gaugerainfall}$ for a given gauge. NS is the Nash-Sutcliffe statistic (*Nash and Sutcliffe*, 1970).

Table 2.2: Evaluation of the influence of the different radar correction steps for the event on October 22-23, 2002. Column headers correspond to: Raw - no radar correction, Clut - correction only for clutter, Atten - correction also for attenuation, VPR - correction also for VPR, Advec - correction also for advection. The last two columns represent the results for the 10 gauges within the Ourthe catchment using either a global (G-VPR) or catchment (C-VPR) VPR estimate. The statistics were calculated on the basis of hourly information and represent the coefficient of determination (ρ^2), the ratio $\sum$Radarrainfall/$\sum$Gaugerainfall and the Nash-Sutcliffe statistic (NS).

Statistic	Raw	Clut	Atten	VPR	Advec	G-VPR	C-VPR
ρ^2	0.85	0.87	0.86	0.84	0.85	0.95	0.95
$\sum$R/$\sum$G	1.19	0.59	0.67	0.66	0.66	0.76	0.75
NS	-4.53	0.60	0.66	0.65	0.65	0.85	0.85

improve the correspondence between both types of data. As mentioned before, the estimated VPR depends heavily on the data sampled close to the radar. Therefore, the benefit of the VPR correction at close ranges may be counteracted by worse results at larger distances. This latter phenomenon can also be observed in Fig. 2.3c and d. For the current event, advection correction did not lead to any serious improvements in the measurement quality of the weather radar data.

In the last two columns of Table 2.2 the impact of using either a global or local VPR is presented, comparing the radar results to the 10 gauges situated inside the catchment. Estimating a VPR based on the volumetric data sampled above the Ourthe catchment only does not lead to any improvement. The main reason for this is related to the large size of the catchment and the fact that it is situated close to the radar. Both aspects result in a large overlap with the reflectivity data used to obtain the global VPR estimate. Differences in the obtained local and global VPR shapes are therefore small.

Overall it can be stated that for this event, up to about 60 km the radar was able to estimate the actual rainfall accumulation well. On average, up to these distances the bias between both instruments is about 25%. At larger distances from the radar, spatial variability of the VPR makes it impossible to obtain better results. Instead of applying one global profile estimate, a spatially varying estimate would probably improve the overall statistics for this event.

2.4.2 Event 2: Large scale stratiform system

The second event analyzed here took place on December 22, 2002 and started around 3:00 UTC, lasting for about 13 hours. From the volumetric radar data (not shown) a clear bright band could be observed at a height of 1800 m above the radar. The precipitation system was relatively uniform and very widespread covering almost the full radar image with average reflectivities in the range 20-30 dBZ.

The widespread character of the precipitation system causes some unwanted results for the GC and advection algorithms (Fig. 2.4a and b). Although most GC is filtered out, some clutter-contaminated spots are still observed. This is related to the fairly uniform reflectivity field, which decreases the amount of spatial irregularity. Some clutter is therefore not identified. As explained in Section 2.3.5, a spatially homogeneous precipitation field and/or residual GC might result in an incorrect identification of the advection direction (*Tuttle and Foote*, 1990; *Li et al.*, 1995). Even though we tried to correct for this, some artifacts (straight/blocky lines) of this problem can be observed Fig. 2.4b, although their impact is small.

The spatial variability of the vertical profile is rather limited, as shown by the narrow frequency diagram of the normalized VPR in Fig. 2.4c. The good correspondence between the observed and simulated ratio profiles in (d) was therefore expected, giving a lot of confidence in the final VPR estimate.

The radar-rain gauge comparisons in Fig. 2.5 show an underestimation of the radar for both the hourly (a) and total event accumulations (b). For the hourly data, the overall spread is much larger than in Fig. 2.3, which is due to variations in the type of precipitation, probably changing from showers into drizzle and vice versa. Especially for the latter the Marshall-Palmer Z–R relationship is known not to be representative, but underestimates precipitation intensities (*Battan*, 1973), as is also clearly the case here. As a result, the radar underestimates the amount of precipitation.

The overall statistics in Table 2.3 reveal a poor correspondence between the 42 radar and rain gauge points. Again the biggest improvement is made by correcting for GC. VPR correction removes the influence of the overestimation due to the bright band, resulting in an increase in the radar quality as seen by the Nash-Sutcliffe statistic (NS). Correcting for attenuation leads to some improvements with respect to the bias in Table 2.3, while advection correction has no serious influence due to the moderate reflectivity variations and velocity of the observed

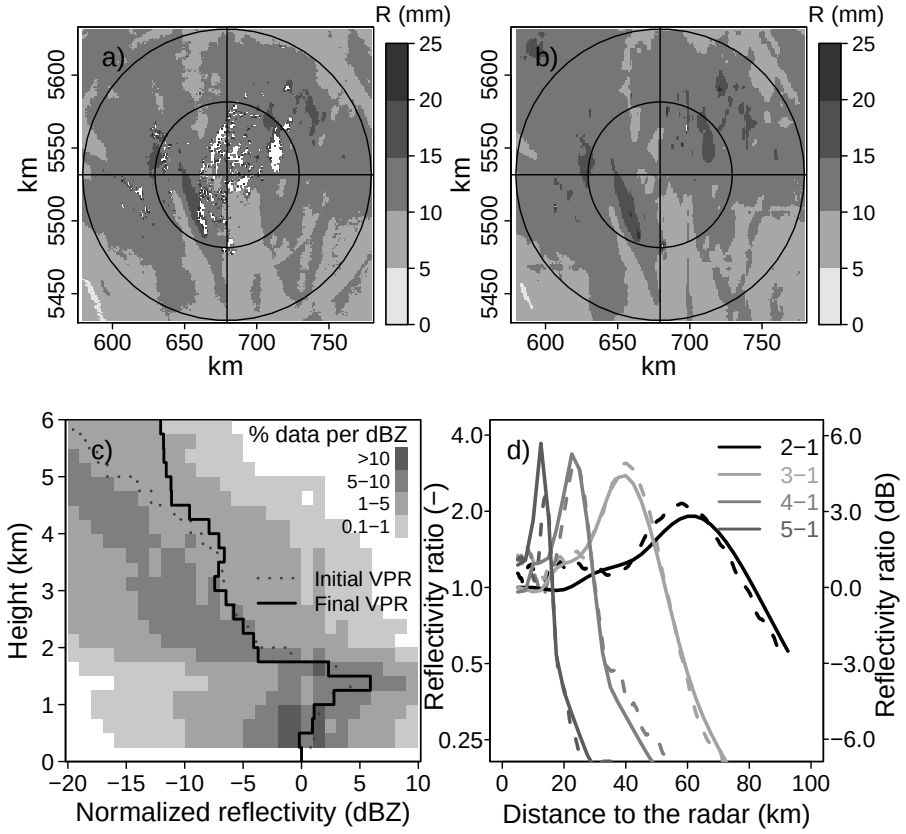

Figure 2.4: As Fig. 2.2, for the event on December 22, 2002. The data for panels c) and d) correspond to a fifteen-minute time window around 9:00 AM UTC on December 22.

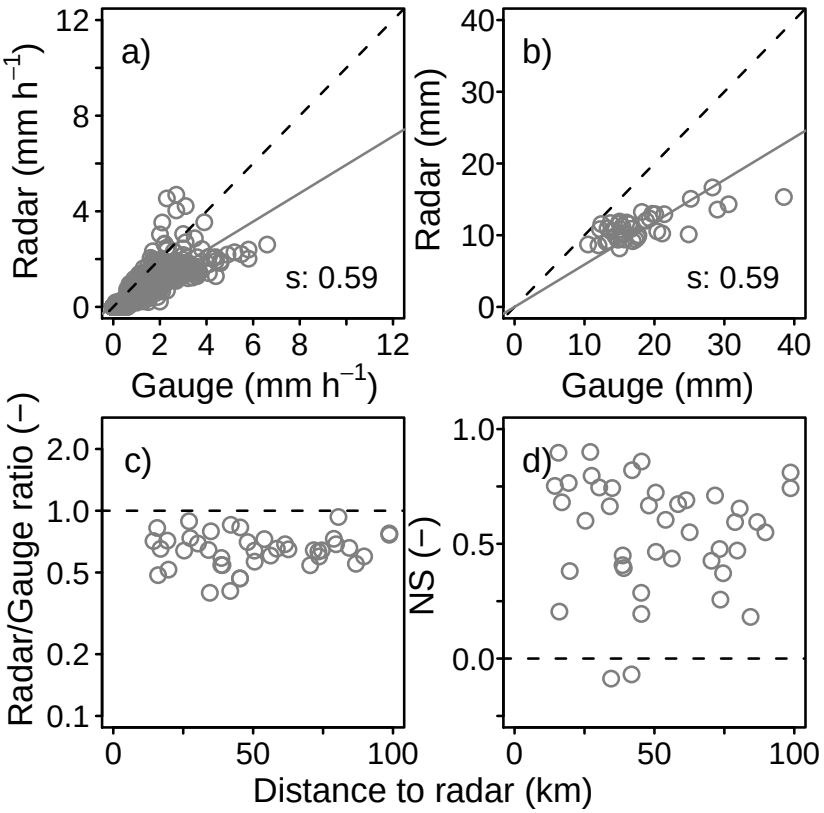

Figure 2.5: As Fig. 2.3, for the event on December 22, 2002.

Table 2.3: As Table 2.2, but for the event on December 22, 2002.

Statistic	Raw	Clut	Atten	VPR	Advec	G-VPR	C-VPR
ρ^2	0.77	0.79	0.78	0.83	0.83	0.87	0.86
$\sum$R/$\sum$G	1.03	0.68	0.72	0.69	0.69	0.72	0.69
NS	-4.89	0.54	0.54	0.58	0.58	0.71	0.67

precipitation field.

The slightly worse result when using a catchment-based VPR estimate instead of the global VPR are related to a slightly larger normalized bright band size estimated on the basis of the catchment reflectivity data (not shown here). Correcting the radar data based on this VPR leads to smaller reflectivity values and rainfall estimates and thus slightly worse results.

2.4.3 Event 3: Fast moving frontal stratiform system

During the third event analyzed here, large overall accumulations could be observed in the Ardennes region, which resulted in the largest flood peak measured within the half-year period. The event started on January 1, 2003 at around 10:00 UTC and had a total duration of about 42 hours. Radar images (not shown) revealed that the storm consisted of a series of fast moving stratiform showers exhibiting considerable horizontal variability of the reflectivity field and, from time to time, well-developed bright bands at around 1500 m above the radar.

Figs. 2.6a and b again show the positive influence of the different radar correction steps on the overall storm accumulations. For the current event hourly radar-gauge values line up well in Fig. 2.7a. On average an underestimation by the radar (29%) can be observed. A closer look at the accumulations in (b) reveals that only five gauges measured much more precipitation than was estimated by the radar. These gauges are all situated to the South-West of the radar. There are three possible reasons for these differences between both instruments. As mentioned, the observed storm field was highly variable in space (Fig. 2.6c), especially in the South-Westward direction from the radar. This resulted in some precipitation to be identified as GC. Spatial variability in the VPR might have produced inappropriate corrections when using the global VPR estimate for the South-Westward region. Besides that, it is possible that the usage of the Marshall-Palmer Z–R relationship was not optimal due to local variation in the type of precipitation for this

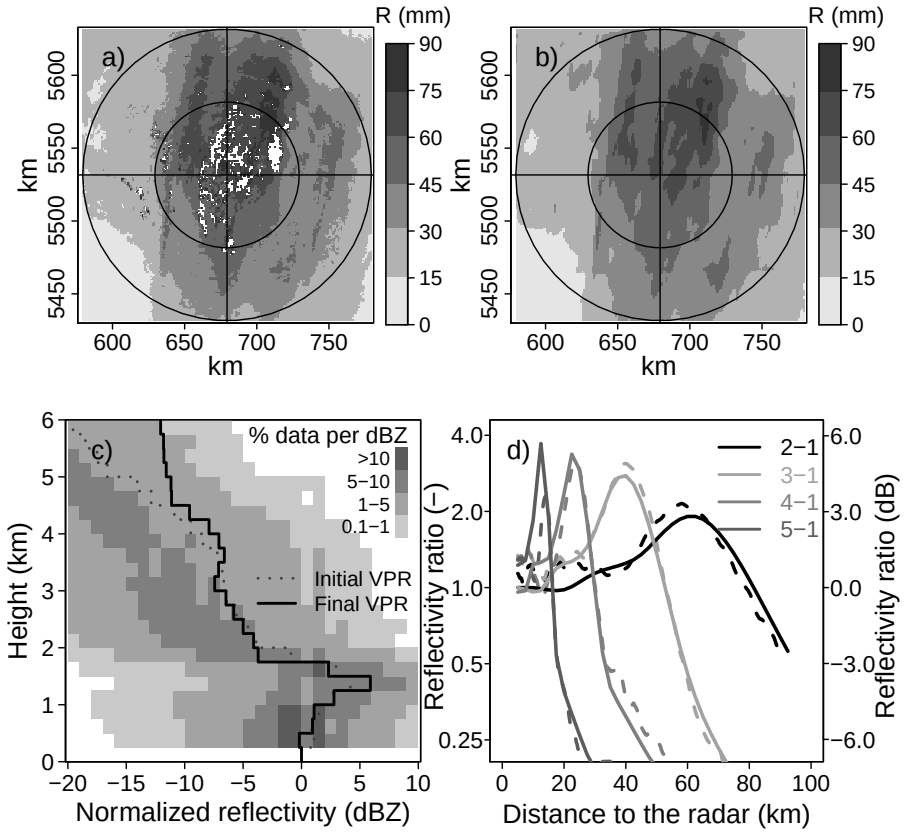

Figure 2.6: As Fig. 2.2, for the event on January 1-3, 2003. The data for panels c) and d) correspond to a fifteen-minute time window around 9:00 AM UTC on January 2.

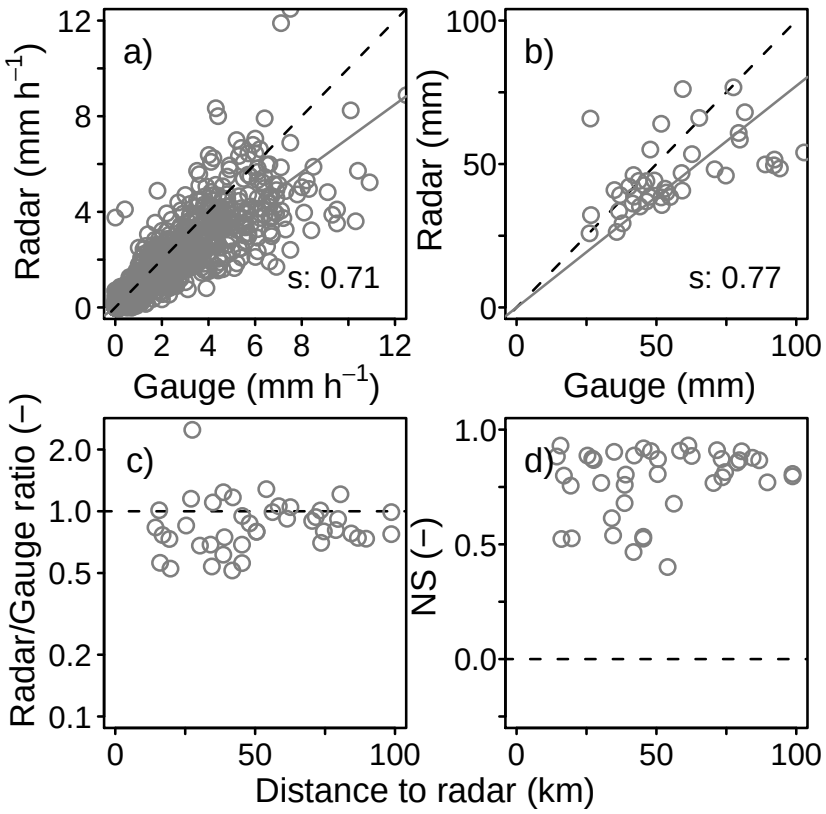

Figure 2.7: As Fig. 2.3, for the event on January 1-3, 2003.

region.

No range effects can be observed in Figs. 2.7c and d. Up to large distances from the radar both statistics stay rather constant. During this event the temporal variability in the estimated VPR was limited as compared to the October event (Event 1). Therefore, using a single VPR for the whole radar umbrella was beneficial.

Table 2.4 presents the influence of the different correction steps on the average hourly goodness-of-fit statistics of the radar-rain gauge comparisons. Except for attenuation which does not play a serious role here, each correction step improved the quality of the data. This on average leads to an overall radar product quality that is comparable to that of the rain gauges.

Table 2.4: As Table 2.2, but for the event on January 1-3, 2003.

Statistic	Raw	Clut	Atten	VPR	Advec	G-VPR	C-VPR
ρ^2	0.84	0.86	0.85	0.86	0.87	0.90	0.90
$\sum R / \sum G$	1.5	0.93	1.05	0.88	0.89	1.11	1.10
NS	-5.13	0.77	0.69	0.75	0.78	0.86	0.86

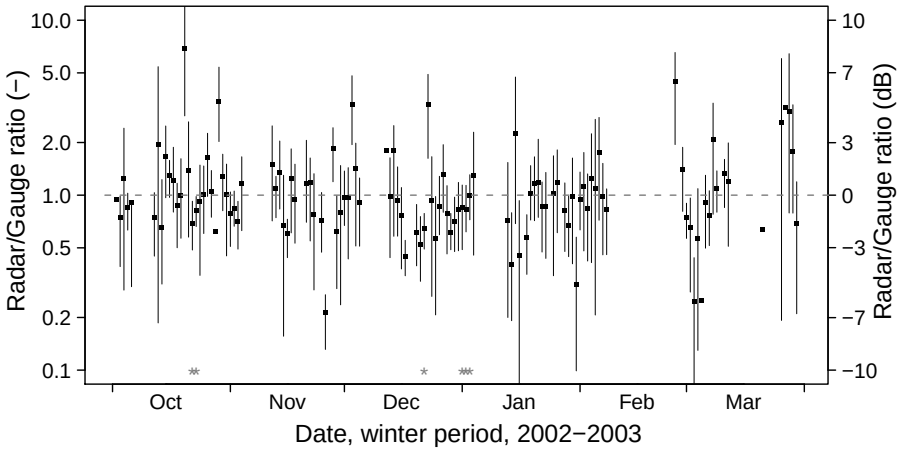

Figure 2.8: Average ratios of the daily radar and rain gauge values for the half-year dataset. Vertical bars indicate the 10-90% percentile range for the 42 rain gauges. The gray stars indicate the three events that have been presented in Section 2.4.

2.5 Overall radar/rain gauge comparison

Results presented in the previous section showed that the impact of a given correction step strongly depends on the spatio-temporal characteristics of the precipitation system. Only the GC algorithm has a clear overall positive impact during all three storms. The next step is to have a closer look at the performance of the currently implemented radar correction algorithm for the total half-year dataset. Such an overall analysis reduces the influence of the individual storm types and enables one to obtain a better understanding concerning the general quality of the algorithms.

Figure 2.8 presents the overall ratios of radar-gauge accumulations for days based on hours when both instruments measure precipitation ($R \geq 0.1$ mm h^{-1}). The average ratio values for the 42 events vary considerably in time without containing any immediate trends. The

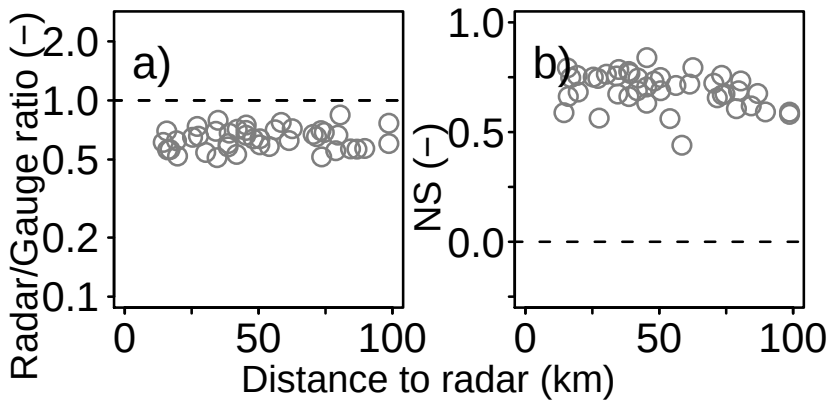

Figure 2.9: Comparison between the hourly radar and rain gauge values for the half-year dataset. Panels a) and b) simular similar to Figs. 2.3c and d, respectively.

impact of changes in the transmitted power of the weather radar (Eq. (2.1)) is therefore assumed to have been small.

Overall results lie close to the ratio value of 1, although from Table 2.5 it can be seen that on average the underestimation is about 28%. However, for a given day, considerable variability is observed between the different gauges as indicated by the width of the bars corresponding to the 10th and 90th percentiles. The average half-year underestimation by the radar for each radar-gauge pair separately is presented in Fig. 2.9a and varies between 5–45% underestimation without showing any range effects. Range effects can be observed from the obtained half-year Nash-Sutcliffe statistics (Fig. 2.9d), where the radar quality starts to decrease beyond 70 km from the radar. During the winter half-year, the average height of the bright band was between 1000–2000 m above the radar elevation. Therefore, the snow region above it starts to be sampled by the lowest radar elevation at a distance of around 70 km. Even though the correction algorithm takes the effects of VPR into account, its quality apparently decreases at these long ranges. This can be related to the fact that the estimated VPR mostly depends on the data measured close to the radar. Similar behavior could also be observed when analyzing Event 1. This again shows the difficulty of taking all types of variability in the precipitation field into account. Besides that, it can be expected that differences in sampling characteristics between the radar and rain gauge such as height and measurement volume will also play a greater role at larger distances (*Austin*, 1987; *Gabella et al.*, 2000).

Table 2.5: Evaluation of the influence of the different radar correction steps for hourly precipitation values of the half-year dataset. Column headers are the same as to those in Table 2.2.

Statistic	Raw	Clut	Atten	VPR	Advec	G-VPR	C-VPR
ρ^2	0.67	0.72	0.71	0.72	0.73	0.72	0.72
$\sum R / \sum G$	5.69	0.77	0.81	0.77	0.73	0.75	0.74
NS	-66.8	0.70	0.67	0.70	0.70	0.70	0.69

Table 2.5 presents the half-year goodness-of-fit statistics. As expected, the largest improvements in the quality of the radar data were obtained after correction for GC, followed by adjusting for VPR. Correction for attenuation only has a positive effect on the radar-gauge ratio but has a slightly negative impact on the other statistics. A possible explanation could be the usage of an inappropriate Z–k relationship for the Ardennes region, leading to incorrect estimation of the average amount of PIA. However, the influence of attenuation at C-band for this type of stratiform systems is small, as expected (*Delrieu et al.*, 1999, 2000). For individual more intense events, such as the ones presented for October, this correction did have a positive impact. Correcting for advection has only a benificial impact in case of faster moving storm systems of considerable variability. During the winter half year, most stratiform storms were slow moving spatially homogeneous systems. Therefore, advection correction has no major impact.

The implementation of a VPR estimate based on the volumetric radar data measured above the catchment does not improve results, compared to applying a global VPR estimate. This could already be observed from the analysis of the individual events, but is different from results obtained in other studies (*Vignal et al.*, 2000). As explained, a significant overlap exists between the areas used to obtain global and catchment VPR estimates. This results in almost identical profiles for both regions.

2.6 Discussion

2.6.1 Algorithm implementation

Removal of GC using the algorithm proposed by *Steiner and Smith* (2002) showed large improvements in the quality of the radar rainfall estimates. Analysis of the third event in Section 2.4.3 showed that for

some specific cases, it might be too sensitive. In addition, for Event 2 in Section 2.4.2 it could be observed that some isolated clutter areas cannot be identified in case of widespread and spatially homogeneous precipitation. Some pixels might have been identified as clutter, while they contained a mixture of both clutter and precipitation. The impact of removing these pixels is expected to be small, because in order to obtain a 2D polar radar estimate, a weighted average of all elevations, corrected for VPR effects, is taken. The radar data used in the current study originate from an early stage of operation. Nowadays, applying Doppler velocity information to discriminate clutter from precipitation has become a standard operational procedure. Unfortunately, these data were not available for the current study. Therefore, it is expected that the erroneous clutter identification and removal still observed in this study will decrease when using more recent data.

Correction for attenuation showed a positive impact only for a few events but had zero or even a slightly negative impact on the overall rainfall estimation capability of the weather radar. As said, the parameters of the Z–k relationship in Eq. (2.5) were obtained from disdrometer measurements in the Netherlands, which might not have been fully representative for the hilly environment of the Belgian Ardennes. Moreover, attenuation is not a major source of error for the Belgian winter climate at C-band in the first place. Wet radome attenuation (*Germann*, 1999) due to rain and snow might have resulted in additional attenuation for some events. However, it is very difficult to correct for this source of error in an operational environment. Therefore, correction for this was not attemted.

The success of the VPR identification algorithm is highly dependent on the spatial variability of the storm field, as was shown by the spread of the frequency diagram of the normalized profiles in Figs. 2.2c, 2.4c and 2.6c. Here the reflectivity information was accumulated over fifteen-minute intervals. *Berne et al.* (2004b) showed that based on such aggregation periods, the estimated VPR is representative on average for an area of about 100 km^2. In this study, the algorithm is applied at such a high temporal resolution to minimize the effect of temporal changes in the VPR. According to *Bellon et al.* (2005) such an implementation could give rise to a highly variable average VPR estimate, which is not representative for ranges further from the radar. In this study we were only interested in the quality of the radar up to a range of 100 km. Therefore, the possible detrimental effects of obtaining a VPR estimate at such a high temporal resolution were considered not to be

problematic. A possible future improvement though, might be to focus on smaller areas for VPR estimation.

Such areas could either be obtained by taking only the volumetric weather radar data sampled above a certain catchment into account, or by focusing more specifically on a given storm cell. Although the former method did not improve the quality of the radar data for the region inside the Ourthe catchment, it can be expected that especially for distances further away such an approach would improve the impact of correcting for VPR. With respect to the latter, it could be possible to make use of a cell-tracking algorithm (*Dixon and Wiener*, 1993; *Handwerker*, 2002). Such an approach will ensure that the obtained average VPR is representative for a given storm-cell. Variability in the shape of the VPR for different storm cells as was observed for Event 1 can then be taken into account. Besides that, such a cell-tracking algorithm can also be applied to obtain advection direction information. Erroneous cross-correlations, of which the impact for some time steps could be observed in Fig. 2.4b, are then removed.

Based on Fig. 2.8 we assume that there were no serious trends in the transmitted power of the weather radar. However, in this study no specific information concerning absolute radar calibration was available. Overestimation in the amount of transmitted power can result in an underestimation of the amount of precipitation (*Ulbrich and Lee*, 1999) as estimated by the radar as seen in this study. *Atlas* (2002) presents a historical overview on how to identify radar calibration problems. In a operational environment, *Holleman et al.* (2010) use the sun to correct for this error source, while *Ulbrich and Lee* (1999) used disdrometer measurements to identify any resulting bias due to calibration issues. Another problem might be the choice of the Marshall-Palmer Z–R relationship which on average might not be optimal for the type of precipitation in the Belgian Ardennes. This aspect will surely play a role in the temporal variability of the type of precipitation. Different types of precipitation contain different drop size distributions, resulting in variations of the Z–R relationship (*Creutin et al.*, 1997; *Uijlenhoet et al.*, 2003a), as could also be observed during Event 2. Polarimetric weather radar could result in an improved understanding of these variations.

2.6.2 Hydrological potential of the weather radar

This study analyzed the quality of the weather radar precipitation measurements based on individual radar-rain gauge pairs. As explained,

range effects and sampling differences complicate comparison between both devices (*Austin*, 1987; *Kitchen and Blackall*, 1992; *Gabella et al.*, 2005). However, it can be expected that this difference becomes smaller when aggregating over longer time periods (*Borga et al.*, 2006) or over a catchment (*Vignal et al.*, 2000). One of the main benefits of using weather radar with respect to rain gauges is the fact that one obtains much more information about the precipitation field. However, for the hydrological analyses presented here, we will only use catchment-averaged rainfall information. Given the lumped model that is currently operationally used by Dutch water management authorities, and given the typical response that can be observed within the Ardennes during a winter period, this is not unreasonable. The hydrological results presented below should be interpreted as a worst case; actually using the full potential of weather radar (i.e. high spatial resolution, combined with a distributed hydrological model) is highly likely to lead to larger improvements than if only rain gauge data are used. This is subject of ongoing investigations.

Measured and simulated hydrographs are presented in Fig. 2.10, where both the radar and rain gauge data have been applied to simulate the discharge response of the Ourthe catchment using the operational HBV model (*Bergström*, 1976, 1992; *Lindström et al.*, 1997). This model is used by the Dutch authorities to simulate the discharge of the river Meuse for the purpose of operational water management. It has been calibrated for the Ourthe using over 30 years of data (*Velner*, 2000; *Booij*, 2002). At the scale of the Ourthe catchment simulation is performed using a single lumped version of the model. Therefore, weather radar data are averaged over the catchment while the rain gauge information is first interpolated before being averaged. Both model simulations are started 6 months in advance using measured catchment average rain gauge values in order to create similar initial conditions for both types of input data.

From the results in Fig. 2.10 it can be observed that the overall differences in obtained hydrographs using either rainfall source are small. The Nash-Sutcliffe values using the radar or rain gauge precipitation as an input are 0.88 and 0.89, respectively. Up to the beginning of November the simulated hydrograph based on the radar data is closer to the observed discharges than the hydrograph obtained from the rain gauge data. The discharge peak at the beginning of January 2003 is underestimated by both hydrographs. This difference is probably related to the lumped character of the model, which cannot take spatial variability of

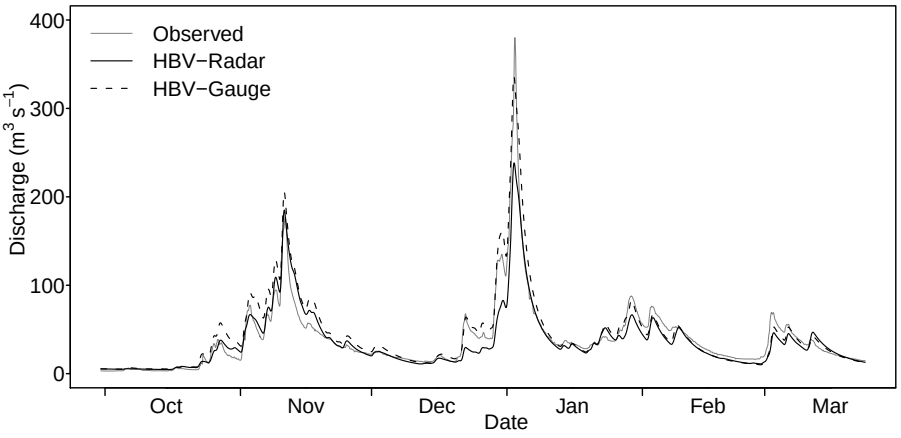

Figure 2.10: Observed and simulated hydrographs for the half-year dataset using catchment-average rain gauge and radar data.

soil moisture into account. It should be noted that for the radar, a larger underestimation of the maximum discharge peak is observed. Evaluation of the third event in Section 2.4 shows little difference between rainfall estimates obtained by radar and rain gauges. The observed difference in the absolute size of the simulated discharge peak, therefore, does not occur as a result of erroneous precipitation estimates by radar during that event. A closer inspection of Fig. 2.10 reveals that the simulated hydrograph based on the radar data starts to underestimate observed discharges during the second half of December 2002. During this period it can be observed from Fig. 2.8 that the radar underestimated the amount of precipitation for several days, as could also be observed for Event 2 (Section 2.4.2). This resulted in lower storage in the catchment before the event of 1–3 January, leading to lower simulated discharge peak. Overall, these simulations clearly reveal the potential of applying weather radar information without using any rain gauge information for operational water management.

2.7 Conclusion

In this chapter the effects of different radar correction steps and their impact on radar rainfall estimates have been investigated for stratiform winter precipitation within a hilly environment. Especially for the more temperate regions, where discharges are largest and cause the biggest problems in winter, correct estimation of the amount of precipitation

for this type of rainfall is important. Based on the current analysis it could be observed that the largest improvement in the quality of the radar data was observed after GC removal. Attenuation correction as expected lead only to an improved quality of the radar data for some of the more intense events. Overall, correcting for attenuation did not have a significant impact on the quality of the data. Correcting for advection of the precipitation field only improves the results for faster moving precipitation systems as presented in Section 2.4.3. For large-scale, slow-moving systems (Section 2.4.1 and 2.4.2) taking advection into account is not necessary.

The impact of correcting for the VPR is highly dependent on the spatial variability of the storm system under consideration. The implemented algorithm to obtain a global estimate of the VPR is heavily influenced by measurements taken close to the radar. Therefore, for cases with highly spatially variable storm systems, such an estimated profile does not always lead to improved results for distances further away. Up to a distance of 70 km from the radar it could be observed that the quality of the corrected radar product became comparable to that of the rain gauges, except for a slight underestimation. At distances beyond 70 km from the radar this quality decreases, although some of this can be related to sampling differences between both instruments.

Overall, the corrected radar data yield slightly lower precipitation amounts than the rain gauges. However, within the current hydrological operational environment this does not immediately lead to erroneous rainfall-runoff simulations (Fig. 2.10). In the future, one of the main challenges is to take the spatial variability of the precipitation system into account. Polarimetric radars, which are gradually replacing non-polarimetric radars all over the world, have the potential to lead to further improvements.

CHAPTER 3

Variability of raindrop size distribution and its effect on radar reflectivity - rain rate relations

3.1 Introduction

Extreme precipitation events that occasionally lead to flash floods are known to exhibit considerable spatio-temporal gradients, which makes the correct estimation of the amount of precipitation during such catastrophic events both very important and challenging (*Delrieu et al.*, 2005; *Uijlenhoet and Sempere-Torres*, 2006). However, the spatial distribution of most conventional raingauge networks is too coarse to grasp this variability (*Berne et al.*, 2004a). Weather radars are in principle able to collect this type of information. Unfortunately, even though it is nowadays possible to correct for many sources of error related to the measuring characteristics of the radar (e.g. *Andrieu and Creutin*, 1995; *Andrieu et al.*, 1997; *Delrieu et al.*, 2009; *Bouilloud et al.*, 2010), one still faces the problem of converting the measured reflectivity values into precipitation intensities.

Generally, the relationship between the radar reflectivity factor Z

This chapter is a slightly modified version of: Hazenberg, P., Y. Nan, B. Boudevillain, G. Delrieu, and R. Uijlenhoet (2011), Scaling of raindrop size distributions and classification of radar reflectivity-rain rate relations in intense Mediterranean precipitation, *J. Hydrol.*, *402 (3-4)* , 179-192, 10.1016/j.jhydrol.2011.01.015.

[$\mathrm{mm}^6\,\mathrm{m}^{-3}$] and the rainfall intensity R [$\mathrm{mm\ h}^{-1}$] is assumed to follow a power law (*Marshall et al.*, 1955; *Battan*, 1973):

$$Z = AR^b. \tag{3.1}$$

In principle the parameters A and b in Eq. (3.1) can be obtained by combining the information sampled by both the weather radar and a rain gauge network. Unfortunately, differences in the sampling characteristics of both devices complicate the representativity of these results (*Kitchen and Blackall*, 1992; *Steiner and Smith*, 2004). Such scale problems do not occur when raindrop size distributions are sampled by disdrometers, from which it is possible to estimate both Z and R directly and simultaneously. In case of disdrometers, the generality of the estimated parameters A and b only depends on the type of instrument used (*Campos and Zawadzki*, 2000; *Tokay et al.*, 1999), the mathematical fitting technique applied (e.g. *Steiner and Smith*, 2000; *Chapon et al.*, 2008), and the representativity of the disdrometer measurement to estimate radar reflectivity values (*Chandrasekar and Bringi*, 1987; *Austin*, 1987; *Steiner and Smith*, 2004).

Both radar reflectivity and rain rate are functions of the precipitation's drop size distribution (DSD), which is generally assumed to follow some statistical distribution (e.g. exponential (*Marshall and Palmer*, 1948), gamma (*Ulbrich*, 1983), or lognormal (*Feingold and Levin*, 1986)). Because both the rainfall intensity and radar reflectivity are functions of the DSD, it is possible to relate the parameters A and b to these statistical distributions. Such analyses show that for a given distribution assumption, the possible range of the Z– R exponent is constrained (*Sekhon and Srivastava*, 1971; *Smith and Krajewski*, 1993; *Steiner et al.*, 2004). For a lognormal DSD, *Smith and Krajewski* (1993) found this exponent to vary between 1–3.125, while for the gamma distribution *Steiner et al.* (2004) obtained a range between 1–1.63.

Sempere-Torres et al. (1994, 1998) showed that all previously proposed distributions can be represented by a scaling law that depends on the drop diameter and one rainfall integral parameter. A direct result of this assumption is that the physical range of the allowed values for the exponent b is fixed, independent of the type of predefined distribution (*Uijlenhoet*, 1999). Once this relationship is known any change in estimated Z–R parameters can directly be related to changes in DSD formation processes associated with different meteorological conditions (*Waldvogel*, 1974; *Ulbrich*, 1983).

Such variations of the DSD arise between different climates, the type of generation process (e.g. continental vs. maritime), and because

of variations in the vertical velocity field (e.g. *Battan*, 1973; *Austin*, 1987; *Uijlenhoet et al.*, 2003b, 2006; *Rosenfeld and Ulbrich*, 2003; *Ulbrich and Atlas*, 2007). This latter property allows a discrimination between convective and stratiform rainfall (*Houze Jr.*, 1993; *Yuter and Houze Jr.*, 1995a). During convective events, spatial variability in vertical wind velocities causes strong horizontal rainfall gradients (*Zeng et al.*, 2001). The DSDs measured in such situations generally consist of large raindrops, because smaller ones are filtered out by updrafts and evaporation below cloud level (*Steiner et al.*, 1995; *Tokay et al.*, 1999). These horizontal variations and the associated vertical velocities are much smaller in stratiform conditions. Here, the formation of raindrops originates from the melting of snow flakes and ice crystals below the zero degree isotherm. Around this elevation melting snow flakes cause an increased radar reflectivity signal known as the bright band (*Klaassen*, 1989; *Sánchez-Diezma et al.*, 2000). While falling, smaller drops are created by drop interactions and spontaneous break-up, resulting in vertical variations of the DSD (*Fabry and Zawadzki*, 1995; *Huggel et al.*, 1996).

This chapter aims to improve our understanding regarding the variability in Z–R relationships between different rainfall events using disdrometer data collected in the Cévennes-Vivarais region in the South of France, a region known to be prone to heavy rainfall and associated flash floods. Based on the scaling-law theory of *Sempere-Torres et al.* (1994) a new technique is proposed to estimate the parameters of the normalized DSD and the resulting coefficients of the Z–R relationship. The latter values are compared to results obtained by statistical least-squares fitting techniques applied to direct calculations of both Z and R from measured individual spectra. Nowadays, weather radar observations allow to descriminate between regions of convective and stratiform precipitation (*Steiner et al.*, 1995; *Sánchez-Diezma et al.*, 2000; *Delrieu et al.*, 2009). Reflecting the inherent differences regarding the meteorological processes behind both types of precipitation, for each event a so-called fraction of convective activity was estimated from the disdrometer data, in a similar way as such radar-based discrimination techniques do. This improves our understanding concerning the observed Z–R parameters and the normalized DSD for a given type of precipitation (*Tokay et al.*, 1999; *Atlas et al.*, 1999; *Lee and Zawadzki*, 2005).

Section 3.2 describes the region of study, the employed dataset, and how to discriminate between convective and stratiform precipitation. In Section 3.3 the details behind the scaling-law theory are explained,

including a new parameter estimation method. This technique is used to obtain the parameters in Eq. 3.1 and these results are compared to direct statistical fitting techniques. Section 3.4 explains the details behind raindrop formation processes and control mechanisms, which are expected to be dominant in different types of precipitation. Results for a couple of characteristic events and the overall dataset are presented in Section 3.5, finishing with conclusions in Section 3.6.

3.2 Dataset

The Cévennes-Vivarais region in the South of France is prone to heavy and long-lasting rainfall events that occasionally lead to severe flash floods. In order to improve the understanding of the micro-physical properties behind such extreme storms, an optical OTT/Parsivel disdrometer was installed in the autumn of 2004 near the city of Alès, as part of the Cévennes-Vivarais Mediterranean Hydro-meteorological Observatory (OHMCV, www.ohmcv.fr). This disdrometer is able to sample 32 different particle size classes (ranging from 0 to 26 mm for variable diameter increments between 0.125 up to 3 mm) and 32 different velocity classes with a measurement time interval of 10 seconds that were aggregated into one-minute intervals. In the vicinity of the disdrometer (2 m) a tipping bucket raingauge is located. In addition, two Meteo France S-band radars are situated near Nîmes and Bollène, at a distance of about 48 and 57 km from the disdrometer, respectively. An overview of the region is presented in Fig. 3.1.

The dataset used here covers a period of 2.5 years. A total of 70 rain events were selected, which all contained a minimum one-minute rainfall intensity of 1 mm h^{-1} and an overall accumulation of at least 5 mm. The data set covers different meteorological origins, ranging from 1) short-duration high-intensity summer storms, 2) autumn mesoscale convective systems that typically generate flash floods within this region, 3) shallow convective events triggered by the Cvennes-Vivarais orography, and 4) long-lasting stratiform winter events. Erroneous one-minute disdrometer samples were removed when the average difference between the actual and theoretical raindrop terminal velocities (*Beard*, 1976, 1977) was more than 40%. An overview of the types of events selected is presented in Fig. 3.2.

Unfortunately, no information on the vertical wind velocities was available. In order to discriminate between convective and stratiform samples, for each event the percentage of one-minute samples that con-

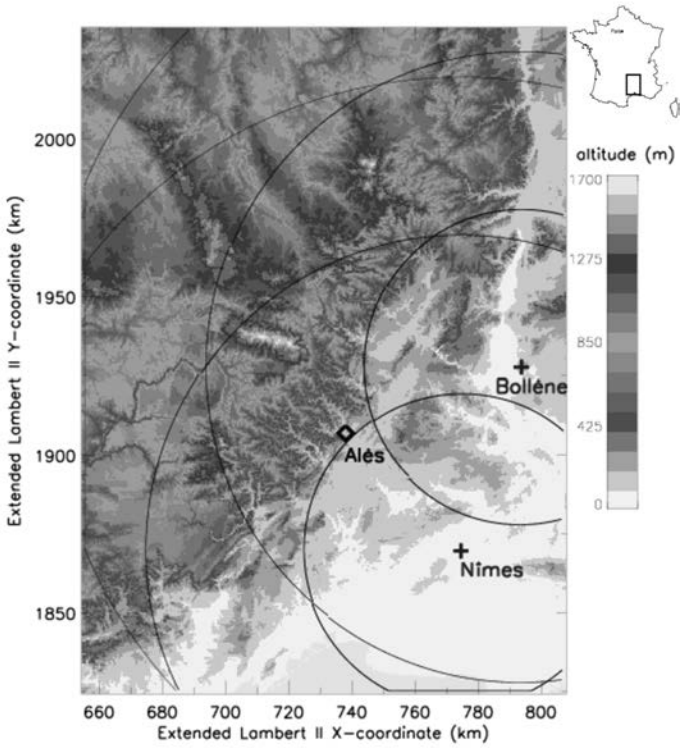

Figure 3.1: Location of the disdrometer in Alès within the Cévennes-Vivarais Mediterranean Hydro-meteorological Observatory (OHMCV) in the South of France. Also presented are the positions of the two Météo-France S-band weather radars near Nîmes and Bollène, with 50 and 100-km range markers.

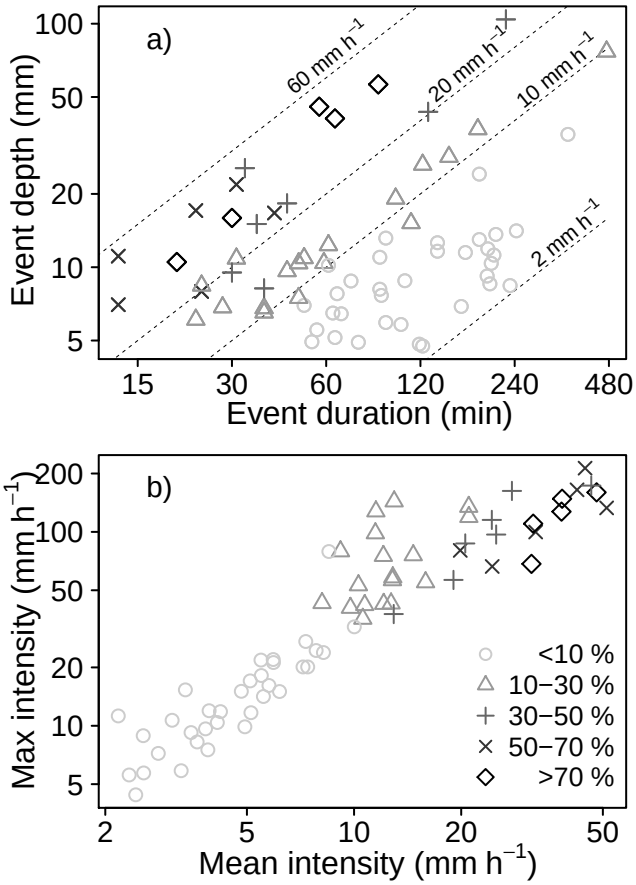

Figure 3.2: General information about the type of precipitation events selected for this study. Part (a) shows the total event accumulation with respect to total event duration. In part (b) the relationship between the mean and maximum event rainfall intensities is given. The different colors and symbols correspond to the fraction of the event for which the reflectivity exceeded 43 dBZ, as shown by the legend in (b).

tained reflectivities exceeding 43 dBZ was estimated. This reflectivity threshold was used by *Delrieu et al.* (2009) to discriminate convective regions in the weather radar data. Although such a straightforward delineation will not lead to perfect estimates of the amount of convection (*Steiner et al.*, 1995; *Delrieu et al.*, 2009), it does give a first indication concerning the convective character of any particular event. For each of the selected rainfall events, the fraction of convectivity obtained in this manner can also be observed in Fig. 3.2. From this figure it can be observed that, in general, events which contain for a given duration, a larger percentage of convection tend to have a larger overall precipitation depth.

It is known that intra-event DSD variability can be caused by changes from convective to stratiform conditions (*Tokay and Short*, 1996; *Atlas et al.*, 1999; *Ulbrich and Atlas*, 2007; *Chapon et al.*, 2008). Such within-storm discrimination was not performed here, because the main interest lies here on the inter-event Z–R variability.

3.3 Methodology

3.3.1 Drop size distributions and Z–R relations

As mentioned in the introduction, both the radar reflectivity factor and rainfall intensity are related to the drop size distribution, $N(D)dD$ (m^{-3}). For raindrops with diameters between D and $D + dD$ (mm) the following mathematical relations hold

$$Z = \int_0^\infty D^6 N(D) dD \approx \frac{1}{A_P \, \Delta T_P} \sum_{i=1}^{i=m} D_i^6 \frac{n(D_i)}{v(D_i)} \tag{3.2}$$

$$R = 6\pi \times 10^{-4} \int_0^\infty D^3 v(D) N(D) dD \approx \frac{6\pi \times 10^{-4}}{A_P \, \Delta T_P} \sum_{i=1}^{i=m} D_i^3 \, n(D_i) \tag{3.3}$$

where $v(D)$ is the theoretical raindrop terminal fall velocity ($\mathrm{m\ s}^{-1}$), $n(D_i)$ is the number of detected raindrops in a given diameter class i, m is the number of diameter classes identified by the disdrometer, and A_P (m^2) and ΔT_P (s) are the sampling area (54 cm^2) and sampling interval (1 minute) of the OTT/Parsivel disdrometer, respectively. Applying Eqs. (3.2) and (3.3) one is able to obtain estimates of the rainfall intensity R and radar reflectivity Z for each spectrum measured by the disdrometer.

3.3.2 Normalization theory

By expressing the DSD as a scaling law, *Sempere-Torres et al.* (1994, 1998) demonstrated that all previously proposed DSD parameterizations mathematically collapse into one single formulation. Besides being able to provide estimates regarding the parameter values of the Z–R relationship, more importantly this method provides information about the intrinsic microphysical properties of the drop size distribution. The main assumption is that most of the DSD variability can be explained by the diameter D and one reference variable, commonly taken as the rain rate R. Mathematically this can be expressed as the scaling law

$$N(D, R) = R^{\alpha} g(R^{-\beta} D), \tag{3.4}$$

where α and β are scaling parameters and $g(x)$ is the normalized raindrop size distribution with $x = R^{-\beta} D$. The main benefit of such a scaling law is that no functional shape is imposed apriori for $g(x)$, and that it naturally leads to power-law relationships between the different rainfall integral variables, such as Eq. (3.1) (*Uijlenhoet*, 1999). If Eq. (3.4) is substituted in the theoretical expression of the radar reflectivity Eq. (3.2), a power law of the form of Eq. (3.1) is obtained, where the parameters A and b are defined as

$$A = \int_0^{\infty} x^6 g(x) dx, \text{ and} \tag{3.5}$$

$$b = \alpha + 7\beta. \tag{3.6}$$

As such, the Z–R exponent is a function of the scaling parameters α and β only, while the prefactor is determined by the sixth order moment of $g(x)$. Introducing Eq. (3.4) into (3.3) yields the self-consistency constraints:

$$1 = 6\pi \times 10^{-4} c \int_0^{\infty} x^{3+d} g(x) dx, \text{ and} \tag{3.7}$$

$$1 = \alpha + (4 + d)\beta, \tag{3.8}$$

where the terminal fall speed is assumed to follow the power law relationship of *Atlas and Ulbrich* (1977)

$$v(D) = cD^d, \tag{3.9}$$

with $c = 3.778$ and $d = 0.67$ (if v is expressed in m s^{-1} and D in mm). According to *Sempere-Torres et al.* (1994) a power law is the only functional form that leads to consistency between the different rainfall integral variables. For the scaled raindrop size distribution $g(x)$ different

functional shapes have been proposed. Here both the exponential and gamma distribution

$$g(x) = \kappa x^{\mu} \exp(-\lambda x) \tag{3.10}$$

are applied, which for $\mu = 0$ leads to the exponential distribution. An equation for the Z–R prefactor is obtained by calculating κ as a function of λ and μ using Eqs. (3.5), (3.7), and (3.10):

$$\kappa = \frac{\lambda^{4+d+\mu}}{6\pi \times 10^{-4} c \Gamma(4+d+\mu)}, \tag{3.11}$$

where $\Gamma()$ denotes the gamma function. This yields

$$A = \kappa \frac{\Gamma(7+\mu)}{\lambda^{7+\mu}} = \frac{\Gamma(7+\mu)}{6\pi \times 10^{-4} c \Gamma(4+\mu+d)} \lambda^{-(3-d)}. \tag{3.12}$$

3.3.3 A novel approach to estimate the scaling-law parameters

The final step is to obtain the scaling exponents and coefficients of the normalized DSD from the measured raindrop size distributions. In the literature different techniques have been presented based on moment estimation methods (e.g. *Ulbrich*, 1983; *Tokay and Short*, 1996; *Smith*, 2003). For a given DSD, the moment of the order m can be defined as

$$\Omega_m = \int_0^{\infty} D^m N(D,R) dD. \tag{3.13}$$

Equation (3.2) for the reflectivity Z is a special case of this equation for the moment of order $m = 6$, whereas the rainfall rate R is related to the moment of order $m = 3 + d$. Substitution of Eq. (3.4) into (3.13) leads to

$$\Omega_m = \theta_m R^{\gamma_m}, \text{ where} \tag{3.14}$$

$$\theta_m = \int_0^{\infty} x^m g(x) dx, \text{ and} \tag{3.15}$$

$$\gamma_m = \alpha + (m+1)\beta. \tag{3.16}$$

Hence, the scaling exponents α and β can be obtained by fitting a power law between different integral variables Ω_m and the rainfall intensity R, where according to Eq. (3.16) the exponent should follow a linear relationship with the moment order $m+1$, with intercept α and slope β.

Different methods have been proposed to estimate the scaling coefficients of $g(x)$ in Eq. (3.10). *Sempere-Torres et al.* (1998) propose to

fit the parameters of $g(x)$ for a given functional shape based on non-linear regression, while *Chapon et al.* (2008) calculated these coefficients based on a moment method (*Tokay and Short*, 1996; *Smith*, 2003) at every timestep. A drawback of this latter approach is that it does not lead directly to any bulk estimates at the event scale. *Uijlenhoet* (1999) developed a slightly different approach using the characteristics of a distribution function. Unfortunately, this method is rather time consuming, especially for large DSD samples. Therefore, here a new method is proposed, which takes into account the values of the prefactors of the power laws between the rainfall integral moments Ω_m and R. In case of a gamma DSD, these prefactors can be written as a function of $g(x)$ in the following way

$$\theta_m = \kappa \int_0^\infty x^{m+\mu} \exp(-\lambda x) dx = \kappa \frac{\Gamma(m+\mu+1)}{\lambda^{m+\mu+1}}. \tag{3.17}$$

By taking the ratio of the prefactors for two consecutive moment orders, using Eq. (3.17) one is able to obtain a linear relationship between the ratios θ_{m+1}/θ_m and the moment order $m+1$:

$$\frac{\theta_{m+1}}{\theta_m} = \frac{\Gamma(m+\mu+2)\,\lambda^{m+\mu+1}}{\lambda^{m+\mu+2}\,\Gamma(m+\mu+1)} = \frac{\mu}{\lambda} + (m+1)\frac{1}{\lambda}. \tag{3.18}$$

This equation implies that the normalized gamma DSD parameters μ and λ can be estimated from the intercept and slope of a linear regression between θ_{m+1}/θ_m and the moment order $m+1$, analogous to Eq. (3.16) for the scaling exponents. It is then possible to obtain an estimate for κ using Eq. (3.11). Both scaling exponents and coefficients were obtained by calculating the parameters γ_m and the ratios θ_{m+1}/θ_m for those moments ($2 \le m \le 5$), which are known to be least sensitive to sampling problems (*Smith et al.*, 1993; *Uijlenhoet et al.*, 2006). Finally, the exponent of the Z–R relationship is obtained using Eqs. (3.6) and (3.8), and the prefactor is calculated from Eq. (3.12).

3.3.4 Statistical evaluation

The quality of the obtained Z–R relationship, assuming either an exponential (EXP) or gamma (GAM) function for the normalized drop size distribution, will be assessed by different goodness-of-fit statistics derived from the measured and estimated rainfall rate time series. These include the storm's root mean square error (RMSE), the model efficiency (R^2, also known as Nash-Sutcliffe coefficient in hydrology), the total bias

error (TBE) and the mean absolute error (MAE):

$$\mathrm{RMSE} = \sqrt{\frac{1}{N-2}\sum_{j=1}^{N}\left[R_j - (Z_j/A)^{1/b}\right]^2}. \tag{3.19}$$

$$\mathrm{R}^2 = 1 - \frac{\frac{1}{N-2}\sum_{j=1}^{N}[R_j - (Z_j/A)^{1/b}]^2}{\mathrm{Var}(R)} \tag{3.20}$$

$$\mathrm{TBE} = \sum_{j=1}^{N} R_j - \sum_{j=1}^{N}(Z_j/A)^{1/b} \tag{3.21}$$

$$\mathrm{MAE} = 100\% \cdot \frac{1}{N}\sum_{j=1}^{N}\frac{\mid R_j - (Z_j/A)^{1/b} \mid}{R_j} \tag{3.22}$$

In this chapter the results of the scaling-law based Z–R parameter values will be compared to two direct regression techniques based on the (Z, R) pairs derived for each individual spectra from (3.2) and (3.3). Although it has been advocated elsewhere to perform regression on R as a function of Z (*Campos and Zawadzki*, 2000; *Morin et al.*, 2003), here the inverse is performed, predicting the behavior of Z on the basis of R. This is done to be consistent with the presented normalization method, where the rainfall rate R serves as the reference variable. The first and most straightforward method, termed as the LG method hereafter, performs linear regression on the logarithmic values of both the radar reflectivity and rain rate. In general, the LG method gives relatively more weight to the smaller radar reflectivity and rainfall intensity values. This may not result in an optimal fit for the most intense phases of an event. Therefore, also a non-linear regression method is applied. This method, referred to as the NR method hereafter, has been implemented to derive an optimal value for the Z–R exponent using the Newton-Raphson optimization technique. For this latter method, once the optimal exponent has been obtained, the prefactor Z–R serves to remove overall bias between the estimated and measured rainfall accumulations. This can be done by estimating A as:

$$A = \left[\frac{\sum_{j=1}^{j=N} Z_j^{1/b}}{\sum_{j=1}^{j=N} R_j}\right]^b. \tag{3.23}$$

As such the implemented NR method leads to a zero TBE between the estimated and actual rain rate (*Ciach and Krajewski*, 1999b; *Steiner and Smith*, 2000).

3.4 Raindrop evolution and control mechanisms

Combining Eq. (3.6) and (3.8) results in a relationship between the obtained scaling coefficients and the Z–R exponent. This relationship can be used to infer information about the type of control mechanisms shaping the drop size distribution. *Uijlenhoet* (1999) and *Uijlenhoet et al.* (2003a) explain that for cases where processes like coalescence and break-up are in equilibrium, the obtained scaling exponents are α=1 and β=0, which results in a Z–R exponent $b = 1$, i.e. a linear Z–R relation. This type of condition is known as equilibrium rainfall (*Blanchard and Spencer*, 1970; *List et al.*, 1987) and corresponds to homogeneous precipitation (*Jameson and Kostinski*, 2002a). During these situations all characteristic raindrop sizes, like the mean raindrop diameter and standard deviation, are constant and changes in reflectivity and rainfall rate values are a direct result of changes in the number concentration of the DSD. Therefore, this type of precipitation is said to be number-controlled.

The opposite happens when variations in reflectivity and rainfall rate are caused by changes in the characteristic drop sizes. The most extreme case is when the number concentration of the DSD is constant. *Uijlenhoet et al.* (2003a) show that during these conditions the sum of α and β becomes zero and precipitation is non-homogeneous (*Jameson and Kostinski*, 2002b), leading to a so-called size-controlled drop size distribution. *Steiner et al.* (2004) explain that based on the gamma distribution, during such size-controlled situations the exponent b becomes 1.63. This also follows from Eqs. (3.6) and (3.8). Because of the assumption of a constant number concentration, the number of drops formed by break-up needs to be equal to that removed by coalescence. Overall changes in the DSD in such situations can occur as a result of accretion of cloud droplets and/or evaporation (*Rogers et al.*, 1991). In general, these extreme types of control mechanisms will be barely encountered. Therefore, the shape of the DSD in most natural rain originates from a mixture of both size- and number-control processes (*Uijlenhoet et al.*, 2003a; *Steiner et al.*, 2004).

The different DSD formation controls enable one to speculate about their importance during convective and stratiform situations, which result from different meteorological drop formation processes. In general, convective events contain a high number concentration of rain drops and are influenced by large vertical velocities (*Ulbrich and Atlas*, 2007). As such, the overall time available for interactions and the resulting number of interactions are large, favoring the type of conditions during which an

equilibrium state could be reached. Generally, for these events the Z–R exponent b is therefore expected to be closer to 1 (*Atlas et al.*, 1999; *Prat and Barros*, 2009).

For most stratiform systems the vertical extent is much smaller and raindrops mainly start to interact below the zero degree isotherm (*Klaassen*, 1989; *Fabry and Zawadzki*, 1995; *Huggel et al.*, 1996). The type of drop size distribution originating from such stratiform situations is, as a result, mainly dependent on the relative size concentration of ice particles above the bright band and whether they are in the form of snow flakes or rimed ice crystals. Generally, a large concentration of snowflakes results in relatively large drop sizes and a stronger bright band after melting, as compared to droplets originating from rimed ice crystals (*Fabry and Zawadzki*, 1995; *Huggel et al.*, 1996). In other words, during stratiform conditions raindrop spectra can contain both large and small average drop diameters, leading to a larger range in Z–R exponent values (*Yuter and Houze Jr.*, 1997; *Atlas et al.*, 1999). The behavior of the Z–R exponent during these conditions is therefore difficult to assess in advance.

3.5 Results and discussion

This section presents an analysis of the DSD properties and corresponding Z–R relationships for three events. Next, these results are generalized based on the data for all 70 events. The three events took place in the autumn season and are typical for the type of systems which may lead to flash floods in the Cévennes-Vivarais region.

3.5.1 Event 1

The first event observed was part of a mesoscale convective system which took place during the night of September 14, 2006. Hot and humid air masses originated from the Mediterranean in the South. While moving North, the air was lifted due to relief and resulted in large precipitation intensities. Figure 3.3 presents the time series of the one-minute reflectivities and rainfall rates as measured by the disdrometer. The estimated fraction of convectivity based on a threshold of Z = 43 dBZ was about 48%, indicating that a considerable part of this event contained convective precipitation, as can also be expected from the large rainfall intensities (*Churchill and Houze Jr.*, 1984; *Steiner et al.*, 1995; *Testud et al.*, 2001).

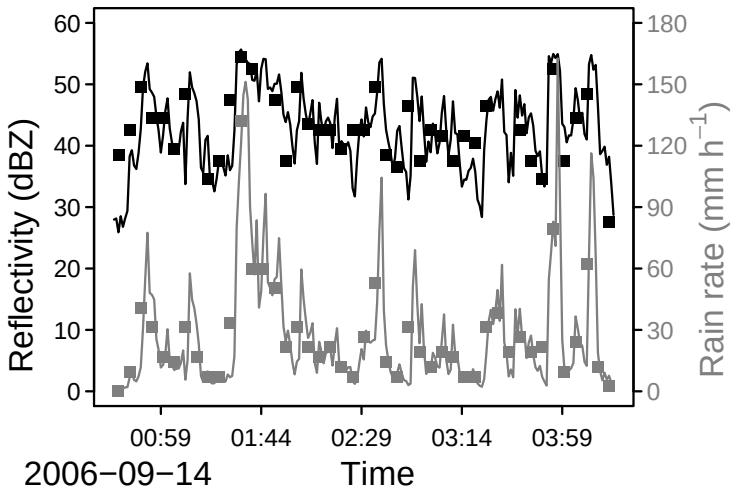

Figure 3.3: Time series of the one-minute reflectivity (dBZ) and rainfall rate (mm h^{-1}) data as measured by the disdrometer for the event on September 14, 2006. Dots correspond to the five-minute measurements, which for reflectivities were obtained from the 1 km^2 radar pixel directly above the disdrometer, based on the measurements by the radar at Bollène at a range of 57 km (black dots), while for the rain rates they were sampled by a nearby tipping bucket rain gauge (gray dots).

Also added in Fig. 3.3 are the observed five-minute radar reflectivity factor values sampled by the weather radar at Bollène and rainfall intensities from the nearby tipping bucket rain gauge. Both types of data show a very good correspondence with the disdrometer measurements. This shows that the point measurements of the disdrometer are quite representative for measurements made by an S-band weather radar at a distance of about 57 km. The total rainfall accumulation registered by the disdrometer during this period is about 104 mm.

Figure 3.4a presents the values of the exponents γ_m calculated by logarithmic regression between a rainfall integral variable of moment m and the rain rate R (Eq. (3.14), for $0 \leq m \leq 6$). The error bars indicate the 68% confidence limits obtained from 100 bootstrap samples (*Efron and Tibshirani*, 1993). The fit was performed over the central moments ($2 \geq m \leq 5$) in order to minimize instrumental effects that might occur measuring the smaller and larger rain drops. Except for the smallest normalized diameters, the overall fit in panels (a) and (b) of Fig. 3.4 is very good, as shown by the high value of the coefficient of determination r^2 of the linear relation following from DSD scaling-law theory. Based on the estimated values for α and β, obtaining the former by Eq. (3.8) to preserve self-consistency, the Z–R exponent b was calculated using Eq. (3.6). An exponent of 1.43 corresponds quite well to the value of 1.4 used for the summertime-convective NEXRAD Z–R relationship, which is known to hold well for convective precipitation systems (*Fulton et al.*, 1997).

Figure 3.4b displays the values of the ratios θ_{m+1}/θ_m (Eq. (3.18), for $0 \leq m \leq 6$). The linear fit predicted by theory holds perfectly for the gamma distribution. For the exponential distribution the fit between the moments of interest ($3 \leq m + 1 \leq 6$) is not very good due to the corresponding DSD shape parameter value $\mu = 0$, forcing the intercept of Eq. (3.18) to be zero. The associated coefficient of determination r^2 is only 0.44. However, this latter aspect does not lead to deviating results for the exponential distribution in Fig. 3.4c. The normalized DSD data can be seen to exhibit an exponential shape, which is well fitted by both parameterizations. Such an exponential distribution has also been observed during similar types of precipitation systems (*Sempere-Torres et al.*, 1998).

The reflectivity values and the rainfall rates as measured by the disdrometer are plotted in Fig. 3.5a. Also presented in this plot are the optimal Z–R relations for the normalized exponential and gamma parameterizations and the two least-squares fitting methods LG and NR.

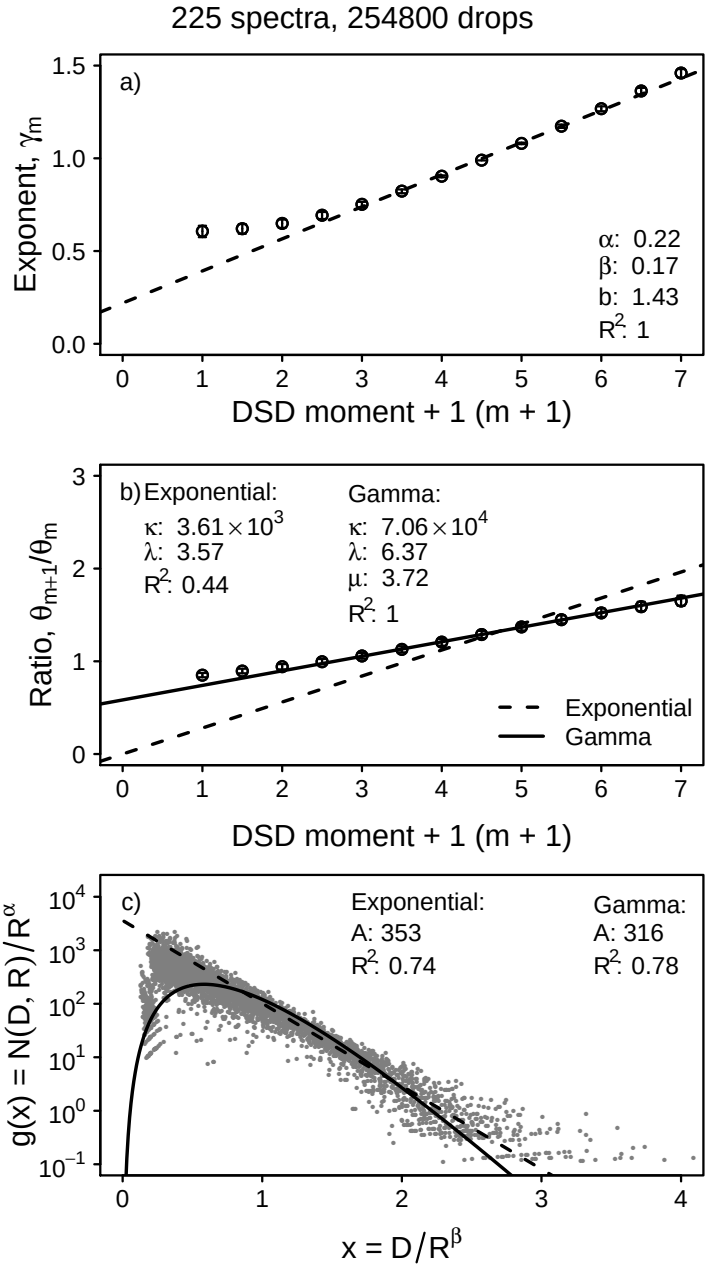
225 spectra, 254800 drops
a)
Exponent, γ_m
α: 0.22
β: 0.17
b: 1.43
R^2: 1
DSD moment + 1 (m + 1)
b) Exponential:
κ: 3.61×10^3
λ: 3.57
R^2: 0.44
Gamma:
κ: 7.06×10^4
λ: 6.37
μ: 3.72
R^2: 1
Exponential
Gamma
Ratio, θ_{m+1}/θ_m
DSD moment + 1 (m + 1)
c)
Exponential:
A: 353
R^2: 0.74
Gamma:
A: 316
R^2: 0.78
$g(x) = N(D, R)/R^\alpha$
$x = D/R^\beta$

Their values and statistics are given in Table 3.1. The fits are almost identical for the EXP, GAM and LG methods and vary only with respect to the value of the prefactor A. The parameters obtained by the NR method are different. This fit performs rather well for the largest intensity values. In Fig. 3.5b the overall rainfall accumulation for the four estimation methods is compared to the actual amount of rainfall sampled by the disdrometer. Between the four different techniques overall differences in total accumulations are small, although as a consequence of its implementation, only zero-bias is observed for the NR method. On the other hand, the RMSE and R^2 in Table 3.1 for this method are rather poor as compared to the other three techniques.

In order to place the results obtained by the various adjustment techniques in a wider perspective, we follow the methodology proposed by *Bouilloud et al.* (2010) who defined so-called equifinality patterns by calculating various assessment criteria (e.g. TBE, R^2) between Z-R transformed and rainrate timeseries for a systematic exploration of the Z-R parameter space. Fig. 3.6 presents the results for the 14 September 2006 event, from which one may note there exists an equifinality pattern in terms of the R^2 criterion as presented by the hyperbolic shape (in Fig. 3.6a) in the (A, b) parameter space, organized along the zero TBE line (in Fig. 3.6b).The most optimal Z–R parameter pairs are therefore those which perform well for both statistics. Of the four methods, espe-

Figure 3.4 ***(preceding page)*:** Scaling analysis of the drop size distributions for the event on September 14, 2006. The slopes (a) and the ratios of intercepts (b) estimated by regression between a rainfall integral moment vs. R. From the slopes γ_m vs. the moment $m+1$ the scaling exponents (α, β) are obtained, from which the corresponding Z–R exponent b can be estimated. The coefficient of determination R^2 is indicated as well. A regression of the ratio of the intercepts θ_{m+1}/θ_m on the moment $m+1$ yields estimates of the parameter values of $g(x)$, assuming either a gamma or an exponential distribution. These shapes are presented in (c) together with the scaled spectra, the prefactor of the Z–R relationship and the coefficient of determination r^2. Both in (b) and (c) the exponential and gamma parameterizations are presented by a dashed and solid line, respectively. Error bars in (a) and (b) indicate the 68% confidence intervals obtained from 100 bootstrap samples (*Efron and Tibshirani*, 1993).

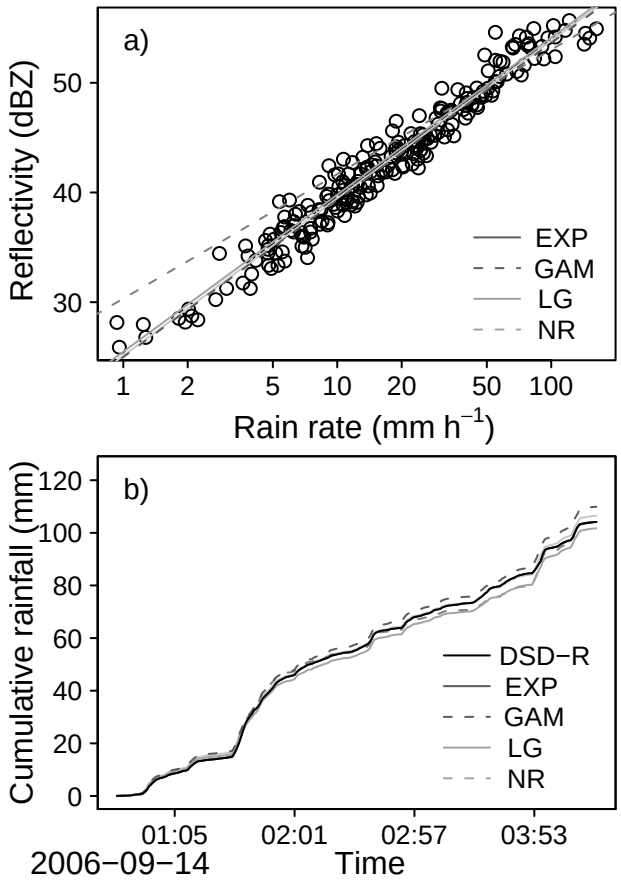

Figure 3.5: Plot (a) shows the one-minute rainfall rate vs. the reflectivity as sampled by the disdrometer for the event on September 14, 2006. The different lines in (a) correspond to the obtained Z–R relationships for the four different estimation techniques. Plot (b) presents a time series of the event accumulation as sampled by the disdrometer (DSD-R) and the rainfall rate estimates based on the four Z–R relationships in (a) and the measured reflectivity values.

Table 3.1: Parameter values of the radar reflectivity – rain rate relationship $Z = AR^b$ based on the four estimation methods and the resulting goodness-of-fit statistics (Eqs. (3.19–3.22)) for the five-minute data for the event on September 14, 2006. The overall accumulation by the disdrometer was 104.1 mm of rainfall. Units of RMSE, R^2, TBE and MAE are [mm h^{-1}], [-], [mm] and [%], respectively.

Method	A	b	RMSE	R^2	TBE	MAE
EXP	353	1.43	36.3	0.88	2.44	18.5
GAM	316	1.43	38.3	0.87	-5.8	19.2
LG	324	1.44	37.0	0.88	-2.35	18.6
NR	1077	1.13	50.3	0.77	0.0	33.1

cially the EXP and the LG estimates lie within this optimal region. Also indicated in this figure are the error bars of the four methods, indicating the 68% confidence intervals based on the bootstrap method (*Efron and Tibshirani*, 1993). It can be observed that for the NR method the uncertainty bars are largest, which is caused by its dependence on the largest reflectivity and intensity values. For the other three methods the uncertainties in the A and b estimates are small.

3.5.2 Event 2

The second event treated was part of a larger period of widespread rainfall lasting over a day. The events started at around 4:55 AM on November 21, 2007, and had a duration of about 6 hours. Precipitation originated from the warm sector of a large-scale Atlantic cyclonic system extending form the UK down to the South of France, moving behind a slow-moving cold front. As compared to Fig. 3.3, the observed timeseries for the current event are much more moderate, with most reflectivities and rainfall rates between 25–35 dBZ and 3–15 mm h^{-1}, respectively. Nevertheless, due to the duration of this event the overall accumulation was 35.1 mm. According to the threshold ($Z > 43$ dBZ), no convective activity was observed. Although it can be observed from the timeseries in Fig. 3.7 that this event could be characterized by two different phases.

In Fig. 3.8 the analyses of the raindrop size spectra are presented. The different nature of this event as compared to the previous resulted in a slightly larger exponent b. The newly proposed method to fit the

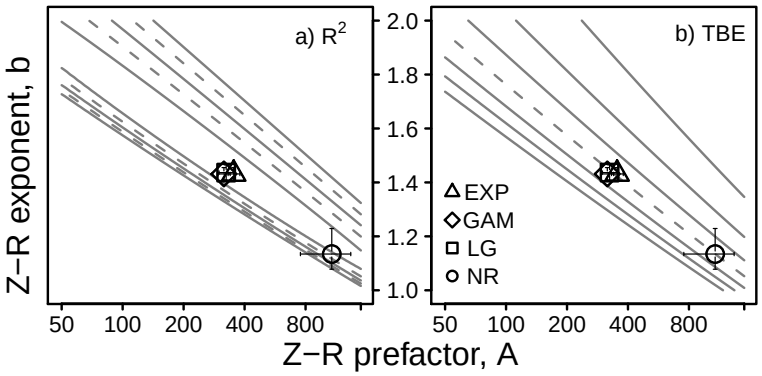

Figure 3.6: Statistical evaluation of the efficiency coefficient R^2 (part (a)) and total bias error (part (b)), for different values of A and b, using measured reflectivity and rainfall rate values for the event on September 14, 2009. In panel (a) the outer gray line represents and efficiency of $R^2 = 0.4$, increasing in steps of 0.1 for each consecutive line inward. In part (b) the bottom gray line represents a total bias error of −60 mm, increasing by 20 mm for each consecutive line. A total bias error of zero (mm) is represented by the the dashed gray line. Also plotted in both pannels are the optimal parameter values obtained by the different estimation methods (EXP, GAM, LG and NR), and their 68% confidence intervals from 100 bootstrap samples (*Efron and Tibshirani*, 1993).

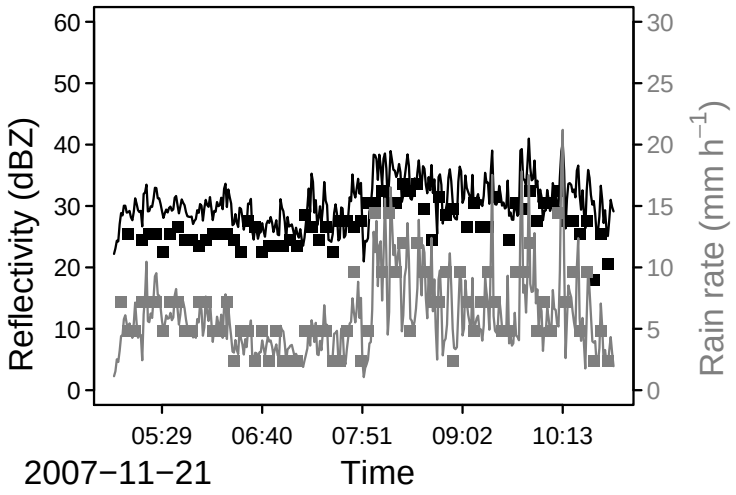

Figure 3.7: Same as Fig. 3.3, but for the event on November 21, 2007.

scaling parameters, for the gamma distribution results in a perfect fit in Fig. 3.8b. This clearly indicates that this method is well able to estimate the scaling-law parameters. For the current event, these parameters are larger, resulting in a smaller Z–R prefactor and more concave shape of the gamma distribution in Fig. 3.8c. The fit for the exponential distribution with respect to the ratios of consecutive intercepts in Fig. 3.8b is rather poor. However, especially for larger normalized raindrops, this distribution fits the normalized DSD better as compared to the gamma distribution. As a result, the coefficient of determination R^2 of both distributions in Fig. 3.8c is similar.

Figure 3.9a shows the regression analysis between the reflectivity and rainfall rates. The observed variation in Z–R pairs correspond to two different intra-event stages. For the first half of the event a given reflectivity value corresponds to a larger rainfall rate as compared to the second half of the event. Such intra-event variability was not taken into account when fitting the Z–R parameters. The EXP and LG methods fit the second stage of this event better, resulting in an underestimation of the amount of rainfall during the first stage (Fig. 3.9b). The non-linear NR fit results in a balance between both phases, where it first slightly underestimates and then overestimates the amount of precipitation for a given reflectivity Z. This results in a zero TBE (see Table 3.2). The

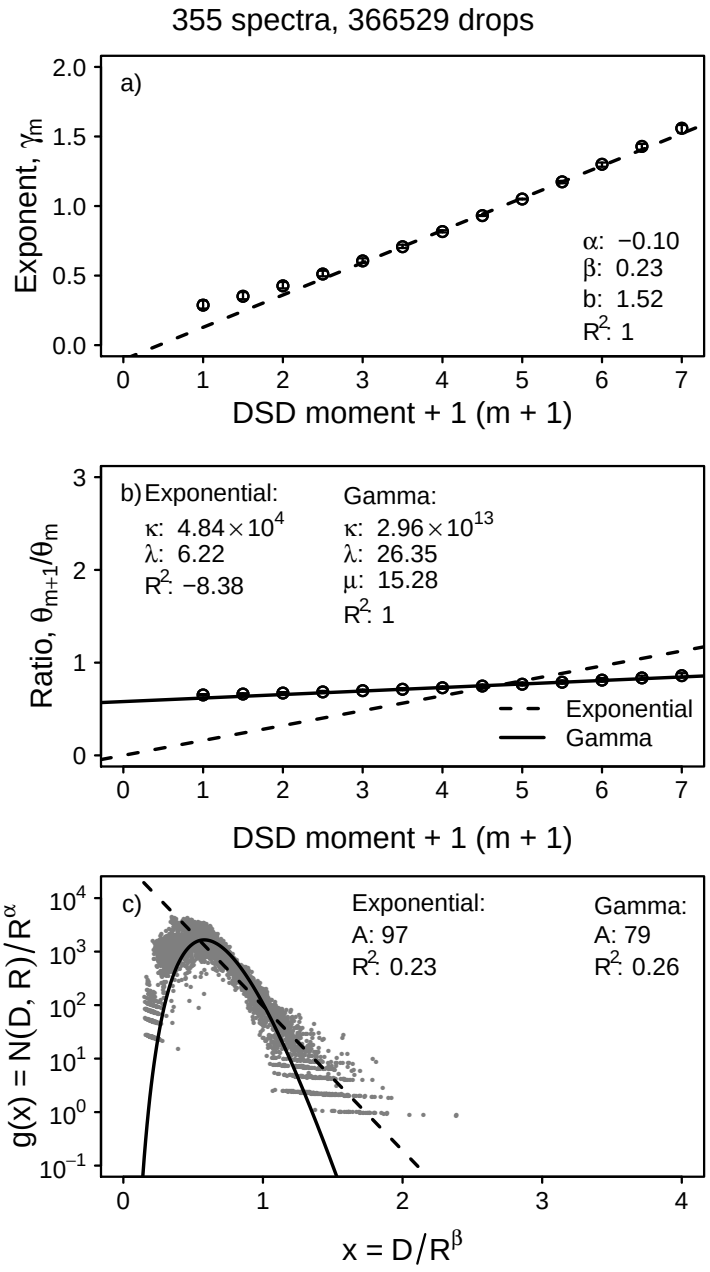

Figure 3.8: Same as Fig. 3.4, but for the event on November 21, 2007.

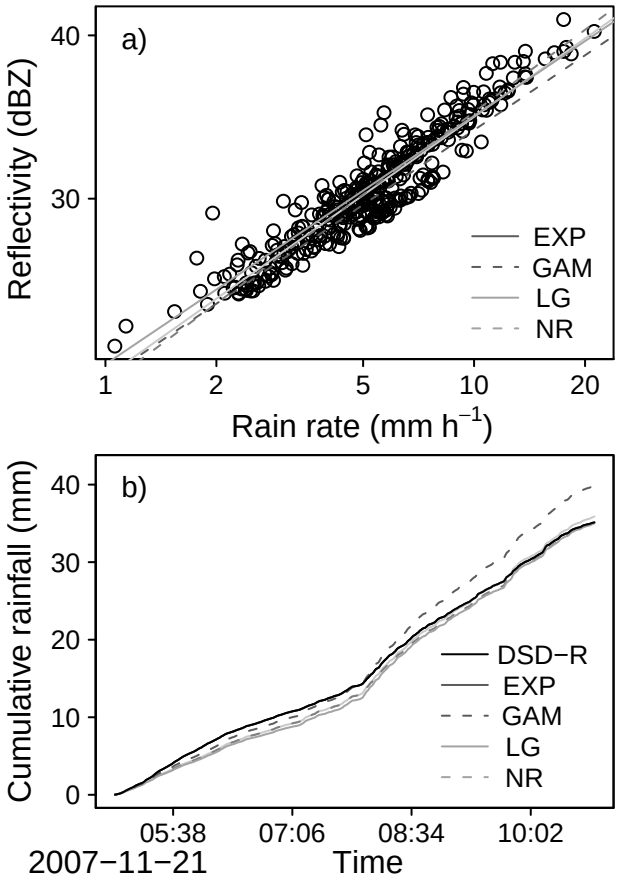

Figure 3.9: Same as Fig. 3.5, but for the event on November 21, 2007.

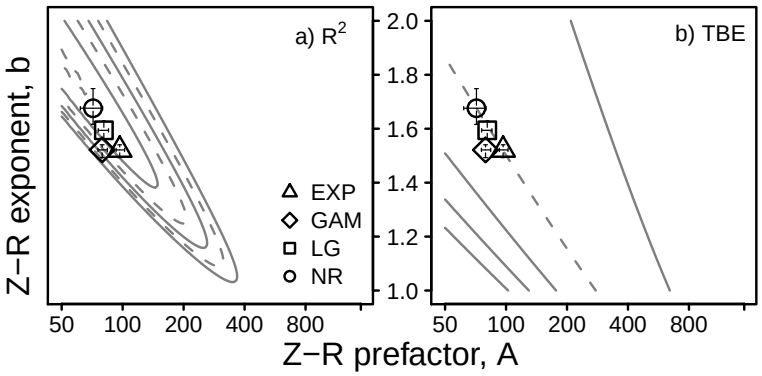

Figure 3.10: Same as Fig. 3.6, but for the event on November 21, 2007.

normalized GAM fit results in a break in the slope in between both phases. As such it underestimates the first stage and overestimates the second one. This shows that, even though the scaling method tries to normalize to observed DSD variability with respect to rainfall, it is not able to grasp all intra-event variability, as could also be observed from the scatter in Fig. 3.8c.

In Table 3.2 the goodness-of-fit statistics of the Z–R fit for this event are presented. As could already be expected from Fig. 3.9 and 3.10, the quality of the EXP, LG and NR methods is similar. Only the GAM method results in a less optimal fit. This emphasizes again the occurrence of a larger range of optimal Z–R parameter pairs, although totally different from the previous event. In Fig. 3.10 this behavior is presented. This plot shows that the NR method performs slightly better as compared to the EXP and LG methods. For the current event the range of optimal exponents b lies between 1.65–1.90, while the prefactor A is less than 100. These ranges compare well with the relationship for orographic rain $Z = 31R^{1.71}$ (*Blanchard*, 1953) and steady rain $Z = 67.6R^{1.94}$ (*Sivaramakrishnan*, 1961) according to *Battan* (1973), which were sampled during similar meteorological conditions. Orographic rainfall is known to contain a large number of small raindrops, leading to relatively small values of the prefactor A (*Rosenfeld and Ulbrich*, 2003), as could also be observed from the normalized DSD in Fig. 3.8c.

As expected from Section 3.4, neither of the normalization methods (EXP or GAM) produces an exponent value in the range 1.65–1.90. From control theory it is expected that the value of the exponent b

Table 3.2: Same as Table 3.1, but for the event on November 21, 2007. Overall accumulation by the disdrometer was 35.1 mm.

Method	A	b	RMSE	R^2	TBE	MAE
EXP	97	1.52	20.4	0.85	0.11	14.1
GAM	79	1.52	29.9	0.67	-4.79	18.4
LG	81	1.59	19.4	0.86	-0.77	13.5
NR	71	1.68	17.1	0.89	0.0	12.6

should lie in the range between 1–1.63. The fact that for this event a larger optimal exponent is observed, is probably related to the fact that the two intra-event stages contain a different prefactor A (see Fig. 3.9a, where both stages overlap each other). In order to obtain the best fits for both regions using a single prefactor therefore results in a larger value for the slope b. Although this value is physically unrealistic, statistically it leads to a better fit.

3.5.3 Event 3

The third event presented here in detail took place on October 22, 2008. Previous to this event, on October 19–21 considerable rain was already observed at Alès. The current event therefore resulted in local flash floods within the region. Radar images (not shown here) revealed that during the evening before, small scale showers originating from the Mediterranean Sea came to a halt above the mountainous area North of Alès. During the night these showers evolved into a series of convective cells of larger reflectivity, which transformed into a squall line that was pushed Eastward at around 1400 UTC. The time series of the event selected during this period is presented in Fig. 3.11. The explained meteorological characteristics can clearly be observed from this series, where the first 45 minutes contained moderate rainfall intensities with reflectivity values smaller than 43 dBZ. During the second convective phase, intensities increased strongly. This event presents a clear example of a mixture type of precipitation, where the second phase can be identified as convective.

Microphysical analysis of the exponents between the power laws of the different rainfall integral parameters versus rain intensity (Fig. 3.12a) leads to a slightly larger scaling exponent β as compared to the previous two events, resulting in a Z–R exponent of b = 1.41. The values of

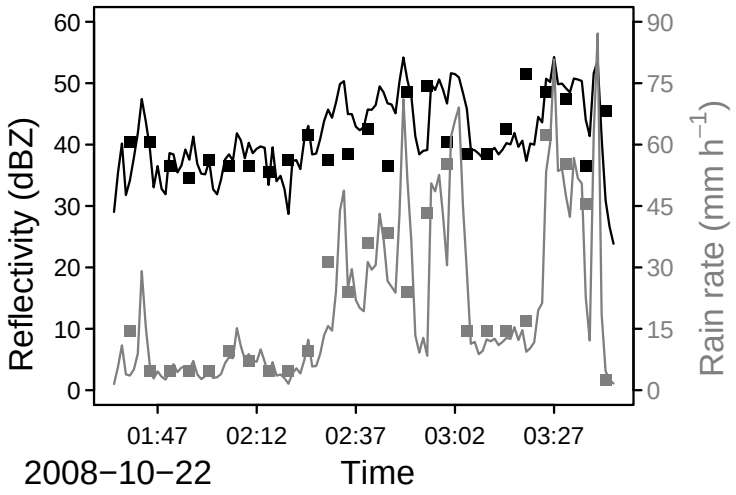

Figure 3.11: Same as Fig. 3.3, but for the event on October 22, 2008.

the scaling coefficients for this event are smaller compared to the other two events, leading to a larger value of the prefactor A, exceeding a value of 400. Such values for both Z–R parameters correspond well to a thunderstorm type of rain according to the list of 69 relationships as presented by *Battan* (1973).

The coefficients of determination in Fig. 3.12c show that the normalized gamma fit clearly outperforms the exponential one. This also leads to a better overall fit between Z and R in Fig. 3.13 and Table 3.3. Comparing the results of the two normalized methods to the direct least-squares fitting techniques shows that the results for the GAM and LG methods are almost identical. As for the former two events, the results of the LG method are close to either one of the microphysical techniques. This is probably due to the fact that for the microphysical methods logarithmic regression was performed between a given moment of the DSD vs. rainfall rate R (Eq. 3.14), resulting in an almost identical value for the Z–R exponent. Although overall differences between the four fitting techniques are small, the NR performs slightly better. This indicates again the occurrence of equifinality in Z–R parameter estimates, as shown in Fig. 3.14.

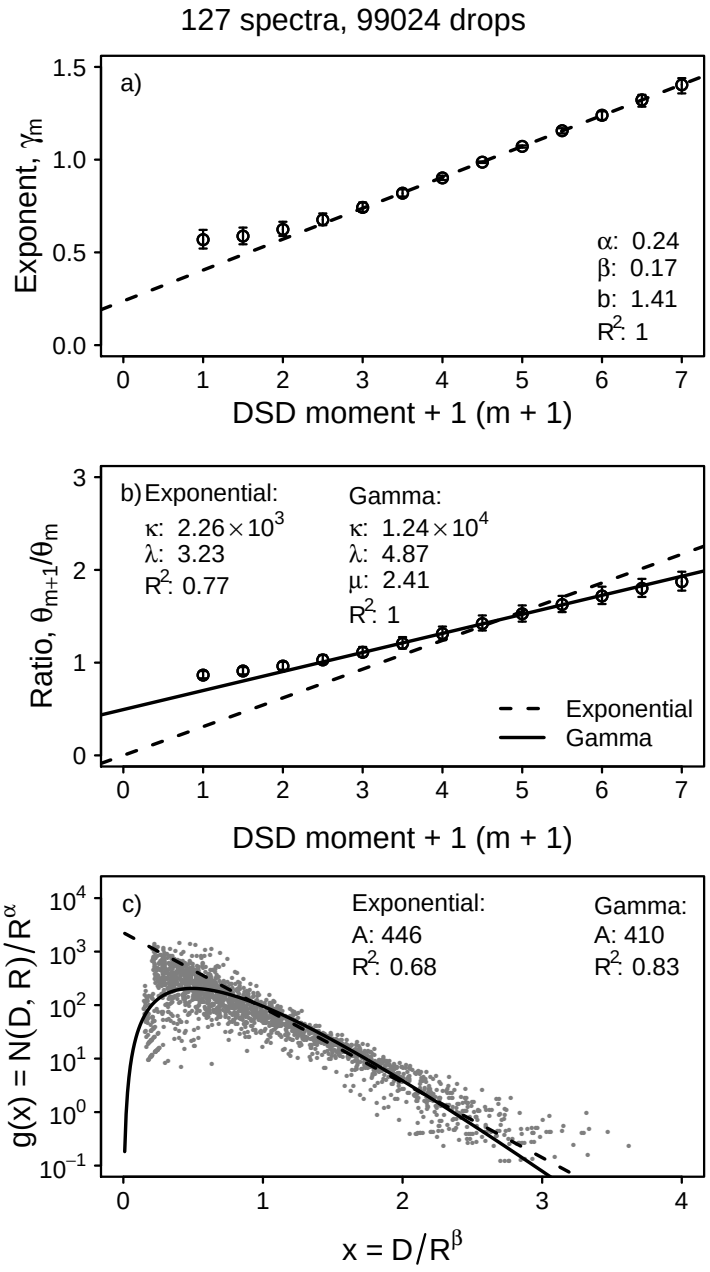

Figure 3.12: Same as Fig. 3.4, but for the event on October 22, 2008.

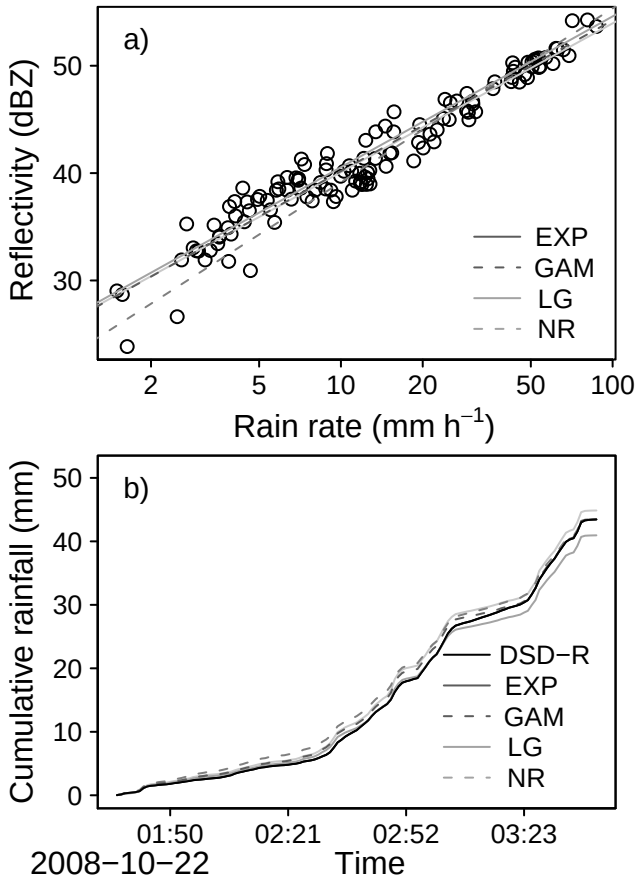

Figure 3.13: Same as Fig. 3.5, but for the event on October 22, 2008.

Table 3.3: Same as Table 3.1, but for the event on October 22, 2008. Overall accumulation by the disdrometer was 43.5 mm.

Method	A	b	RMSE	R^2	TBE	MAE
EXP	446	1.41	21.8	0.95	2.5	19.6
GAM	410	1.41	22.4	0.95	-0.02	19.8
LG	419	1.39	25.0	0.94	-1.41	20.3
NR	198	1.61	20.0	0.96	0.0	26.1

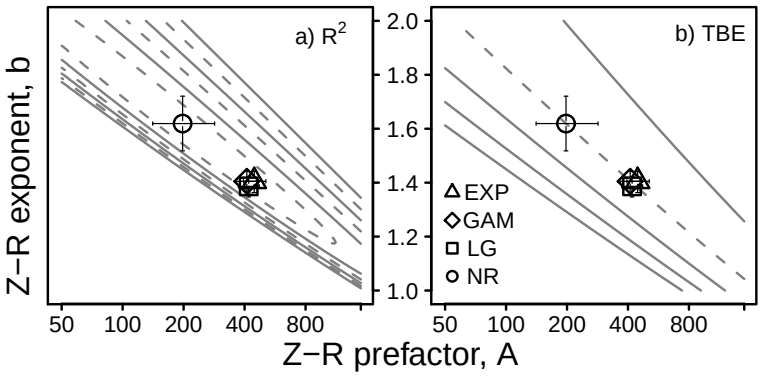

Figure 3.14: Same as Fig.3.6, but for the event on October 22, 2008.

3.5.4 Inter-event Z–R variability

The previous sections showed that different meteorological characteristics lead to considerable variation in microphysical rainfall properties. Similar types of analyses were performed on the entire dataset of 70 rainstorms. The overall variability in Z–R relations for the different events is presented in Fig. 3.15. As could already be observed for the three individual events discussed above, the obtained A and b values behave very similarly between the EXP, GAM and LG methods. As explained before, this is probably related to the fact that for both microphysical methods, logarithmic regression was performed between rainfall integral variables and rainfall rate.

For the NR method a slightly different behavior can be observed. The largest range in Z–R parameters is found for this technique, where large prefactors tend to correspond to small exponent values and vice versa (*Atlas et al.*, 1999; *Steiner and Smith*, 2000). For some events this even leads to exponents in excess of 2. Although such values might be optimal from a statistical point of view and have been observed in snow (*Sekhon and Srivastava*, 1970), in general they tend to be rather large (*Battan*, 1973; *Rosenfeld and Ulbrich*, 2003) and physically unrealistic (*Uijlenhoet et al.*, 2003a; *Steiner et al.*, 2004). During the second event it could be observed that these large values generally occur as a result of intra-event variations. In that particular case an actual intra-event change in the prefactor A was compensated through a larger exponent b. Similar reasonings lie behind the exceptionally large values of b fitted

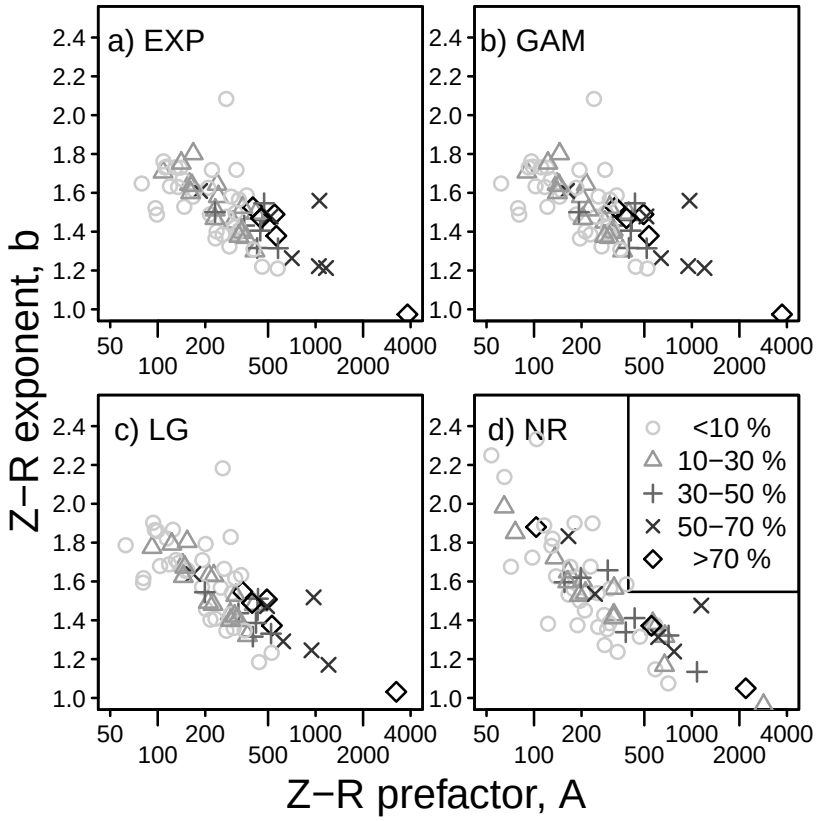

Figure 3.15: Optimal Z–R parameter values obtained by the four different methods for all 70 events. The different colors and symbols correspond to the fraction of the event for which the reflectivity exceeded 43 dBZ, as shown by the legend in (d).

by the NR method for some of the events presented in Fig. 3.15.

The goodness-of-fit statistics for the 70 events are shown in Fig. 3.16. Although the Z–R parameters for the two microphysical methods are derived in a totally different manner as compared to the two least-squares fitting techniques, the overall differences in the statistics are small. Especially between the EXP, LG and NR methods, the ranges of the RMSE and R^2 (exceeding 0.70) are similar. For the GAM method slightly larger ranges in goodness-of-fit statistics can be observed. Apparently, although that gamma distribution is well able to represent the normalized DSD shapes (see also Fig. 3.4, 3.8, and 3.12), in case one is interested in relating Z to R this distribution does not necessarily lead

to the best results. *Joss and Gori* (1978) found that when aggregating over larger intervals the DSD tends to become more exponential, which might result in a slightly better fit for the normalized exponential distribution as compared to the gamma one. Next to that, below cloud evaporation observed in more tropical regions (*Sauvageot and Lacaux*, 1995; *Atlas et al.*, 1999) likely does not play a major role here, hence increasing the amount of smaller droplets arriving at the ground and leading to a more exponential DSD shape. Also for larger droplets, it can be observed from Fig. 3.4 and 3.8 that the fit of the exponential distribution is rather good. The larger raindrops have a bigger effect on the higher moments of the DSD, like the reflectivity Z. This explains why for a given reflectivity factor the gamma fit overestimates the rainfall rate for certain events, leading to a more negative TBE as compared to the exponential DSD (Fig. 3.15). As explained in Section 3.3.4, this latter statistic is always zero for the NR method, which makes it more appealing from a hydrological perspective.

3.5.5 Storm-type specific Z–R values and microphysical parameter ranges

Besides presenting an overview, Fig. 3.15 also provides the convective character of the 70 events. Recall that this was based on a threshold value of 43 dBZ to indicate convective DSD samples. In Section 3.4 it was tried to explain the variability of the Z–R exponent between convective and stratiform events based on raindrop size distribution evolution and control mechanisms. Convective events in general have larger number concentrations and higher vertical extents. Overall this increases the amount of coalescence and break-up and decreases the time required to reach equilibrium conditions (e.g. *Blanchard and Spencer*, 1970; *Hu and Srivastava*, 1995; *Prat and Barros*, 2009). As a result, observed DSD spectra are more number-controlled.

For stratiform events such an analysis is not so straightforward. Drop interaction starts to occur below the zero-degree isotherm. Variability with respect to this height of the bright band and the question whether solid hydrometeors are present in the form of snow flakes or rimed ice crystals have a large impact on the types of raindrop size distributions observed. Therefore, for stratiform conditions a much larger range of exponents b can be expected, ranging from a number-controlled to a size-controlled situation.

A recent study by *Lanza and Vuerich* (2009) showed that the OTT/Parsivel disdrometer, which was also used in this chapter, generally

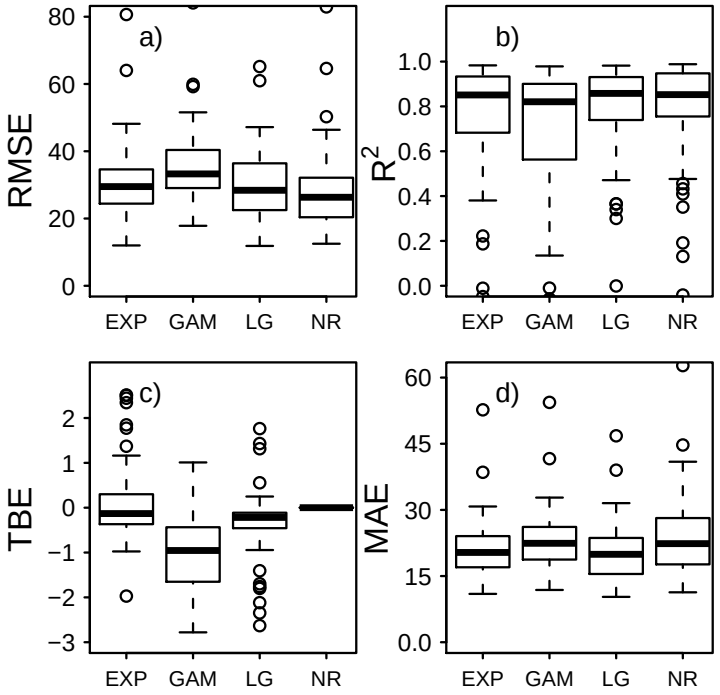

Figure 3.16: Quality of the obtained Z–R relationships based on the four different methods for the 70 events on the basis of different goodness-of-fit statistics.

overestimates the precipition intensity. Since this overestimation occurs during both stratiform and convective precipition, it is expected that the relative differences between the Z–R relationships for the different types of precipitation as presented in Fig. 3.15, will not be significantly affected. Next to that, it has been suggested that the OTT/Parsivel disdrometer generally understimates the amount of smaller raindrops while overestimating the amount of larger raindrops. However, since the parameters of the normalized drop size disdribution were obtained based on the central moments ($2 \geq m \leq 5$) of the DSD (see e.g. Fig. 3.4a and b), such instrumental effects were minimized.

The large dataset of 70 precipitation events clearly shows this expected type of behavior. Based on the EXP, GAM and LG results, more than half of the more serious convective events have exponents between 1–1.5. For the more stratiform type of events this range is much larger, between 1.2–2.0. This larger range in exponents b for the more stratiform precipitation events can also be observed for the scaling exponents α and β (see Fig. 3.17). Note that the combination of α and β defines the value of the exponent b (see Eq. 3.6). Events which contain at least 30% of convective activity exhibit values of $\alpha > -0.20$ and $\beta < 0.25$. Only for one of the 70 events an almost perfect number-controlled situation ($\beta = 0$) occurs. For all other events, size-controlled mechanisms play a role in determining the scaling exponents of the normalized DSD and as such the value for exponent b.

Fig. 3.15 also shows that generally smaller values of the exponent b result in larger values of the prefactor A. This inverse relation has also been observed for tropical maritime rain by *Atlas et al.* (1999). However, for the 70 events studied here, for a given value of the exponent b generally larger fractions of convectivity lead to larger prefactor values as compared to the more stratiform situations. The results for the NR method shows a slightly different behavior as compared to the other three. As explained, the optimal Z–R parameter pair resulting from this method depends heavily on the largest values measured. In addition, the associated parameter estimates exhibit larger 68% confidence intervals, as could also be observed from Fig. 3.6, 3.10, and 3.14. But even for this method, the more convective events contain larger prefactor values for a given Z–R exponent.

This behavior is different from that reported by *Atlas et al.* (1999) and *Tokay and Short* (1996). Besides the fact that in this study no intra-event separation was performed, differences with respect to these two studies are probably related to the more continental character of the

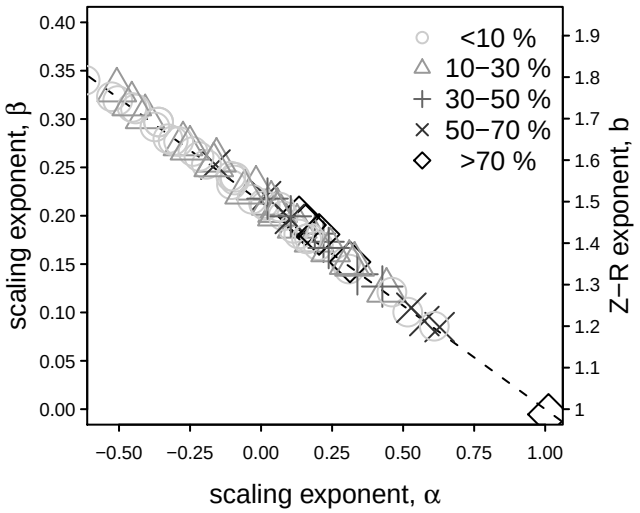

Figure 3.17: Self-consistency relationship between the scaling exponents α, β and the Z–R exponent b for the 70 events. The different colors and symbols correspond to the fraction of the event for which the reflectivity exceeded 43 dBZ, as shown by the legend.

precipitation events observed in the Cévennes-Vivarais region as compared to the more maritime character of the precipitation events analyzed by *Atlas et al.* (1999) and *Tokay and Short* (1996). For continental convective precipitation the Z–R prefactor generally tends to be larger compared to maritime convection (*Rosenfeld and Ulbrich*, 2003). In addition, in the Cévennes-Vivarais region many stratiform events have an orographic origin. This type of precipitation system generally tends to have a smaller median raindrop diameter and thus a smaller value of the prefactor A.

These latter characteristics can also be observed by analyzing the scaling-law parameters in Fig. 3.18. Events which have a more convective character either have smaller value of λ for the exponential distribution or a combination of either a smaller value of λ or μ for the gamma distribution, as compared to the more stratiform events. This indicates a larger amount of small and large drops for the convective events within the Cévennes-Vivarais region, which could also be observed when comparing Fig. 3.4c to 3.8c. Such behavior is different from DSDs observed in more tropical regions, where wind sorting and below cloud evaporation decreases the amount of small raindrops resulting in a more concave

DSD shape (*Yuter and Houze Jr.*, 1995b; *Sauvageot and Lacaux*, 1995; *Atlas et al.*, 2000; *Atlas and Ulbrich*, 2000). Apparently, climatological conditions within the Cévennes-Vivarais region, together with a smaller vertical extent of the precipitation systems as compared to the tropics, prevents this from happening. A similar reasoning probably also explains the fact that here a relatively large amount of large normalized raindrops are observed as compared to the tropical maritime situations. Due to the smaller vertical convective extents, the time for raindrop interactions to occur is smaller. This therefore decreases the amount of destruction of large raindrops by collisions.

The resulting smaller values of both μ and/or λ for the more convective precipitation events therefore lead to larger values of the prefactor A as compared to more stratiform type of events. From Fig. 3.17c it can be observed that for the more stratiform type of events the overall range in values of μ is rather large. As indicated in Section 3.4, during these situations raindrops originate from either snow flakes or rimed ice crystals. As a result, the observed DSDs for this type of precipitation can exhibit both small and large drop spectra (*Yuter and Houze Jr.*, 1997), which is reflected by the large range in observed μ values.

3.6 Summary and conclusions

This chapter presented the results of a hydrometeorological analysis of 2.5 years of disdrometer data collected in the South of France. In total 70 events were selected, of which both the reflectivity Z, the rainfall rate R, and the microphysical characteristics were identified. With respect to the latter aspect, based on the single-moment DSD normalization theory, a new method was presented by which the scaling-law parameters could be estimated. Compared to previous techniques presented in the literature, the main benefit of the current method is that the estimation process is much faster, leading to bulk event-based estimates of the different scaling-law coefficients and exponents. From these characteristics it is then possible to calculate the parameters of the Z–R relationship (Eq. 3.1) per event.

The objectives of this chapter were twofold, namely 1) to compare the obtained results from the newly proposed estimation method with respect to two more traditional Z–R parameter estimation techniques, and 2) to estimate the fraction of convectivity for each of the 70 events

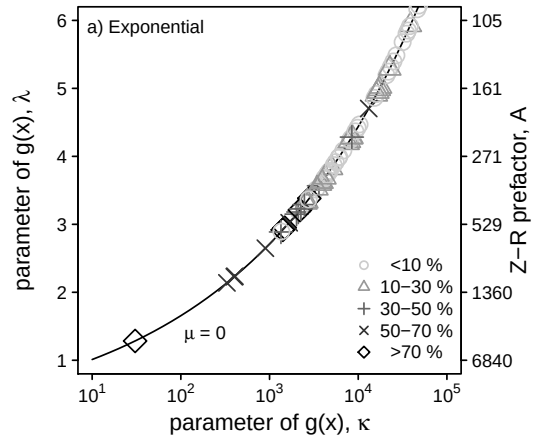
a) Exponential
parameter of g(x), λ
Z−R prefactor, A
parameter of g(x), κ
μ = 0
<10 %
10−30 %
30−50 %
50−70 %
>70 %

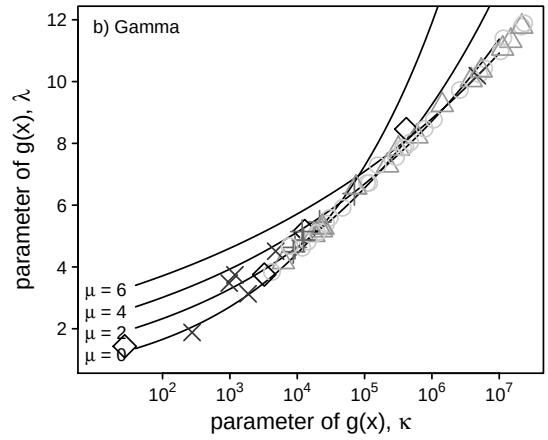
b) Gamma
parameter of g(x), λ
parameter of g(x), κ
μ = 6
μ = 4
μ = 2
μ = 0

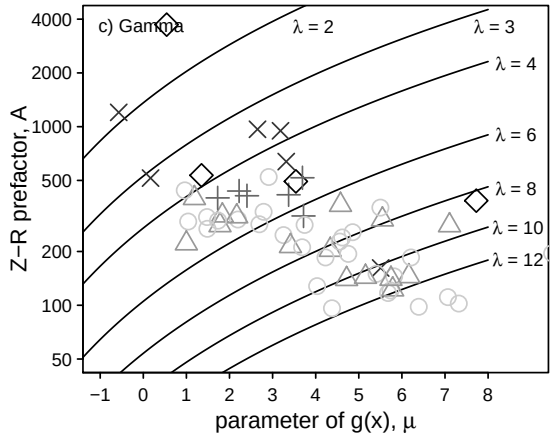
c) Gamma
λ = 2
λ = 3
λ = 4
λ = 6
λ = 8
λ = 10
λ = 12
Z−R prefactor, A
parameter of g(x), μ

and investigate whether a different type of event (convective vs. stratiform) leads to a different behavior in both the Z–R coefficients and microphysical parameter values. With respect to the first point the following main conclusions can be drawn:

1. The newly proposed estimation technique is well able to obtain estimates of both the different microphysical rainfall properties, as well as the parameter values of the Z–R relationship. From Fig. 3.4b, 3.8b, and 3.12b it can be observed that the mathematically expected linear relation as implied by Eq. 3.18 does indeed hold, especially for the normalized gamma distribution. But even the slightly worse fit as obtained from the exponential distribution does not immediately lead to a deviating fit of the normalized DSD. Especially for larger normalized diameters the fit of the exponential distribution for most events outperforms the gamma distribution. Because the higher moments of the DSD depend more on these larger drop sizes, for a lot of events the estimated Z–R prefactors from the exponential distribution are statistically slightly better as compared to those obtained from the normalized gamma fit (see Fig. 3.16).

2. When these Z–R parameters are compared to the results of the two statistical least-squares fitting techniques, overall results are very similar, although all methods produce different parameter estimates. The individually analyzed events showed that especially the differences between the EXP, GAM and LG methods are small, which is probably related to the fact that for the former two logarithmic regression was performed between the different moments

---

Figure 3.18 ***(preceding page)*****:** Analysis of the normalized DSD parameters for the 70 events analyzed. Plot (a) shows the self-consistency relationship between the parameters κ, λ and the Z–R prefactor A, assuming an exponential distribution. In (b) the values κ and λ are presented, assuming a gamma distribution. Also shown are the self-consistency relations for a given value of μ based on Eq. 3.11. Plot (c) presents the variability of μ and the Z–R exponent A, based on the gamma distribution. The presented lines for λ correspond to Eq. 3.11. The different colors and symbols correspond to the fraction of the event for which the reflectivity exceeded 43 dBZ, as shown by the legend in (a).

of the DSD versus the rainfall intensity. Therefore, the implemented mathematical techniques of the normalized DSD analyses and the direct logarithmic regression are similar. The non-linear statistical regression method, NR, gives rise to slightly different results for individual events, although its overall behavior is still quite similar. A positive aspect, which is a direct consequence of the way in which it was implemented, is the fact that it produces zero overall bias at the event scale. However, the uncertainty in its Z–R parameter estimates is much larger as compared to the other three methods and the zero bias does not always lead to proper intra-event behavior (see e.g. the RMSE in Table 3.1). In addition, intra-event variability can result in exponent b estimates which are, although statistically optimal, physically too large and unrealistic.

3. The fact that different techniques lead to similar statistical results gives rise to the possibility of equifinality. This means there is a larger range of values A and b which provides an equally good fit between values of R estimated via the Z–R relationship and those computed directly from the observed DSDs.

With respect to the second aspect of this chapter, a similar approach was adopted as in the local operational weather radar precipitation classification scheme. Convective regions were identified as those having a reflectivity exceeding 43 dBZ. Although this straightforward method is not able to identify all types of convection, it does give a first estimate of the overall convective fraction. Based on these results it can be concluded that:

4. Precipitation which contains a larger convective fraction generally exhibits smaller values of the exponent b. This property can be related to the fact that convective precipitation is generally associated with larger raindrop number concentrations and larger vertical extents. Both aspects increase the overall interaction time between raindrops, leading to a more number-controlled situation and thus smaller values of the prefactor. For the more stratiform precipitation a much larger range of prefactor values is observed.

5. For a given Z–R exponent the convective events generally exhibit a larger prefactor A. This latter aspect is different from DSD studies performed in tropical regions (*Tokay and Short*, 1996; *Atlas et al.*, 1999), for which the precipitation had a maritime character. For

the region of study, the more convective precipitation generally exhibits smaller values of λ and/or μ as compared to the more stratiform type. It is assumed that the latter properties are the result of less below cloud evaporation of the smallest droplets, and less destruction of large raindrops due to a more limited vertical precipitation extent, as compared to more tropical regions.

In this chapter some limited attempts have been made to compare the disdrometer-derived results to local weather radar samples. Although measured reflectivities by the disdrometer were comparable to those obtained from the radar (see Fig. 3.3, 3.7, and 3.11) a more extensive analysis should also have to focus on differences in sampling characteristics and vertical raindrop size distribution variations, which are beyond the scope of this study. This also holds for intra-event variability of the DSD.

CHAPTER 4

Precipitation region identification using a contour tracing grid-based algorithm

4.1 Introduction

In Chapter 2 the current potential of weather radar correction methods were presented. In order to improve the quality of the VPR correction algorithm, in Section 2.6 it was mentioned that more emphasis should be placed on smaller areas, more specifically by focusing on precipitation regions. There are multiple ways to identify precipitation regions from volumetric weather radar. However, a main constraint to implement this identification step is that the applied segmentation method should be computationally efficient, in order to be applicable for real-time purposes. The current chapter describes the details of a method that was specifically developed to deal with this issue.

Over the last decades, increasing amounts of spatial geographic data from spaceborne satellite and ground-based radar, remote sensing, and other types of data, have led to a considerable focus on smart and efficient solutions to extract the most essential information from different types of spatial images (e.g. *Wang et al.*, 1997; *Jain et al.*, 1999; *Sheik-*

This chapter is a slightly modified version of: Hazenberg, P., P.J.J.F. Torfs, H. Leijnse, and R. Uijlenhoet (2013), RoCaSCA: A contour tracing grid-based algorithm to identify similarity regions and clusters in spatial geographical data, *In prep.*

holeslami et al., 2000). Many of these methods either use a specific image segmentation technique or apply some kind of cluster identification method. The foremost benefit of identifying the dominant regions in a spatial image is that it leads to a considerable data reduction (*Zamperoni*, 1981; *Iñesta et al.*, 1996; *Shih and Wong*, 1999).

In general, three different types of spatial segmentation can be performed: 1) thresholding, 2) edge detection and 3) region extraction (*Rosenfeld and Kak*, 1982; *Fu and Mui*, 1981; *Zucker*, 1976; *Jain et al.*, 1999). However, many image segmentation algorithms make use of a combination of these three types (e.g. *Chang et al.*, 2004; *Wagenknecht*, 2007; *Wu et al.*, 2009).

Connected-component labeling is a widely used procedure in spatial image segmentation. The method was specifically developed for grid-based binary data, where neighboring pixels of a similar type are linked and assigned a unique label (the connected component) (*Rosenfeld and Pfaltz*, 1966; *Rosenfeld*, 1970; *Dillencourt et al.*, 1992). For cases where the application uses a continuous image, the connected-component labeling is preceded by a thresholding step to transform the input into binary information (*Fu and Mui*, 1981; *Jain et al.*, 1999). Most connected-component labeling algorithms can be classified into three categories: 1) multi-pass algorithms, 2) two-pass algorithms, and 3) single-pass algorithms, where the number of passes defines how many times a given input image is being analyzed sequentially (*Wu et al.*, 2009).

Another type of image segmentation method which is often applied for binary image data makes use of a tracing-type algorithm e.g. contour or border-tracing methods (e.g. *Freeman*, 1974; *Ren et al.*, 2002). Instead of specifically focusing on regions of connected pixels, contour-tracing techniques are mainly used for boundary detection. However, since boundary shapes define the semantics of an image, contour tracing techniques are able to extract the dominant information, leading to considerable data reduction. In general, such contours are obtained using a single outer border traverse procedure without repetition (*Freeman*, 1974; *Zamperoni*, 1981; *Testi et al.*, 2001). However, a number of algorithms that are able to deal with inner borders have been developed as well (*Xiao et al.*, 2001; *Chang et al.*, 2004; *Ren et al.*, 2002). Unfortunately, according to *Wagenknecht* (2007) many contour-tracing methods still have difficulties dealing with single pixel or inner contour regions.

Chang et al. (2004) implemented an image segmentation method, where the properties of both the contour tracing method and the connected-component labeling method were merged. By combining the benefits

of both techniques, a highly efficient single-pass algorithm was developed (*Wu et al.*, 2009; *He et al.*, 2009).

A drawback of both the connected-component labeling as well as the tracing-type algorithms is the fact that these methods only define an equivalent region which is closed-connected. As such, these algorithms assume that regions are separated by a hard boundary (*Fu and Mui*, 1981). For many application in hydrology, like weather radar precipitation region identification, such a hard boundary is too strict (*Steiner et al.*, 1995; *Johnson et al.*, 1998). Instead, cluster identification can be used, which also makes use of a certain proximity measure. However, this technique does not specifically make use of a hard boundary to identify a given region (*Gath and Geva*, 1989; *Jain et al.*, 1999).

Historically, cluster identification algorithms can be divided into hierarchical and partitional methods (*Jain et al.*, 1999; *Ma and Chow*, 2004). The former results in a nested series of clusters which are obtained using either an agglomerative bottom-up or a divisive top-down approach, where successively clusters are merged (split) into larger (smaller) clusters (*Jain et al.*, 1999). Examples of partitional clustering techniques are variants of the K-means and fuzzy C-means algorithms. Generally, these methods link individual objects to a given cluster based on some kind of distance or cost function criterion which is to be optimized. These algorithms are dependent on the initial choice and the number of clusters. Since such estimates are subjective, generally these algorithms are run multiple times (e.g. *Gath and Geva*, 1989). Originally, a drawback of partitional identification methods was their dependency on a predefined number of output clusters and initial guess positions, however, during the last decades a number of algorithms have been developed in which this process was automated (e.g. *Gath and Geva*, 1989; *Wong et al.*, 2001).

Another way to perform cluster identification is to make use of a density or grid based algorithm (*Ma and Chow*, 2004). These types are generally computationally more efficient, partitioning the data space first into a grid structure, before clusters can be identified. The main benefit of grid-based approaches over other partitioning techniques is that they are able to identify clusters of arbitrary shapes, positioned in a nested sequence or containing a concave shape, while being insensitive to outliers (*Wang et al.*, 1997; *Agrawal et al.*, 1998; *Sheikholeslami et al.*, 2000; *Ma and Chow*, 2004; *Lin et al.*, 2007). However, compared to segmentations techniques, cluster identification methods are computationally inefficient. This especially holds when dealing with large amounts

of gridded data as obtained within many hydrological applications, e.g. weather radar data.

This chapter presents an image segmentation method that was specifically developed to identify regions, using a tracing-type algorithm approach. However, compared to previously defined algorithms (e.g. *Suzuki et al.*, 2003; *Chang et al.*, 2004; *He et al.*, 2009) the implementation presented in the current chapter is not limited to direct neighbor linking only. On the contrary, connecting-component labeling forms a special case, but the algorithm developed here also has similarities to the density and grid-based cluster algorithms. As such, the image segmentation method presented here is specifically interesting to be used in earth science applications, e.g. weather radar image analysis. By applying the computational efficiency provided by most segmentation methods, in combination with a flexible distance metric similar to most cluster identification methods, the algorithm presented here merges both types of approaches.

This chapter is organized as follows. Section 4.2 presents the main aspects of the contour-based cluster algorithm presented here, by focusing on neighboring (Section 4.2.1) and non-neighboring pixels (Section 4.2.2). In Section 4.3 the potential of our algorithm are presented for a number of typical examples for grid-based. Section 4.4 finishes with conclusions as well as some discussion.

4.2 The rotational carpenter square cluster algorithm (RoCaSCA)

The aim of the algorithm presented in the current chapter is to identify regions within a given continuous weather radar image, represented by a grid of $l \times b$ pixels. A region is then defined as a minimum of N_p pixels which receive a similar label. All pixels belonging to a given region exceed a user-defined reflectivity threshold T and lie within a maximum inter-pixel distance I_h in the horizontal and I_v in the vertical direction. By providing the possibility of using variable lengths for I_h and I_v, the current algorithm is able to deal with rectangular grid pixels.

4.2.1 Connecting neighboring pixels

As explained in the introduction, the segmentation algorithm developed in the current chapter takes a similar approach as the tracing-type algorithm developed by *Chang et al.* (2004). As such, regions are identified

using first a contour tracing algorithm to identify their boundaries, followed by a similar approach to label the inner pixels of a precipitation region.

In their paper, *Chang et al.* (2004) used the contour tracing method originally developed by *Haig and Attikiouzel* (1989). This method takes a clockwise search approach to identify the next contour pixel based on the eight neighboring pixels, which could be implemented in a single function call. The interest here lies in finding the next neighbor that lies within given distances I_h and I_v in the horizontal and vertical direction, respectively. Therefore, this procedure is executed in four individual steps, using the properties of a carpenter square with dimensions $I_h + 1$ and $I_v + 1$. Computationally, a carpenter square can be represented by two separate vectors. By reversing the order of either of these vectors, the carpenter square (CS) can rotate and move in four different directions around a given boundary. Another benefit of applying a CS is that the algorithm becomes rotationally invariant. As such, pixels belonging to a given precipitation region are clustered together. Hence, we call this the Rotational Carpenter Square Cluster Algorithm (RoCaSCA).

In Fig. 4.1a the basic graphical representation of this procedure is shown for a precipitation region represented by a single pixel, which exceeds the predefined threshold T. After encountering the first pixel belonging to a given contour (second panel of Fig. 4.1a), the CS rotates along the boundary of the cluster. This rotation continues until the initial position is reached again by the CS (last panel in Fig. 4.1a). As such, the contour delineation uses a a single outer border traverse procedure similar to other algorithms (*Chang et al.*, 2004; *Wagenknecht*, 2007). Rotation of the CS (i.e. reversing either the horizontal or vertical vector) is implemented as part of an internal procedure. This means that once a positive pixel is identified, the CS traverses to its initial position in 4 steps (for clarity, the internal rotation procedures are shown as separate steps in Fig. 4.1). During each step only one side of the CS is being analyzed to contain the next positive boundary pixel (i.e. the vector perpendicular to the moving direction). In case no new boundary pixel is encountered the CS is rotated in clockwise direction by reversing the tangent vector and moving the position of the other vector one pixel. In Fig. 4.1b and c the contour tracing procedure of RoCaSCA for two horizontally (b) and diagonally (c) neighboring pixels is shown. When a new boundary pixel is encountered by the perpendicular vector of the CS, the CS either moves to the next position forward (i.e. when the new pixel is encountered at a corner point (Fig. 4.1b)), or rotates in clockwise

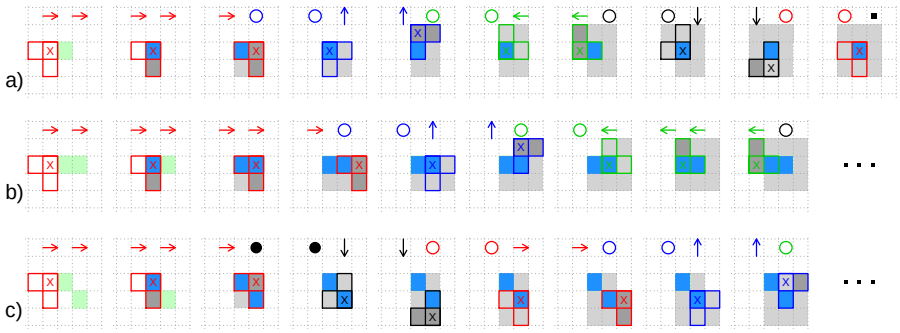

Figure 4.1: General technique behind the contour tracing algorithm of RoCaSCA for a) an individual pixel, b) two horizontally neighboring pixels, and c) two diagonally neighboring pixels. The color of the carpenter square indicates its direction of movement for the four different directions (i.e. red (right), blue (up), green (left) and black (down)). These directions and coloring are also indicated by the arrows on top of each subplot, where the left (right) indicates its last (next) direction. A closed (open) circle on top of a subplot indicates a(n) (anti)clockwise shift in the direction of the carpenter square, where the former (latter) indicates when a new pixel belonging to the same cluster is identified. Gray pixels will be left out from further analyses by RoCaSCA.

direction before moving forward (i.e. when new pixel is not encountered elsewhere by the perpendicular vector of the CS (Fig. 4.1c)).

The complete segmentation procedure of RoCaSCA to label neighboring connected-object pixels is presented in Fig. 4.2. Here the following steps are performed:

1. Define the size of the CS with length 2 in both horizontal the (I_h = 1) and vertical (I_v = 1) direction, respectively.

2. Sequentially scan the input image until the first pixel ($> T$) is identified belonging to the contour of a given precipitation region (Fig. 4.2a).

3. Perform the rotational CS procedure as shown in Fig. 4.1 to identify the region boundary until the first pixel is encountered again (Fig. 4.2b).

4. Start connecting the inner pixels of a given region using an inward

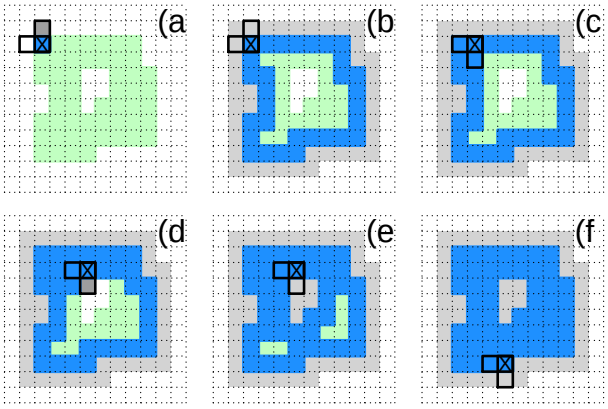

Figure 4.2: Example of the combined step of tracing the outer (a-b) and inner (d-e) contour for a given region and labeling all individual pixels (c-f) using a connected component approach to identify all inner pixels part of a given region, as implemented in RoCaSCA.

facing CS, until all are labeled (Fig. 4.2c,f). The inward facing CS moves between the identified boundaries of the outer contour.

5. In case an inner contour is identified (Fig. 4.2d), the inward facing CS identifies the inner boundary by rotating in the opposite direction (Fig. 4.2e).

Besides identifying individual precipitation regions, RoCaSCA also immediately identifies boundary pixels not part of the identified region (gray pixels in Fig. 4.1 and 4.2). These pixels are left out of further analyses while passing through the rest of the image. The amount of memory used as part of this identification procedure consists of two grids (one input grid and one output grid of size $(l+I_h+1) \times (b+I_v+1)$) as well as the information on the position and size of the CS. The dimensions of the input grid are increased to remove any possible boundary effects at of the border the image.

4.2.2 Connecting non-neighboring pixels

The previous section described the most basic implementation of RoCaSCA, where only neighboring object pixels are labeled as part of the same precipitation region. This implementation leads to similar results

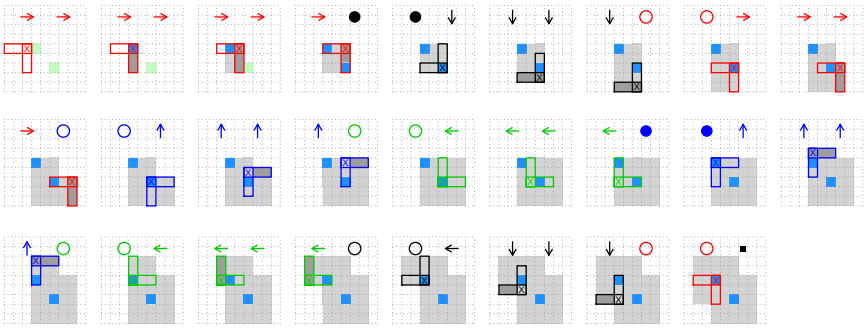

Figure 4.3: Example of two non-neighboring (light-green) pixels becoming part of the same precipitation region as a result of an increased size of the carpenter square. The colors and the symbols above each subplot have a similar meaning as in Figure 4.1.

as other connected-component labeling (e.g. *Dillencourt et al.*, 1992; *Fiorio and Gustedt*, 1996; *Suzuki et al.*, 2003; *Chang et al.*, 2004; *Wu et al.*, 2009; *He et al.*, 2009) and tracing-type algorithms (*Chang et al.*, 2004). However, for many precipitation systems as observed by weather radar, non-neighboring pixels can belong to the same rainfall region (*Steiner et al.*, 1995; *Johnson et al.*, 1998). Therefore, the capabilities of most standard segmentation algorithms provide too strict dependencies since they only label connected pixels. RoCaSCA does not have such a limitation. By increasing the size of each side of the CS, the assumption of a hard boundary is relaxed, making it more flexible to identify precipitation regions. Here lies the main benefit of applying RoCaSCA compared to other image segmentation algorithms. Increasing the size of the CS (i.e. the size of the two vectors) does not lead to any changes in the specific programming code.

A simple example of the use of RoCaSCA to label non-neighboring pixels to the same region is presented in Fig. 4.3, by increasing the length of each side of the CS. It can be observed from this figure that the individual rotating steps are similar to the ones presented in Figure 4.1.

In Fig. 4.4 the implementation of RoCaSCA to label a larger precipitation region of loosely connected pixels is presented. The different steps performed are similar to the procedure executed in Fig. 4.2. In case one would only be interested in labeling neighboring pixels, analysis of Fig. 4.4 would lead to a total of three different precipitation regions. However, the increased size of the CS identifies a single contour, instead of three. Note from Fig. 4.4c that pixels that do not surpass the

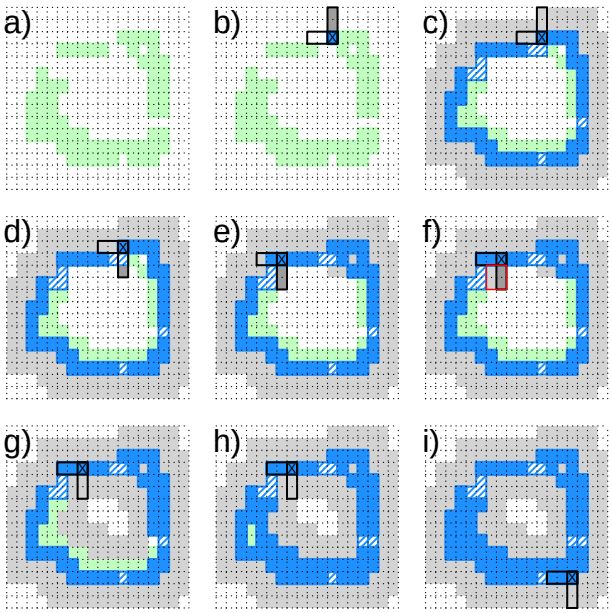

Figure 4.4: Example of the combined step of tracing the outer (a-b) and inner (d-e) contour for a given hypothetical precipitation region and labeling all individual pixels (c-f) belonging to that region using a connected component approach, as implemented within RoCaSCA. The red box in (f) delineates the minimal requirement to start the inner-contour identification procedure.

threshold value T but are part of the identified contour, get temporarily a value (dashed blue pixels) different from the excluded objects (gray pixels). To identify the inner cells of a given region (Fig. 4.4d,e), RoCaSCA temporarily assumes these boundary pixels to be part of the same precipitation region. In order to proceed with identification of an inner contour boundary, a rectangle of $I_h \times I_v$ background pixels should be identified (red square in Fig. 4.4f) before its delineation is executed (Fig. 4.4g).

4.2.3 RoCaSCA implementation specifics and complexity

In the previous sections the basic ideas behind RoCaSCA were presented. For the current implementation, in line with *Chang et al.* (2004), the following properties hold:

1. Each pixel belonging to the boundary contour is analyzed a maximum amount of $2I_h + 2I_v$ times, depending on the complexity of the boundary.

2. Pixels belonging to the same precipitation region are assigned the same label.

Many weather radar rainfall cell-tracking algorithms as presented in the literature identify precipitation regions at different levels of intensity (e.g. *Dixon and Wiener*, 1993; *Johnson et al.*, 1998; *Handwerker*, 2002). Given the fact that a precipitation region identified at a higher threshold also belongs to a region at a lower threshold, the algorithm was implemented in a hierarchical manner (see Section 5.3.4). This ensures that computation time is optimized when identifying precipitation regions for a higher reflectivity threshold. For volumetric weather radar data, the raw polar image data contains a vertical boundary that is periodic (i.e. the pixel to the left of the left boundary is the right-most pixel). Pixels exceeding the reflectivity threshold at both sides of this boundary actually belong to the same precipitation region. In the current implementation of RoCaSCA, these pixels are indeed identified as belonging to the same cluster (see Section 4.3.1 and Fig. 4.5).

4.2.4 Runtime comparison: RoCaSCA vs. FLCCL

In order for RoCaSCA to be a useful tool for precipitation region identification using the information provided by volumetric weather radar, its computation time should be short. Given the complexity to identify precipitation regions and correct for all sources of error affecting weather radar measurements, only an efficient algorithm can be used for real-time applications. To give an indication of the computation speed of RoCaSCA with respect to traditional image segmentation methods, it will be compared to the Fast Linear Connected Component Labeling (FLCCL) algorithm. The FLCCL algorithm, as developed by *He et al.* (2009), is the fastest segmentation algorithm in the world for 2D binary data (*Wu et al.*, 2009).

RoCaSCA was originally developed to efficiently segment a weather radar image into its dominant precipitation regions, providing the possibility of taking both a flexible distance metric and transition pixels into account. This is completely different from the purpose of FLCCL, which purely focuses on connected component labeling. Therefore, in case the computation speed of RoCaSCA is of a similar order of magnitude as

the FLCCL algorithm, it can be considered as a useful tool for real-time precipitation region identification purposes.

For the comparison of RoCaSCA with respect to FLCCL, a total of 94 binary images of 512 $\times$ 512 pixels are used. These images are generally used as standard testing material to assess the computation speed of a given segmentation algorithm (*Suzuki et al.*, 2003; *He et al.*, 2009; *Wu et al.*, 2009). They are subdivided into 5 different categories; natural, noise, photo, special and textural images. Next to that, random binary images are created for varying grid dimensions, with $n = 2, 4, ..., 2048$ pixels on each side. For each of these images, binary values were randomly drawn from a binomial distribution with probability of success varying from $p = 0.02, 0.04, .., 0.98$. By using RoCaSCA as a standard segmentation algorithm it is compared to FLCCL. Based on this last test example, it becomes possible to assess its computational efficiency for varying image sizes with varying pixel density. The comparison was executed on a notebook (Intel(R) Core(TM) 2 Duo CPU T9300 @ 2.50GHz, 2048 MB Memory, Ubuntu Linux OS)

4.3 Results

4.3.1 Runtime comparison

Neighbor connecting

As explained in Section 4.2.4 the 94 test images are separated into 5 different categories. An example of a typical image used in each category is presented in Fig. 4.5. Also presented at the bottom of each label is the runtime and the number of identified components. As anticipated, both algorithms identify a similar amount of connected components, although the runtime of RoCaSCA is slightly slower compared to FLCCL. However, the overall segmentation time of RoCaSCA is very short.

Histograms of the runtime of RoCaSCA and FLCCL to segment all 94 images are given in Fig. 4.6. RoCaSCA has most difficulty with connecting components in noisy images. In general, noisy images contain irregularly shaped contour boundaries, which take a relatively long time to be identified. For images that contain more closely connected regions, RoCaSCA runs much faster, since the number of CS rotations is much smaller (see also Fig. 4.5). From this figure it also immediately becomes clear why FLCCL is the fasted neighbor segmentation algorithm in the world, its runtimes are considerably shorter than those of RoCaSCA.

To gain a better understanding on the computation speed difference

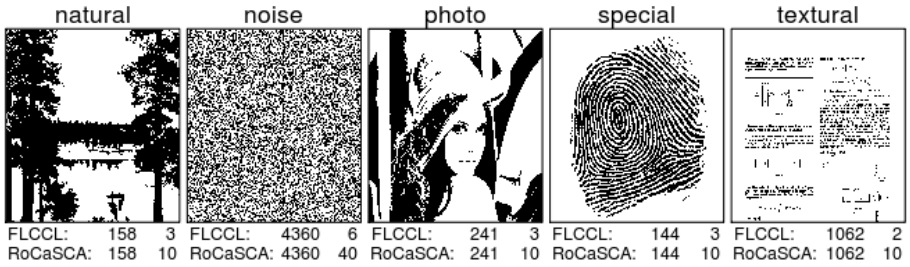

Figure 4.5: Example of each of the 5 categories of images used to test to computation speed of RoCaSCA with respect to FLCCL. Each image has a size of 512 × 512 pixels. At the bottom of the image, for both algorithms the number of connected components and the computation speed (msec) is given.

between both algorithms, the ratios of both computation times are taken and presented in Fig. 4.7. For the 94 test images RoCaSCA on average is about 6.5 times slower than FLCCL. However, it should be emphasized that FLCCL was specifically developed and optimized for connecting neighboring pixels. The fact that RoCaSCA is able to achieve runtimes similar order of magnitude as FLCCL shows it is efficient to identify individual regions, especially, when considering the fact that RoCaSCA runs relatively fast for natural images that contain continuous areas. This type of images are generally also observed by weather radar.

To further test the capabilities of RoCaSCA, a number of random binary images with varying grid sizes are created. In Fig. 4.8 the runtime results of this analysis are presented, as well as those of using the FLCCL algorithm. In general, both RoCaSCA and FLCCL run more efficiently in case the pixel density is lower or higher (i.e. a small and large value of the binomial distribution probability p). However, the overall impact of density variability is small. Similar to the previous results, RoCaSCA is slower than FLCCL, with runtime increasing for larger images. From Fig. 4.9 it can be observed that this increase in runtime is about linear with a slope of 2. This indicates that the runtime of RoCaSCA doubles in case the input grid becomes twice as large, just as FLCCL. Again this shows that RoCaSCA is an efficient algorithm to be applied for image segmentation.

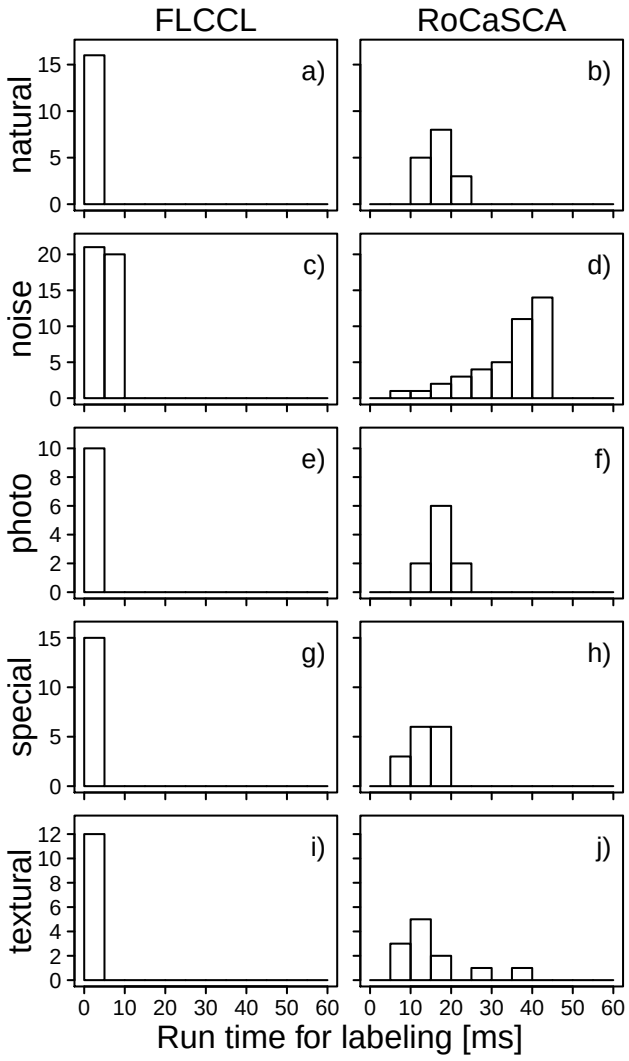

Figure 4.6: Histograms of the runtime (msec) used for segmentation by RoCaSCA and FLCCL for the five different test image categories.

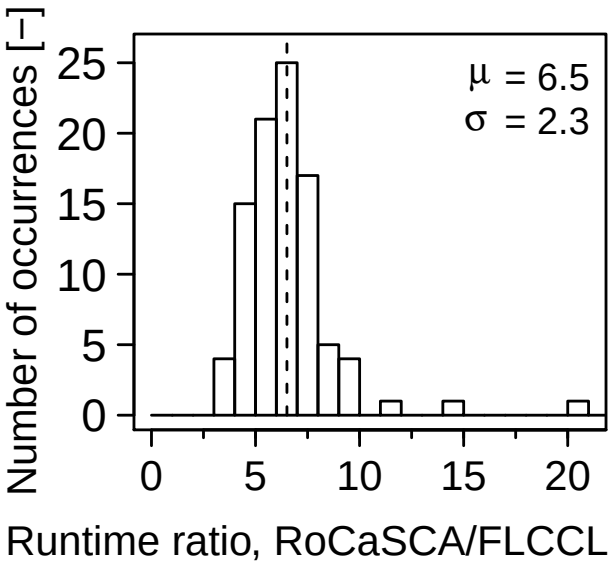

Figure 4.7: Histogram of the runtime ratio between RoCaSCA and FLCCL for all 94 test images. The mean runtime ratio μ (dashed vertical line) and standard deviation σ are given on the top right.

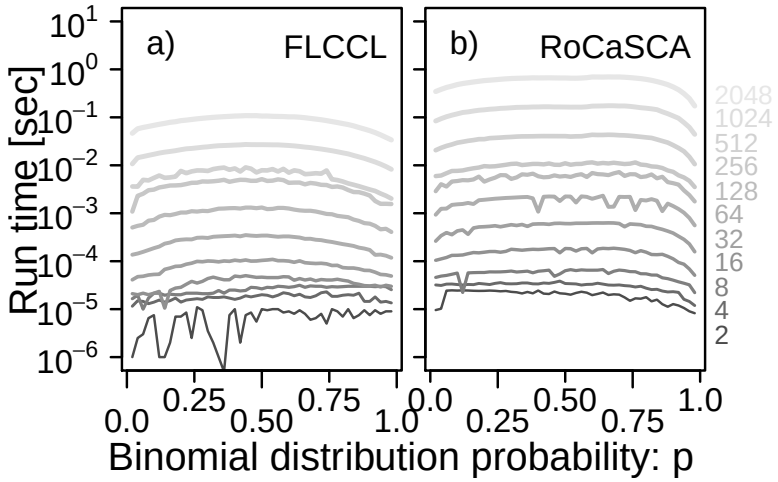

Figure 4.8: Runtime comparison (msec) between FLCCL (a) and RoCaSCA (b) to segment random binary images of varying sizes $n = 2, 4, ..., 2048$ and different densities. The image size is given by the different gray shades, while densities are created by randomly drawing from the binomial distribution for probability values $p = 0.02, 0.04, ..., 0.98$.

Non-neighbor connecting

In the previous section, the ability of RoCaSCA to link neighboring pixels was tested. Overall, runtime results are very promising, although its efficiency is not as good as FLCCL. However, as explained before, RoCaSCA was not specifically developed nor optimized to handle linking of neighboring pixels only. On the contrary, connected component labeling is just a special case. In Fig. 4.9 the runtime statistics of RoCaSCA for both neighboring ($I_h = I_v = 2$) and non-neighboring ($I_h = I_v > 2$) pixels are shown. For increasing maximum inter-pixel distances I_h and I_v, runtime on average only slightly increases. However, this effect is hardly noticeable.

The results presented in Fig. 4.9 also show the limitation of FLCCL. Even though this algorithm outperforms RoCaSCA when focusing on connected pixel labeling, it was not developed for and is unable to deal with the linking non-neighboring pixels to the same region. Therefore, in practice, this algorithm is not very useful to identify precipitation regions on weather radar images, since for this type of image two non-neighboring pixels can belong to the same precipitation region in case their proximity lies within a certain user-defined distance (e.g. *Johnson et al.*, 1998). As such, RoCaSCA provides a much more useful alternative, which is quite computationally efficient as well.

As a last example, in Fig. 4.10 the runtime and number of delineated components by RoCaSCA for varying sizes of the CS are presented. This example provides a clear overview of the potential of RoCaSCA to link non-neighboring pixels to the same region.

4.4 Conclusion and discussion

In the current chapter a grid-based image segmentation algorithm is presented which is able to label pixels belonging to the same region using the properties of a rotational carpenter square. RoCaSCA can be defined as a tracing type image segmentation method, where a region or cluster is identified by delineating first its outer contour. Once the outer boundary is known, inner regions and contours are defined in a similar manner. This approach results in a single-pass segmentation algorithm with considerable similarities to the contour tracing identification method of *Chang et al.* (2004). However, compared to their algorithm, the method presented here is not dependent on neighboring pixels only. On the contrary, the current chapter shows the ability of RoCaSCA to also link non-neighboring pixels to the same region by in-

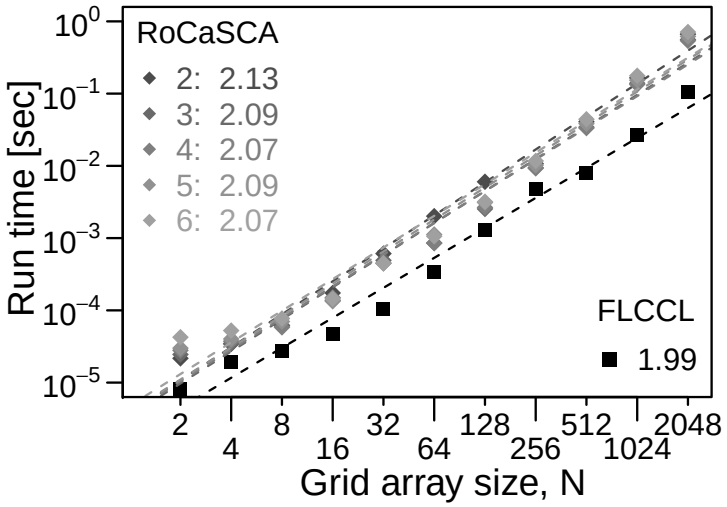

Figure 4.9: Runtime comparison (msec) to segment random binary images with varying sizes $n = 2, 4, ..., 2048$. RoCaSCA is used with different sizes of the CS ($I_h = I_v = 2, 3, ..., 6$) as given by the different gray shades, while FLCCL is only able to connect neighboring pixels. These binary images are created by drawing randomly from the binomial distribution with expectation $p = 0.5$. The values provided in the legend represent the slope of the linear relationship of image size and runtime.

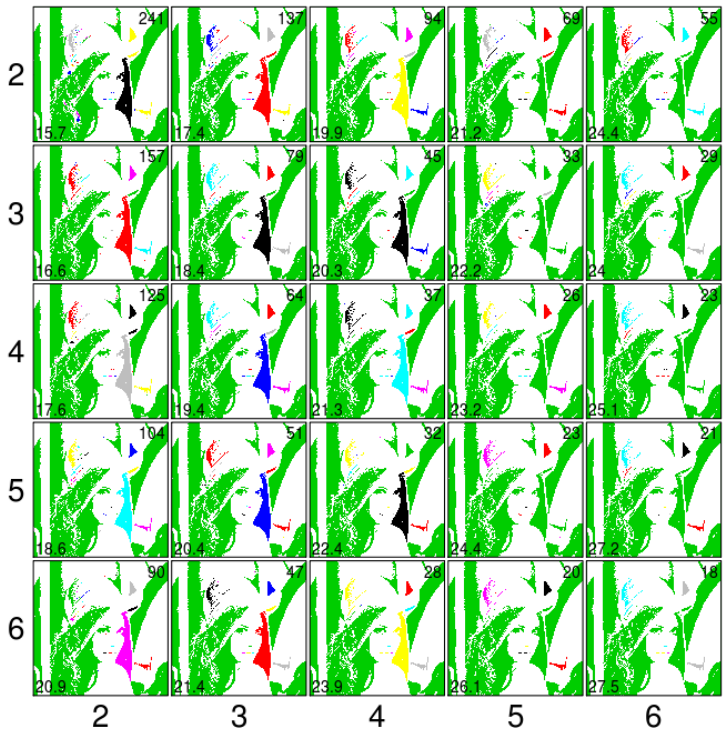

Figure 4.10: Example of the segmentation potential of RoCaSCA for varying sizes of the CS, I_h and I_v given on the x and y-axis. The number of identified regions is presented on the top right of each panel, while at the bottom left the runtime (msec) is given.

creasing the size of the CS. This enables closely located pixels to become part of the same region, but also filters the impact of noise.

In order for RoCaSCA to be applicable to identify precipitation regions on weather radar images for real-time applications, its implementation should be efficient. Therefore, its computation speed has been compared to the FLCCL algorithm, which is generally accepted as the fastest segmentation algorithm in the world (*He et al.*, 2009; *Wu et al.*, 2009). Results show that the computation speed of RoCaSCA is of a similar order of magnitude as that of FLCCL, although the latter clearly outperforms RoCaSCA. However, since FLCCL is not able to deal with the linking of non-neighbor pixels to the same region, it is not very useful for precipitation region identification. RoCaSCA, on the other hand, is shown to be highly efficient when it comes to linking non-neighboring pixels. This makes this algorithm very useful to be applied for the identification of precipitation regions.

CHAPTER 5

Region based VPR identification and uncertainty estimation

5.1 Introduction

The wide-scale implementation of weather radar systems over the last decades has increased our understanding of precipitation dynamics. These devices provide information at a much higher spatial and temporal resolution than conventional rain gauge networks (*Zawadzki*, 1975; *Joss and Lee*, 1995; *Smith et al.*, 2001; *Zhang et al.*, 2005; *Gourley et al.*, 2009). However, quantitative estimation of precipitation by weather radar is affected by many sources of error related to the physical characteristics of both the instrument, the surrounding environment and the atmosphere (e.g. *Waldvogel*, 1974; *Delrieu et al.*, 1995; *Fabry et al.*, 1997; *Gabella and Perona*, 1998; *Steiner and Smith*, 2002; *Dinku et al.*, 2002; *Germann et al.*, 2006; *Uijlenhoet and Berne*, 2008).

Over the last decades a large number of methods has been proposed to correct for these different error sources (see e.g. *Joss and Waldvogel* (1990); *Andrieu et al.* (1997); *Villarini and Krajewski* (2010); *Hazenberg*

This chapter is a slightly modified version of a manuscript submitted to *J. Geoph. Res.*: Hazenberg, P., P.J.J.F. Torfs, H. Leijnse, G. Delrieu, and R. Uijlenhoet (2013), Identification and uncertainty estimation of vertical reflectivity profiles using a Lagrangian approach to support quantitative precipitation measurements by weather radar.

et al. (2011a) and the references therein). A dominant source of error results from vertical variations in hydrometeor properties (including their size distribution and phase) known as the vertical profile of reflectivity (VPR) (e.g. *Battan*, 1973; *Smith*, 1986; *Joss and Pittini*, 1991). This especially holds for stratiform systems, where snow and ice particles at higher altitudes generally lead to a decrease in the returned radar signal. Around the zero degree isotherm, the melting of snow gives rise to relatively large, water-coated particles. Within this region, known as the bright band (BB), the return signal is intensified. Since radar beam height and beam volume both increase with distance (the so-called range effect), for stratiform precipitation, serious overestimation of surface reflectivity by radar occurs when sampling within the melting layer, while above this region underestimation takes place. Overall, this has a detrimental impact on the quality of radar precipitation estimates (*Fabry et al.*, 1992; *Kitchen and Jackson*, 1993; *Bellon et al.*, 2005). An example of the impact of the VPR on the quality of the radar measurement for a typical stratiform profile is presented in Fig. 5.1a and b.

Due to vertical mixing by intense up and down drafts, such a clear vertical segmentation of the hydrometeor size distribution is generally not observed for convective precipitation. Therefore, identification of the impact of a convective VPR on the measurement characteristics of the radar is not straightforward.

In meso-scale convective systems, once the dominant convective activity decreases, the precipitation system evolves towards a stratiform type of precipitation (*Yuter and Houze Jr.*, 1995a; *Uijlenhoet et al.*, 2003b). During this transition phase with moderate precipitation intensities, before the formation of a BB occurs, the coalescence of small raindrop particles generally leads to an increase of reflectivity towards the surface (see Fig. 5.1d) (*Yuter and Houze Jr.*, 1995c). Therefore, rainfall intensities for this transition type of precipitation tend to be underestimated by the weather radar, especially as the range increases (Fig. 5.1e).

Historically, the physical properties of the VPR for different types of precipitation are well known (*Austin and Bemis*, 1950; *Battan*, 1973). However, due to a dominant focus on weather radar measurements of convective precipitation, correcting for the impact of range effects and VPR in stratiform precipitation only started to receive attention since the middle of the 1970s and early 1980s of the previous century (*Harrold and Kitchingman*, 1975; *Smith*, 1986; *Collier*, 1986).

Since then, two main approaches have been developed to correct for

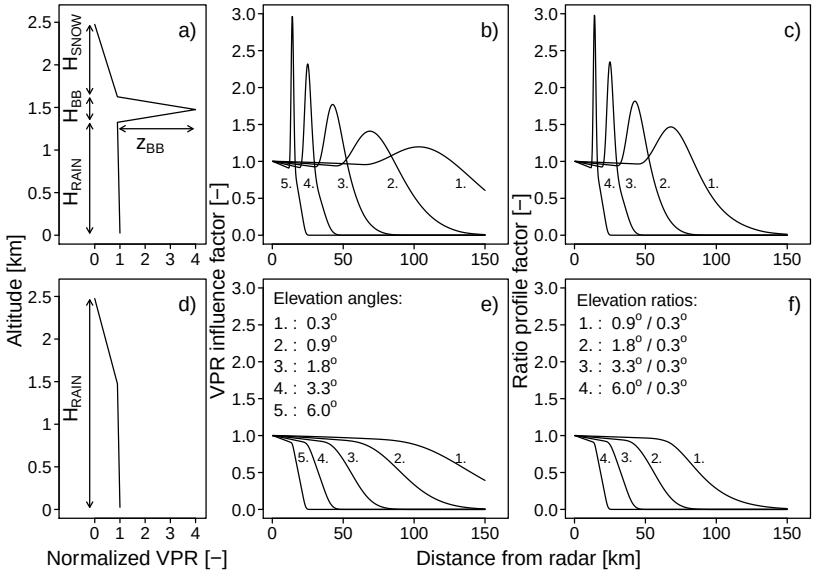

Figure 5.1: Example of the impact of the vertical profile of reflectivity (VPR) for stratiform (upper panels) and transition/non-stratiform precipitation (lower panels) for the C-band weather radar used in the current study. Left panels present the average shape of the VPR, generally assumed to be spatially uniform for a given type of precipitation. Middle panels show the impact of the VPR on the radar measurement for five different elevation angles. Right panels present the identified ratio profiles, defined as the ratio of one of the higher elevation angles with respect to the lowest one as a function of distance.

the impact of range and VPR effects. The first approach uses an empirical range-dependent correction function for a given type of precipitation and season. This function can either be obtained from historical/climatological information (*Collier*, 1986) or estimated from the apparent scaling properties of the radar measurements (*Chumchean et al.*, 2004). However, since the height of the bright band varies over time, real time implementation of such an approach does not immediately lead to an increase in the quality of the weather radar measurements.

A second way is to estimate the VPR at a given point (*Kitchen et al.*, 1994; *Smyth and Illingworth*, 1998) or to identify its mean profile representative for a larger region (*Smith*, 1986; *Andrieu and Creutin*, 1995; *Germann and Joss*, 2002). Based on such profiles and the measurement characteristics of the radar, it is then possible to correct for the impact of VPR as a function of range. The benefit of the former procedure to apply point corrections is that the small scale variability of the VPR is taken into account, that is generally also observed from in situ measurements by vertically pointing radars (*Joss and Waldvogel*, 1990; *Fabry and Zawadzki*, 1995; *Cluckie et al.*, 2000; *Berne et al.*, 2004b; *Martner et al.*, 2008). However, for many precipitation systems such local variabilities are difficult to identify by most conventional radar systems. Therefore, the latter approach provides a compromise, where a mean representative VPR is estimated for either a static fixed part of the radar umbrella (*Vignal et al.*, 1999, 2000; *Seo et al.*, 2000; *Germann and Joss*, 2002; *Vignal and Krajewski*, 2001) or for a given type of precipitation (*Delrieu et al.*, 2009; *Kirstetter et al.*, 2010a).

These second type of methods, estimate the VPR based on an Eulerian procedure without specifically taking the temporal movement and change in spatial location of the precipitation field into account. Estimation and correction of the VPR for a given precipitation region using a Lagrangian approach, to the authors' knowledge, has not been performed so far. Nevertheless, for highly dynamical systems like precipitation, such an approach would seem to be highly recommended. Therefore, the current chapter presents a Lagrangian-based VPR correction method that focuses on precipitation regions and their temporal evolution. The correction method proposed here combines and extends the VPR identification methods proposed by *Smith* (1986) and *Andrieu and Creutin* (1995).

Even though correcting weather radar measurements for range and VPR effects improves the quality of the radar surface rainfall product, still considerable differences with respect to the measurements from

rain gauges are expected. These can be attributed to uncorrected error sources or to the differences in the measurement characteristics of both devices. However, instead of using in situ rain gauge information for radar bias correction (e.g. *Austin*, 1987; *Kitchen and Blackall*, 1992; *Steiner et al.*, 1999; *Ciach and Krajewski*, 1999a; *Morin et al.*, 2003; *Goudenhoofdt and Delobbe*, 2009), we believe much more information can be obtained by focusing on weather radar rainfall uncertainty estimates. This approach is in line with *Villarini and Krajewski* (2010) who note that after having corrected for many of the weather radar measurement errors, the next step "*we should be focusing on is the characterization of the total uncertainties associated with radar-rainfall estimates of the true ground rainfall*". Over the last decade a number of studies have tried to address this issue (e.g. *Ciach et al.*, 2007; *Villarini et al.*, 2009; *Germann et al.*, 2009; *Mandapaka et al.*, 2010; *Kirstetter et al.*, 2010b). However, none of these approaches identified the impact of VPR variability on radar measurement uncertainty. Therefore, besides focusing on the correction of weather radar data for range and VPR effects, the current chapter also presents a method to identify radar-rainfall uncertainties due to VPR variability.

This chapter is organized as follows. In Section 5.2 the study area and a brief summary of a recently developed region delineation method is presented. Section 5.3 describes the VPR identification procedure and uncertainty estimation technique developed within this study. The impact of this approach is presented in Section 5.4 for three precipitation events. Sections 5.5 and 5.6 present the discussion and conclusions, respectively.

5.2 Materials and methods

5.2.1 Study area and radar characteristics

In this study the impact of VPR correction and uncertainty estimation is assessed using data from a C-band Doppler weather radar installed at an elevation of 600 m ASL of the Belgian Ardennes region in the eastern part of Belgium (see Fig. 5.2). During the winter half-year most precipitation observed in this region has a stratiform character, with BBs usually occurring below 2000 m above the surface. In the current study three events were selected that were observed within the region during the winter of 2002-2003. For a description of these events the reader is referred to Chapter 2.

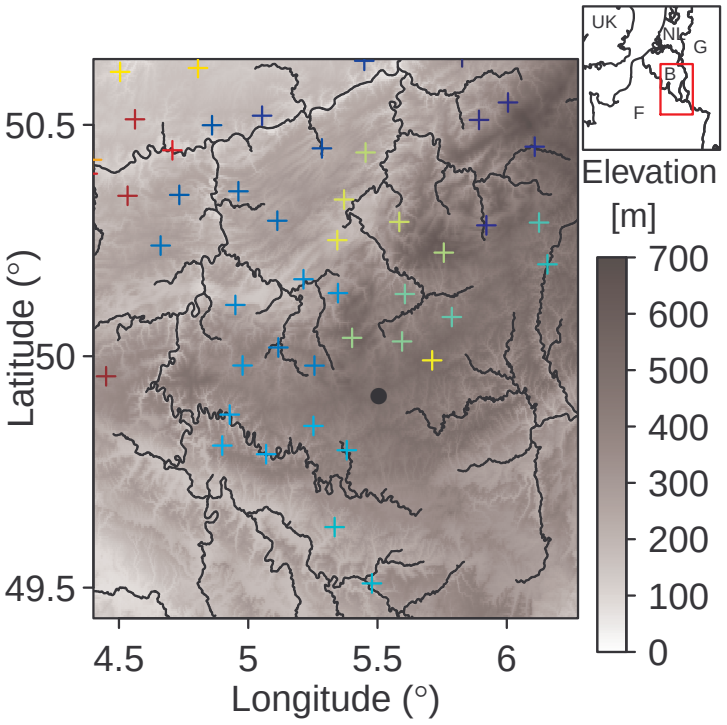

Figure 5.2: Topographic map of the Belgian Ardennes. Also shown are the location of the radar (•) and the location of the rain gauges (+). The inset shows the location of the study area, with a 200 by 200 km box indicating the area shown in the figure.

The radar has two scan sequences; one every five minutes at five different elevations and a second scan at another ten elevations every fifteen minutes. In this study the five-minute data were used to obtain areal information about the precipitation field. The impact of an idealized stratiform and transition precipitation type VPR on the measurement capabilities of this weather radar are presented in Fig. 5.1. A summary of the radar characteristics is presented in Table 2.1.

To assess the quality of the radar precipitation estimates, a total of 64 hourly rain gauges were used, situated up to a distance of 150 km from the radar (see Fig. 5.2).

5.2.2 Precipitation region identification

As explained in Section 5.1, the VPR correction method presented in this chapter focuses on precipitation regions in which for each cell the

rainfall type will be identified. In order to perform such analyses, a flexible method is needed that is able to identify such regions from continuous polar-based volumetric weather radar data. For this purpose, the recently developed grid-based Rotational Carpenter Square Cluster Algorithm (RoCaSCA) was applied to the polar (r,θ) grid observed by the lowest elevation angle of the radar. RoCaSCA is able to label pixels belonging to the same region using a tracing type image segmentation method (*Chang et al.*, 2004; *Wagenknecht*, 2007). Regions or clusters are identified by delineating first their outer contours, followed by a procedure to delineate inner regions and contours in a similar manner. Such a single-pass segmentation algorithm is generally assumed to be computationally efficient (*Suzuki et al.*, 2003; *He et al.*, 2009; *Wu et al.*, 2009). However, compared to other image segmentation algorithms, RoCaSCA is not limited to linking neighboring pixels only. Especially this latter property makes RoCaSCA highly suitable to delineate precipitation regions. Similar distance characteristics were also used in other studies to identify and track convective storm cells from weather radar images (e.g. *Johnson et al.*, 1998; *Handwerker*, 2002).

In Fig. 5.3 the outer contour delineation procedure of RoCaSCA is presented for a hypothetical precipitation image with three separate regions with reflectivity values larger than a user-defined threshold. The identification is performed by rotating a carpenter square along the outer boundary of a given precipitation region. Since the sides of the carpenter square in the current hypothetical example have a size of 3, non-neighboring cells can be identified as belonging to the same precipitation region. The final outcome results in two different precipitation regions (two separate regions have been merged because of their proximity to each other) identified by RoCaSCA (see Fig. 5.3). For further details concerning the region or cluster identification procedure, the reader is referred to Chapter 4.

Once a region has been delineated, each pixel is identified as stratiform (*Sánchez-Diezma et al.*, 2000), convective (*Steiner et al.*, 1995) or non-stratiform type of precipitation before VPR estimation takes place (see also *Delrieu et al.* (2009)).

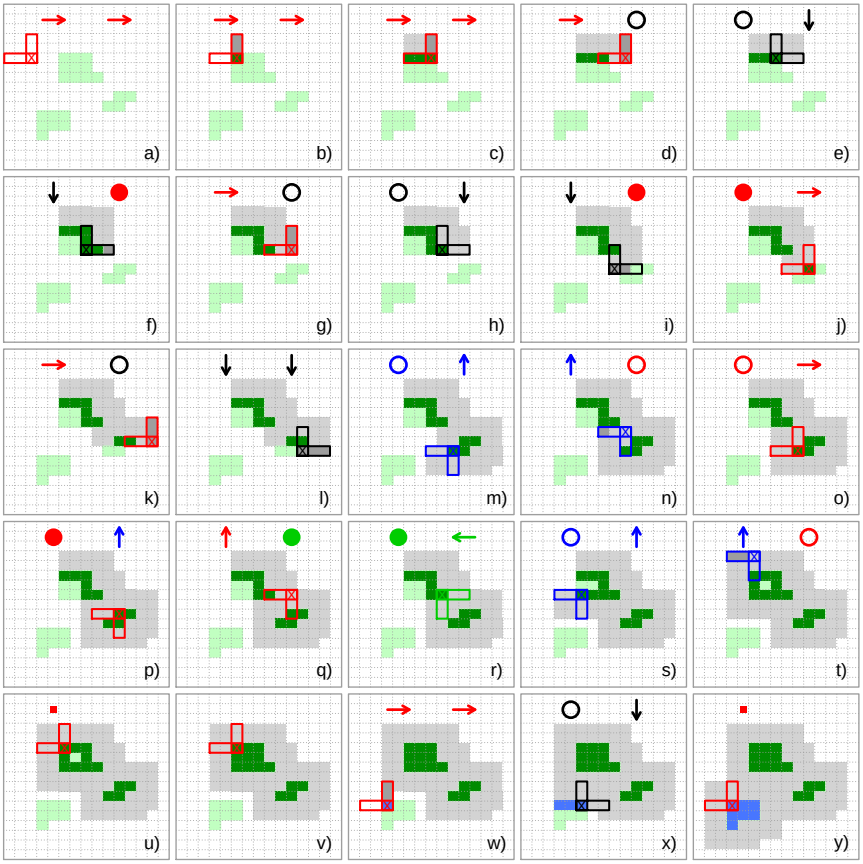

Figure 5.3: General technique behind the contour tracing algorithm of RoCaSCA for a hypothetical precipitation field. The color of the carpenter square indicates its direction of movement for the four different directions (i.e. red (right), blue (up), green (left) and black (down)). These directions and coloring are also indicated by the arrows on top of each subplot, where the left (right) indicates its last (next) direction. A closed (open) circle on top of a subplot indicates a(n) (anti)clockwise shift in the direction of the carpenter square, where the former (latter) indicates when a new pixel belonging to the same cluster is identified.

5.3 VPR identification and uncertainty estimation

5.3.1 Identification of the VPR for a given precipitation region

The VPR identification procedure implemented in the current chapter combines the characteristics of the algorithms presented by *Smith* (1986) and *Andrieu and Creutin* (1995). Both algorithms assume the VPR to be spatially uniform over a given region. As such, it becomes possible to decompose the spatial variation of the apparent reflectivity $Z_a(r,h)$ as measured by the weather radar into a horizontal and vertical component

$$Z_a(r,h) = Z_{REF}(r) z_a(r,h). \tag{5.1}$$

Here, $Z_{REF}(r)$ is the reflectivity at the chosen reference level at distance r, and $z_a(r,h)$ is the apparent vertical profile of reflectivity, which is influenced by the increase in height and volume of the radar beam as a function of range. In *Smith* (1986) this profile is represented by a simple piecewise linear function, similar to Fig. 5.1a. Unfortunately, computational limitations prohibited proper implementation of the VPR estimation proposed method by *Smith* (1986) until a decade later (*Kitchen et al.*, 1994; *Smyth and Illingworth*, 1998).

In *Andrieu and Creutin* (1995) the VPR follows a step profile of n_z increments, where within a given height interval increment, the vertical reflectivity component $\Delta\ z_i$ is assumed to be constant. Since, it is possible to calculate the proportion of the beam section within a given height increment using the characteristics of the radar, according to *Andrieu and Creutin* (1995) the normalized VPR can be defined as

$$z_a(r,h) = \int f^2(\theta_0,h) z(h) dh = \sum_{i=1}^{n_z} \beta_i(r,A) \Delta z_i, \tag{5.2}$$

where f^2 is the half-power beam distribution of the radar signal, θ_0 is the radar beam width, A is the elevation angle, $\beta_i = \int_{h_i}^{h_{i+1}} f^2(\theta_0,h,A)dh$, and $z(h)$ represents the actual average vertical reflectivity profile assumed to be constant over the region.

To estimate the shape of the VPR for a given precipitation event, ratio profiles $q(r,A_1,A_j)$ obtained from the volumetric weather radar measurement were used (i.e. the ratio between the measured reflectivity at a higher elevation j with respect to the lowest one (see Fig. 5.1 right panels)). For the VPR given by Eq. 5.2, these profiles are defined as

$$q(r, A_1, A_j) = \frac{Z_a(r, A_j)}{Z_a(r, A_1)} = \frac{\sum_{i=1}^{n_z} \beta_i(r, A_j)\Delta\ z_i}{\sum_{i=1}^{n_z} \beta_i(r, A_1)\Delta\ z_i}. \tag{5.3}$$

In order to estimate the actual VPR, an initial discretized profile was adjusted using an inverse optimization procedure (*Menke*, 1989), minimizing the difference between the theoretical and observed ratio profiles. This initial apriori VPR could either be obtained from climatological information or from volumetric radar measurements.

Since its first appearance, variations of the VPR estimation method of *Andrieu and Creutin* (1995) have been presented in a number of papers (e.g. *Borga et al.*, 1997; *Vignal et al.*, 1999, 2000; *Seo et al.*, 2000; *Delrieu et al.*, 2009; *Hazenberg et al.*, 2011a). The most detailed implementation was presented by *Kirstetter et al.* (2010a), who tried to estimate the VPR for a given type of precipitation (convective, stratiform, non-stratiform). These authors also presented the limitations of this approach, focusing on the difficulties of obtaining an initial VPR from volumetric weather radar data, and the observation uncertainties influencing the estimated ratio functions. These uncertainties, together with the large degree of freedom in the parameters of the step profile, can result in erroneous estimates of the VPR.

Kirstetter et al. (2010a) tried to limit the impact of these uncertainties using a range-related weighting function to estimate the initial median VPR for a given type of precipitation and employed only those reflectivity profiles for which the spatial variability at a given range was limited. In the current chapter, we try to account for the impact of these measurement variabilities without performing any predefined selection. However, instead of performing an unconstrained optimization procedure with many degrees of freedom, linear constraints are introduced between the parameters of the stepwise VPR. These constraints are similar to what was originally proposed by *Smith* (1986). The main benefit of this approach is that it ensures the VPR follows a physically realistic profile for a given type of precipitation (see Fig. 5.1a and d), as is observed from in situ vertically pointing radar measurements (e.g. *Joss and Waldvogel*, 1990; *Fabry and Zawadzki*, 1995; *Martner et al.*, 2008).

5.3.2 Theoretical piecewise linear VPRs

The current chapter presents a method to estimate VPRs for both stratiform and non-stratiform precipitation, where the latter is assumed to contain either transition type precipitation or snow. We do not intend to identify VPRs for convective precipitation, since we feel that the horizontal variability in vertical variations of the hydrometeor properties, as explained in the introduction, is too large to result in appropriate estimates of VPRs. In Fig. 5.4 the specific piecewise linear shapes are presented, which form the basis of our estimation method. For stratiform precipitation, this representation enables one to focus on five different vertical regions comprising a total of ten linear layers each with slope $\Delta = dz/dh$. These regions exhibit the following properties:

1. Layers $h_1 - h_3$ (rain): Vertical variation of the VPR mainly occurs due to collisional and spontaneous breakup as well as coalescence of raindrops, influenced by vertical and horizontal variation of the wind field, orographic effects and below BB evaporation (*Austin*, 1987). Therefore, no a priori directions of the slopes Δ_i are defined for these layers.

2. Layers $h_3 - h_5$ (BB): Large rain drops developed as part of the BB start to collapse, within these layers, and raindrop fall velocities increase (*Stewart et al.*, 1984). Hence, within this region the VPR is assumed to decrease towards the surface ($\Delta_i \geq 0$).

3. Layers $h_5 - h_7$ (BB): The melting and aggregation of snow particles causes a liquid water coating at their surface, which results in an intensification of the returned radar reflectivity signal (the BB) (*Austin and Bemis*, 1950; *Smith*, 1986; *Klaassen*, 1988, 1989; *Russchenberg*, 1992; *Steiner and Smith*, 1998). Hence, within these layers the slopes Δ of the VPR are positive in downward direction ($\Delta_i \leq 0$).

4. Layer $h_7 - h_8$ (snow): Descending snow flakes and ice crystals aggregate leading to a moderate increase of the returned radar signal while descending (*Stewart et al.*, 1984; *Willis and Heymsfield*, 1989). The slope is therefore assumed to be positive towards the surface ($\Delta_8 \geq 0$).

5. Layers $h_8 - h_{10}$ (snow): Within this region, snow flakes and ice crystals are formed, which interact and slowly descent. Although in general reflectivities are small and slightly increasing downwards,

we allow for a secondary maximum to occur as a result of enhanced aggregation within the dendritic growth region (−10 ℃ to −17 ℃) (*Hobbs et al.*, 1974; *Steiner and Smith*, 1998). Hence, Δ_9 can have both signs, while $\Delta_{10} \leq 0$.

For non-stratiform precipitation, less vertical variability is expected. Therefore, the VPR of non-stratiform precipitation is represented by a piecewise linear shape consisting of only four linearly sloping layers. As such, it is expected that both transition type precipitation containing mostly rain drops, as well as snow can be represented by such a piecewise linear profile.

For stratiform precipitation the actual values of z_i are bounded by constraining the allowed reflectivity values as well as enforcing interdependence between the piecewise linear segments (see Table 5.1). This approach limits the number of degrees of freedom, ensuring a physically realistic shape of the VPR. In order to reduce the number of estimated parameters for stratiform precipitation, the majority of the height parameters (h) presented in Fig. 5.4a can be obtained directly from volumetric radar measurements (see Section 5.3.4). The slopes (Δ) and remaining heights (h) are then estimated using a Monte Carlo optimization approach, minimizing the difference between the observed and simulated ratio profiles. Although Monte Carlo simulations are known to be time-intensive, for the current VPR parameterization this approach gives proper results within an acceptable amount of time for operational practices.

5.3.3 Radar rainfall variability estimation from VPR uncertainty

The VPR identification method presented in the previous section can be regarded as a median field bias correction for an identified precipitation region of a given type. In practice, however, considerable local fluctuations around the median VPR are expected due to horizontal variability in vertical variations of the precipitation microstructure (size, shape, number concentration and phase of the hydrometeors) (*Joss and Waldvogel*, 1990; *Hazenberg et al.*, 2011b). In addition, since radar measurements at different elevation angles are not performed simultaneously, temporal evolution of the VPR results in further deviations from the median profile. Therefore, besides correcting for VPR effects, we also wish to obtain an estimate of the amount of uncertainty around its median value and assess its impact on weather radar rainfall estimation.

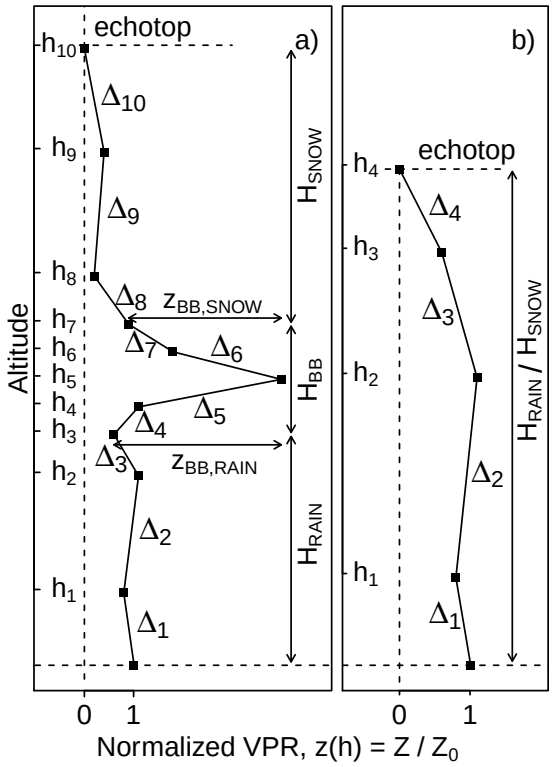

Figure 5.4: Theoretical vertical reflectivity profiles for stratiform (panel (a)) and non-stratiform precipitation (e.g. transition, snow) (panel (b)). Different height (h) and slope parameters (Δ) are optimized with respect to observed ratio profiles using a Monte Carlo optimization approach, where $\Delta = dz/dh$.

Table 5.1: Minimum and maximum values of the normalized VPR segments $\Delta\ z_i$ (Eq. 5.2) at the corner of each piecewise linear segment as presented in Fig. 5.4. Different precipitation types are rain (R), bright band (BB), and snow (S).

	Stratiform			Non-stratiform		
Height	Type	Min	Max	Type	Min	Max
h_1	R	0.30	1.40	R/S	0.40	1.40
h_2	R	0.20	1.50	R/S	0.30	1.20
h_3	R	0.20	1.50	R/S	0.20	1.00
h_4	BB	z_{h_3}	2.00	R/S	0.00	0.05
h_5	BB	z_{h_4}	10.00			
h_6	BB	0.30	z_{h_5}			
h_7	BB	0.25	z_{h_6}			
h_8	S	0.05	0.50			
h_9	S	0.01	0.40			
h_{10}	S	0.00	0.05			

An example of the variability in observed ratio profiles for the precipitation event described in Section 5.4.1 is presented in Fig. 5.5 (top) for different percentile statistics. This figure was obtained after having identified the stratiform pixels within a precipitation region identified by RoCaSCA (see Section 5.2.2). It can be observed that close to the radar the median ratio profile indeed has an expected value of about 1 (see also Fig. 5.1), although considerable deviations occur for the other percentiles. As mentioned, these deviations result from horizontal variations in the vertical variability of the precipitation microstructure, from temporal changes in the precipitation field as well as from the radar sampling properties.

However, once these percentiles are scaled with respect to the median by calculating their ratio, these overall deviations become rather constant with range (Fig. 5.5 (middle)). Similar results (not shown here) were obtained for other time steps and during other precipitation events. Therefore, based on this property, we propose to account for VPR variability by reformulating Eq. 5.3 as follows:

$$q_P(r, A_1, A_j) = f_P\, q_N(r, A_1, A_j) = f_P\, \frac{\sum_{i=1}^{i=n_z} \beta_i(r, A_j)\Delta\ z_i}{\sum_{i=1}^{i=n_z} \beta_i(x, A_1)\Delta\ z_i}, \qquad (5.4)$$

where q_P is the estimated ratio profile for a given percentile value P.

The factor f_P is a scaling factor for a given ratio percentile, which results from the observed uniform deviation as a function of range. After rescaling the observed ratio profiles for a given percentile (q_P) using this factor, the majority of the observed variability is accounted for (see Fig. 5.5(bottom)). The remaining variability is then taken into account by identifying a normalized segmented VPR ($\Delta\ z_{i,P}$) representative for the normalized ratio profiles of a given percentile ($q_{N,P}$).

It was decided to estimate the scaling factor f_P as part of the Monte Carlo procedure explained in Section 5.3.2 while identifying the VPR, since for some precipitation regions it is difficult to obtain such well defined ratio profiles as in Fig. 5.5. Hence, for a given ratio profile percentile, both the piecewise linear segmented VPR $\Delta\ z_i$ and the scaling factor f_P are estimated. By selecting a broad range of percentiles (here 20 – 80) based on experience obtained for the region of study, we believe that the majority of the VPR uncertainty can be identified and accounted for. Next to that, this approach enables one to study its impact on radar rainfall estimation uncertainty.

5.3.4 Practical implementation

The previous sections described the specific VPR identification and uncertainty estimation method used here. The complete algorithm to estimate a VPR for a given precipitation region and type is implemented as follows:

1. Identify ground clutter and pixels containing positive reflectivity values and remove these pixels from further analyses (see Chapter 2 for further details).

2. Use RoCaSCA to identify precipitation regions for the radar data obtained at the lowest elevation and track each of these regions over time. As such, the implementation follows a Lagrangian procedure.

3. For each region, identify the precipitation type of each individual polar radar pixel, i.e. convective (*Steiner et al.*, 1995), stratiform (*Sánchez-Diezma et al.*, 2000), or non-stratiform precipitation.

4. For all stratiform pixels within a given precipitation region, calculate the 20^{th}, 40^{th}, 50^{th}, 60^{th}, 80^{th} percentiles of the estimated BB height sampled at the different polar points (*Sánchez-Diezma et al.*, 2000). These heights are assumed to correspond to h_3, h_4,

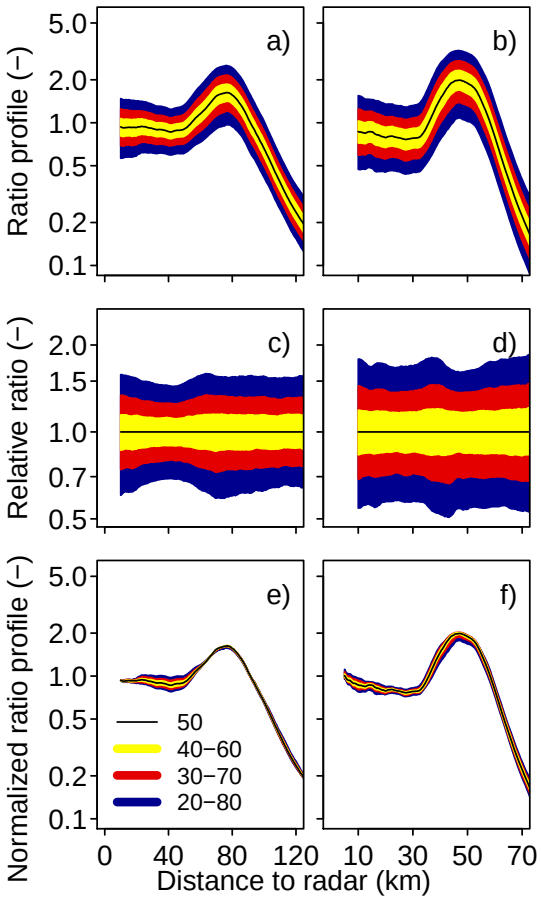

Figure 5.5: Variability in observed ratio profiles as represented by different percentiles for the precipitation event described in Section 5.4.1 on October 22, 2002 at 20:30 UTC. Upper two panels present the ratios of the weather radar measurements at elevations 2 (a) and 3 (b) with respect to the lowest one. In the middle two panels (c) and (d), the ratios with respect to the median profiles are shown. Based on the mean values in panels (c) and (d), as a final step, the original ratio profiles presented in panels (a) and (b) were rescaled. In panels (e) and (f) these normalized ratio profiles are shown.

h_5, h_6, h_7 in Fig. 5.4, which reduces the number of parameters to be estimated in the stratiform VPR optimization procedure.

Then, for each precipitation region of a given type:

5. Estimate the echo top, corresponding to h_{10} and h_4 in Fig. 5.4 for stratiform and non-stratiform precipitation, respectively. The echo top was defined as the maximum elevation at which the reflectivity $Z \geq 1$ dBZ.

6. Calculate the ratios between the reflectivities measured at higher elevations with respect to the lowest. Then, based on all ratio information at a given distance from the radar, obtain a number of percentiles (see Fig. 5.1c and f, and 5.5). Here, we used the 20^{th}, 30^{th}, 40^{th}, 50^{th}, 60^{th}, 70^{th}, and 80th percentiles.

7. Identify the final ratio profiles for a given percentile by aggregating temporally over a number of consecutive time steps to increase the robustness of the statistics. In current study, all ratio information sampled within 60 minutes of the time step of study for the moving precipitation system was taken into account.

8. Estimate the slope parameters Δ, the scaling factor f_P and the remaining height parameters h based on the procedure explained in Sections 5.3.2 and 5.3.3 using a Monte Carlo based optimization procedure, minimizing the sum of squared differences between the theoretical and observed ratio profile quantiles for a given percentile.

9. Based on each of the identified normalized segmented VPRs ($z_{i,P}$) and scaling factors f_P obtained for a given ratio profile percentile, calculate VPR correction factors for each radar elevation as a function of range.

10. In order to obtain a final 2D radar reflectivity field, a weighted average of all VPR corrected elevations is taken (for details, see Chapter 2). This approach decreases the impact and uncertainty of an individual measurement at a given elevation (*Joss and Lee*, 1995).

11. As a final step, the reflectivity data are transformed into rainfall intensities using the Marshall-Palmer relationship $Z = 200R^{1.6}$ for stratiform precipitation (*Marshall et al.*, 1955) and $Z = 250R^{1.5}$ for non-stratiform precipitation (*Battan*, 1973).

The identification of precipitation regions by RoCaSCA was done at two different reflectivity levels, >7 and >23 dBZ, using a carpenter square of size 3 and 2, respectively. These reflectivity values correspond to a precipitation of >0.1 and >1.0 mm h^{-1}, respectively in case a Marshall and Palmer $Z = 200R^{1.6}$ relationship is assumed (*Marshall et al.*, 1955). In order to ensure that each precipitation region contains enough statistical information, to obtain robust ratio profile estimates, each region should have a minimum area of 2500 (>7 dBZ) and 2000 (>23 dBZ) km^2, respectively. These sizes are similar to the minimum areas originally proposed by *Vignal et al.* (1999, 2000), although for the current approach, their locations and actual sizes vary dynamically in time. In case it becomes impossible to estimate a VPR for a given pixel identified as being part of a region surpassing the larger threshold (>23 dBZ), if available, the VPR estimated for the region identified at the smaller threshold level (>7dBZ) is used.

As a next step, tracking of each of these regions is performed by moving each of the identified pixels forward in time using the velocity estimate of the previous time step if possible, or else based on the mean wind information. Then, a region observed during two time steps, is identified as a tracking pair in case their area overlap with >10 %.

Temporal information obtained through the tracking of each region is used to increase the amount of data on which the different ratio profile statistics are based. It was decided to perform up to 1 hour of temporal aggregation to obtain the ratio statistics from the volumetric data (similar to *Delrieu et al.* (2009); *Kirstetter et al.* (2010a)), which is defined as ‘backward’ identification. Potential problems arise for precipitation regions identified at larger distances from the radar (>100 km), for which it can be difficult to obtain any ratio information. Therefore, as a second approach, temporal aggregation of the ratio profiles was also performed using the reflectivity information sampled both 1 hour before and after a given time step (‘back/forward’ identification). If a precipitation region moves closer to the radar, it is expected that the quality of the ratio profile statistics improves. Although for real time implementation such an approach is impossible to implement, this latter approach enables one to identify how much the quality of the weather radar precipitation estimates observed at larger ranges can potentially be improved, while more information on the precipitation system becomes available (as it possibly moves towards the radar).

To assess the quality of the Lagrangian VPR identification method presented in this chapter, VPR identification was also implemented for

the entire radar volume for given precipitation type (the Eulerian perspective). This approach takes all volumetric reflectivity information sampled by the radar into account, but does not distinguish between different precipitation regions. As a last procedure, the global static Eulerian and local dynamic Lagrangian VPR identification methods were merged, where it is tried to correct for VPR locally for each precipitation region separately, while for the remainder part of the radar umbrella, the global estimate is used to correct for VPR effects. The benefit of this combined procedure is that also reflectivity points that are not identified as part of a precipitation region are still VPR-corrected based on global information.

5.4 Results

5.4.1 Event 1: A stratiform system

The first event presented this chapter, is a fast moving stratiform system that started to be observed by the radar during the late afternoon on October 22, 2002 and lasted until the early morning of the next day. The corrected rainfall intensity field measured by the radar is presented in Fig. 5.6 for a number of time steps. Also shown in this figure are the precipitation regions identified by RoCaSCA at >7 (red) and >23 (black) dBZ. RoCaSCA is well able to discriminate between the different precipitation regions, although at the >7 dBZ level during a number of time steps, multiple cells merge into a single region. This generally does not occur at the >23 dBZ level.

The specific region characteristics for the stratiform precipitation region (>23 dBZ) that was first recognized in the South-West corner of the radar image at 18:00 UTC (see Fig. 5.6), are presented in Fig. 5.7. The increase in the region mean reflectivity during the first hour can be related to the high altitude of the initial radar measurements (i.e. reduction of returned signal due to snow and the possibility overshooting). From 18:30 UTC onward, it becomes possible to estimate the median height of the BB and its uncertainty (as represented by the 20-80th inter percentile range, see Fig. 5.7b). Overall, the temporal variation of the BB height for this precipitation region is rather small and has a similar depth (H_{BB}, in Fig. 5.4) as observed in other studies (*Gourley and Calvert*, 2003; *Zhang et al.*, 2008).

The resulting panels of Fig. 5.7 present the properties of the estimated VPR, obtained by aggregating the ratio profile information dur-

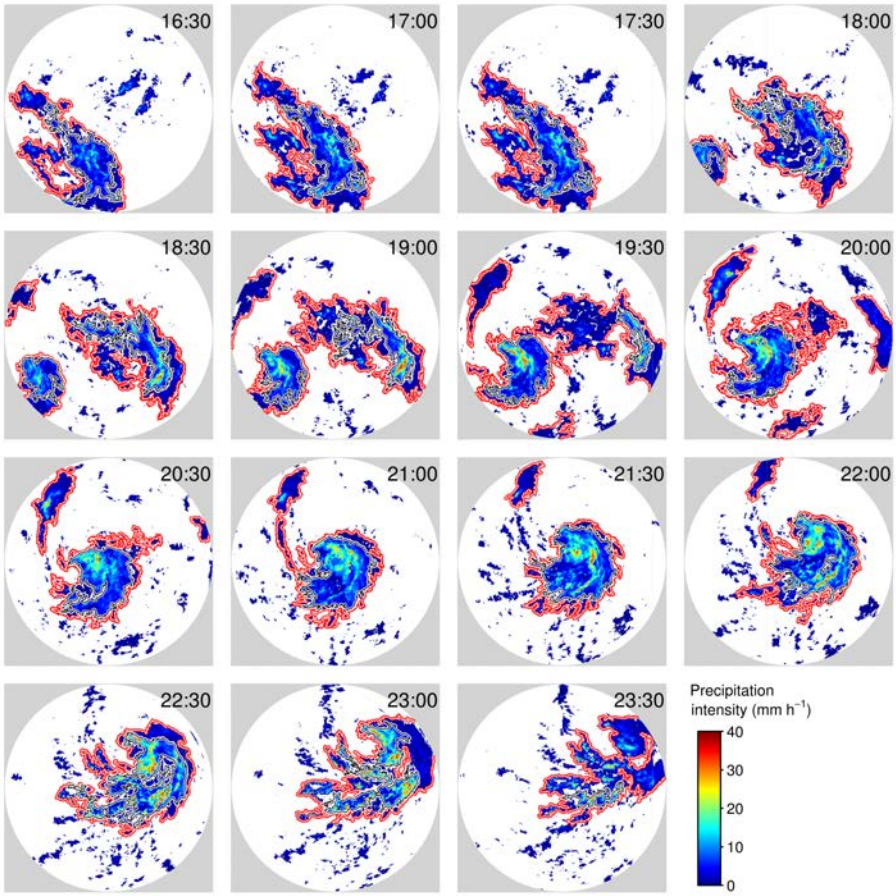

Figure 5.6: Temporal evolution of the stratiform precipitation system as observed by the weather radar on October 22, 2002 up to a distance of 225 km. The time steps (UTC) of the different snapshots are presented in the upper right hand corner of the different panels. The boundaries of the major precipitation regions for which VPRs are estimated, as identified by the cluster algorithm RoCaSCA at > 7 (red) and >23 (black) dBZ, are presented as well.

ing the previous hour (backward, red) or from both the previous and the next hour (back/forward, green). With the latter option it is expected that for precipitation regions observed at further ranges from the radar, using the information obtained within the next hour, especially for precipitation region situated further away from the radar, a better estimate of the VPR can be obtained.

In Fig. 5.7c estimates of the strength of the BB are given ($z_{BB,Rain}$ in Fig. 5.4). Although the results for both methods line up well, it can be observed that around 20:30 UTC a deviation occurs. This arises from the decrease in estimated BB strength from 21:00 UTC onward. The combination of back- and forward temporal aggregation causes the volumetric radar data sampled at these time steps to be used earlier in time, as part of the ratio profile identification procedure. Since the assumption of a temporally stable VPR is clearly violated during this hour, a difference between both estimates of the BB size occurs.

The total variation of the VPR scaling factor f_P (Fig. 5.7d) ranges between 60–140%. This indicates that the horizontal variation of the vertical precipitation structure as well as temporal differences between the different radar scans have a considerable impact on the measured ratio profile variability. The approach presented in the current chapter is able to account for this overall variability. Figure 5.7e presents the quality of the estimated VPR to simulate the observed ratio profile between the lowest two elevations, using the Nash-Sutcliffe statistic (*Nash and Sutcliffe*, 1970). Overall, the correspondence between the observed and simulated ratio profiles is good. Only during the later phase of the event (after 22:00 UTC) the quality of the fit decreases for the highest ratio percentiles. This can be related to the fact that the cell starts to decompose and looses its spatial coherence (see Fig. 5.6), leading to an increase in ratio variability.

In order to identify the spatial variability of the VPR between different precipitation systems, similar characteristics presented in Fig. 5.8 were identified for the precipitation region (>23 dBZ) observed in the top panels of Figure 5.6. The sampling of this region by the weather radar has considerable temporal overlap with the region presented Fig. 5.7. Visual analysis of Fig. 5.6 already reveals a clear difference between both regions, where the former (Fig. 5.8) is more elongated, while the latter (Fig. 5.7) has a more spiral structure. Although the estimate height of the BB is similar between both systems, indicating a rather uniform height of the zero degree isotherm, the identified strength of the

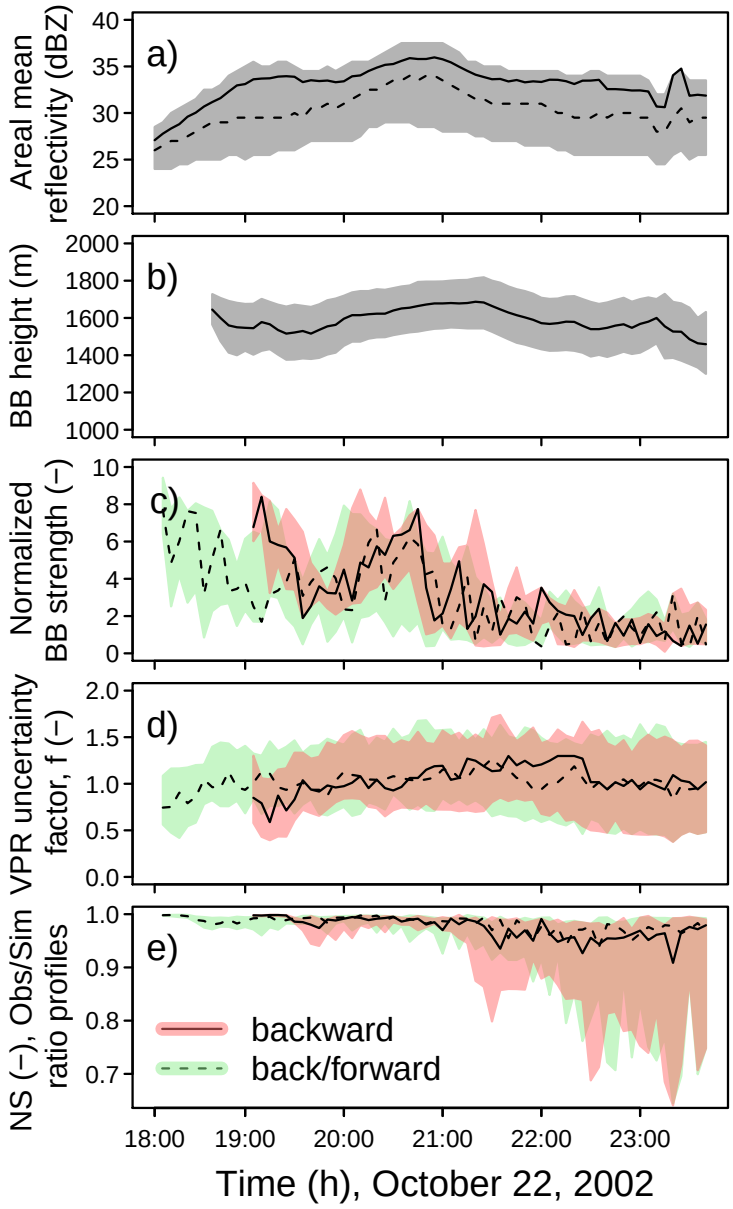
a)
Areal mean reflectivity (dBZ)
40
35
30
25
20
b)
BB height (m)
2000
1800
1600
1400
1200
1000
c)
Normalized BB strength (–)
10
8
6
4
2
0
d)
VPR uncertainty factor, f (–)
2.0
1.5
1.0
0.5
0.0
e)
NS (–), Obs/Sim ratio profiles
1.0
0.9
0.8
0.7
backward
back/forward
18:00
19:00
20:00
21:00
22:00
23:00
Time (h), October 22, 2002

BB varies considerable and is smaller for the former. This clearly shows the possibilities of differentiating between different precipitation regions using an automatic procedure.

Figure 5.9 presents the comparison between the hourly region-based Lagrangian VPR-corrected radar rainfall accumulations and the 64 rain gauges based on the combined back- and forward obtained ratio information. It should be noted that none of the radar measurements were bias-corrected using rain gauge information. This allows an objective assessment of the true quality of corrected radar data. Although considerable variability between both instruments is observed, the corrected radar data correspond well with the gauge measurements. On average, the hourly and event-based rainfall accumulations obtained from the radar slightly underestimate the precipitation amounts sampled by the gauges (see Fig. 5.9a and b). The impact of range effects is strongly reduced once the weather radar data is corrected for VPR effects, as reflected by the rather constant bias as a function of range in Fig. 5.9c (see also Table 5.2). It should be noted that the hourly deviations between both devices increases with distance (Fig. 5.9d). This can be explained by the increase in measurement height difference between both devices and the possible impact of wind drift (*Gabella and Perona*, 1998; *Seo et al.*, 2000; *Gabella et al.*, 2000, 2005).

Figure 5.7 *(preceding page)*: Temporal evolution of the stratiform anti-clockwise rotating precipitation region for the 23 dBZ reflectivity threshold. Upper two panels show the region's mean (black line) and median (dashed line) reflectivity (a) and estimated height of the bright band (b) as observed by the weather radar. The uncertainty in these measurements is given by the gray contour region, representing the 20-80th inter percentile range. The bottom three panels present the estimated bright band strenght (c, $z_{BB,RAIN}$ in Fig. 5.3), the spatial VPR uncertainty factor f, and the goodness-of-fit between the simulated and observed ratio profiles for the lowest two elevations as respresented by the Nash-Sutcliffe statistic (NS) (*Nash and Sutcliffe*, 1970). These results were obtained by aggregating using all ratios observed within the previous hour (backward, solid line/red region) or using the next hour ratio information as well (back/forward, dashed line/green region). The uncertainty in the VPR measurements is represented by the different contour regions and define the 20-80th inter percentile ranges.

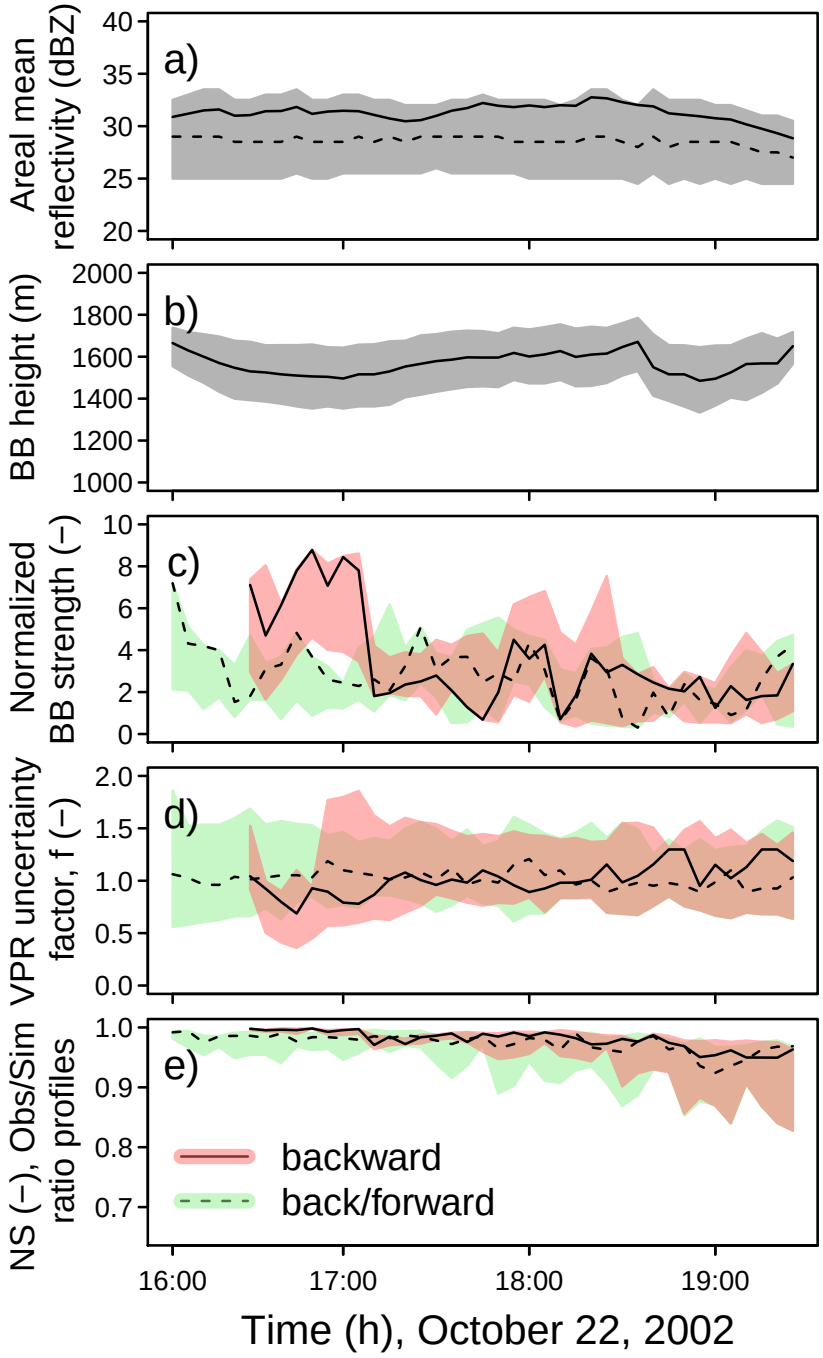

Figure 5.8: As Fig. 5.7, but for the precipitation system first observed in the upper panels of Figure 5.6.

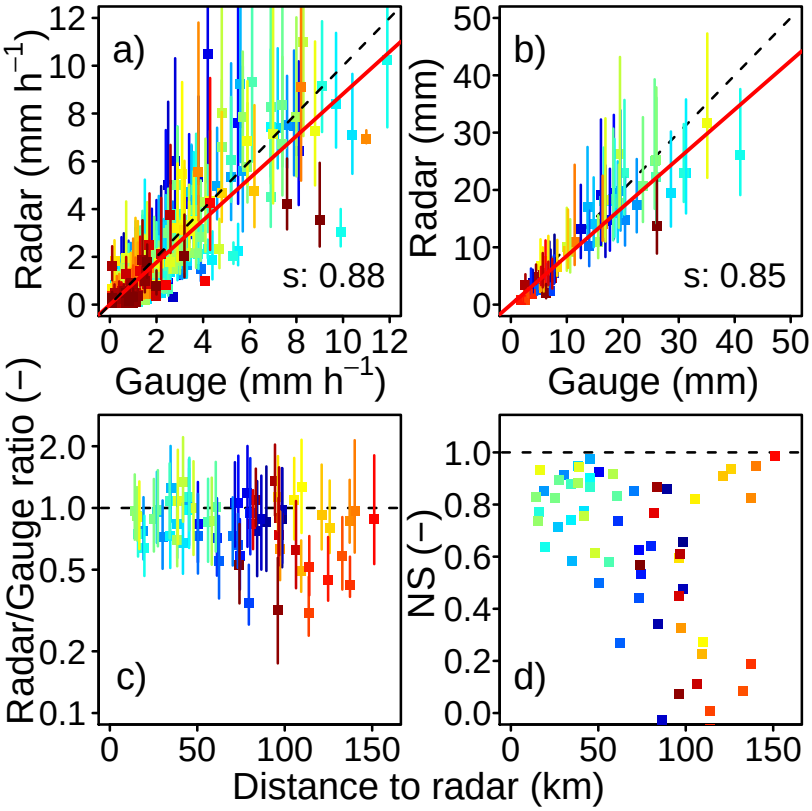

Figure 5.9: Comparison of rainfall accumulations obtained from 64 rain gauges and sampled by the corresponding radar pixels above, using the ratio information obtained within the previous and next hour (back/forward), for the event on October 22-23, 2002. For all 64 pairs, the upper panels show scatter plots of the hourly a) and total event b) rainfall accumulation. The correspondence between the weather radar corrected using the median VPR (dots) w.r.t. the rain gauges is given by the red line with slope s, obtained from linear regression. The bottom panels show the quality of the radar measurement as a function of range from the radar, where radar/-gauge ratio is defined as $\sum$Radar rainfall/$\sum$Gauge rainfall. NS is the Nash-Sutcliffe statistic (*Nash and Sutcliffe*, 1970). The uncertainty in the radar rainfall estimates as a result of VPR variability and uncertainty is indicated by the error bars (20-80th percentiles). Different colors correspond to the gauges as shown in Fig. 5.2.

In Table 5.2 the quality of the region-based VPR correction (R) is compared to the implementation of a global estimation of the VPR (G), and a combination of both approaches (G&R). For completeness, the impact of not correcting for VPR is also given (N). In general, VPR-correction leads to a large improvement in radar rainfall estimation quality. The quality of the region-based VPR-corrected radar measurements (R), based on the ratio information from the previous hour (backward) decreases considerably beyond 100 km. This can be related to visibility problems if a region is still located far away. By taking the volumetric data of the next hour into account as well (back/forward), VPR-correction also leads to improved results at these distances (see also first hour in Fig. 5.7).

When compared to the global VPR-corrected radar measurements (G), the region-based technique (R) performs less well. This is because not all radar measurements are VPR-corrected with the latter approach, as well as the difficulty to identify a VPR for a region located at longer distances from the radar. The combination of applying region-based VPR-correction for pixels belonging to a precipitation cell and a global VPR-correction elsewhere (G&R), gives a slight improvement in both the hourly and event based bias statistics beyond 50 km when compared with the global correction (G). However, the latter observation is not reflected by the Nash-Sutcliffe statistic.

Besides the impact of median VPR radar rainfall correction, the impact of VPR uncertainty on the radar measurements is also presented in Fig. 5.9. As explained in Section 5.3.3 this uncertainty was obtained using the ratio profiles for different percentiles. It can be observed that the overall variability as a result of VPR-effects is considerable. What is striking about this figure is that, when compared with the rain gauge accumulations, the majority of the difference between radar-gauge pairs can be attributed to the uncertainty in the estimated VPR.

In Fig. 5.10 the impact of VPR-uncertainty on the quality of the three different identification approaches is assessed using the ratio profile information obtained during the previous hour (backward identification). From the top panel it can be observed that the overall impact of VPR-uncertainty increases with range, as was also reflected by the decrease of the Nash-Sutcliffe statistic in Table 5.2. Close to the radar (<50 km) the overall VPR uncertainty is similar for the three different approaches. This can be related to the relatively large size of the different precipitation zones observed during this event and the fact that most ratio information is obtained close to the radar. Therefore, the global

Table 5.2: Impact of the different VPR identifiction methods on the quality of hourly radar rainfall estimates compared to the 64 rain gauges at different ranges, for the event on October 22-23, 2002. Row headers correspond to: N - no VPR correction, R - region-based VPR identification, G - global VPR identification, and G&R - global and region-based VPR identification. The latter were estimated using the ratio information obtained within the previous hour (backward) or both the previous and next hour (back/forward). The quality is assessed using the hourly bias $E(\mathrm{R/G})$ between the radar and rain gauge measurement, the total event bias $E(\sum \mathrm{R}/\sum \mathrm{G})$ and the Nash-Sutcliffe statistic (NS).

		$E(\mathrm{R/G})$			$\sum \mathrm{R}/\sum \mathrm{G}$			NS		
	(km)	0-50	50-100	100-150	0-50	50-100	100-150	0-50	50-100	100-150
	N	0.76	0.59	0.49	0.79	0.68	0.57	0.79	0.47	0.25
backward	R	0.90	0.80	0.61	0.97	0.93	0.77	0.83	0.40	0.24
	G	0.90	0.84	0.81	0.98	0.98	0.98	0.82	0.51	0.44
	G&R	0.89	0.85	0.89	0.98	1.00	1.04	0.84	0.49	0.39
back/forward	R	0.92	0.82	0.71	0.98	0.94	0.83	0.82	0.38	0.33
	G	0.91	0.86	0.82	0.98	1.00	1.00	0.83	0.49	0.42
	G&R	0.90	0.88	0.86	0.98	1.03	1.08	0.84	0.48	0.42

VPR estimates (G) for the type of precipitation field observed during the current event are quite similar to the region-based VPR-estimates (R). Further from the radar, the overall uncertainty of the region-based VPR-estimate increases. With the other two approaches (G and G&R) similar radar rainfall uncertainty estimates are obtained. For these ranges the differences between R on the one hand and G and G&R on the other hand, may be caused by the fact that for first approach, no VPR correction is applied and hence no uncertainty is attributed.

Comparing these results with the rain gauge measurements, it can be observed that for all three approaches, the majority of the maximum rainfall accumulations are higher than those estimated by the gauges, whereas the minimum accumulations are lower than the gauge accumulations. This result again confirms that the majority of the precipitation differences between both devices can be attributed to VPR-variability. Only for the region-based approach (R) at longer distances from the radar (>100 km), the maximum precipitation intensities are still underestimated by the radar compared to the gauges, which again is probably caused by the fact that not during all time steps a VPR could be estimated for precipitation systems further away from the radar. Radar data observed during these time steps were not VPR corrected using the region-based approach only.

5.4.2 Event 2: Large scale stratiform system

As a second example to present the possibilities of region-based VPR-identification and uncertainty estimation, a large-scale precipitation system observed on December 22, 2002 is analyzed. In Fig. 5.11 the rainfall intensity field as observed by the radar is presented. Compared to the event described in Section 5.4.1, precipitation intensities for the current event are much smaller. Generally, such type of widespread precipitation is expected to produce drizzle.

The characteristics of the precipitation region as identified by RoCaSCA (>7 dBZ) are shown in Fig. 5.12. Also for the current event, the mean cell reflectivities increase while moving closer to the radar (i.e. influence of overshooting and the measurement of snow). However, even once its location is close to the radar (beyond 5:00 UTC) the reflectivity field still intensifies. Similar behavior is also observed for the estimated height of the BB, which increases as well. The explanation for this is that both occur as a result of increased solar activity during the morning, resulting in an influx of energy. At around 9:00 UTC it can be observed from Fig. 5.12b that the variability in the estimated BB-height changes.

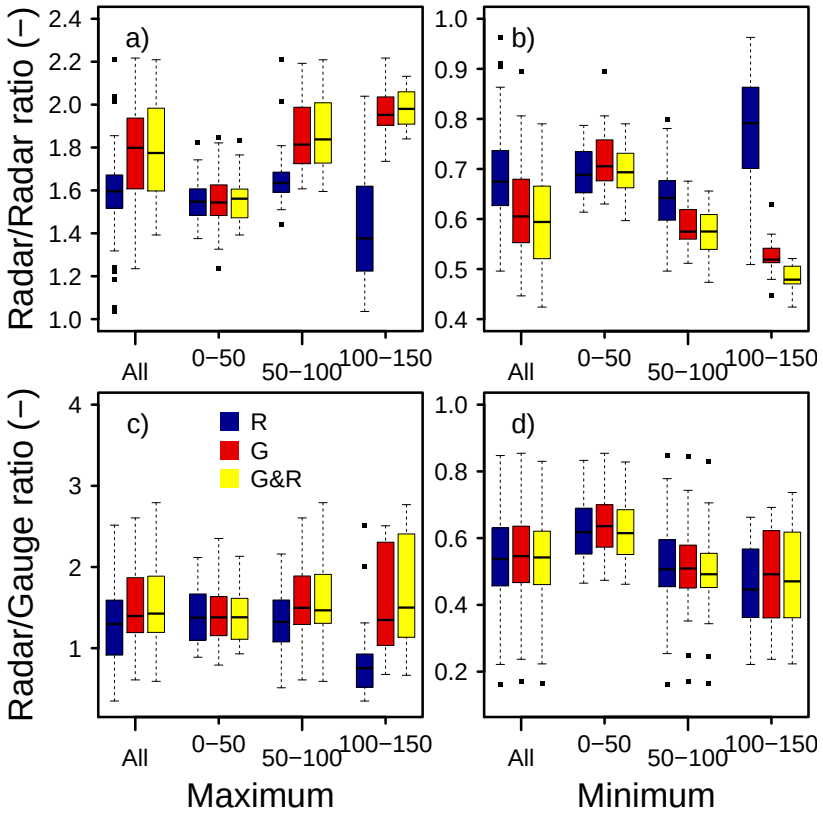

Figure 5.10: Impact of radar rainfall estimation uncertainty on hourly accumulations for the radar pixels above the 64 rain gauge locations for four different distance intervals from the radar. In the upper panels box plots present the ratios between the maximum (a) and minimum (b) with respect to the median VPR-corrected radar event accumulation. In the lower panels the maximum (c) and minimum (d) VPR-corrected event accumulations are compared to the measurements obtained from the rain gauges.

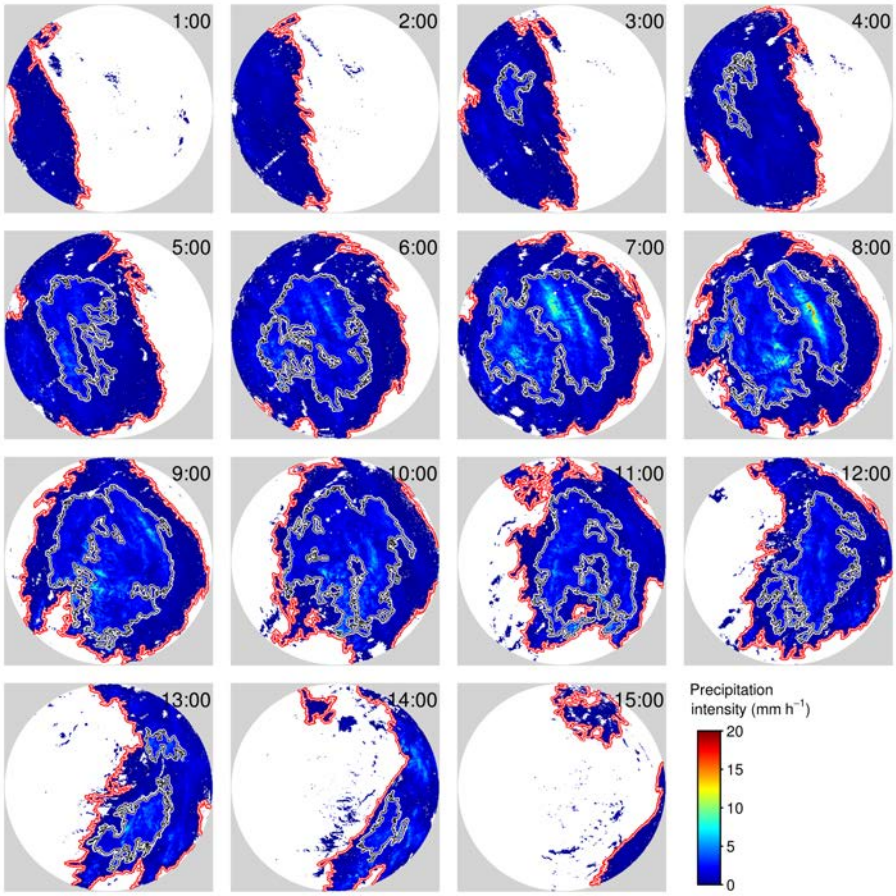

Figure 5.11: As Fig. 5.6, but for the large-scale stratiform precipitation system observed on December 22, 2002.

Detailed analyses (not presented here) show that this resulted from a situation of two BB heights (with 200m height difference) at different horizontal locations. Unfortunately, due to the widespread character of this event, the current implementation of RoCaSCA was unable to distinguish between both regions. This can also be observed from Fig. 5.12c where for about an hour (09:00-10:00 UTC), considerable differences between both aggregation methods (backward and back/forward) occur, reflecting the situation of two different BB heights.

The impact of the two different BB levels for a period of about two hours can also be observed in Fig. 5.13. In general, the radar underestimates the amount of precipitation as compared to the gauges. However, the identification of a single spatially uniform VPR is unable to account for all horizontal variability of the vertical precipitation variability in a situation with two different BB levels. Hence, this leads to an overestimation of the rainfall intensities for a number of gauges, while at other locations an underestimation is observed. This is further reflected by the variability of the Nash-Sutcliffe statistic, which does not show a clear tendency with range.

In Table 5.3 the quality of the region-based VPR-corrected radar measurements are presented as a function of range. As a result of the large-scale character, only a single precipitation region at both intensity levels was identified for the majority of the event. Therefore, it was decided to present only the results for region based VPR (R), since both the global (G) and the combined (G&R) approach make use of the same reflectivity data. VPR-correction results in a large improvement in the quality of the radar rainfall estimates. However, making use of the weather radar data observed during the next hour (back/forward) does not lead to a quality improvement. This can be attributed to the widespread character of the current system, from which it is possible to obtain proper ratio information based on reflectivity data from the previous hour alone.

Although the uncertainty in the identified VPR explains some of the variability between the radar and gauge accumulations, considerable differences between both devices are still observed. As mentioned, the main part of this event consisted probably of drizzle. Application of the Marshall-Palmer relationship therefore resulted in an underestimation of the rainfall intensity. Hence, for the current event it is expected that the majority of the difference between the radar-gauge pairs can be related to the characteristics of the DSD, which deviate from standard stratiform precipitation for this event.

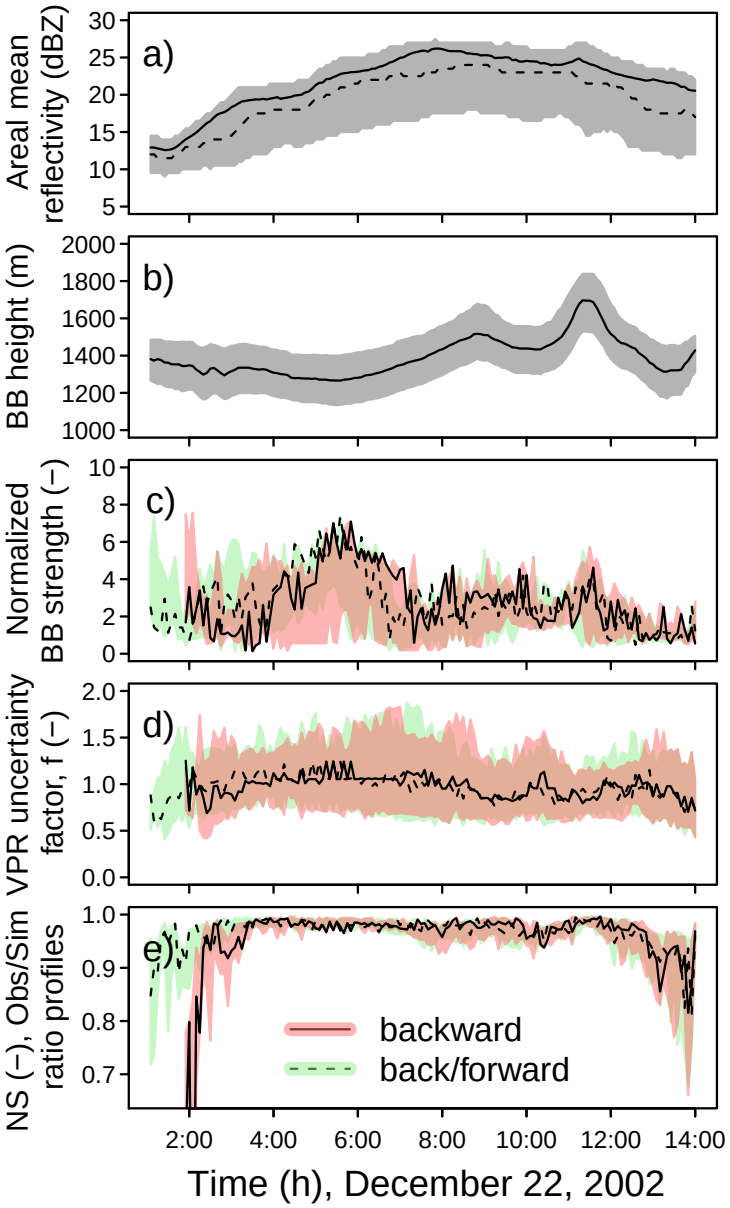

Figure 5.12: As Fig. 5.7, but for the large-scale stratiform precipitation system observed on December 22, 2002.

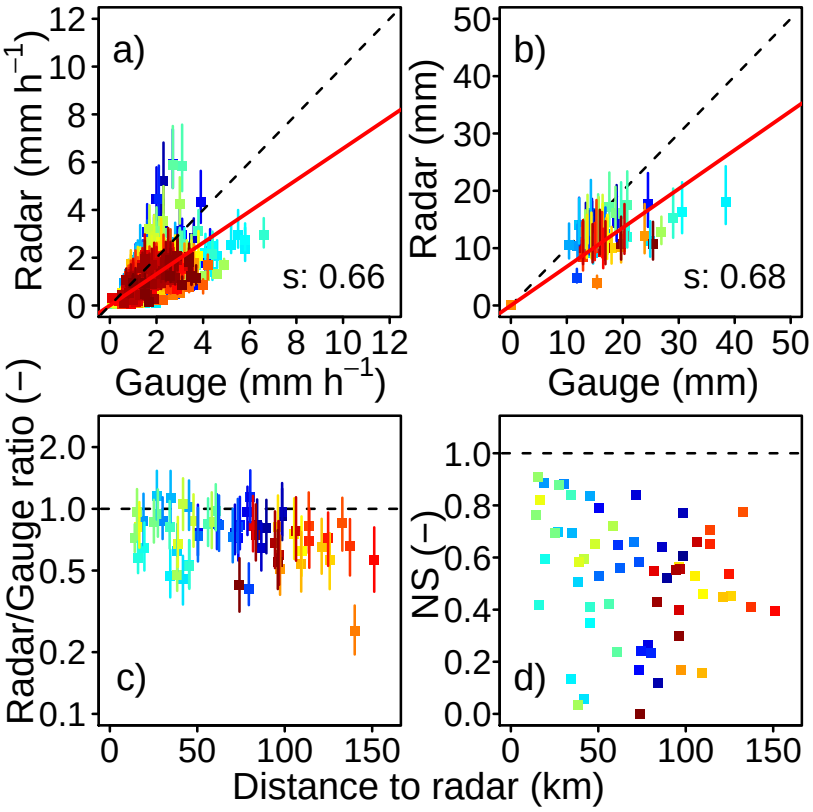

Figure 5.13: As Fig. 5.9, but for the large-scale stratiform precipitation system observed on December 22, 2002.

Table 5.3: As Table 5.2, but for the large-scale stratiform precipitation system observed on December 22, 2002.

	E(R/G)			$\sum$R/$\sum$G			NS		
(km)	0-50	50-100	100-150	0-50	50-100	100-150	0-50	50-100	100-150
N	0.66	0.62	0.41	0.66	0.62	0.44	0.49	0.30	0.03
$R_{backward}$	0.78	0.77	0.68	0.78	0.79	0.72	0.59	0.42	0.50
$R_{back/forward}$	0.78	0.76	0.66	0.77	0.78	0.71	0.60	0.44	0.46

5.4.3 Event 3: Fast-moving frontal stratiform system

As a last example, the performance of the VPR-identification and uncertainty estimation procedure is tested for a fast-moving frontal precipitation system. The event started on January 1, 2003 around 10:00 UTC and had a total duration of about 42 hours. The precipitation region identified by RoCaSCA (not shown here) was much smaller in size and better defined than for the event of October, 2002 (see Section 5.4.1 and Fig. 5.6. Therefore, a clearer deviation can be expected between the result obtained using the region-based VPR-estimate and applying a global VPR-estimate.

In Fig. 5.14 the quality of the region-based VPR-corrected radar rainfall estimates are presented. Although on average the radar slightly underestimates the amount of precipitation, the majority of the radar-gauge pairs match well. Only for a number of gauges situated in the South at relatively close distance (within 60 km, light blue points) the understimation by the radar is considerable during a number of hours. Since these gauges are situated in the same region, it is expected that the observed underestimation results from other sources of error not taken into account here (e.g. DSD variability). From the lower panels of Fig. 5.14 it can be observed that the impact of range effects is well accounted for using the region-based VPR estimates. In addition, the variability in the hourly estimates for the different radar-gauge pairs is rather constant, as can be observed from the relatively large values of the Nash-Sutcliffe statistic. Hence, after correcting, the current event was well captured by the radar.

In Table 5.4 the impact of the region-based VPR identification (R) is again compared to identification in a global (G) or combined (G&R) manner. Up to 100 km the region-based estimate is well able to estimate the amount of precipitation based on the information obtained during the previous hour (backward) and gives better results compared to applying a global VPR identification procedure. In case the ratio information observed during the next hour is taken into account as well (back/forward), also beyond these distances the quality of the region-based VPR corrected radar data increases. Again this can be attributed to the visibility problems affecting a precipitation region which is located at further range from the radar. However, by applying the combined procedure (G&R) a major part of the radar-gauge difference can already be accounted for using the precipitation data obtained during the previous hour alone. An important result, since this procedure can be implemented in real-time operational weather radar applications.

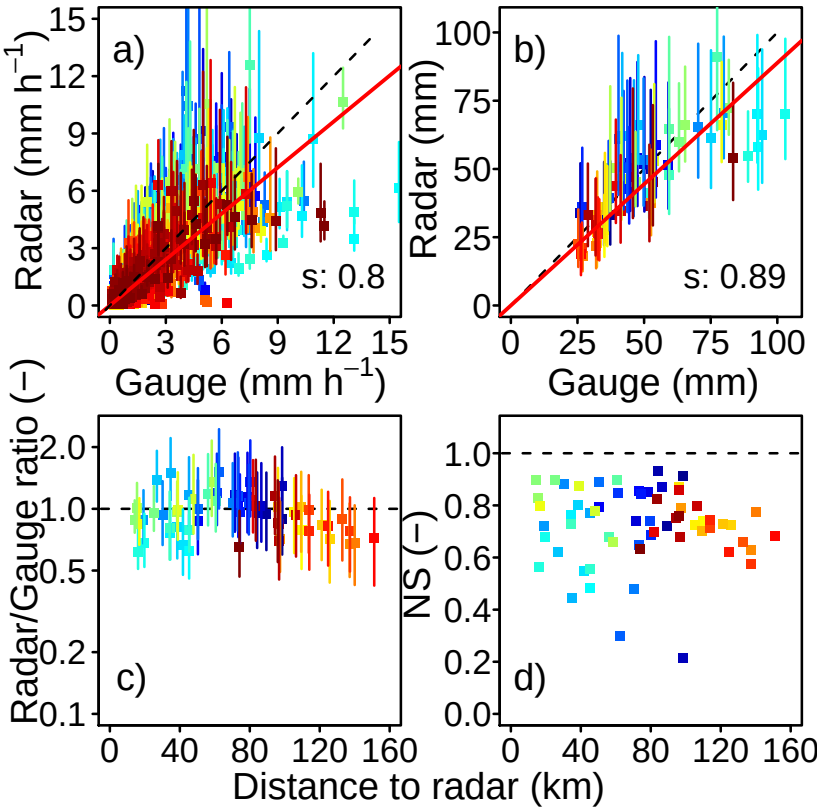

Figure 5.14: As Fig. 5.9, but for the fast-moving frontal stratiform system observed on Januari 1–3, 2003.

Table 5.4: As Table 5.2, but for the fast-moving frontal stratiform system observed on January 1–3, 2003.

			E(R/G)			$\sum$R/$\sum$G			NS		
		(km)	0-50	50-100	100-150	0-50	50-100	100-150	0-50	50-100	100-150
	N		0.84	0.87	0.52	1.04	1.00	0.60	0.63	0.77	0.51
backward	R		0.92	1.04	0.77	1.14	1.21	0.87	0.66	0.70	0.64
	G		0.93	1.12	0.92	1.18	1.30	1.00	0.64	0.66	0.71
	G&R		0.93	1.05	0.82	1.17	1.25	0.95	0.66	0.73	0.67
back/forward	R		0.92	1.05	0.83	1.15	1.22	0.92	0.66	0.74	0.70
	G		0.93	1.12	0.92	1.18	1.31	1.02	0.64	0.69	0.72
	G&R		0.92	1.06	0.84	1.17	1.25	0.95	0.65	0.74	0.73

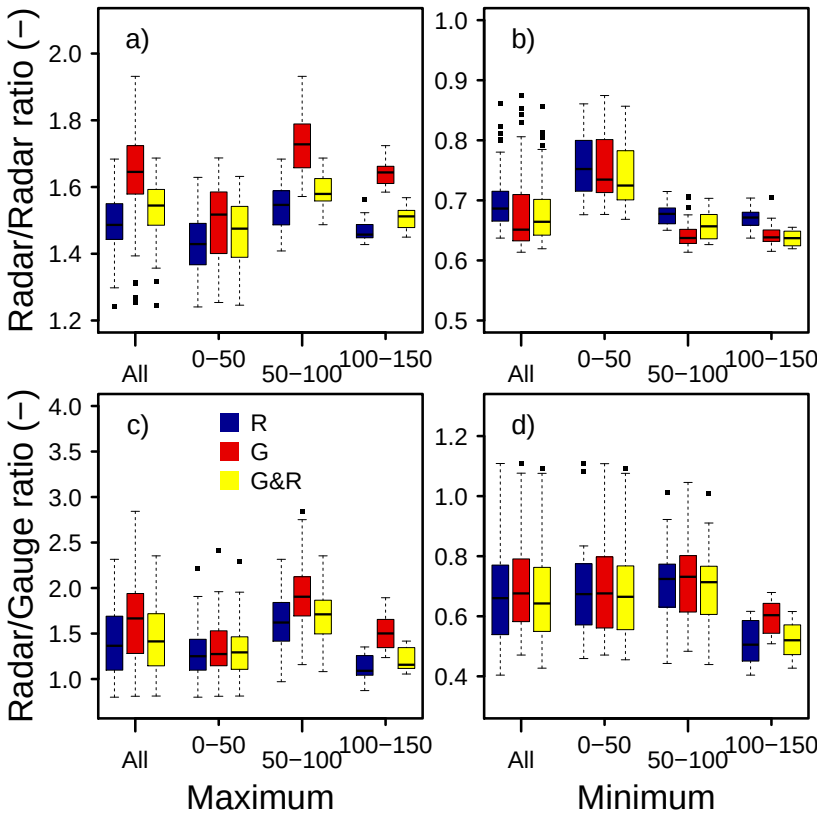

Figure 5.15: As Fig. 5.10, but for the fast-moving frontal stratiform system observed on Januari 1–3, 2003.

Also for the current event, the major part of the variability in the observed radar-gauge difference can be accounted for by taking the uncertainty in the estimated VPR into account (see Fig. 5.14 and Fig. 5.15 (bottom)). The impact of VPR uncertainty for the three different approaches is further demonstrated in Fig. 5.15. Close to the radar, region-based VPR correction leads to smaller uncertainties as compared to a global estimate. This is a direct consequence of the fact that with the former procedure spatial variability in the characteristics of the VPR between different zones is accounted for. With the latter approach, all variability is combined, leading to an increase of the VPR uncertainty. The combined procedure estimates a VPR using the region-based estimate if available, and applies the global estimate elsewhere. As a result, the overall variability lies between the other two approaches.

5.5 Discussion

The constrained piecewise linear VPR identification procedure presented in the current chapter results in improved quantitative precipitation estimates by weather radar. The procedure proposed here focuses specifically on identifying and tracking precipitation regions of given type. The importance of such an implementation has been addressed in a number of papers (*Fabry et al.*, 1992; *Vignal et al.*, 1999; *Delrieu et al.*, 2009). These authors recognized the necessity to estimate the VPR within a region of uniform precipitation with limited spatial variability regarding vertical variations of the precipitation microstructure. We believe the Lagrangian approach presented here provides a way forward in reaching this goal.

The results shown in the current chapter reveal that up to distances of about 100 km, proper identification of the VPR for a given precipitation region can be achieved. Unfortunately, beyond this distance, visibility problems prevent proper identification of the ratio profiles. It is expected that these ranges are extended during summer conditions and in warmer climates (i.e. larger vertical extent of precipitation and higher level of the BB). However, for operational applications, we propose to make use of the combined global and regional VPR identification approach (G&R). Although this approach is computationally more intensive, experience has shown it can be implemented in real-time. In addition, the results presented here show that up to distances of 150 km this combined procedure provides proper quantitative precipitation estimates.

For regions closer to the radar, thresholding at >7 dBZ results in relatively large regions, although the delineation of precipitation regions has a positive impact on the quality of the estimated VPR. Hence, it was decided in this study to add a second threshold of >23 dBZ, similar to what was historically proposed as part of many storm cell identification and tracking procedures (*Dixon and Wiener*, 1993; *Johnson et al.*, 1998; *Handwerker*, 2002). In its current implementation, these thresholds therefore function to delineate uniform precipitation regions. For the type of systems observed within the Ardennes region, this assumption holds rather well for the second threshold level (>23 dBZ). However, the results of this study have shown that considerable variability is still encountered within a given delineated region (see Section 5.4.2) and this uncertainty can have an impact on the identified VPR. Therefore, as a next step, the identification of precipitation regions could be improved further by making use of multiple variables such as reflectivity,

BB height and echotop information. These properties can all be obtained from conventional volumetric radar measurements. The usage of polarimetric radar information provides even more possibilities (*Seliga and Bringi*, 1976; *Doviak and Zrnic*, 1993). In principle, RoCaSCA should be able to take multiple properties into account, although its current 2-dimensional implementation should then be extended.

Even if such an extension would provide the possibility to further discriminate between precipitation regions, the random nature of hydrometeor size interactions and the temporal differences between the measurements at different radar elevations will always result in uncertainty and variability in the observed ratio profiles. The VPR uncertainty identification method presented here provides a manner to take this variability into account. These results have indicated that the overall uncertainty due to the VPR can be considerable, and is able to account for a large part of the observed radar-gauge differences. Such an approach, therefore, provides a direct way to take VPR uncertainty into account and should be identified together with other radar rainfall uncertainty identification procedures (*Villarini and Krajewski*, 2010). The importance of the latter aspect could also be observed from the analyses presented in Section 5.4.2.

The current uncertainty identification procedure is not able to discriminate deviations of the observed DSD from 'standard' stratiform conditions. Such deviations can have a large impact on the rainfall measurement capabilities of the radar. The possibility of being able to discriminate between different precipitation regions, as presented in the current chapter, could also provide extra information that is usable to identify such situations. Detailed analyses of the different precipitation regions and their physical properties (e.g. BB height and depth, vertical structure) could for instance result in the identification of a region specific $Z - R$ relationship. Another option would be to make use of real-time rain gauge networks, which nowadays have similar temporal resolutions as radar. Merging the obtained precipitation region identification procedure with measurements from rain gauges would allow estimation of region specific $Z - R$ relationships. This would then further improve radar rainfall estimates.

5.6 Conclusion

In this study a Lagrangian procedure to estimate the vertical profile of reflectivity from volumetric weather radar data was presented. Al-

though the dynamic nature of precipitation stimulates the use of such a procedure, such an approach has not been implemented before, to the authors knowledge. The developed tracing type cluster identification algorithm RoCaSCA is well able to delineate precipitation regions at different levels of intensity, without focusing on linking neighboring pixels only. By tracking each of these regions in time, it is possible to extract the reflectivity ratio information in a Lagrangian manner. The VPR is then identified by combining and extending the methods originally proposed by *Andrieu and Creutin* (1995) and *Smith* (1986) for two different piecewise linear profiles discriminating between stratiform and non-stratiform precipitation.

The results presented in this chapter show that for the region of study, up to a distance of 100 km, the VPR identification method is able to correct for range effects. Beyond this distance, reduced visibility of the radar due to overshooting and sampling within the snow region decreases the possibility to obtain proper ratio information. The identification of a representative VPR therefore becomes difficult.

Two methods are proposed to increase the effective VPR identification range. The first approach uses data observed within the next hour as well. During this second hour, some of the precipitation regions move closer to the radar, leading to an increase in the quality of the ratio data. However, for precipitation regions moving away from the radar, this obviously does not lead to improved results of the estimated VPR. Also for situations where the assumption of a temporally stable VPR is violated, the quality of the estimated VPR is not improved by taking a second hour into account. As a second approach, the Lagrangian region-based procedure was combined with an Eulerian global VPR identification approach. This latter option enables one to estimate a VPR for all positive reflectivity pixels that were not used in the Lagrangian approach. Results show that this approach is able to generate proper quantitative precipitation estimates up to a distance of 150 km. Since this procedure only takes the precipitation information of the previous hour into account, another benefit of this procedure is that it can be implemented in real-time. As such, this latter approach provides better possibilities as compared to the former.

In general, considerable spatial variability in the characteristics of the VPR are observed. Therefore, besides implementing a region-based median VPR estimation procedure, this chapter also presents an approach to identify the impact of VPR uncertainty on weather radar measurements. To the authors' knowledge, such a procedure to estimate radar

rainfall uncertainty resulting from VPR identification uncertainty has not been presented before. Analyses of two precipitation events showed that this type of uncertainty is able to account for the majority of radar-gauge differences. Although this partly holds for another event analyzed here as well, further deviations between the measurements of both devices are caused by variations of rainfall microstructure.

In the current chapter, we have not tried to implement any bias correction mechanisms to account for such deviations. For the future, we believe it can become possible to identify these situations by performing extended analyses on the characteristics of the identified precipitation regions (e.g. size, velocity, characteristics of the delineated VPR). As such, we hope to be able to recognize such variations in the DSD from volumetric radar data. Polarimetric radars, which are gradually replacing non-polarimetric radars all over the world, could provide even more possibilities. Such an approach would allow the corrected weather radar data to be directly applicable for hydrological applications, using the rain gauge information only for verification. These results have not been presented here, but will be the focus of future contributions.

CHAPTER 6

Hydrological potential of weather radar

6.1 Introduction

To account for the complexity to measure the amount of surface precipitation and model the resulting catchment response, nowadays operational hydrological centers start to make use of ensemble stream flow simulations for flood forecasting (e.g. *Carpenter and Georgakakos*, 2006; *Cloke and Pappenberger*, 2009; *Germann et al.*, 2009; *Rossa et al.*, 2011). The motivation behind this approach is generally to account for three different types of uncertainty: 1) in the input data, 2) from temporal changes in the catchment response resulting in uncertainty in the hydrological model parameters, and 3) due to a limited understanding and representativity of the applied hydrological model (*Dawdy and Bergmann*, 1969; *Obled et al.*, 1994; *Arnaud et al.*, 2011). The current chapter focuses on the first two types of uncertainty and their interrelationship.

The impact of the variability and uncertainty in the observed precipitation on the modeled discharge response of a catchment has been a research topic in hydrology for many years (*Dawdy and Bergmann*,

This chapter is a slightly modified version of a manuscript submitted to *Water Resour. Res.* : Hazenberg, P., H. Leijnse, and R. Uijlenhoet (2013), Conceptual radar rainfall ensemble generation and its impact on the catchment hydrological response during cold season precipitation.

1969; *Wilson et al.*, 1979; *Woods and Sivapalan*, 1999). It is generally accepted that the spatial variability of precipitation becomes important when focusing on large basins (>3000–10000 km^2), as well as for small-scale intense convective showers within urban, arid or mountainous catchments, where shallow sloping soils lead to a fast runoff response (*Anquetin et al.*, 2010). For most other cases, a correct representation of the basin mean rainfall input provides sufficient information to model the rainfall-runoff response. Any additional variability in the precipitation field will be filtered by the catchment through its hillslopes and channel network (*Wilson et al.*, 1979; *Obled et al.*, 1994; *Segond et al.*, 2007; *Nicotina et al.*, 2008; *Younger et al.*, 2009).

Traditionally, rain gauges have been used to obtain precipitation estimates at the (sub)catchment scale. However, measurement errors and limited spatial representativeness, give rise to considerable uncertainty around the mean basin precipitation value estimated from rain gauges (*Moulin et al.*, 2009). Therefore, a number of methods have been developed to account for the amount of uncertainty around the mean estimate, such as conditional simulation or perturbation of the rainfall signal with a stochastic variable (*Clark and Slater*, 2006; *Pauwels and De Lannoy*, 2006; *McMillan et al.*, 2011; *Rakovec et al.*, 2012a). However, the accuracy of these methods depends on the density of the employed gauge network and the assumed representation of stochastic variability.

Volumetric weather radars provide a wealth of information on the characteristics of the precipitation field at a much higher spatial resolution than rain gauges (*Joss and Waldvogel*, 1990). Unfortunately, rainfall measurements by radar are known to be affected by multiple sources of error, leading to unrealistic estimates of catchment-scale precipitation intensity (*Joss and Pittini*, 1991; *Steiner et al.*, 1999; *Seo and Breidenbach*, 2002; *Borga*, 2002; *Dinku et al.*, 2002; *Hazenberg et al.*, 2011a). If not properly accounted for, these biases can propagate through the hydrological model resulting in erroneous discharge simulations (*Vivoni et al.*, 2007; *Collier*, 2009).

In general, volumetric weather radar measurement errors can be separated into 1) reflectivity measurement errors and 2) reflectivity conversion errors (*Jordan et al.*, 2000; *Chumchean et al.*, 2008). The former are related to the characteristics of the radar (e.g. location, radar calibration, wavelength, etc.) and the surrounding measurement environment (e.g. type of precipitation, bright band contamination, range effects, etc.). Errors related to the latter are associated with temporal changes in the hydrometeor phase and the shape of the size distribution, result-

ing in the problem that similar radar reflectivity values Z [$\mathrm{mm^6\,m^{-3}}$] as measured by radar can be the result of two completely different raindrop size distributions with different rainfall intensity values R [$\mathrm{mm\ h^{-1}}$].

To improve the measurement capability of the radar, different methods have been developed to systematically correct for errors related to the characteristics of the radar (e.g. *Hitschfeld and Bordan*, 1954; *Delrieu et al.*, 1995; *Pellarin et al.*, 2002; *Ulbrich and Lee*, 1999; *Joss and Lee*, 1995; *Delrieu et al.*, 1999, 2000; *Serrar et al.*, 2000; *Steiner and Smith*, 2002), and the surrounding environment (e.g. *Smith*, 1986; *Andrieu and Creutin*, 1995; *Vignal et al.*, 1999; *Steiner et al.*, 1995; *Gourley et al.*, 2009). In order to account for variability in the radar rainfall Z–R relationship, it is nowadays well accepted to use a precipitation type specific Z–R relation (e.g. *Austin*, 1987; *Fulton et al.*, 1997; *Haddad and Rosenfeld*, 1997; *Uijlenhoet et al.*, 2003b; *Zhang et al.*, 2011).

However, once the weather radar signal has been corrected for errors, considerable uncertainty around the estimated precipitation value remains, either due to aspects unaccounted for, imperfect error correction algorithms, or from small-scale temporal changes of the precipitation field. To improve the quality of operational rainfall-runoff forecasts using radar data, this uncertainty needs to be accounted for (*Villarini and Krajewski*, 2010). Therefore, a number of approaches have been developed based on specialized additive and multiplicative statistical error methods, taking into account the spatial correlation structure of the precipitation field (e.g. *Ciach et al.*, 2007; *Germann et al.*, 2009; *AghaKouchak et al.*, 2010; *Seo and Krajewski*, 2011). In order to apply these data intensive methods, long term precipitation data comprising different storm types observed in different seasons are needed. Even though such long term series nowadays become more available (e.g. *Overeem et al.*, 2009; *Wright et al.*, 2012; *Smith et al.*, 2012), in many operational environments insufficient data has been stored or the rain gauge density is too limited to apply these procedures and obtain an estimate of the radar-rainfall uncertainty characteristics.

In the current chapter, we present two different approaches to account for the amount of uncertainty in the radar-rainfall signal, based on the volumetric information directly. As such, the method as developed in Chapter 5 is used to estimate the uncertainty originating from vertical variation in the precipitation field, i.e. resulting from reflectivity interpretation errors. Next to that, a stochastic procedure is proposed to estimate the uncertainty that arises from the applied radar reflectivity-rainfall rate conversion. The main benefit of these approaches is that

both can be applied in a real-time operation setting, without having to analyze long term radar-rain gauge records a priori.

As mentioned above, besides the uncertainty that originates from precipitation measurements, a considerable fraction of the total uncertainty in rainfall-runoff modeling can be associated with the parameter values and process representation of the hydrological model. Every hydrological model is a simplification of the true behavior of a catchment, using a limited number of parameters to describe the hydrological response (*Carpenter et al.*, 2001). As such, different parameter sets can lead to similar results, i.e. the equifinality problem (*Beven*, 2000). Therefore, the second part of this chapter focuses on the impact of the radar-rainfall estimation uncertainty on the hydrological response of a basin and how this relates to the uncertainty originating from parameter variability.

This chapter is set up as follows. Section 6.2 presents the region of the study and the details behind the applied hydrological model. In Section 6.3, the two different methods to obtain an estimate of the amount of radar-rainfall uncertainty are presented. The first aspect focuses on the observed variability of vertical profile of reflectivity (VPR, see Chapter 5), while the second approach uses a statistical technique to generate Z–R uncertainty. In Section 6.4 the generated uncertainty from weather radar measurements is compared to observations by rain gauges, proceeding with an analysis focusing on the impact of precipitation uncertainty on the rainfall-runoff simulations. Sections 6.5 and 6.6 present the discussion and conclusions, respectively.

6.2 Materials and methods

6.2.1 Study area and radar characteristics

Weather radar measurement uncertainty estimation in this study is performed for the C-band Doppler radar situated in the hilly plateaus of the Ardennes region in the eastern part of Belgium (see Fig. 6.2). Volumetric information of the precipitation field is available at five different scanning elevations at a five-minute temporal resolution, sampled during the period October 2002 until March 2003. During this winter half-year most precipitation has a stratiform character, with the zero degree isotherm usually situated in the lowest 2 km of the atmosphere. As such, spatial and temporal variations of the vertical profile of reflectivity (VPR) have a large impact on the measurement quality of the radar (*Berne et al.*,

Table 6.1: Basin size (km^2) and maximum and minimum Nash-Sutcliffe (NS) statistics of the 200 optimal parameters sets obtained from 100,000 Monte Carlo simulations. Different subbasins are ordered from upstream to downstream. The station numbers (Nr) correspond to the values given in Fig. 6.1

Station	Nr	Size (km^2)	NS_{max}	NS_{min}
Ourthe	1	1620.0	0.872	0.863
Ortho	6	385.1	0.895	0.886
Mabompré	5	322.0	0.842	0.832
Nisramont	4	32.0	0.893	0.890
Hotton	3	222.8	0.899	0.896
Durbuy	2	263.7	0.914	0.913
Tabreux	1	394.2	0.910	0.909

2005; *Hazenberg et al.*, 2011a).

In the Ardennes region a network of 64 rain gauges is available within a 150 km distance from the radar (see Fig. 6.2). These hourly rain gauges are used here both for radar-gauge comparisons at the point and catchment scale, and for the calibration and validation of the hydrological model employed to simulate the discharge response of the Ourthe catchment upstream of Tabreux (see Section 6.2.2). In order to obtain a mean catchment precipitation estimate from the rain gauge data, the inverse distance weighting methodology was applied (*Goovaerts*, 2000).

Within the Ourthe basin runoff measurements are performed at six different locations (see Fig. 6.1). The size of each of the (sub)basins upstream of these points is given in Table 6.1. Both the rain gauge and discharge data are available at a hourly resolution for the period 1995–2005.

6.2.2 Rainfall runoff simulations

The current study uses the hydrological topography-based TOPMODEL (*Beven and Kirkby*, 1979; *Beven et al.*, 1995) to simulate the discharge response at the 6 different outlets as presented in Fig. 6.1. The semi-distributed soil moisture accounting TOPMODEL, as implemented by *Nguyen* (2011), provides a compromise between fully physically-based models and lumped conceptual models (*Robson et al.*, 1993). The model uses a limited number of parameters while effectively making use of a catchment's topographic index distribution and channel width function.

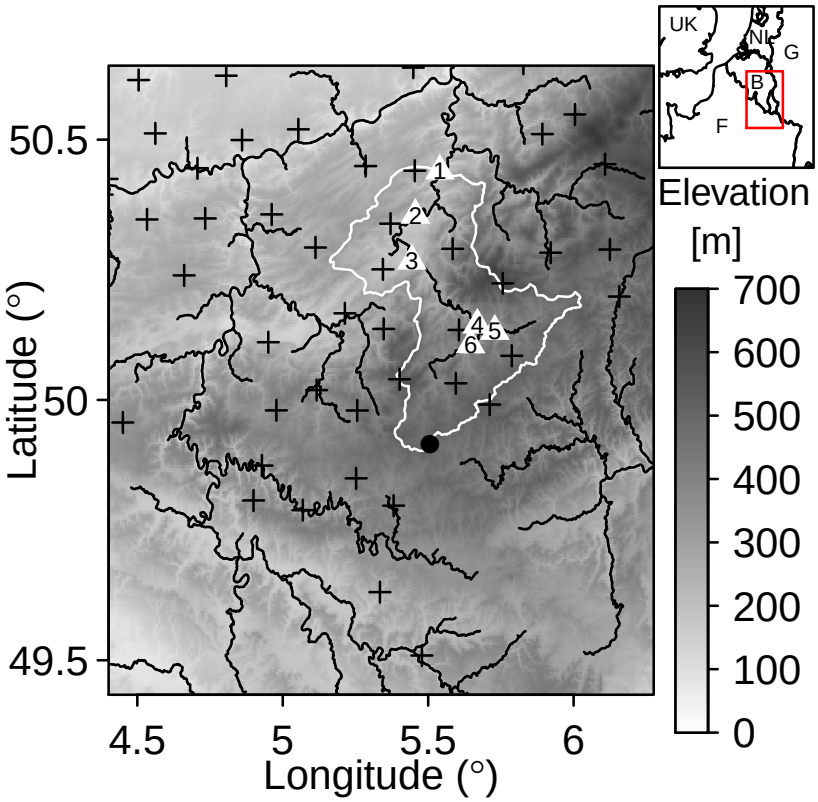

Figure 6.1: The small panel shows the location of the study area, with a 200 by 200 km box indicating the area shown in the right panel. The main panel shows a topographic map of the Belgian Ardennes, where the solid lines represent the channel network. Also shown are the position of the radar (•) and the position of the rain gauges (+). Discharge measurements are taken at six different locations given by the white △, of which the numbers correspond to Table 6.1.

The 5 physically interpretable parameters are 1) T_0, representing the lateral transmissivity at the topsoil (m^2 h^{-1}), 2) a shape parameter m, indicating the rate of exponential decline of transmissivity with depth (m), 3) a time constant T_d for the mean residence time of vertical flow per unit of deficit (h m^{-1}), 4) S_{rzmax}, indicating the maximum root zone deficit (m), and 5) v^*, indicating the mean channel flow velocity (km h^{-1}).

Since different parameter sets are able to generate similar results (the equifinality problem), the generalized likelihood uncertainty estimation (GLUE) methodology (*Beven and Binley*, 1992; *Beven*, 2000, 2009) was used. In this manner, the best 200 parameter sets were selected out of 100,000 Monte Carlo simulations, using the hourly rainfall as obtained from the rain gauge measurements and discharge data for the period 1995–2005 to ensure a sufficient size of the calibration period (*Brath et al.*, 2004). The optimal Nash-Sutcliffe (NS) statistics (*Nash and Sutcliffe*, 1970) obtained for this calibration period are presented in Table 6.1. An example of the resulting dotty plots from this calibration procedure is presented in the bottom panel of Fig. 6.2 for the Ourthe basin. The upper part of Fig. 6.2 also presents the interdependencies between the different parameter values. From these panels, it can be observed that m and S_{rzmax} show a dependence, while this can not be discerned for the other parameter combinations.

In the current work, discharge simulations for the Ourthe at Tabreux are performed, both in a lumped and distributed manner. For flood forecasting in medium-sized basins, generally distributed models are preferred over lumped ones, providing more detailed information. However, the former do not always lead to a better performance at the outlet (*Carpenter and Georgakakos*, 2006). For the distributed case, TOPMODEL was implemented for each of the six subbasins described in Table 6.1. Downstream catchments use upstream simulated discharge originating from the parameter set providing the best simulation. As such, TOPMODEL was calibrated for the Ourthe in a lumped, as well as a distributed manner for each of the 6 subbasins, where except for the two subbasins upstream of Ortho and Mabompré, all basins receive upstream simulated inflow through the channel network.

Since only a limited radar dataset was available, it was decided not to recalibrate TOPMODEL based on these data, even though we recognize that variations in precipitation input can give rise to different optimal parameter sets. However, recalibration can lead to compensation of model parameters in case the radar data contain errors regarding the

estimated precipitation input (*Andreassian et al.*, 2001; *Brath et al.*, 2004).

6.3 Radar-rainfall estimation and uncertainty identification

6.3.1 Error correction of weather radar data

As explained in the Introduction, weather radar rainfall measurements are known to be affected by multiple sources of error. Therefore, as a first step, contamination from clutter and anomalous propagation have been identified within each of the five radar elevations using the raw polar data (*Steiner and Smith*, 2002). The uncontaminated volume data are then used to discriminate between convective, stratiform and non-stratiform precipitation based on documented algorithms (*Steiner et al.*, 1995; *Sánchez-Diezma et al.*, 2000; *Delrieu et al.*, 2009). For the latter two rainfall types the vertical profile of reflectivity (VPR) is estimated for each storm region (see Chapter 5 and Section 6.3.1). Based on this VPR estimate, measured radar data can be corrected for mean deviations within the observed vertical precipitation field. Since it is recognized that each type of precipitation requires a specific power-law Z–R relationship to convert the measured reflectivity to a rainfall estimate, $Z = 300\ R^{1.4}$ was applied for convective (*Fulton et al.*, 1997), $Z = 200\ R^{1.6}$ for stratiform (*Marshall et al.*, 1955) and $Z = 250\ R^{1.5}$ for non-stratiform precipitation (*Battan*, 1973), respectively. As a last step, the volumetric data are converted to a single 2D Cartesian 1-km resolution rainfall grid, interpolating the clutter contaminated regions with corrected radar data. For the current radar and region of study, these different sources of error were considered to have the most dominant impact on the rainfall measuring capabilities of the radar (*Hazenberg et al.*, 2011a). The radar data are not corrected for temporal changes in the transmitted power since these were expected not to play a significant role during the period of study.

In the current chapter two different sources are identified that lead to uncertainty around the measured radar precipitation value. One source focuses on the amount of uncertainty originating from spatial and temporal variations of the VPR, while the second one focuses on the uncertainty associated with the Z–R relationship. Both implementations are described in the following sections.

It was decided not to correct the weather radar data for any addi-

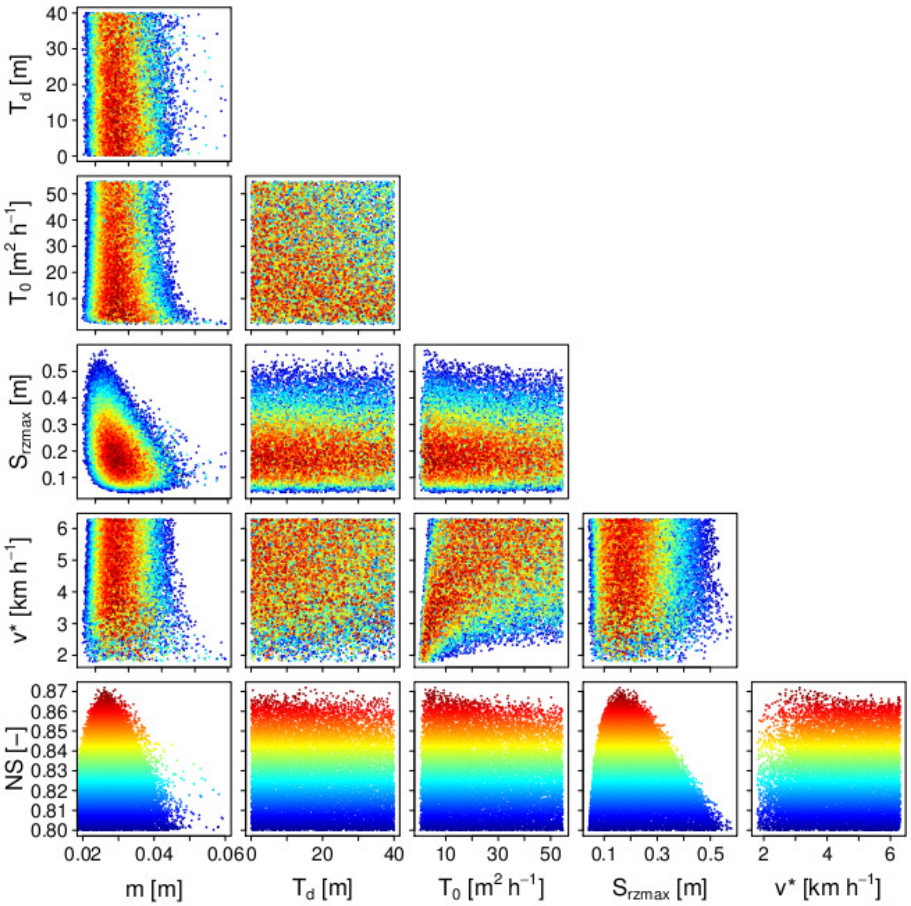

Figure 6.2: Lower panel provides dotty plots of the Nash-Sutcliffe (NS) statistic for the 5 different parameters of TOPMODEL. These parameters represent: T_0 for the lateral transmissivity at the topsoil (m^2 h^{-1}), m for the rate of exponential decline of transmissivity with depth (m), T_d for the mean residence time of vertical flow per unit of deficit (h m^{-1}), S_{rzmax} for the maximum root zone deficit (m), and v^* for the mean channel flow velocity (km h^{-1}). The inter-dependencies between the different parameters is presented in the upper four panels. Only the results are shown for which the simulations obtained a NS value >0.8.

tional bias with respect to the rain gauges. This because of the difficulty to account for the influence of scale issues when comparing the measurements of both devices (e.g. *Austin*, 1987; *Kitchen and Blackall*, 1992; *Steiner et al.*, 1999; *Ciach and Krajewski*, 1999a; *Morin et al.*, 2003), and because of issues related to the quality of gauge measurements (*Molini et al.*, 2001; *Habib et al.*, 2001). Since the weather radar is corrected for the most dominant sources of error, by taking the impact of measurement uncertainty into account, in the current study a true assessment of the potential of weather radar within an operational setting is performed, without employing rain gauge data to adjust weather radar data in any way.

6.3.2 Uncertainty identification from VPR

Spatial and temporal variations in the vertical distribution of hydrometeor properties (including their size distribution and phase), have a large impact on the measurement capabilities of radar (e.g. *Battan*, 1973; *Smith*, 1986; *Joss and Pittini*, 1991). Especially for stratiform systems, the melting of snow flakes below the zero degree isotherm results in an intensification of the return signal known as the bright band, leading to an overestimation of surface precipitation by radar if not accounted for. For the snow region above the bright band, on the other hand, the returned signal is much smaller than that from the precipitation observed at the surface, resulting in an underestimation of the surface rainfall rate. Overall, this can have a detrimental impact on the quality of radar precipitation estimates (*Fabry et al.*, 1992; *Kitchen and Jackson*, 1993; *Bellon et al.*, 2005).

In Chapter 5 a Lagrangian procedure was presented to estimate the VPR for stratiform and non-stratiform precipitation from volumetric weather radar data for a given precipitation region. This method combines the characteristics of the VPR identification procedures originally presented by *Smith* (1986) and *Andrieu and Creutin* (1995), where the VPR is assumed to be spatially uniform for a large part of the radar umbrella. This enables one to decompose the apparent reflectivity $Z_a(r,h)$ as measured by the weather radar into a horizontal and vertical component

$$Z_a(r,h) = Z_{REF}(r) z_a(r,h), \tag{6.1}$$

where $Z_{REF}(r)$ is the reflectivity at the chosen reference level at a distance r from the radar, and $z_a(r,h)$ is the apparent vertical profile of

reflectivity (VPR). Chapter 5 assumed the VPR can be described by a piecewise linear function. To estimate the actual shape of this piecewise linear VPR for a given precipitation region from the volumetric radar measurements, ratio profiles $q(r, A_1, A_j)$ are obtained (i.e. the ratios between the measured reflectivity at a higher elevation j with respect to those at the lowest one):

$$q(r, A_1, A_j) = \frac{Z_a(r, A_j)}{Z_a(r, A_1)} = \frac{z_a(r, A_j)}{z_a(r, A_1)}. \tag{6.2}$$

In this manner, the median of all ratios at a given range obtained within the last 60 minutes, together with the measurement characteristics of the radar, are used to estimate the median VPR. As such, a piecewise linear VPR is estimated minimizing the difference between the theoretical and observed ratio profiles.

Even though correcting weather radar measurements for range and VPR effects improves the quality of the radar surface rainfall product, considerable differences with respect to the measurements from rain gauges are expected to remain. These variations result from local fluctuations around the median VPR due to horizontal variability in vertical variations of the precipitation microstructure (size, shape, number concentration and phase of the hydrometeors) (*Joss and Waldvogel*, 1990; *Hazenberg et al.*, 2011b). In addition, since radar measurements at different elevation angles are not performed simultaneously, the temporal evolution of the VPR leads to further deviations from the median profile. Therefore, besides correcting for VPR effects, we also wish to obtain an estimate of the amount of uncertainty around its median value and assess its impact on weather radar rainfall estimation.

To estimate this uncertainty, again use can be made of the information contained in observed ratio profiles information. These profiles show considerable variability for a given distance from the radar. In Chapter 5 it was found that once these percentiles are scaled with respect to the median, these overall deviations become rather constant with range. As such, instead of making use of the median ratio profile only, at a given distance, usage was made of the 20th, 30th, 40th, 50th, 60th, 70th and 80th percentile values of the observed ratio value to estimate 7 possible shapes of the VPR. These profiles can then be used to generate 7 different VPR-corrected radar rainfall fields, from which an estimate of the amount of uncertainty associated with VPR variability can be obtained. For further details on the specific implementation of this method, the reader is referred to Chapter 5.

Since the gauge information and hydrological simulations are available at an hourly resolution, VPR-corrected five-minute weather radar rainfall fields for a given VPR percentile are aggregated to hourly estimates. This ensures the uncertainty of the VPR is properly aggregated in time, without merging different percentile values for different five-minute time steps. This latter approach could lead to a minimization of the random variability around the VPR, which would underestimate the true uncertainty around the median VPR profile. In addition, since the ratio profiles are estimated using the data obtained within the last 60 minutes, by aggregating the five-minute VPR-corrected radar data for a given ratio percentile, we aim to ensure that uncertainty estimates of VPR variability are temporally consistent. As such, for each hour, 7 different VPR-corrected weather radar estimates are generated, from which the uncertainty due to vertical variations of the precipitation field can be estimated.

6.3.3 Uncertainty identification from Z–R variability

For a given event, precipitation phase and drop size distribution $N(D)$ continuously change in space and time as a result of external meteorological forcings or due to interactions among droplets. Both the radar reflectivity factor Z and rainfall intensity R are related to the drop size distribution, $N(D)dD$ (m^{-3}), with

$$Z = \int_0^\infty D^6 N(D) dD, \tag{6.3}$$

and

$$R = 6\pi \times 10^{-4} \int_0^\infty D^3 v(D) N(D) dD, \tag{6.4}$$

where D (mm) is the equivalent spherical drop diameter and $v(D)$ ($\mathrm{m\ s}^{-1}$) is the theoretical raindrop terminal fall velocity ($\mathrm{m\ s}^{-1}$). The dependence between the radar reflectivity factor and rain rate is generally described by a power-law relationship (*Battan*, 1973)

$$Z = A\ R^b. \tag{6.5}$$

In case the terminal fall velocity is assumed to follow a power-law relationship, the prefactor A becomes a function of $N(D)$, while the exponent b can be related to the temporal evolution of $N(D)$ (*Uijlenhoet et al.*, 2003a; *Steiner et al.*, 2004; *Hazenberg et al.*, 2011b). Since it is

impossible to measure $N(D)$ using conventional weather radar, the parameters of the Z–R relationship are assumed to be fixed values for a given type of precipitation (*Battan*, 1973), even though in reality these parameters vary in space and time (e.g. *Waldvogel*, 1974; *Uijlenhoet and Berne*, 2008; *Schleiss et al.*, 2009; *Jaffrain et al.*, 2011; *Schleiss and Berne*, 2012).

Fixed Z–R parameter values can be estimated from disdrometer or combined radar-gauge data analyses (*Battan*, 1973; *Austin*, 1987). Generally, these analyses show a negative correlation between the logarithm of the prefactor A and the exponent b (*Bouilloud et al.*, 2010; *Hazenberg et al.*, 2011b). As such, as a first order approximation, the relationship between the logarithm of the prefactor A and the exponent b is assumed to follow a bivariate normal distribution (*Mood et al.*, 1974).

Instead of trying to generate spatially coherent fields of drop size distribution from which Z–R parameters can be derived (*Schleiss et al.*, 2009; *Schleiss and Berne*, 2012), a practical statistical approach is adopted here. Logarithmic values of the prefactor A for a given precipitation type are randomly drawn from a normal distribution with mean and standard deviation as given in Table 6.2. Based on these random estimates of the logarithm of the prefactor, the expected value and standard deviation of the exponent, as well as the correlation between both parameters (see Table 6.2), the properties of the bivariate normal distribution are used to generate random values of b (*Mood et al.*, 1974).

Using this statistical procedure, 50 probable realizations of the Z–R power-law parameters for each precipitation type are obtained. These relationships are used to transform the observed five-minute radar reflectivity field into 50 equally likely corresponding rainfall intensity fields, which are then aggregated into hourly intervals without assuming any temporal consistency among different realizations. We are aware that this approach does not take temporal coherence into account, which might result in an underestimation of the true uncertainty in the radar precipitation signal (e.g. *Rakovec et al.*, 2012b), especially regarding the uncertainty originating from Z–R variability. However, the approach presented here does provide a first order indication of the amount of uncertainty related to radar conversion errors.

6.3.4 Implementation of both uncertainty generation methods

The two methods as described in the previous two sections are used to obtain uncertainty values around the mean radar precipitation esti-

Table 6.2: Parameters used to generate random estimates of the Z–R power-law parameters for a given precipitation type. The assumed value of the prefactor is given by E(A), while the properties of its logarithmically transformed distribution are given by its expected value E(log(A)) and standard deviation sd(log(A)). For the exponent b the mean and standard deviation are given by E(b) and sd(b). The parameters are assumed to follow a bivariate normal distribution (*Mood et al.*, 1974), with an assumed negative correlation ρ(log(A),b) between the logarithm of the prefactor A and the exponent b.

Type	E(A)	E(log(A))	sd(log(A))	E(b)	sd(b)	ρ(log(A),b)
Conv.	300	5.659	0.3	1.4	0.08	-0.6
Strat.	200	5.293	0.1	1.6	0.1	-0.4
Non-Strat.	250	5.517	0.1	1.5	0.15	-0.5

mates. As such, based on the variability in the observed VPR 7 different ensemble members are obtained, while using the uncertainty regarding the Z–R parameters 50 realizations are generated.

In order to analyze the total radar rainfall estimation uncertainty during the winter half-year of study, the bootstrap method is applied to generate an ensemble of 1000 half-year radar precipitation realizations. For a given hourly estimate, the total rainfall estimation uncertainty is then obtained using

$$P_{Unc} = \frac{P_{90} - P_{10}}{P_{50}}, \tag{6.6}$$

where the subscript indicates a given precipitation intensity percentile. Given the computational constraints, it was decided to select 100 half-year precipitation time series as input for our hydrological model. As such, the impact of precipitation estimation and model parameter uncertainty was assessed using 100 precipitation and 50 parameter ensembles, respectively. The resulting uncertainty in the discharge, similar to Eq. 6.6, is estimated as

$$Q_{Unc} = \frac{Q_{90} - Q_{10}}{Q_{50}}. \tag{6.7}$$

6.4 Results

6.4.1 Radar-Gauge analysis

In Fig. 6.3 the quality of the hourly corrected weather radar rainfall estimates as compared to rain gauge observations are presented. These weather radar observations were corrected using the median VPR estimate and the three storm type specific Z–R relations. The relatively large correlation between the individual radar and gauge measurements indicates that the radar is capable to observe most precipitation. For the winter period analyzed here, both correlation and Nash-Sutcliffe (NS) statistic (*Nash and Sutcliffe*, 1970) slowly decrease with distance from the radar, which can be related to range-dependent sampling issues. More specifically, since the sample volume and measurement height both increase with distance from the radar, larger differences between both devices occur. However, on average up to a distance of 150 km the radar-gauge ratio values are around one, as can be observed from the lower part of Fig. 6.3. This indicates that the implemented correction steps lead to weather radar precipitation measurements that on average provide estimates similar to what is observed by in situ rain gauges. Nevertheless, considerable differences between radar and gauge measurements can occur during individual intervals, generally increasing with range from the radar.

To provide more detail regarding the temporal quality of the radar measurements, the half-year daily mean hourly and daily radar-gauge ratios and their variability are presented in Fig. 6.4. These values were obtained for cases when both instruments measure precipitation ($R \geq 0.1$ mm). Both for the hourly and for the daily values, considerable differences between both devices are observed, with mean ratios close to one, similar to Fig. 6.3c and d. However, no immediate trends can be identified. This indicates that the quality of the corrected weather radar rainfall estimates is rather constant in time during the period of study.

To obtain more information on the variability between the radar and rain gauge measurements, in Fig. 6.5a the probability density functions of the radar-gauge bias are given. For the complete dataset the mean bias between both estimates lies close to zero (-0.01 mm h^{-1}) independent of distance from the radar (see also Fig. 6.5b and Table 6.4). Once the bias estimates are differentiated with respect to rainfall intensity, considerable variations are observed. For the lowest intensity range (0.1–0.5 mm h^{-1}) the radar on average slightly overestimates the rainfall with a bias of 0.13 mm h^{-1}, while for the larger intensity val-

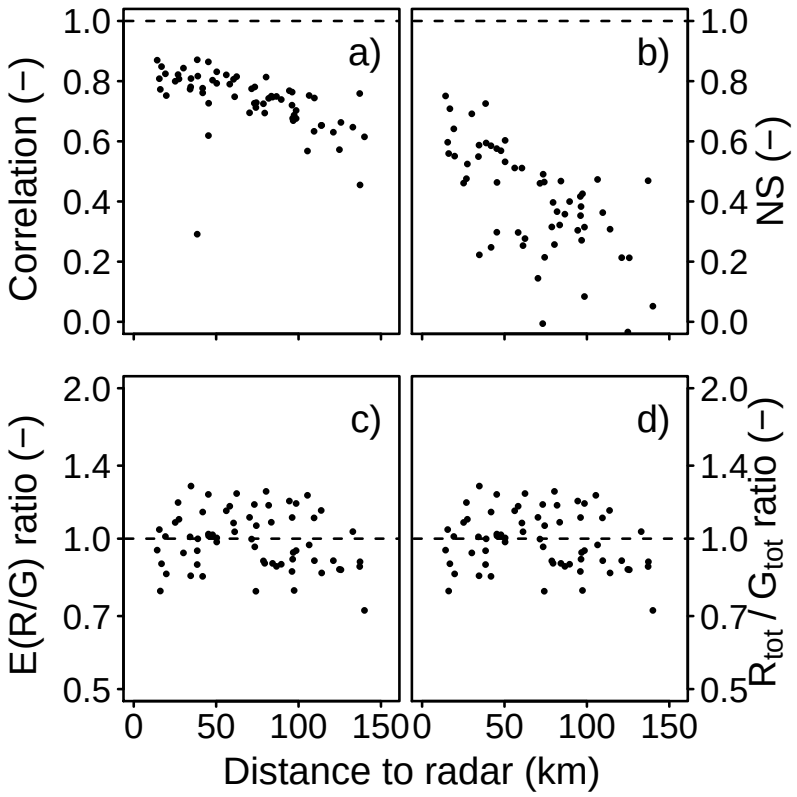

Figure 6.3: Comparison of rainfall intensities and accumulations from 69 rain gauges and the corresponding radar pixels for the half-year dataset. Different panels show the correlations (a), the Nash-Sutcliffe (NS) statistic (b), the mean hourly (c) and the overall radar/gauge ratio $\sum$Radar rainfall/$\sum$Gauge rainfall (d) for the 69 pairs as a function of range from the radar.

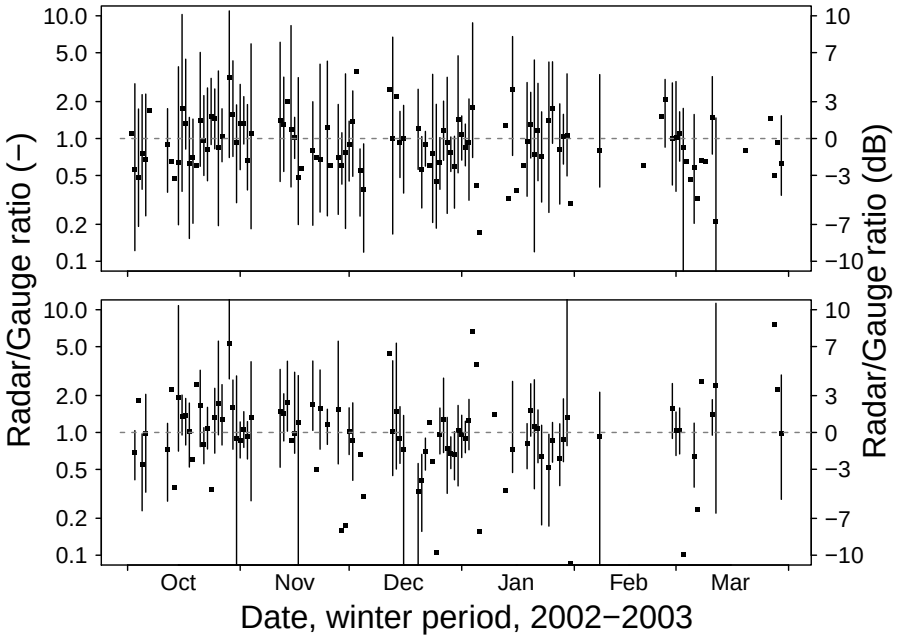

Figure 6.4: Daily averaged radar and rain gauge ratios for hourly (upper panel) and daily (lower panel) rainfall data for the half-year dataset. Vertical bars indicate the 10-90% percentile range for the 69 rain gauges. In case less than 10 positive radar and gauge measurements were available, only the mean ratio value is given.

ues (>2.0 mm h^{-1}) the radar underestimates with 0.52 mm h^{-1} (see Table 6.4). However, since during the majority of hours precipitation intensities are low, for the complete dataset mean bias values are close to zero. In Fig. 6.5b, besides the mean also the standard deviation of the error distribution of radar with respect to gauge is presented. These values generally increase with distance from the radar, again pointing to the impact of sample volume and measurement height increase with range.

Even though the weather radar on average is capable to estimate hourly precipitation values, these results show that considerable differences between both devices occur. Since the radar values are known to display a considerable amount of uncertainty, in the current study the variability of the VPR and Z–R relation was taken into account separately, to generate a number of precipitation realizations (see Section 6.3). Therefore, in Fig. 6.5c and d the half-year error functions are provided for the radar-gauge bias using the realization that minimizes the difference between both devices. Compared to Fig. 6.5a the optimal density functions are much narrower. On average the biases are slightly lower as compared to the mean correction steps. Except for the largest intensity range (>2.0 mm h^{-1}), the standard deviation decreases, indicating a narrowing of the error distribution (see Table 6.4). This especially holds when taking the uncertainty in the vertical precipitation field into account (Fig. 6.5c). In Table 6.4 also the mean and standard deviation of the error function are given for those realizations that lead to the maximum and minimum radar-gauge bias. The former are all positive, while the latter are negative. This indicates that, on average, both weather radar rainfall ensemble generation methods provide precipitation ranges encompassing the amounts observed by rain gauges.

In Fig. 6.6a and b the relative uncertainty due to VPR and Z–R variability as defined by Eq. 6.6 is presented for a given surface rainfall intensity. The uncertainties obtained from both sources generally decrease considerably with intensity. When comparing both sources of uncertainty, it can be observed that the mean uncertainty due to variability associated with the VPR lies around 0.8, while that due to Z–R variability is about 0.3. At the point scale, this corresponds to an uncertainty in the estimated radar rainfall value of 40% and 15%, respectively.

The bottom part of Fig. 6.6 presents the precipitation estimation uncertainty for a given individual radar-gauge pair. The uncertainty due to VPR variability increases up to a distance of 70 km. Closer to the radar, measurements are performed at lower elevation well within the

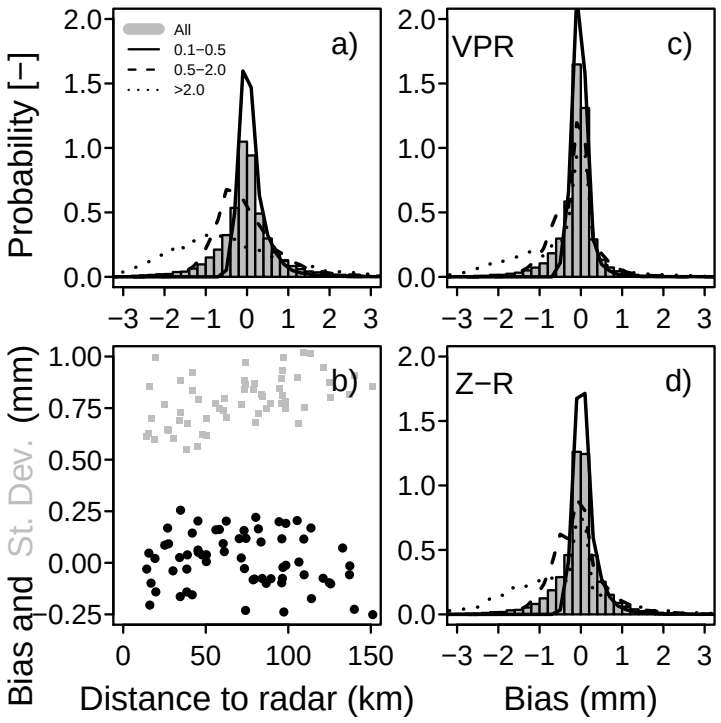

Figure 6.5: Panel (a) presents a density plot of the half-year mean hourly bias (mm) between corrected weather radar and observed rain gauge precipitation estimates for all data and three different intensity ranges (mm h^{-1}). Panel (b) shows the mean (black dots) and standard deviation (gray dots) of the bias as presented in panel (a) for the 69 gauges as a function of range from the radar. Panels on the right present the optimal bias values as obtained from VPR (panel c) and Z–R (panel d) variability estimates (by minimizing the difference between hourly radar and gauge estimates).

Table 6.3: Half-year mean hourly bias (mm) and standard deviation (in brackets) between corrected weather radar and observed rain gauge precipitation estimates for all data and three different intensity ranges. Impact of obtained radar rainfall uncertainty from VPR and Z–R variability is presented by the bias w.r.t. the optimal (minimal difference with rain gauge), minimum and maximum estimated hourly radar values.

		Intensity range (mm h^{-1})			
		All	0.1-0.5	0.5-2.0	> 2.0
	Mean	-0.01 (0.87)	0.13 (0.43)	-0.02(0.85)	-0.52 (0.85)
VPR	Optimal	-0.12 (0.6)	-0.01 (0.29)	-0.15(0.58)	-0.47 (1.2)
VPR	Min	-0.43 (0.82)	-0.11 (0.32)	-0.51(0.67)	-1.44 (0.67)
VPR	Max	+0.30 (1.22)	+0.21 (0.57)	+0.33(1.2)	+0.58 (1.2)
Z–R	Optimal	-0.04 (0.69)	+0.1 (0.34)	-0.07(0.66)	-0.53 (1.34)
Z–R	Min	-0.13 (0.78)	+0.08 (0.35)	-0.15(0.69)	-0.91 (0.69)
Z–R	Max	+0.17 (1.2)	+0.19 (0.61)	+0.16(1.18)	+0.06 (1.18)

liquid precipitation region. As such, additional VPR uncertainty due to variability in the size of the bright band for stratiform precipitation, or due to measurements within the snow region have a limited impact on the quality of the radar rainfall estimates. For distances beyond 70 km these additional sources of uncertainty are almost always part of the radar measurement and become rather constant irrespective of range. Such distance effects are not observed when considering the uncertainty originating from Z–R variability. This is because a given radar reflectivity rainfall rate relationship is applied to the whole rain field for given precipitation type.

6.4.2 Radar rainfall estimation at the catchment scale

So far hourly precipitation measurements from individual radar-rain gauge pairs have been analyzed. Even though the uncertainty in the weather radar measurement was taken into account, range effects and sampling differences complicate comparison between both devices (*Austin*, 1987; *Kitchen and Blackall*, 1992; *Gabella et al.*, 2005; *Borga et al.*, 2006). To improve the spatial coherence, the measurements of both instruments are aggregated to the scale of the different catchments as described in Section 6.2.1.

In Fig. 6.7 the correspondence between the hourly radar and gauge

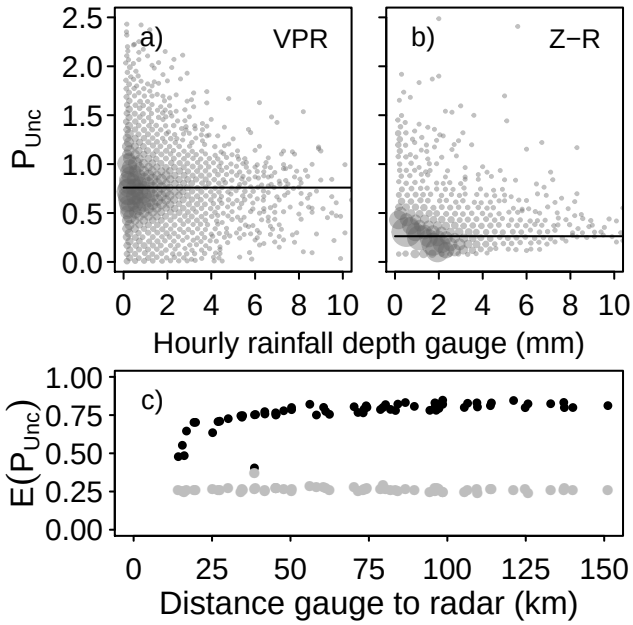

Figure 6.6: Upper panels present the hourly relative radar precipitation uncertainty estimate (P_{Unc}, see Eq. 6.6) obtained from taking the uncertainty in VPR (a) or Z–R (b) into account. Horizontal lines present the mean of the hourly estimates (E(P_{Unc})). Mean uncertainty, for each of the individual gauges (lower panel) as a function of range from the radar, taking the uncertainty in VPR (black) and Z–R (gray) into account. In the upper panels the size of a dot indicates the density of the original data.

measurement for the Ourthe catchment and the 6 subcatchments as described in Table 6.1 is given. Even though considerable variability can be observed at the catchment scale, overall the measurements of both instruments line up very well. Similar to the comparisons between the individual radar and gauge measurements. Also at the catchment scale corrected weather radar data on average resemble the estimates from the rain gauges quite well. However, in addition to providing a mean catchment value, ensembles of radar catchment rainfall realizations are also available from our methods to generate variability due to the VPR and the Z–R relation.

Some additional statistical information using the corrected weather radar information as well as the impact of the generated precipitation ensembles is given in Fig. 6.8. The large correlation values between the radar and gauge measurements indicate again that the radar is capable of observing precipitation. On average larger uncertainty ranges are observed when taking the variability in the VPR into account. This is similar to Fig. 6.6 where VPR variability lead to larger precipitation ranges. This is not the case, however, for the subcatchment upstream of Ortho, which lies directly adjacent to the radar. At this close range, the uncertainty in the estimated VPR is rather small, since most radar measurements are taken within the liquid precipitation region close to the surface. The rather large uncertainty range taking Z–R variability into account originates from residual clutter that still affects weather radar measurements during some hours.

Similar to Fig. 6.7, the radar-gauge ratios in Fig. 6.8b are close to one, indicating relatively small biases between radar and gauge measurements. The Nash-Sutcliffe (NS) statistic (*Nash and Sutcliffe*, 1970) in Fig. 6.8c shows a similar behavior as the correlation coefficient.

To gain more information on the radar-gauge bias at the catchment scale, the half-year error distribution for all catchments jointly is given in Fig. 6.9. When compared to the individual distribution in Fig. 6.5a, the distribution at the catchment scale is narrower. As such, mean bias values are close to zero and variances are smaller (see Table 6.5). The results shown in Fig. 6.9b indicate that the variance of the error distribution slightly decreases with catchment size, although it should be emphasized that the limited number of catchments studied prevents us from drawing any firm conclusion. However, these results do confirm previous observations, where range effects and sampling differences between radar and gauge measurements have been reported to decrease with spatial scale (*Creutin et al.*, 1997; *Vignal et al.*, 2000).

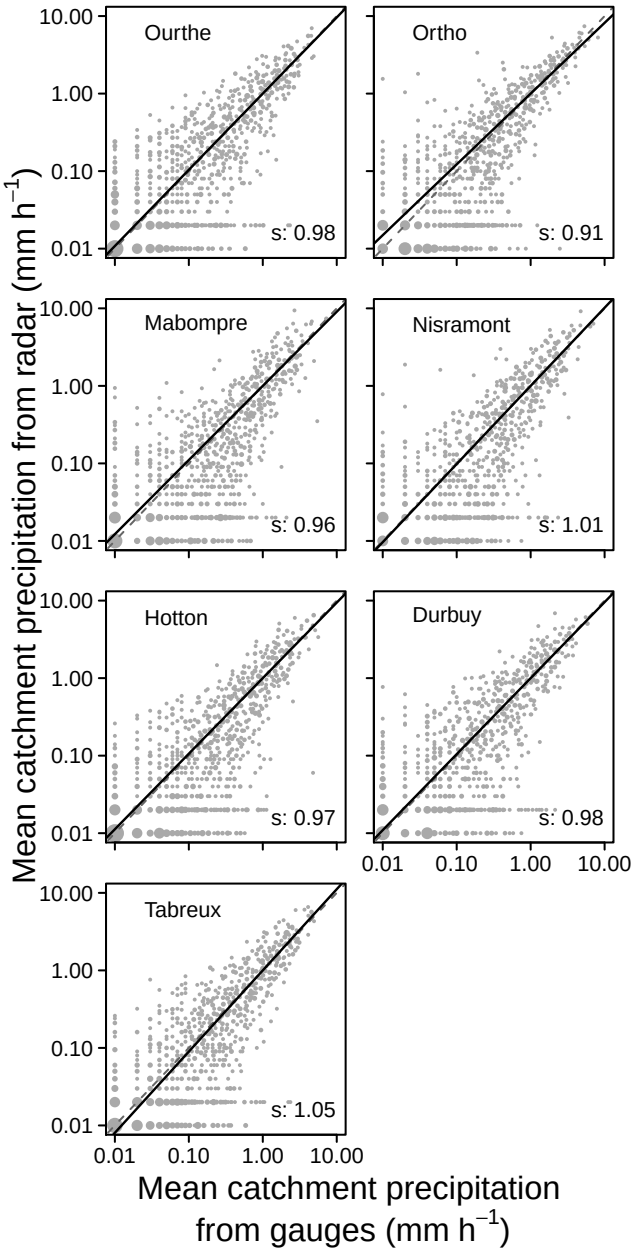

Figure 6.7: Comparison of hourly rainfall accumulations as estimated by the weather radar and from rain gauges for the 7 different catchments for the half-year winter period. The size of a dot indicates the density of the original data.

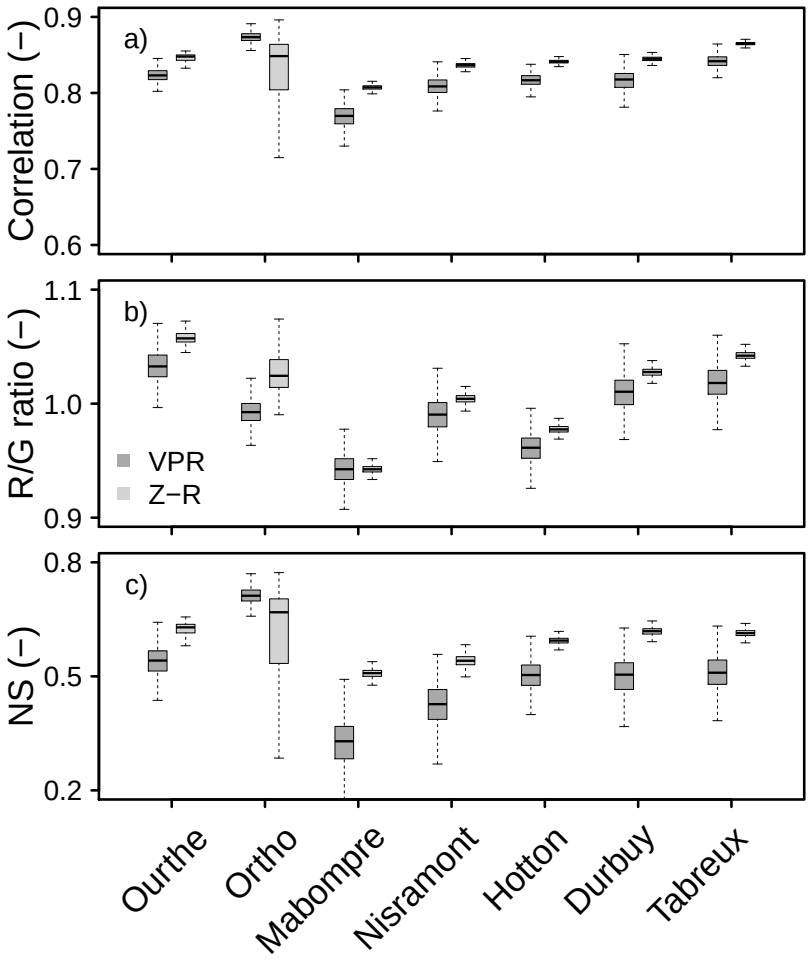

Figure 6.8: Half-year uncertainty estimates as obtained from 1000 bootstrap samples, expressed in terms of hourly correlation (a), radar/gauge ratio (b), and the Nash-Sutcliffe (NS) statistic (c) based on estimated VPR and Z–R variability for the 7 different catchments.

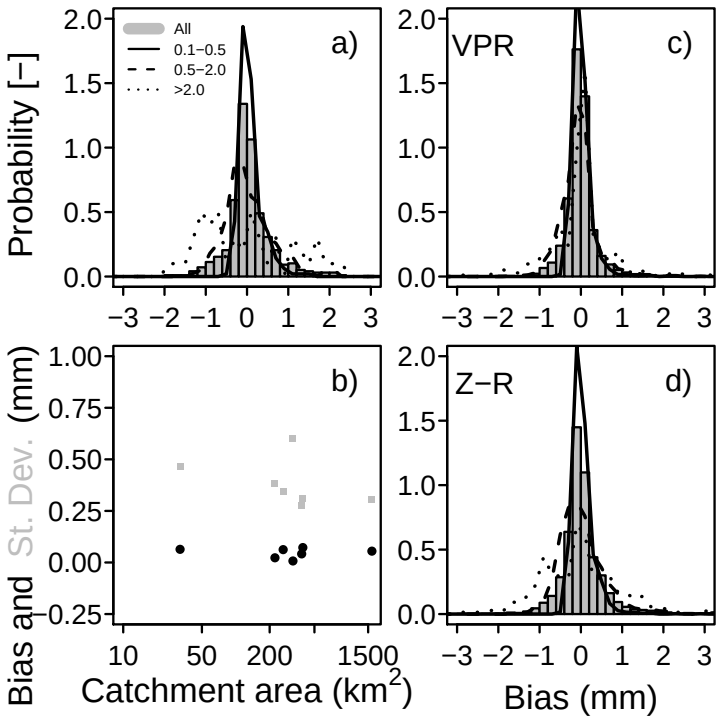

Figure 6.9: Similar to Fig. 6.3 for the half-year radar and rain gauge hourly catchment mean precipitation estimates. In panel (b) the mean (black dots) and standard (gray dots) of the bias are presented as a function of catchment size.

In Fig. 6.9c and d the error distribution using the optimal radar realizations due to variability in VPR and Z–R relation is shown. As expected, the optimal ensemble member leads to a narrower distribution with a mean closer to zero. The uncertainty generated by both radar ensemble methods is given in Fig. 6.10. The spread of the distribution decreases slightly with precipitation intensity, in line with the individual radar-gauge measurements (see Fig. 6.6). In addition, at the catchment scale, the realizations generated on the basis of VPR variability yield larger uncertainty ranges varying between 0.51–0.74, which corresponds to a measurement uncertainty of 26–37% (see Table 6.5). The ensemble generated on the basis of Z–R variability varies between 0.19–0.23 for the different catchment sizes, indicating a mean catchment uncertainty of 10–12%. From Fig. 6.10b it can be observed that these values are independent of catchment size.

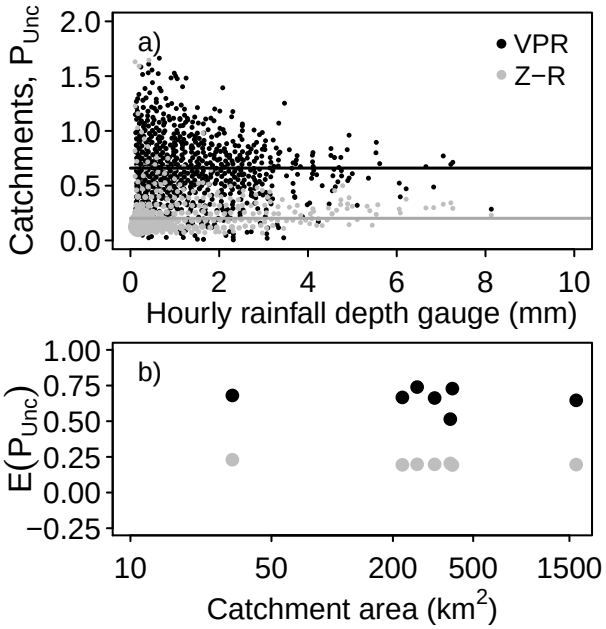

Figure 6.10: Upper panel presents the hourly catchment mean relative radar precipitation uncertainty estimate (P_{Unc}, see Eq. 6.6) obtained from taking the uncertainty in VPR (black) or Z–R (gray) into account (similar to Fig. 6.4). In the lower panel, the hourly estimates E(P_{Unc} for each of the 7 catchments are presented as a function of catchment size, taking the uncertainty in VPR (black) and Z–R (gray) into account. In the upper panel the size of a dot indicates the density of the original data.

Table 6.4: Half-year mean hourly bias (mm) and standard deviation (in brackets) between catchment averaged corrected weather radar and rain gauge precipitation estimates for the 7 different catchments. Last two columns provide the catchment mean relative radar precipitation uncertainty estimate (P_{Unc}) obtained from taking the uncertainty in VPR or Z–R into account.

	Intensity range (mm h^{-1})				E(P_{Unc})	
	All	0.1-0.5	0.5-2.0	> 2.0	VPR	Z–R
Ortho	0.04 (0.52)	0.07 (0.36)	0.05 (0.54)	-0.14 (0.54)	0.51	0.20
Mabompré	0.01 (0.78)	0.00 (0.27)	0.00 (0.71)	0.05 (0.71)	0.66	0.20
Nisramont	0.06 (0.68)	0.05 (0.34)	0.08 (0.73)	0.06 (0.73)	0.68	0.23
Hotton	0.02 (0.62)	0.02 (0.23)	0.06 (0.68)	-0.09 (0.68)	0.67	0.19
Durbuy	0.06 (0.59)	0.07 (0.28)	0.07 (0.65)	-0.01 (0.65)	0.74	0.20
Ourthe	0.06 (0.55)	0.08 (0.28)	0.04 (0.60)	-0.01 (0.60)	0.65	0.20

6.4.3 Hydrological potential of weather radar

In the previous sections the quality of the radar to measure precipitation and the impact of both radar precipitation ensemble generation methods was analyzed. Overall, corrected weather radar and rain gauge data correspond well, where the variability in VPR gives rise to a larger uncertainty in the precipitation estimates than the variability in the Z–R relationship. In the current section, the application of weather radar data and the associated precipitation uncertainty is assessed within a rainfall-runoff modeling setting.

Figure 6.11 presents the TOPMODEL discharge simulations of the Ourthe catchment for the period considered. These results are obtained using both the uncertainty sources in the radar rainfall estimates (from 50 ensembles based on VPR and Z–R variability) and using the 200 optimal parameter sets of the rainfall-runoff model (see Table 6.1). In case rain gauge data are used as input, only the hydrological model parameter uncertainty is taken into account.

In general, it can be observed from Fig. 6.11 that TOPMODEL is able to simulate the observed discharge of the Ourthe for either type of precipitation input quite well. This is also shown in Table 6.5, where maximum Nash-Sutcliffe (NS) statistics are given for a given precipitation time series in combination with a given parameter set. Based on Fig. 6.11a it can be observed that a considerable fraction of uncertainty in the simulated discharge response originates from variability in the optimal parameter set. However, not a single parameter set is able to generate the observed peak discharge (grey regions). When taking the uncertainty in the observed radar precipitation values into account as well, simulated peak discharge ranges do encompass the observed values.

Table 6.5 presents the median simulated peak discharges ($\mathrm{Qp}_{S,50}$) and their uncertainty range as given by the 1st ($\mathrm{Qp}_{S,1}$) and 99th ($\mathrm{Qp}_{S,99}$) percentiles. In case the observed peak values lie within the simulated uncertainty ranges, these values are presented in bold. Using both versions weather radar ensembles, this specifically holds for the Ourthe as a whole (as was also shown in Figs. 6.11b and c) and for the subcatchment of Mabompré using the ensemble generated on the basis of VPR variability. For all other subcatchments all of the different input time series lead to simulated peak values smaller then the observations. However, simulations based on the weather radar precipitation ensembles provide a much better resemblance in terms of peak discharges.

For each hourly timestep, the relative uncertainty of the simulated discharges Q_{Unc} (see Eq. 6.7) as a function of the observed discharge is

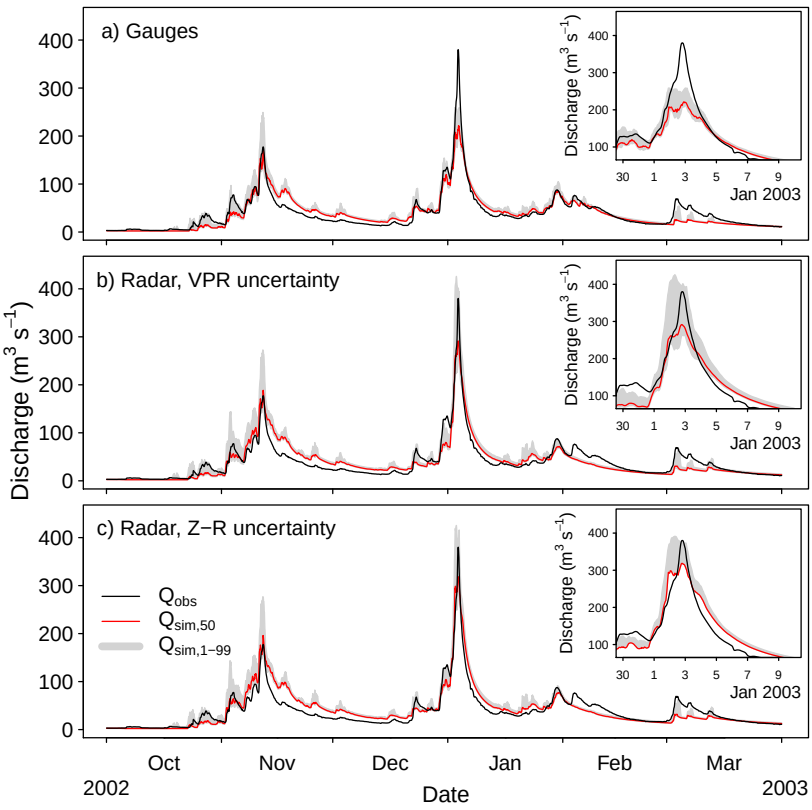

Figure 6.11: Discharge observations and simulations for the Ourthe catchment as performed by TOPMODEL using the 50 optimal parameter sets for the three different types of precipitation input. The median of the simulated values is given by the red line, while the uncertainty range as represented by the 1st and 99th percentiles is given by the gray band. Insets show details of model performance during peak discharge.

Table 6.5: Half-year observed (Obs) and simulated discharge statistics (S) using the three different types of precipitation input based on the 50 optimal parameter values of TOPMODEL for the 7 different catchments. Qp_{Obs} are the observed peak flow dischages ($m^3\ s^{-1}$), NS the Nash-Sutcliffe statistic, $E(Q_{Unc}$ the mean relative simulated runoff uncertainty (see Eq. 6.7). The simulated peak flow uncertainty ranges are given by $Qp_{S,N}$ for the different simulations, where N indicates the given percentile. Cases for which the observed peak discharge falls within the simulated uncertainty range are given in bold.

		Ourthe	Ortho	Mabompré	Nisramont	Hotton	Durbuy	Tabruex
	Qp_{Obs}	380	130	98	237	269	315	380
Gauges	NS	0.87	0.83	0.82	0.87	0.88	0.93	0.91
	$Qp_{S,50}$	234	97	76	179	229	278	331
	$Qp_{S,1}$	207	84	69	175	216	272	302
	$Qp_{S,99}$	251	110	83	183	239	282	338
	$E(Q_{Unc})$	0.18	0.14	0.18	0.05	0.07	0.03	0.06
VPR	NS	0.83	0.84	0.81	0.88	0.89	0.91	0.89
	$Qp_{S,50}$	331	84	107	203	254	304	352
	$Qp_{S,1}$	**250**	68	**82**	198	239	296	300
	$Qp_{S,99}$	**397**	103	**139**	212	264	311	366
	$E(Q_{Unc})$	0.21	0.15	0.22	0.05	0.09	0.03	0.08
$Z-R$	NS	0.81	0.82	0.76	0.88	0.88	0.9	0.87
	$Qp_{S,50}$	354	90	117	199	249	296	353
	$Qp_{S,1}$	**256**	76	99	194	231	289	308
	$Qp_{S,99}$	**391**	103	135	206	258	299	359
	$E(Q_{Unc})$	0.19	0.15	0.19	0.05	0.08	0.03	0.07

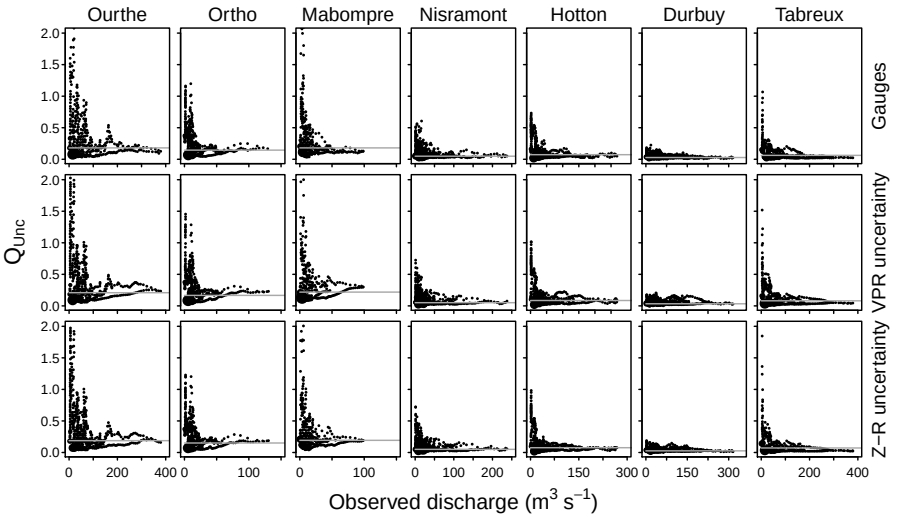

Figure 6.12: Simulated relative discharge uncertainty Q_{Unc} by TOPMODEL for the 50 optimal parameter sets using the three different types of precipitation input for the different basins w.r.t. the observed discharges. The size of a dot indicates the density of the original data.

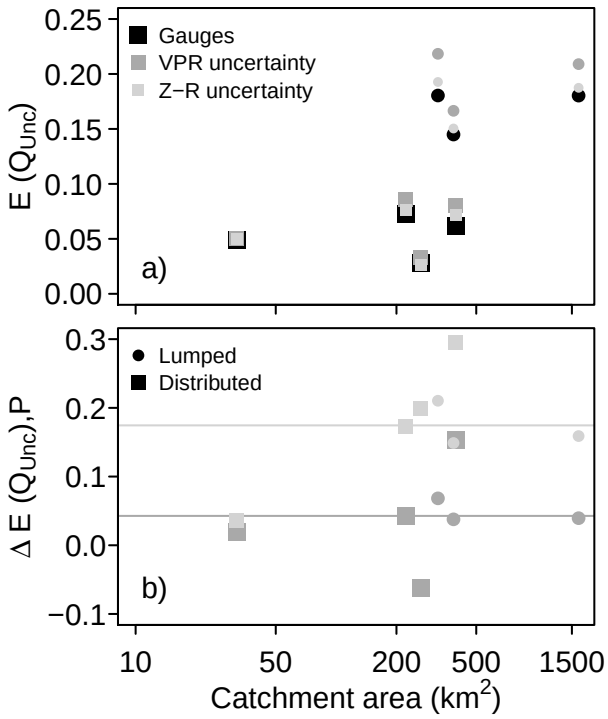

Figure 6.13: Upper panel shows the mean relative discharge uncertainty as simulated by TOPMODEL using the 50 optimal parameter sets for the three different types of precipitation input (similar to the horizontal lines in Fig. 6.12). Lower panel provides the relative additional runoff uncertainty obtained when taking precipitation uncertainty into account.

given in Fig. 6.12. Smaller discharges generally give rise to larger uncertainty ranges, similar to that observed for precipitation (see Figs. 6.6 and 6.10). In Fig. 6.13a the mean catchment discharge uncertainty (similar to the red lines in Fig. 6.12) is presented as a function of catchment size. At first sight, relative discharge uncertainty seems to increase with catchment size, similar to the observations of *Carpenter and Georgakakos* (2004). However, differentiation between the lumped and the distributed implementation shows that for a given implementation, the overall uncertainty shows a rather constant behavior. More specifically, in case the upstream mean simulated dicharge values are used as input, overall mean uncertainty values are smaller.

From Fig. 6.13a as well as Table 6.5 it can further be observed that discharge uncertainty increases when radar rainfall ensembles are used as input. However, their overall increase is limited as shown in Fig. 6.13b, which is obtained by taking the ratio between the mean discharge simulation uncertainty using the weather radar ensembles with respect to that obtained from using the rain gauge information. The added uncertainty due to the precipitation ensembles is rather constant with catchment size. In particular, the added uncertainty associated with variability of the VPR or Z–R relation is found to be 18% and 5%, respectively.

6.5 Discussion

6.5.1 Precipitation uncertainty generation

The results presented in the current chapter show that when properly accounting for all known dominant sources of error affecting weather radar rainfall estimates, precipitation estimates correspond well to those obtained from in situ rain gauge measurements. Chapter 2 already noted the importance of taking different sources of error into account, however, results presented there were not as promising. In the current study, further improvements in the quality of the weather radar rainfall measurements are related to an improved VPR estimation method for each precipitation region separately (see Chapter 5) and the use of a specific precipitation type dependent Z–R relationship. Even though considerable differences between weather radar and rain gauge measurements still occur, from a hydrological perspective both provide precipitation estimates of comparable quality as shown in Figs. 6.3, 6.7 and 6.11. As such, any additional bias removal in the radar data using the rain gauge information becomes unnecessary for the studied winter period.

Instead, the goal of the current chapter has been to present two separate weather radar precipitation ensemble generation methods, accounting for uncertainty related to either reflectivity measurement errors (from VPR) or reflectivity conversion errors (from Z–R relations). Both uncertainty generation methods are able to account for the majority of the differences between radar and gauge measurement as shown in Figs. 6.5 and 6.9, and Tables 6.3 and 6.4.

It was decided not to combine both uncertainty generation methods, since the uncertainty in the VPR can be related to spatial and temporal variability in the drop size distribution and phase, giving rise to variability in the Z–R relationship. As such, both methods cannot

directly be merged since this would lead to an overestimation of the actual uncertainty. In practice, given the characteristics of the weather radar, additional sources of uncertainty can be expected, both having an additive (e.g. radar calibration and beam overshooting) and multiplicative (e.g. signal attenuation, partial beam shielding) impact. However, given the operational environment, the studied winter period and the implemented radar correction steps, we believe these additional sources of error only lead to limited additional uncertainty. As such, the two uncertainty generation sources here are considered to be dominant.

Given the fact that there is a relations between both VPR and Z–R uncertainty, one can hypothesize why the former leads to much larger uncertainty ranges in precipitation estimates even though the obtained variability in the latter results in values spanning most of the observed relationships obtained from disdrometer measurements (*Battan*, 1973). We expect that the generated VPR uncertainty leads to slight overestimations of the true uncertainty in the spatial VPR field. This is due to the fact that the estimated ratio profiles, as needed in Eq. 6.2, are not obtained simultaneously. Since the vertical behavior of the precipitation field changes continuously, small differences in sample times between different scans can lead to an overestimation of the true uncertainty. On the other hand, the current implementation of the Z–R uncertainty generation method is expected to underestimate the observed radar-rainfall uncertainty. As explained in Section 6.3.3, this is because no temporal consistency in the generated Z–R parameters is implemented in the current version of the algorithm.

6.5.2 Impact of precipitation uncertainty on runoff response

The use of corrected weather radar data for rainfall-runoff modeling leads to a similar performance as when applying rain gauge information. What is interesting about the current results is the relatively limited impact of radar rainfall uncertainty on the simulated hydrological response as compared to the uncertainty originating from parameter variability of TOPMODEL. The latter impact is much larger. On the other hand, this does not hold for the simulation of peak flows. For these situations, taking the impact of radar rainfall uncertainty into account leads to improved results. As such, from an operational perspective using precipitation ensembles improves forecast performance.

The fact that uncertainty in model parameters has a larger impact on the runoff uncertainty simulations than rainfall variability can partly

be attributed to the rather simple representation of TOPMODEL to estimate the hydrological response of the catchments. In reality the hydrological response of a catchment is rather complex. Next to that, since catchments behave as non-linear filters and precipitation has an intermittent character, large uncertainties in rainfall estimates are filtered out into a continuous runoff signal. This can also be observed when the results presented in Fig. 6.10 are compared to those in Fig. 6.13. Radar ensembles represent a total of 26-37% to 10-12% in terms of precipitation uncertainty for the variability from VPR and Z–R, respectively. However, this results in an additional mean runoff uncertainty of only 18% and 5%, respectively.

The fact that using radar rainfall ensembles improves peak flow estimates does not directly indicate that mean catchment rainfall originating from either rain gauge or radar measurements underestimates the true catchment rainfall input. During the days before the peak flow period, weather radar and gauge measurements correspond well (see Fig. 6.2 and Chapter 5). An alternative explanation can be related to the fact that none of the optimal parameter sets were specifically obtained by calibrating TOPMODEL on peak flows. As such, all parameters provide optimal results for the complete discharge time series, including low flow situations. This can lead to a general underestimation of peak flow response. Therefore, by using precipitation realizations that slightly overestimate the actual amount of precipitation, better peak flow estimates are obtained. These results indicate that a limited representativity of the hydrological model parameters can partly be corrected for using ensemble precipitation estimates.

A final important aspect to discuss is the dominant impact of the use of upstream discharge inflow within the distributed modeling framework. As explained in Section 6.2.2, the upstream inflows originate from the time series generated using the most optimal simulation response. Therefore, no uncertainty in simulated upstream input is taking into account. Any differentiation between simulations and observations upstream is therefore still observed downstream. Since the use of mean radar or gauge precipitation input has been shown to underestimate peak discharges (Fig. 6.11a), downstream peak discharges are underestimated as well. Additional uncertainty generated using the precipitation ensemble input on the downstream catchment response, provides insufficient variability to account for this underestimation (see also Fig. 6.13). However, it was decided not to use measured upstream discharges to assess all aspects of the hydrological model, as the use of an ensemble of

upstream inflows would result in too large computational demands and was considered to be beyond the scope of the current chapter.

6.6 Summary and conclusions

In this chapter different manners of generating precipitation ensembles from volumetric weather radar data and their potential for rainfall-runoff uncertainty modeling are assessed. There are two important motivations for the application of such an ensemble approach: 1) radar rainfall estimates are uncertain, 2) ensemble stream flow simulations provide a more complete representation of the model response by identifying both input and parameter uncertainty (e.g. *Carpenter and Georgakakos*, 2006; *Germann et al.*, 2009). However, compared to previous approaches, instead of employing purely statistical methods to generate precipitation uncertainty, in the current study two conceptual approaches are used that allow the generation of ensembles from volumetric weather radar data directly using the observed variability of the VPR and the Z–R relations. These data are used to simulate the hydrological discharge response of a 1600 km^2 catchment and 6 subcatchments using the conceptual TOPMODEL. Since an ensemble of 200 optimal parameter sets were available for rainfall-runoff simulations, an assessment of the interaction between rainfall and model parameter uncertainty could be made.

From these analyses the following main conclusions can be drawn:

1. In case one properly accounts for all dominant sources of error, weather radars are able to provide precipitation estimates with similar quality to those obtained from in situ rain gauge measurements. Any additional source of uncertainty associated with the difference between both instruments can for the major part be accounted for by generating precipitation ensembles based on the variability in either the VPR or the Z–R relation. At the point scale, these two methods generate an uncertainty of the estimated hourly radar rainfall amounts of around 40% and 15%, respectively, slowly decreasing when aggregating over larger regions. Uncertainty arising from variability in the VPR slightly increases with distance from the radar, as a result of the increase in sample volume and measurement height with range.

2. Because of the large correspondence, hydrological simulations with TOPMODEL using corrected weather radar data provides similar

results as when rain gauges are used, even though in the current study the former have not been bias-corrected using the latter. The additional uncertainty in the generated precipitation ensembles provide improved peak flow uncertainty estimates compared to using a single precipitation estimate alone. As such, the usage of precipitation ensembles both leads to improved mean catchment precipitation estimate and to an added uncertainty that accounts for the limited representativeness of hydrological model parameters.

3. In the current study, variability of the hydrological model parameters gives much larger simulated discharge uncertainty ranges than the uncertainty arising from the application of precipitation ensembles. For the complete winter period the additional uncertainty as a result of precipitation variability is much smaller ($< 20\%$), than the uncertainty related to the equifinality of the hydrological model parameters. These results show the dominant impact of catchments to filter the precipitation input, leading to a decrease in input uncertainty in the discharge response by halve.

4. For the distributed simulation cases, the inflow from the upstream channel network has a significant reducing impact on the simulated discharge uncertainty. This can be related to the fact that a single upstream discharge input value was used, instead of applying additional simulated variability. For the medium-sized catchments analyzed here, these results show the dominant importance of the channel network in the hydrological response of catchments.

Based on these results, one might question the usefulness of precipitation ensembles, even though such procedures have been advocated in the literature (*Ciach et al.*, 2007; *Villarini and Krajewski*, 2010). However, it should be emphasized that the results presented here were obtained during a winter period when the majority of precipitation has relatively small intensities and spatial variations are relatively small. As such, threshold behavior in the hydrological response, possibly moving from complete infiltration to overland flow are not expected to occur based on the applied precipitation ensembles.

CHAPTER 7

Discussion

7.1 Introduction

A central theme of this thesis has been to focus on the impact of correcting volumetric weather radar measurements for all known sources of error, so that its precipitation product becomes directly useful for hydrology without using rain gauges for adjustment. The results presented in Chapters 5 and 6 show that in case the data are corrected properly for the most dominant individual error sources, the radar rainfall product has a similar quality as can be obtained from in situ rain gauge measurements, although considerable differences between both devices remain. It should be noted that these results were obtained during a winter half year, when the majority of precipitation systems observed are of stratiform type and have a relatively uniform character.

Another central aspect of this thesis is the lack of knowledge on the actual Z–R relation. As shown in Chapter 3, the parameters of this relation vary between and during different precipitation events. Therefore, applying a single relationship for a given precipitation type will result in considerable uncertainty. Unfortunately, the impact of ground clutter, partial beam blockage and the distance between the weather radar and disdrometer limited the possibilities to investigate the relationship between the three-dimensional character of the precipitation field as measured by the radar and the raindrop samples taken by the disdrometer. However, it is fully recognized and advocated in this the-

sis that the quality of the weather radar rainfall product can only be improved by considering these small-scale precipitation properties.

This chapter provides some further thoughts on these aspects by analyzing volumetric weather radar measurements in combination with disdrometer data for a mesoscale convective system (MCS). This event was observed on August 25-27, 2010 in The Netherlands and led to some of the largest precipitation sums ever recorded in this country (*Brauer et al.*, 2011; *van de Beek et al.*, 2013). Weather radar precipitation measurements taken within an MCS are known to be a challenge (*Zhang and Smith*, 2003; *Delrieu et al.*, 2005; *Borga et al.*, 2007; *Krajewski et al.*, 2010), since these systems show considerable small-scale variability in the precipitation characteristics. Therefore, the impact of the chain of weather radar correction steps as developed as part of this thesis are assessed and compared to the operational radar rainfall product. Next to that, given the fact that the employed weather radar and disdrometer are at close distance, and that radar visibility aspects do not cause a major problem, it is possible to provide a first assessment on the link between the three-dimensional properties of the precipitation field and the rainfall measurements taken at the surface.

Based on the analyses presented here, an attempt is made to put the results of this thesis in a proper perspective and assess their benefits and limitations. This subsequently leads to a number of suggestions on how to possibly proceed with further improving the quality of radar rainfall measurements for hydrological applications.

7.2 Data availability and event description

The Royal Netherlands Meteorological Institute (KNMI) operates two weather radars, one in De Bilt and one in Den Helder in the Netherlands. Only data from the former radar are analyzed here. The weather radar in De Bilt is a C-band Doppler radar located on top of a tower at 44 m above sea level and operating at 5.6 GHz (i.e. at a wavelength of 5.3 cm). Volumetric information is obtained every 5 minutes for 14 scan elevations (0.3°, 0.4°, 0.8°, 1.1°, 2.0°, 3.0°, 4.5°, 6.0°, 8.0°, 10.0°, 12.0°, 15.0°, 20.0°, and 25.0°). In close vicinity of the radar (within 1 km) an OTT Parsivel disdrometer is located, which provides information on the observed raindrop sizes and their fall velocities at a one-minute resolution. This disdrometer is similar to one used to analyze the DSD data observed in the southern part of France in Chapter 3. Next to that, at a national level information from a network of 34 rain gauges operated

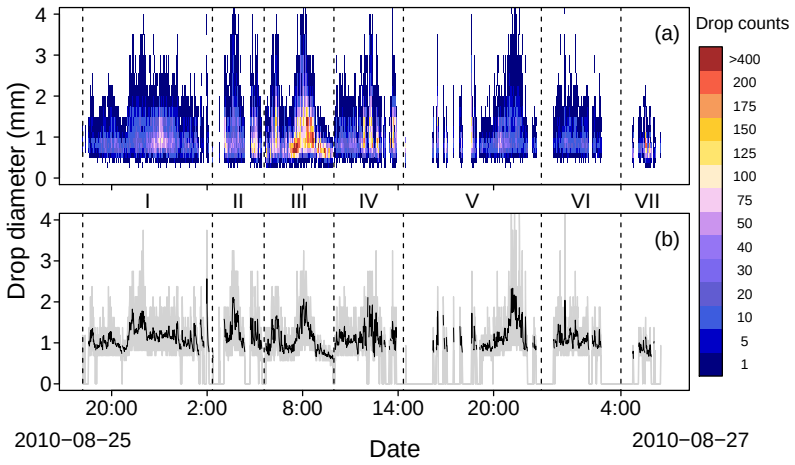

Figure 7.1: Upper panel shows the number of raindrops per diameter size interval as sampled by the disdrometer for the event on 25-27 August, 2010. Also indicated are the 7 different temporal phases, between which considerable variability in the DSD is observed. Lower panel presents the median (black line) and the 10-90th percentile drop diameter.

by KNMI is available. These data are aggregated to hourly intervals and will be compared to the precipitation measurements as obtained from the weather radar.

Between 25 and 27 August 2010 a long-duration mesoscale convective system was observed above the Netherlands. The event originated from a narrow band of low pressure passing over the country from the direction of the English Channel towards Southern Denmark, in between high pressure zones over Southern Europe and Scotland. In the eastern part of the Netherlands, total event accumulations were extreme leading to local event accumulations exceeding 150 mm (*Brauer et al.*, 2011).

At De Bilt this event led to over 18 hours of near-continuous precipitation, resulting in an accumulation exceeding 50 mm. The time series of the number of drops per diameter class as observed by the disdrometer are given in Fig. 7.1.

Based on visual inspection of these drop size data, it is decided to divide this time series into seven different sub-event periods. The transition between the different periods is given by the dashed lines and Roman numbers in Fig. 7.1. To provide additional information on the specific spatial patterns of the rainfall field, for each of these 7 peri-

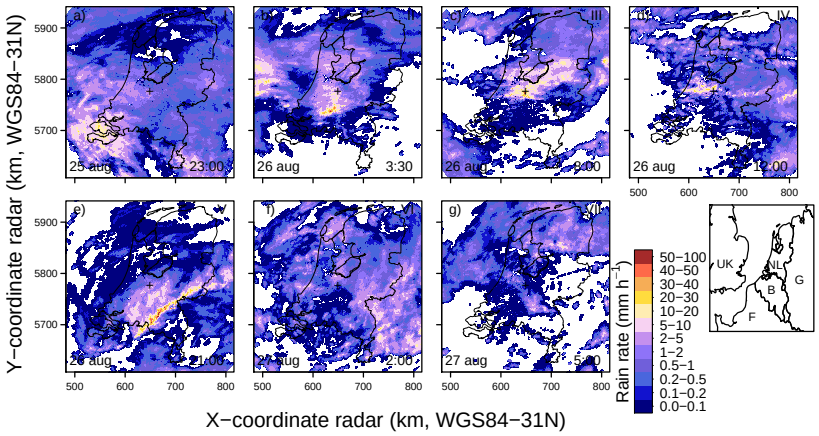

Figure 7.2: Each panel shows a temporal snapshot of the spatial precipitation field as observed by radar for each of the 7 different phases as identified in Fig. 7.1. The date and time of each snapshot are given at the bottom left and right of each panel. The location of the radar is indicated by the +. The map presents the location of The Netherlands within Western Europe.

ods an example of the two-dimensional rainfall field as measured by the weather radar is presented in Fig. 7.2.

The mesoscale convective system (MCS) as shown in panels a-b of Fig. 7.2 consists of widespread rainfall containing mostly stratiform precipitation (as will be shown later). Locally embedded convective precipitation as part of this MCS is observed close to the radar during phase III (Fig. 7.2c). During phase IV (Fig. 7.2d) the convective activity has transformed into a squall-line moving in an eastward direction situated just North of the radar. Because of this, only some remnants of this line of convective activity were observed by the disdrometer during this phase. During the afternoon of August 26 another squall-line of convective precipitation moves from the South-West in a North-Eastward direction. However, this system passes East of the radar. The final phases of the storm again consist mainly of widespread precipitation moving in an Eastward direction.

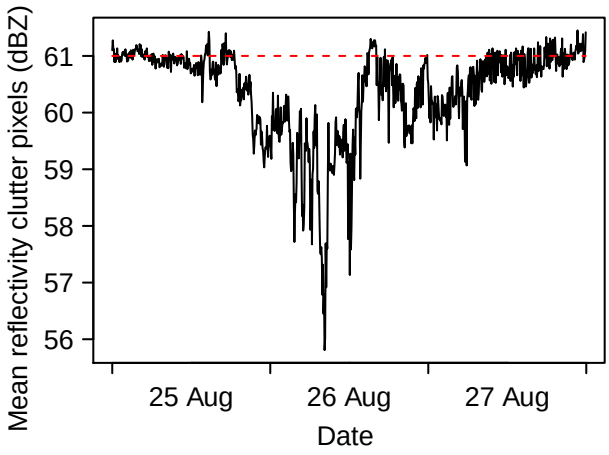

Figure 7.3: Total wet radome attenuation as obtained from the mean of the reflectivity value of all identified clutter pixels with a dry weather reflectivity exceeding 55 dBZ for the event on 25-27 August, 2010.

7.3 Volumetric error correction and rainfall estimation

7.3.1 Weather radar error correction steps

The operational weather radar product as provided by KNMI uses a Doppler clutter filter to identify stationary echoes. This filter is applied to all pixels, and can cause an underestimation of precipitation-related reflectivity. Next, the reflectivity information for all elevation scans is linearly interpolated in altitude to the 1500 m level, resulting in a two-dimensional polar weather radar product (a so-called constant altitude plan position indicator (CAPPI)). This product is transformed into Cartesian grid by selecting the individual polar pixel lying closet to the Cartesian pixel. For operational purposes, these data are then bias-corrected using rain gauge data. However, this latter procedure is not available in real-time. Therefore, the non-bias corrected operational product will be compared to the result of implementing a detailed radar error correction procedure.

For the current event different sources of error possibly affecting the quality of the weather radar rainfall measurements are identified. In line with Chapter 6 the following steps are identified to correct for individual sources of error:

1. *Clutter (Clu)* – Clutter and anomalous propagation are identified using both a fixed dry weather clutter map and applying the algorithm originally developed by *Steiner and Smith* (2002) to identify variable clutter sources. For the current event anomalous propagation was not observed, however, the latter algorithm is in principle able to detect and correct for this.

2. *Radar calibration (RaC)* – The sensitivity of the receiver and the alignment of the radar at KNMI is operationally monitored by using the position of the sun (*Holleman et al.*, 2010). Detailed analysis shows that during the current event radar reflectivities are underestimated by 1 dBZ.

3. *Precipitation region and type identification* – RoCaSCA is used to identify individual precipitation regions for which the reflectivity exceeds 7 and 23 dBZ (see Chapter 5). Next, the volumetric information is used to identify convective, stratiform and undefined precipitation type (*Steiner et al.*, 1995; *Sánchez-Diezma et al.*, 2000; *Delrieu et al.*, 2009). For the current event, the basic threshold for convection was set at 35 dBZ.

4. *Path-integrated attenuation (Att)* – Based on the disdrometer data in combination with the identified types of precipitation from the volumetric radar data, the parameters of the power-law relations between reflectivity and specific attenuation $Z = c\ k^d$ are obtained for each type of precipitation. These parameters are given in Table 7.1.

5. *Wet radome effect (WRa)* – Given the long duration of precipitation observed at the radar site, the occurrence of a wet radome results in an underestimation of the atmospheric reflectivity. To assess the impact of wet radome effects, the time series of the mean reflectivity of all fixed clutter pixels with a dry weather reflectivity Z exceeding 55 dBZ is presented in Fig. 7.3. From this figure it can be observed that the total amount of wet radome attenuation is considerable. Therefore, for each time step volumetric weather radar data are corrected for signal attenuation using the estimates obtained from the fixed background clutter pixel signal loss.

6. *Vertical profile of reflectivity (VPR)* – The identification method as presented in Chapter 5 is used to correct stratiform and undefined precipitation for the impact of VPR.

Table 7.1: Parameters of the reflectivity-rain rate relation $Z = A\,R^b$ and the reflectivity-specific attenuation relation $Z = c\,k^d$ as estimated from the observed disdrometer data for the complete event as well as for each individual precipitation type for the event on 25-27 August, 2010.

Type	A	b	c (x10^6)	d
All	229	1.28	1.04	1.334
Convective	404	1.25	1.24	1.394
Non-Stratiform	163	1.17	0.51	1.258
Stratiform	268	1.34	0.45	1.131

7. *Radar reflectivity-rainfall rate relation (Z–R)* – Instead of applying the Marshall-Palmer relation $Z = 200\ R^{1.6}$ (*Marshall et al.*, 1955) which is applied operationally, the disdrometer data are used to identify the optimal Z–R relation for a given rainfall type. The parameters of this relation are given in Table 7.1.

7.3.2 Spatial accumulations and radar-gauge comparison

In Fig. 7.4 the impact of each individual error correction step on the total event rainfall accumulations is presented. Maximum accumulations in the eastern part of the Netherlands for the operational product lie between 40 and 50 mm. As mentioned above, actual accumulation observed within this region exceeded 150 mm. As such, the operational product leads to a strong underestimation of the observed precipitation. From an operational perspective, such a performance can have a detrimental impact on whether the appropriate warnings and precautions can be taken by hydrological authorities, especially when it comes to responding properly during such an extreme precipitation event.

The overall underestimation by the operational product resulted from the fact that, except for clutter, none of the individual error sources as identified above were corrected for. Next to that, the implemented operational clutter Doppler filter was too strict, removing part of the reflectivity from actual precipitation. This resulted in a further decrease in the estimated precipitation. When correcting for each individual error source, the weather radar rainfall product changes completely. Correcting for each individual error source leads to an increase in the total

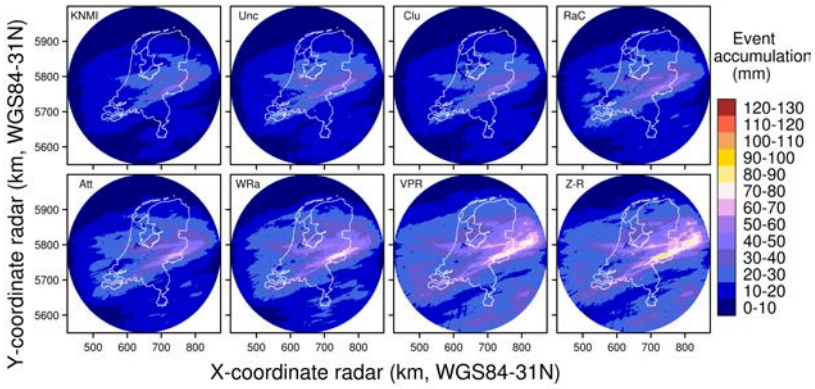

Figure 7.4: Spatial overview of the accumulated precipitation as estimated from the weather radar for the event on 25-27 August, 2010. The operational product as distributed by the Royal Netherlands Meteorological Institute (KNMI) is given in the top-left panel. Other panels indicate the impact of each additional radar error correction step on the total storm accumulations. These correspond to no correction (Unc), clutter identification (Clu), radar calibration (RaC), path-integrated attenuation (Att), wet radome effects (WRa), vertical profile of reflectivity (VPR) and precipitation type specific reflectivity-rain rate relation (Z–R).

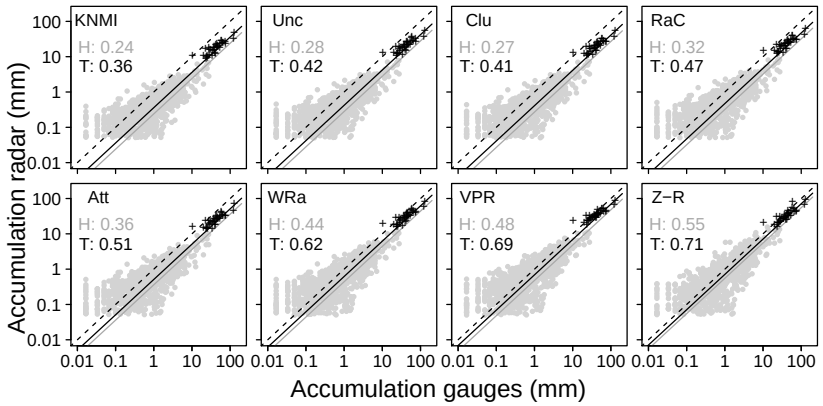

Figure 7.5: Comparison of rainfall accumulations from 34 rain gauges and the corresponding radar pixels for hourly (gray •) and total event (black +) interval for the event on 25-27 August, 2010. The operational product as obtained by the Royal Netherlands Meteorological Institute (KNMI) is given in the top left panel. Other panels indicate the impact of each additional radar error correction step. These correspond to no correction (Unc), clutter identification (Clu), radar calibration (RaC), path-integrated attenuation (Att), wet radome effects (WRa), vertical profile of reflectivity (VPR) and precipitation type specific reflectivity-rain rate relation (Z–R). The gray and black lines correspond to linear regression between the two for the hourly (H) and total event (T) interval, of which the slope is given in the legend. The dashed lines represent the 1:1 correspondence.

accumulation, as expected. The final corrected product, locally, leads to an estimated rainfall accumulation of about 120 mm for the eastern part of the Netherlands. Even though this value still underestimates the rain gauge observations, these results definitely show the positive impact of correcting the radar for each individual source of error. This is in agreement with what was shown in the remainder of this thesis when analyzing the impact of radar error correction for winter precipitation in Belgium. Also for the current event, the corrected weather radar rainfall product outperforms the operational product.

Figure 7.5 presents the comparison between rainfall accumulation from the 34 rain gauges and the corresponding radar pixels. Results are shown for hourly and total event accumulations. Each individual correction step yields an incremental improvement in the quality of the radar

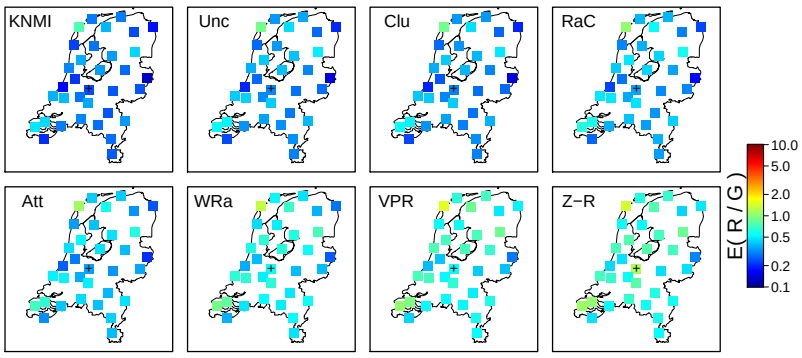

Figure 7.6: Spatial overview of the mean ratio between the hourly rainfall accumulations for the 34 radar and rain gauge pairs for the event on 25-27 August, 2010. The operational product as obtained by the Royal Netherlands Meteorological Office (KNMI) is given in the topleft panel. Other panels indicate the impact of each additional radar error correction step. These correspond to no correction (Unc), clutter identification (Clu), radar calibration (RaC), path-integrated attenuation (Att), wet radome effects (WRa), vertical profile of reflectivity (VPR) and precipitation type specific reflectivity-rain rate relation (Z–R).

precipitation measurements. Linear regression results using the hourly estimates still show a large underestimation by the weather radar. This is caused by a large underestimation by the radar for a number of individual gauge locations during hours when high precipitation intensities were observed (exceeding 10 mm h^{-1}). The impact of these individual hours decreases when focusing on the total event accumulations. However, total event accumulations are still underestimated.

It is recognized here that from a hydrological perspective, correct estimation of the large hourly precipitation amounts is important, since extreme precipitation events can have a severe societal and economic impact. As such, even though the impact of the algorithms implemented here lead to a considerable quality improvement in weather radar rainfall estimates, there is still room for further improvements. Therefore, to assess the limitations of the currently implemented procedures, Figs. 7.6 and 7.7 provide spatial information on the mean ratio of the individual radar and gauge measurements for the hourly and event rainfall accumulations, respectively. Although precipitation accumulations are

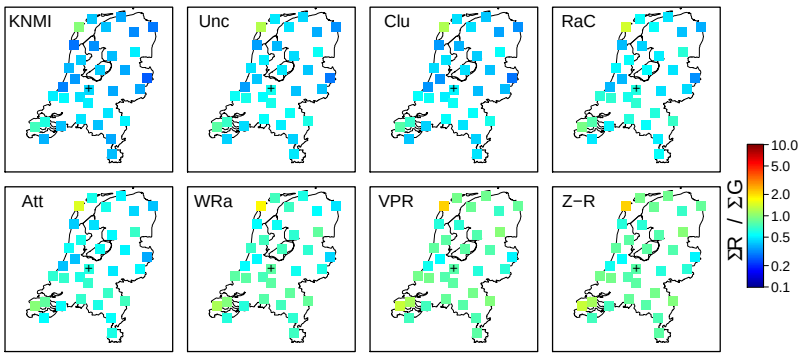

Figure 7.7: Spatial overview of the ratio between the total event rainfall accumulations for the 34 radar and rain gauge pairs for the event on 25-27 August, 2010. The operational product as obtained by the Royal Netherlands Meteorological Office (KNMI) is given in the topleft panel. Other panels indicate the impact of each additional radar error correction step. These correspond to no correction (Unc), clutter identification (Clu), radar calibration (RaC), path-integrated attenuation (Att), wet radome effects (WRa), vertical profile of reflectivity (VPR) and precipitation type specific reflectivity-rain rate relation (Z–R).

underestimated by the radar at almost every location, a slightly larger underestimation occurs in the middle of the Netherlands for a horizontal band moving from East to West, just North of the radar. This band corresponds with the direction of the squall-line as shown in panel c of Fig. 7.2.

One possible explanation might be the underestimation of the amount of signal attenuation in the forward and backward direction of the squall-line. The parameters of the Z–k relation for the convective type of precipitation were obtained from disdrometer measurements taken close to the radar. Even though some convective activity was observed at the location of the radar (phase III in Fig. 7.1), these data do not originate from the squall-line itself. Also, no DSD data were sampled as part of the second squall-line observed in the afternoon of August 26 (see Fig. 7.2e). This could have led to a further underestimation of the amount of attenuation in the eastern part of the Netherlands, the region were the largest hourly accumulations were observed.

Another possible explanation related to this issue is related to the

applied reflectivity-rain rate relations. In case the DSD derived Z–R relation for convective type of precipitation is not representative for the squall-line, this can lead to further underestimations of the precipitation intensity by weather radar.

7.4 Radar rainfall error identification - Where to go from here?

The results presented in the previous section showed a large improvement in the quality of the weather radar rainfall data, after correcting for each individual source of error. However, considerable bias with respect to in situ rain gauge measurements remains in the corrected weather radar data. It was mentioned above that a possible explanation could be related to the employed disdrometer data, which were sampled close to the weather but might not be representative for both squall-lines observed during this event.

Another aspect that has not been taken into account so far, but which has been a central focus of this thesis, is the uncertainty associated with the weather radar measurements. In order to provide some more detail on both of these aspects, Sections 7.4.1 and 7.4.2 focuses on the weather radar observations taken close to the radar in combination with the drop size measurements (see Fig. 7.1). Based on these analyses, a number of possible directions can be defined on how to further improve volumetric weather radar measurements.

7.4.1 Radar rainfall uncertainty estimation

A large part of this thesis has been focusing on the estimation of the amount of uncertainty around the measured radar reflectivity value. Two methods were used to obtain an estimate of this, either based on the variability of the VPR or on the uncertainty in the Z–R relation. However, both uncertainty estimates are affected by small-scale variability in the observed reflectivity field as well as by the temporal sampling properties of the radar (see also Sections 5.5 and 6.5). To gain more understanding on these aspects, the reflectivity values as measured by radar and obtained from the disdrometer for the complete event and for the 7 different phases are presented in Fig. 7.8. The median reflectivity value of the radar data was obtained from all volumetric reflectivities measured between 500-1000 meter elevation within a distance of 2 km from the radar. The underestimation by the radar as compared to the

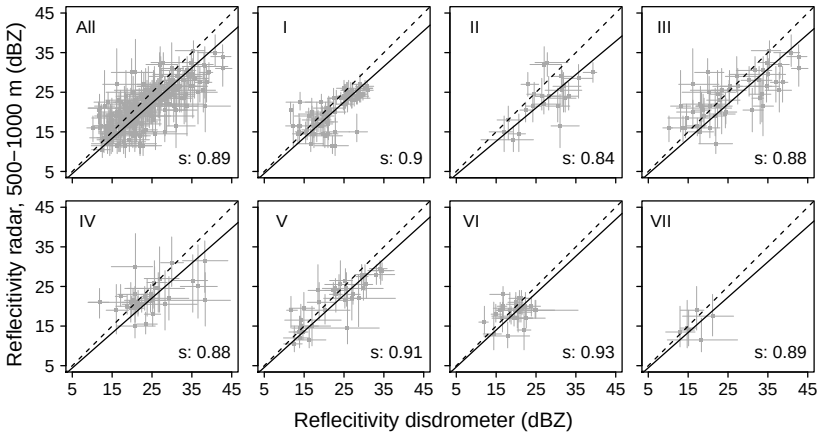

Figure 7.8: Comparison between mean one-minute reflectivity obtained from the DSD data for five-minute interval and the median five-minute reflectivity value estimated from all volumetric weather radar measurements at elevations between 500 and 1000 meter within 2 km from the radar. Error bars for DSD data indicate the minimum and maximum one-minute reflectivity observed during the five-minute interval, while error bars for the weather radar measurements present the observed 10th and 90th reflectivity percentile. Different panels represent the complete event (All) and the 7 different phases as identified in Fig. 7.1. The slope of the linear regression line between both properties is given by s, while the dashed line represents the 1:1 relation.

disdrometer measurements taken at the surface can be related to radar calibration and wet radome attenuation issues, which were shown above to affect the radar measurements. However, it can be observed that within a given five-minute time step, the overall variability in reflectivity values is considerable within such a small region. Next to that, when comparing different individual one-minute reflectivity values for a given five-minute interval, again considerable variability is observed. Therefore, given the fact that volumetric measurements at a given location are not continuous, reflectivity measurements will give rise to a considerable measurement uncertainty, even when weather radar data are perfectly corrected for all possible sources of error and use is made of the optimal Z–R relation.

Further away from the radar, a large measurement volume results in reflectivity measurements which are an integral of these small scale vari-

ations in drop size distributions. However, given the fact that the radar measurement is performed during a small time-step, it is difficult to assess how representative this measurement is for the five-minute interval. Fortunately, both of the methods presented in this thesis partly account for this type of uncertainty, limiting its overall impact, especially, when aggregating the weather radar measurements over time and space. This was also observed when comparing point-scale to the catchment-scale measurements in this thesis (see Chapters 2 and 6). However, it is recognized that it is important to consider the small-scale variability aspect when comparing weather radar and rain gauge data.

7.4.2 Precipitation microphysics - Impact of spatial and temporal variations

To provide additional details on these small-scale precipitation aspects, in line with Chapter 3, the scaling law theory is used to assess the properties of the observed DSDs (*Sempere-Torres et al.*, 1994, 1998; *Uijlenhoet*, 1999). In Fig. 7.9 the normalized spectra and the scaled raindrop size distribution $g(x)$ for the gamma and exponential distribution are presented for the complete event as well as for each individual phase. From both distributions the parameters of the Z–R relation are derived (see Section 3.3 for more detail). For each of the different phases a different Z–R relation is obtained. This immediately provides some indications on the uncertainty that arises when using a single Z–R relation. In addition, it also motivates the use of an ensemble of Z–R relations to account for this uncertainty (see Chapter 6).

As explained in Chapter 3 the DSD varies between different precipitation types and meteorological origins. As such, these DSDs observed at the surface are the final result of continuous drop interactions aloft. Therefore, all volumetric weather radar data sampled within a distance of 30 km from the radar are used to obtain the contoured frequency by altitude diagram (CFAD), as originally developed by *Yuter and Houze Jr.* (1995b). For each phase, these CFADs are temporally accumulated as shown in Fig. 7.10. The dominant occurrence of stratiform precipitation can immediately be observed from these panels, as the clear appearance of a bright band is visible during almost all phases. Only for Phases III and VII its impact is less pronounced. During Phase III, as explained above, convective precipitation is observed in the region surrounding the radar, while Phase VII originates from the rain-out phase of the widespread system. The normalized DSDs for these panels also show marked differences compared to the other phases. Both have a

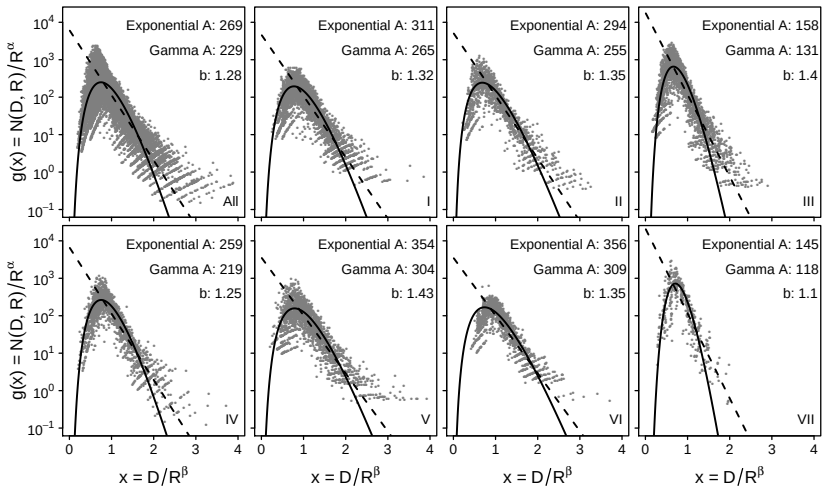

Figure 7.9: Scaling analysis of the drop size distributions for the event on 25-27 August, 2010. Different panels show the normalized spectra for the complete event (All) and for the 7 different phases as identified in Fig. 7.1. The scaled raindrop size distribution $g(x)$ for the gamma and exponential distribution is given by the solid and dashed lines. The prefactor A of the Z–R relations based on either distribution, as well as the exponent b for each period are shown in the legend.

much more pronounced concave shape (see Fig. 7.9). Also during phase IV the obtained Z–R parameters are different from the other stratiform phases and give rise to both a smaller prefactor A and exponent b. However, these pronounced differences in the obtained DSDs are not reflected in the accumulated CFAD, which shows a similar shape and bright band pattern as observed during Phases I, II, V and VI. Only at the surface a considerably larger fraction of higher reflectivity values is observed. As mentioned above, during Phase IV a squall line passes North of the radar. Some remnants of this convective type of precipitation are observed at De Bilt and have been captured by the volumetric measurements. These are reflected in the observed rain drop size distributions, where in Fig. 7.1 during some instances quite a large number of drops is observed.

It was speculated in Chapter 3 that in case of convective precipitation, the high number concentration of raindrops and the influence of large vertical velocities leads to a large amount of raindrop interactions (*Ulbrich and Atlas*, 2007). This favors conditions during which an equi-

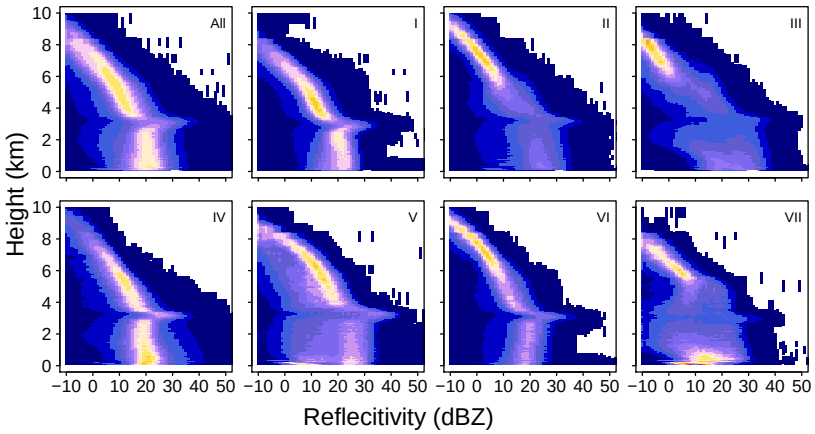

Figure 7.10: Accumulated Contoured Frequency by Altitude Diagrams (CFADs) (*Yuter and Houze Jr.*, 1995b) for the volumetric reflectivity data observed within a distance of 30 km from the weather radar for the event on 25-27 August, 2010. Different panels represent the complete event (All) and the 7 different phases as identified in Fig. 7.10.

librium state could be reached, resulting in a Z–R exponent b closer to 1 (*Atlas et al.*, 1999; *Prat and Barros*, 2009). For the current event this is not observed for Phase III. Even though this phase is most influenced by convective precipitation, for this phase the highest Z-R exponent was obtained. We expect that this results from the fact that the type of precipitation observed during this phase originates from a combination of both convective and stratiform precipitation, as Fig. 7.10 shows a slight bright band signature. The complete dataset observed during this phase consists of a mixture of precipitation types, leading to relatively larger value of the Z-R exponent, similar to the results presented in Fig. 3.9. For Phase VII an exponent close to one is observed. However, given the relatively low reflectivity values and the small rain drop concentrations, it is difficult to assess what gave rise to this low exponent value. A possible explanation is the relatively limited number of observations that were obtained during this phase. In case these originate from the same active remnant of the widespread system, with raindrop interactions taking place in a rather constant manner in time, the resulting temporal behavior of the observed DSD can be relatively constant as well, leading to a small value of the exponent close characteristic of a number-controlled situation.

7.4.3 A small-scale 4-dimensional approach - The holy grail for weather radar rainfall estimation?

These in-depth analyses of the small-scale aspects of the observed precipitation field from volumetric radar and disdrometer measurements show the difficulty of relating point-scale information to the variability of the precipitation system aloft. First, because of the smaller scale variability of the precipitation field, changing constantly in space and time. Second, because of the difficulty to infer any general information on the three-dimensional properties of the precipitation field from point measurements at the surface. More specifically, even though the selection of intra-event phases in Fig. 7.1 makes sense from a visual perspective, the volumetric weather radar data in the region above the disdrometer for a number of phases shows a much more complicated behavior. This partly results from the fact that a relatively large region around the radar was used to generate the accumulated CFAD profiles. Most convective precipitation cells have a much smaller radius than 30 km.

Therefore, based on these results and what has been presented in this thesis, the only way to move forward in improving precipitation measurements by weather radar is by focusing on the small-scale aspects of the precipitation field, effectively taking the variability and uncertainty into account. Standard approaches focusing on a fixed spatial region of the radar umbrella or a specific rainfall type, can contain too large variations in the small-scale properties of precipitation (precipitation phase and DSD).

As such, it is necessary to develop efficient methods that are able to detect these small-scale variations and to identify relatively uniform regions within the observed precipitation field. In this thesis, by developing RoCaSCA and taking a Lagrangian approach to follow the evolution of a precipitation region of given type, a first step in this direction was taken. In addition, the techniques developed as part of this thesis include two different ways to assess the uncertainty in the weather radar precipitation measurements.

However, the precipitation regions identified by RoCaSCA are still too large. This is because in its current implementation, RoCaSCA only takes the reflectivity information into account as sampled by a given radar elevation. As a next step forward, the algorithm needs to be extended by taking the full three-dimensional properties of the precipitation field into account and the sampling characteristics of the radar. By tracking this information for a number of consecutive time steps, a full four-dimensional procedure should be developed from which it should be

able to identify relatively uniform regions within the identified regions. The temporal information can then be used to infer information on the small-scale processes and their temporal evolution. By linking this information to local disdrometer measurements taken at the surface, it is expected that the next quality improvement in the radar estimated precipitation rates can be obtained, which is extremely useful for hydrological applications.

Polarimetric radars, which are gradually replacing non-polarimetric radars all over the world, have the potential to contribute to this small scale four-dimensional approach. The added information obtained by taking the differential reflectivity into account, could provide extra information, which could be used by RoCaSCA to discriminate individual precipitation regions in more detail. This also holds for making use of the information available from X-band radars, which generally provide reflectivity data at a much higher resolution.

It is also anticipated that the focus on smaller cells within a given precipitation region as the focus of radar error correction, will result in smaller uncertainties around the mean radar precipitation estimates. However, it is expected that considerable uncertainty will always remain, as shown by the results presented in Fig. 7.5. However, smaller regions will lead to less uncertainty in the estimated VPR, decreasing the total variability in the estimated radar-precipitation field (see Section 5.5). Next to that, a given Z–R relation, in case it is derived from DSD data, will be more representative for a smaller region than when used for a given precipitation type observed within the entire radar umbrella.

CHAPTER 8

Conclusions

In this thesis the possibilities for estimating precipitation amounts from volumetric weather radar data and its potential for hydrology have been assessed. A number of research questions were defined as the central focus of this thesis. Based on the research results presented here, the following answers to these questions can be given:

What are the most dominant sources of error in radar precipitation estimation and what is the best way to correct for them?

In Fig. 1.1 an overview of the different sources of error was presented and further details were provided in Sections 1.2 and 1.3. Based on the results presented in this thesis it is clear that the answer to this questions is far from straightforward and depends on the region of study, the characteristics of the weather radar and the type of precipitation observed.

For the Ourthe region, the combined effects of clutter and precipitation region-based VPR correction resulted in the largest improvement in the quality of the weather radar precipitation product. However, each of the other error correction algorithms, such as taking the full volumetric radar information into account and the use of different Z–R relations based on precipitation type, definitely had a beneficial impact on the weather radar rainfall product.

A completely different situation could be observed for the mesoscale convective system analyzed in the discussion (Chapter 7). These analy-

ses showed that each of the identified errors indicated in Fig. 1.1 had an impact on the radar precipitation estimates. Therefore, in order to properly estimate surface precipitation amounts using radar, is to account for each error source because the impact of each error source depends on the precipitation event. The novel precipitation region-based approach in combination with precipitation type identification as taken in this thesis is shown to yield good results, and is the proper direction to go when dealing with weather radar precipitation estimation.

How are the parameters of the Z–R relation related to the characteristics of the DSD, and how do these parameters relate to each other?

The fact that both the radar reflectivity and rainfall rate are inherent properties of the DSD implies that the values of the parameters of the Z–R relation depend on the DSD as well. More specifically, the prefactor A can be directly related to a scaled DSD, while the exponent b results from its temporal behavior. The results shown in Chapter 3 indicate that there is a negative correlation between both parameters. Convective precipitation is generally associated with a smaller exponent than stratiform precipitation. This can be related to the larger amount of drop interactions, resulting from a higher number concentration and larger overall interaction time. For the prefactor, such general observations on behavior specific for different types of precipitation cannot be made, and results depend heavily on the atmospheric environment shaping the DSD. The negative correlation between both parameters, however, does provide the possibility to gain some insight in the amount of uncertainty that can be expected when using a given fixed Z–R relation.

Is it possible to define a method that is efficiently able to discriminate between regions with different precipitation types?

In this thesis, the grid-based image segmentation algorithm RoCaSCA was presented, which is efficiently able to detect precipitation regions within the radar umbrella. RoCaSCA is shown to be highly efficient when it comes to linking non-neighboring pixels. This makes this algorithm very useful for the identification of precipitation regions, which can then be tracked in time. By combining this information with the three-dimensional measurements taken by the weather radar, it becomes possible to assign precipitation types to a given precipitation area. This can then be used to obtain an improved understanding on their temporal behavior.

For a given precipitation region, is it possible to improve the radar estimates of the vertical profile of reflectivity, and to provide uncertainties of these estimates?

As part of this thesis, a constrained piecewise linear VPR identification method was developed, which leads to improved quantitative surface precipitation estimates by weather radar. The procedure proposed here is focused specifically on identifying and tracking precipitation regions of a given type. It was shown that up to distances of about 150 km, proper identification of the VPR is achieved by combining the region-based Lagrangian procedure developed in this thesis with the classical Eulerian VPR identification approach. In general, considerable spatial variability in the characteristics of the VPR can be observed. Therefore, the median VPR correction procedure was extended with a method to identify the uncertainty around a given VPR estimate. This uncertainty can easily be obtained from the volumetric weather radar measurements. The analyses presented in this thesis show that this type of uncertainty accounts for the majority of the radar-gauge differences when dealing with stratiform precipitation systems.

How well can the response of a catchment be modelled using corrected radar precipitation estimates?

If the weather radar data are properly corrected for all known sources of error, their quality is comparable to rain gauge measurements for the winter half-year analyzed in this thesis. Therefore, the simulated discharges of a medium-sized catchment do not show large differences when either corrected radar or rain gauge data are used as the input of a hydrological model. The simulated discharges using weather radar data correspond well to observations. Besides that, the results presented in this thesis show that using weather radar precipitation ensembles, a better correspondence to the observed flood peak occurs than when using rain gauge information. Because weather radar provides much more detailed information on the spatial structure of the precipitation field, it is anticipated that simulations of catchment response will have an even higher quality when using a spatially-distributed high-resolution hydrological model. Only by using such a model can the full potential of corrected weather radar data be exploited. This can only lead to further improvements in the modelled hydrological response.

What are the contributions to the uncertainties in hydrologic model output of VPR and DSD uncertainties relative to hydrologic model parameter uncertainties?

As part of this thesis, two separate procedures were developed to assess the uncertainty in weather radar precipitation estimates: 1) originating from the variability of the VPR; and 2) resulting from the applied Z–R relation. At the point scale this leads to an overall uncertainty in the estimated surface precipitation amounts of around 40% and 15%, respectively. These numbers slowly decrease when aggregating over larger scales. However, compared to the uncertainty in hydrological model output that originates from uncertainty in the hydrological model parameters, the impact of precipitation uncertainty on the catchment response is an order of magnitude smaller. This shows that the dominant impact of catchments is to filter the precipitation, leading to a approximately 50% decrease of input uncertainty in the discharge response.

Samenvatting

Weerradars bieden de mogelijkheid tot het verkrijgen van een enorme hoeveelheid informatie over de ruimtelijke en temporele karakteristieken van regenbuien. Omdat actuele neerslagschattingen van weerradars worden beïnvloed door meetfouten, dient hiervoor gecorrigeerd te worden. Dit proefschrift richt zich op het corrigeren van weerradarmetingen voor de meest dominante meetfouten, waardoor het neerslagproduct direct toepasbaar wordt voor het operationele waterbeheer.

Fouten in weerradarmetingen kunnen in het algemeen worden onderverdeeld in twee categorieën: 1) fouten in de reflectiviteitsmetingen van de weerradar en 2) fouten die ontstaan tijdens het converteren van een gegeven reflectiviteit naar een neerslagintensiteit. Fouten die onderdeel uitmaken van de eerste categorie ontstaan ten gevolge van de karakteristieken van de radar (b.v. onnauwkeurigheden in de radarcalibratie), de locatie van de weerradar (b.v. het blokkeren van het signaal door hoge obstakels, de interactie van het signaal met het landschap en de demping van het signaal), of ten gevolge van het foutief interpreteren van radarmetingen (b.v. door vertikale variaties in het reflectiviteitsprofiel). Meetfouten die vallen onder de tweede categorie ontstaan ten gevolge van ruimtelijke en temporele variaties in de grootteverdeling van hydrometeoren, in het geval van regen dus de druppelgrootteverdeling. Over het algemeen wordt de relatie tussen de radarreflectiviteit en de regenintensiteit beschreven door een machtsrelatie. Aangezien zowel de radarreflectiviteit als de regenintensiteit functies zijn van de druppelgrootteverdeling, verandert deze machtsrelatie continu. Dit leidt tot het probleem dat twee identieke reflectiviteitswaardes het gevolg kun-

nen zijn van verschillende druppelgrootteverdelingen met verschillende neerslagintensiteiten.

Dit proefschrift houdt zich specifiek bezig met het meten van regen met behulp van weerradar tijdens stratiforme buien. In Noordwest Europa is deze vorm van neerslag met name dominant gedurende de winter. Dit leidt vervolgens tot de grootste hydrologische reactie van stroomgebieden. Een groot nadeel van het gebruik van weerradar tijdens stratiforme buien is dat de kwaliteit van de metingen reeds op korte afstand van de radar sterk afneemt. Om de kwaliteit hiervan te verbeteren is in dit proefschrift allereerst gepoogd gebruik te maken van bestaande weerradarcorrectiemethodes. Hoewel het implementeren van deze methodes leidt tot een verbetering in de kwaliteit van de weerradarregenmetingen, laten deze methodes veel mogelijkheden open tot verdere kwaliteitsverbetering. Dit is het gevolg van het relatief uniforme karakter van de bestaande correctiemethodes, die slechts in beperkte mate rekening houden met de ruimtelijke variatie van het neerslagveld.

Aangezien de karakteristieken van regenbuien ruimtelijk en temporeel variëren, stelt dit proefschrift een vernieuwde aanpak voor, die zou moeten leiden tot een verbetering van de kwaliteit van de weerradar regenmetingen. Hierbij wordt er specifiek onderscheid gemaakt tussen verschillende ruimtelijke neerslagzones en de ontwikkeling hiervan in de tijd. Om dit te kunnen bewerkstelligen wordt er gebruik gemaakt van het speciaal hiervoor ontwikkelde Rotational Carpenter Square Cluster Algoritme (RoCaSCA), dat op efficiënte wijze in staat is neerslagzones te identificeren en te onderscheiden, waarna de ontwikkeling van een gegeven zone gevolgd kan worden in de tijd. Voor een gegeven geïdentificeerde neerslagzone wordt vervolgens voor ieder pixel bepaald tot welk type neerslag het behoort, waarbij onderscheid gemaakt wordt tussen convectieve, stratiforme en niet-stratiforme/niet-convectieve neerslag. Vervolgens wordt er voor de laatste twee typen neerslag een nauwkeurige schatting gemaakt van de vertikale neerslagstructuur op basis van een nieuw ontwikkelde methode, voortbouwend op reeds bestaande technieken. Deze regionale aanpak voor het corrigeren van weerradarmetingen is vervolgens gecombineerd met bestaande correctiemethodes, waarna voor het verkrijgen van neerslagintensiteiten uit gecorrigeerde radarreflectiviteitsgegevens er gebruik gemaakt wordt van een neerslagstype-afhankelijke machtsrelatie.

Analyses laten zien dat voor een winterhalfjaar de vernieuwde correctiemethode tot een sterke verbetering in de kwaliteit van het regenproduct leidt tot afstanden van 150 km van de radar. Wanneer gecor-

rigeerd wordt voor dominante foutenbronnen, zijn de weerradarschattingen van gelijke kwaliteit als metingen met behulp van regenmeters op de grond. Hierdoor is het niet noodzakelijk gebruik te maken van deze regenmetergegevens voor een aanvullende correctie van systematische fouten, hetgeen tradioneel wel in operationele algoritmes wordt toegepast.

Ondanks de sterke kwaliteitsverbetering van het regenproduct van de weerradar verkregen met behulp van de vernieuwde correctiemethode, blijven er verschillen ten opzichte regenmeters bestaan. Deze zijn het gevolg van niet geïdentificeerde foutenbronnen, kleinschalige neerslag variaties, alsmede schaalproblemen die voortkomen uit meetverschillen tussen radar en regenmeters. Echter, in plaats van gebruik te maken van bestaande methodes waarbij radarmetingen op basis van regenmeters gecorrigeerd worden, is er in dit proefschrift de voorkeur aan gegeven inzicht te krijgen in de onzekerheid van radarmetingen. Speciaal hiervoor zijn twee conceptuele methodes ontwikkeld. Allereerst worden de volumetrische weerradargegevens op efficiënte wijze gebruikt voor het verkrijgen van een schatting van de ruimtelijke en temporele variatie van het verticale reflectiviteitsprofiel. Daarnaast is er een statistische methode toegepast waarmee een schatting gemaakt kan worden van de onzekerheid als gevolg van de conversie van reflectiviteit naar regenintensiteit. Hierbij wordt aangenomen dat de twee parameters van de machtsrelatie (waarvan er één is log-getransformeerd) een bivariate lognormale verdeling hebben. De veronderstelling van log-normaliteit werd verkregen op basis van de analyse van een meerjarig gegevensbestand van druppelgrootteverdelingen verkregen met behulp van een disdrometer in Zuid-Frankrijk. Beide vormen van onzekerheid kunnen dominant worden verondersteld in stratiforme neerslag, hetgeen bevestigd wordt in dit proefschrift. Resultaten laten zien dat, indien de onzekerheid in weerradarregenmetingen wordt meegenomen, de verschillen ten opzichte van regenmeters verklaard kunnen worden.

In het laatste deel van dit proefschrift zijn de hydrologische mogelijkheden van de gecorrigeerde radarregenmetingen geanalyseerd aan de hand van neerslag-afvoersimulaties van het Ourthe stroomgebied. Dit stroomgebied bevindt zich in de heuvelachtige Belgische Ardennen, waar dunne hellende bodems leiden tot een relatief snelle hydrologische reactie in geval van regen. Aangezien dit stroomgebied één van de grotere zijtakken van de rivier de Maas vormt voordat deze Nederland instroomt, is het correct voorspellen van het afvoergedrag van dit stroomgebied van groot belang voor operationele hydrologische diensten in Nederland.

Gecorrigeerde weerradarregenmetingen bieden even goede resultaten in het voorspellen van de hydrologische reactie van dit stroomgebied als wanneer regenmetergegevens worden gebruikt. Echter, het gebruik van regenmetergegevens leidt tot een forse onderschatting van de grootste afvoerpiek in de studieperiode. Dit is niet het geval wanneer de weerradarinformatie gebruikt wordt. Het gebruik van gecorrigeerde weerradargegevens, inclusief de informatie over de meetonzekerheden afkomstig van één van beide methodes, leidt tot een sterk verbeterde voorspelling van de afvoerpiek. Dit toont het voordeel aan van het gebruik van weerradarinformatie in neerslag-afvoertoepassingen. Gegeven het feit dat de resolutie van de toegepaste hydrologische modellen verder zal toenemen, de radar in staat zal zijn op steeds hogere resolutie neerslagmetingen te geven en de kwaliteit van weerradars door middel van nieuwe technieken (zoals polarimetrie) alleen maar toe zal nemen, ligt het in de lijn der verwachting dat het gebruik van weerradarinformatie voor hydrologische toepassingen in de nabije toekomst sterk zal toenemen.

Bibliography

AghaKouchak, A., E. Habib, and A. Bardossy (2010), Modeling radar rainfall estimation uncertainties: random error model, *J. Hydrol. Eng.*, pp. 265–274.

Agrawal, R., J. Gehrke, D. Gunopulos, and P. Raghavan (1998), Automatic subspace clustering of high dimensional data for data mining applications, *SIGMOD Rec.*, *27*, 94–105.

Alberoni, P. P., T. Andersson, P. Mezzasalma, D. B. Michelson, and S. Nanni (2001), Use of the vertical reflectivity profile for identification of anomalous propagation, *Meteorol. Appl.*, *8*, 257–266.

Anagnostou, E. N., and W. F. Krajewski (1999a), Real-time radar rainfall estimation. Part 1: Algorithm formulation, *J. Atmos. Oceanic. Technol.*, *16*, 189–197.

Anagnostou, E. N., and W. F. Krajewski (1999b), Real-time radar rainfall estimation. Part 2: Case study, *J. Atmos. Oceanic. Technol.*, *16*, 198–205.

Andreassian, V., C. Perrin, C. Michel, I. Usart-Sanchez, and J. Lavabre (2001), Impact of imperfect rainfall knowledge on the efficiency and the parameters of watershed models, *J. Hydrol.*, *250*, 206–223.

Andrieu, H., and J. D. Creutin (1995), Identification of vertical profiles of radar reflectivity for hydrological applications using an inverse method. Part 1: Formulation, *J. Appl. Meteorol.*, *34*, 225–239.

Andrieu, H., G. Delrieu, and J. D. Creutin (1995), Identification of vertical profiles of radar reflectivity for hydrological applications using

an inverse method. Part 2: Sensitivity analysis and case study, *J. Appl. Meteorol.*, *34*, 240–259.

Andrieu, H., J. D. Creutin, G. Delrieu, and D. Faure (1997), Use of weather radar for the hydrology of a mountainous area. Part 1: radar measurement interpretation, *J. Hydrol.*, *193*, 1–25.

Anquetin, S., I. Braud, O. Vannier, P. Viallet, B. Boudevillain, J. D. Creutin, and C. Manus (2010), Sensitivity of the hydrological response to the variability of rainfall fields and soils for the Gard 2002 flash-flood event, *J. Hydrol.*, *394*, 134–147.

Arnaud, P., J. Lavabre, C. Fouchier, S. Diss, and P. Javelle (2011), Sensitivity of hydrological models to uncertainty in rainfall input, *Hydrol. Sci. J.*, *56*(3), 397–410.

Atlas, D. (2002), Radar calibration - some simple approaches, *B. Am. Meteorol. Soc.*, pp. 1313–1316.

Atlas, D., and C. W. Ulbrich (1977), Path- and area-integrated rainfall measurement by microwave attenuation in the 1-3 cm band, *J. Appl. Meteorol.*, *16*, 1322–1331.

Atlas, D., and C. W. Ulbrich (2000), An observationally based conceptual model of warm oceanic convective rain in the tropics, *J. Appl. Meteorol.*, *39*, 2165–2181.

Atlas, D., C. W. Ulbrich, F. D. Marks Jr., E. Amitai, and C. R. Williams (1999), Systematic variation of drop size and radar-rainfall relations, *J. Geophys. Res.*, *104*(D6), 6155–6169.

Atlas, D., C. W. Ulbrich, F. D. Marks Jr., R. A. Black, E. Amitai, P. T. Willis, and C. E. Samsury (2000), Partitioning tropical oceanic convective and stratiform rains by draft strength, *J. Geophys. Res.*, *105*(D2), 2259–2267.

Austin, P. M. (1987), Relation between measured radar reflectivity and surface rainfall, *Mon. Weath. Rev.*, *115*, 1053–1070.

Austin, P. M., and A. C. Bemis (1950), A quantitative study of the "bright band" in radar precipitation echoes, *J. Meteorol.*, *7*, 145–151.

Battan, L. J. (1973), *Radar observation of the Atmosphere*, 324 pp., The University of Chicago Press.

Beard, K. V. (1976), Terminal velocity and shape of cloud and precipitation drops aloft, *J. Atmos. Sci.*, *33*, 851–864.

Beard, K. V. (1977), Terminal velocity adjustment for cloud and precipitation drops aloft, *J. Atmos. Sci.*, *34*, 1293–1298.

Bellon, A., G. Lee, and I. Zawadzki (2005), Error statistics of VPR

corrections in stratiform precipitation, *J. Appl. Meteorol.*, *44*, 998–1015.

Bellon, A., G. W. Lee, A. Kilambi, and I. Zawadzki (2007), Real-time comparisons of VPR-corrected daily rainfall estimates with a gauge mesonet, *J. Appl. Meteorol. Climatol.*, *46*, 726–741.

Berenguer, M., and I. Zawadzki (2008), A study of the error covariance matrix of radar rainfall estimates in stratiform rain, *Weath. Forecasting*, *23*, 1085–1101.

Berenguer, M., G. W. Lee, D. Sempere-Torres, and I. Zawadzki (2002), A variational method for attenuation correction of radar signal, *Proceedings of ERAD(2002)*, pp. 11–16.

Berenguer, M., C. Corral, R. Sánchez-Diezma, and D. Sempere-Torres (2005), Hydrological validation of a radar-based nowcasting technique, *J. Hydrometeorol.*, *6*, 532–549.

Berenguer, M., D. Sempere-Torres, C. Corral, and R. Sánchez-Diezma (2006), A fuzzy logic technique for identifying nonprecipitating echoes in radar scans, *J. Atmos. Oceanic. Technol.*, *23*, 1157–1180.

Bergström, S. (1976), Development and application of a conceptual runoff model for Scandinavian catchments, *SMHI Report*, *RHO No.7*.

Bergström, S. (1992), The HBV model – its structure and applications, *SMHI Report*, *RH No.4*.

Berne, A., G. Delrieu, J. D. Creutin, and C. Obled (2004a), Temporal and spatial resolution of rainfall measurements required for urban hydrology, *J. Hydrol.*, *299*, 166–179.

Berne, A., G. Delrieu, H. Andrieu, and J. D. Creutin (2004b), Influence of the vertical profile of reflectivity on radar-estimated rain rates at short time steps, *J. Hydrometeorol.*, *5*, 296–310.

Berne, A., M. ten Heggeler, R. Uijlenhoet, L. Delobbe, P. Dierickx, and M. de Wit (2005), A preliminary investigation of radar rainfall estimation in the Ardennes region and a first hydrological application for the Ourthe catchment, *Nat. Hazards Earth Syst. Sci.*, *5*, 267–274.

Beven, K. J. (2000), *Rainfall-runoff modelling: The primer*, Wiley, Chichester, England.

Beven, K. J. (2009), *Environmental modelling: An uncertain future?*, 1 ed., Routledge, 2 Park Square, Milton Park, Abingdon, Oxon.

Beven, K. J., and A. Binley (1992), The future of distributed models: model calibration and uncertainty prediction, *Hydrol. Proc.*, *6*, 279–298.

Beven, K. J., and M. J. Kirkby (1979), A physically based, variable contributing area model of basin hydrology, *Hydrol. Sci. J.*, *24*, 43–69.

Beven, K. J., R. Lamb, P. Quinn, R. Romanowicz, and J. Freer (1995), *TOPMODEL*, vol. Computer models of watershed hydrology, Singh, V.P. (Ed.), pp. 627–668, Water Resources Publications, Highlands Ranch, CO.

Blanchard, D. C. (1953), Raindrop size distribution in Hawaiian rains, *J. Meteorol.*, *10*, 457–473.

Blanchard, D. C., and T. Spencer (1970), Experiments on the generation of raindrop size distributions by drop breakup, *J. Atmos. Sci.*, *27*, 101–108.

Booij, M. (2002), Appropriate modelling of climate change impacts on river flooding, Ph.D. thesis, Twente University.

Borga, M. (2002), Accuracy of radar rainfall estimates for streamflow simulation, *J. Hydrol.*, *267*, 26–39.

Borga, M., E. N. Anagnostou, and W. F. Krajewski (1997), A simulation approach for validation of a brightband correction method, *J. Appl. Meteorol.*, *36*, 1507–1518.

Borga, M., S. Degli Esposti, and D. Norbiato (2006), Influence of errors in radar rainfall estimates on hydrological modeling prediction uncertainty, *Water Resour. Res.*, *42*, W08409, doi:10.1029/2005WR004559.

Borga, M., P. Boscolo, F. Zanon, and M. Sangati (2007), Hydrometeorological analysis of the 29 August 2003 flash flood in the Eastern Italian Alps, *J. Hydrometeorol.*, *8*, 1049–1067.

Boudevillain, B., G. Delrieu, B. Galabertier, L. Bonnifait, L. Bouilloud, P. E. Kirstetter, and M. L. Mosini (2011), The Cevennes-Vivarais Mediterranean Hydrometeorological Observatory database, *Water Resour. Res.*, *47*(W07701), doi:10.1029/2010WR010353.

Bouilloud, L., G. Delrieu, B. Boudevillain, M. Borga, and F. Zanon (2009), Radar rainfall estimation for the post-event analysis of a Slovenian flash-flood case: application of the mountain reference technique at C-band frequency, *Hydrol. Earth Syst. Sci.*, *13*, 1349–1360.

Bouilloud, L., G. Delrieu, B. Boudevillain, and P. E. Kirstetter (2010), Radar rainfall estimation in the context of post-event analysis of flash floods, *J. Hydrol.*, *394*, 17–27.

Brath, A., A. Montanari, and E. Toth (2004), Analysis of the effects of different scenarios of historical data availability on the calibration of a spatially-distributed hydrological model, *J. Hydrol.*, *291*, 232–253.

Brauer, C. C., A. J. Teuling, A. Overeem, Y. van der Velde, P. Hazenberg, P. M. M. Warmerdam, and R. Uijlenhoet (2011), Anatomy of extraordinary rainfall and flash flood in a Dutch lowland catchment, *Hydrol. Earth Syst. Sci.*, *15*, 1991–2005.

Campos, E., and I. Zawadzki (2000), Instrumental uncertainties in Z-R relations, *J. Appl. Meteorol.*, *39*, 1088–1102.

Carpenter, T. M., and K. P. Georgakakos (2004), Impacts of parametric and radar rainfall uncertainty on the ensemble streamflow simulations of a distributed hydrologic model, *J. Hydrol.*, *298*, 202–221.

Carpenter, T. M., and K. P. Georgakakos (2006), Intercomparison of lumped versus distributed hydrologic model ensemble simulations on operational forecast scales, *J. Hydrol.*, *329*, 174–185.

Carpenter, T. M., K. P. Georgakakos, and J. A. Sperfslagea (2001), On the parametric and NEXRAD-radar sensitivities of a distributed hydrological model suitable for operational use, *J. Hydrol.*, *253*, 169–193.

Chandrasekar, V., and V. N. Bringi (1987), Simulation of radar reflectivity and surface measurements of rainfall, *J. Atmos. Oceanic. Technol.*, *4*, 464–478.

Chang, F., C. J. Chen, and C. J. Lu (2004), A linear-time component-labeling algorithm using contour tracing technique, *Computer Vision and Image Understanding*, *93*(2), 206–220.

Chapon, B., G. Delrieu, M. Gosset, and B. Boudevillain (2008), Variability of rain drop size distribution and its effect on the Z-R relationship: A case study for intense Mediterranean rainfall, *Atm. Res.*, *87*(1), 52–65.

Cho, Y. H., G. Lee, K. E. Kim, and I. Zawadzki (2006), Identification and removal of ground echoes and anomalous propagation using the characteristics of radar echoes, *J. Atmos. Oceanic. Technol.*, *23*, 1206–1222.

Chumchean, S., A. Seed, and A. Sharma (2004), Application of scaling in radar reflectivity for correcting range-dependent bias in climatological radar rainfall estimates, *J. Atmos. Oceanic. Technol.*, *21*, 1545–1556.

Chumchean, S., A. Seed, and A. Sharma (2008), An operational approach for classifying storms in real-time radar rainfall estimation, *J. Hydrol.*, *363*, 1–17.

Churchill, D. D., and R. A. Houze Jr. (1984), Development and structure of winter monsoon cloud clusters on 10 december 1978, *J. Atmos. Sci.*, *41*(6), 933–960.

Ciach, G. J., and W. F. Krajewski (1999a), On the estimation of radar rainfall error variance, *Adv. Water Resour.*, *22*(6), 585–595.

Ciach, G. J., and W. F. Krajewski (1999b), Radar-rain gauge comparisons under observational uncertainties, *J. Appl. Meteorol.*, *38*, 1519–1525.

Ciach, G. J., W. F. Krajewski, E. N. Anagnostou, M. L. Baeck, J. A. Smith, J. R. McCollum, and A. Kruger (1997), Radar rainfall estimation for ground validation studies of the tropical rainfall measuring mission, *J. Appl. Meteorol.*, *36*, 735–747.

Ciach, G. J., W. F. Krajewski, and G. Villarini (2007), Product-error-driven uncertainty model for probabilistic quantitative precipitation estimation with NEXRAD data, *J. Hydrometeorol.*, *8*, 1325–1347.

Clark, M. P., and A. G. Slater (2006), Probabilistic quantitative precipitation estimation in complex terrain, *J. Hydrometeorol.*, *7*(1), 3–22.

Cloke, H. L., and F. Pappenberger (2009), Ensemble flood forecasting: a review, *J. Hydrol.*, *375*(3-4), 613–626.

Cluckie, I. D., R. J. Griffith, A. Lane, and K. A. Tilford (2000), Radar hydrometeorology using a vertically pointing radar, *Hydrology and Earth System Sciences*, *4*(4), 565–580.

Collier, C. G. (1986), Accuracy of rainfall estimates by radar, part 1: Calibration by telemetering raingauges, *J. Hydrol.*, *83*, 207–223.

Collier, C. G. (2009), On the propation of uncertainty in weather radar estimates of rainfall through hydrological models, *Meteorol. Appl.*, *16*, 35–40.

Collier, C. G., and J. M. Knowles (1986), Accuracy of rainfall estimates by radar, Part 3: Application for short-term flood forecasting, *J. Hydrol.*, *83*, 237–249.

Creutin, J. D., H. Andrieu, and D. Faure (1997), Use of weather radar for the hydrology of a mountainous area. Part 2: radar measurement validation, *J. Hydrol.*, *193*, 26–44.

Dawdy, D. R., and J. M. Bergmann (1969), Effect of rainfall variability of streamflow simulation, *Water Resour. Res.*, *5*(5), 958–966.

Delrieu, G., J. D. Creutin, and I. Saint-André (1991), Mean K-R relationships: Practical results for typical weather radar wavelengths, *J. Atmos. Oceanic. Technol.*, *8*, 467–476.

Delrieu, G., J. D. Creutin, and H. Andrieu (1995), Simulation of radar mountain returns using a digitized terrain model, *J. Atmos. Oceanic Technol.*, *12*, 1038–1049.

Delrieu, G., S. Caoudal, and J. D. Creutin (1997), Feasibility of using mountain return for the correction of ground-based X-band weather radar data, *J. Atmos. Oceanic. Technol.*, *14*, 368–385.

Delrieu, G., L. Hucke, and J. D. Creutin (1999), Attenuation in rain for X- and C-band weather radar systems: Sensitivity with respect to the drop size distribution, *J. Appl. Meteorol.*, *38*, 57–68.

Delrieu, G., H. Andrieu, and J. D. Creutin (2000), Quantification of path-integrated attenuation for X- and C-band weather radar systems operating in Mediterranean heavy rainfall, *J. Appl. Meteorol.*, *39*, 840–850.

Delrieu, G., et al. (2005), The catastrophic flash-flood event of 8–9 September 2002 in the Gard region, France: A first case study for the Cevennes–Vivarais Mediterranean Hydrometeorological Observatory, *J. Hydrometeorol.*, *6*, 34–52.

Delrieu, G., B. Boudevillain, J. Nicol, B. Chapon, P. E. Kirstetter, H. Andrieu, and D. Faure (2009), Bollène-2002 experiment: Radar quantitative precipitation estimation in the Cévennes-Vivarais region (France), *J. Appl. Meteorol. Climatol.*, *48*(7), 1422–1447.

Dillencourt, M. B., H. Samet, and M. Tamminen (1992), A general approach to connected-component labeling for arbitrary image representations, *J. ACM*, *39*(2), 253–280.

Dinku, T., E. N. Anagnostou, and M. Borga (2002), Improving radar-based estimation of rainfall over complex terrain, *J. Appl. Meteorol.*, *41*, 1163–1178.

Dixon, M., and G. Wiener (1993), Titan: Thunderstorm idenfication, tracking, analysis and nowcasting - a radar-based methodology, *J. Atmos. Oceanic Technol.*, *10*(6), 785–797.

Doviak, R. J., and D. S. Zrnic (1993), *Doppler radar and weather observations*, Academic Press, 562pp.

Driessen, T. L. A., R. T. W. L. Hurkmans, W. Terink, P. Hazenberg, P. J. J. F. Torfs, and R. Uijlenhoet (2010), The hydrological response of the Ourthe catchment to climate change as modelled by the HBV model, *Hydrol. Earth Syst. Sci.*, *14*(4), 651–664.

Efron, B., and R. Tibshirani (1993), *An introduction to the bootstrap*, 436 pp pp., Chapman and Hall.

Fabry, F., and I. Zawadzki (1995), Long-term radar observations of the melting layer of precipitation and their interpretation, *J. Atmos. Sci.*, *52*(7), 838–851.

Fabry, F., G. L. Austin, and D. Tees (1992), The accuracy of rainfall

estimates by radar as a function of range, *Q. J. R. Meteorol. Soc.*, *118*, 435–453.

Fabry, F., A. Bellon, M. R. Duncan, and G. L. Austin (1994), High resolution rainfall measurements by radar for very small basins: the sampling problem reexamined, *J. Hydrol.*, *161*, 415–428.

Fabry, F., C. Frush, I. Zawadzki, and A. Kilambi (1997), On the extraction of near-surface index of refraction using radar phase measurements from ground targets, *J. Atmos. Oceanic. Technol.*, *14*, 978–987.

Feingold, G., and Z. Levin (1986), The lognormal fit to raindrop spectra from frontal convective clouds in Isreal, *J. Cl. Appl. Meteorol.*, *25*, 1346–1363.

Fiorio, C., and J. Gustedt (1996), Two linear time union-find strategies for image processing, *Theoretical Computer Science*, *154*(2), 165–181.

Fornasiero, A., J. Bech, and P. P. Alberoni (2006), Enhanced radar precipitation estimates using a combined clutter and beam blockage correction technique, *Nat. Hazards Earth Syst. Sci.*, *6*, 697–710.

Freeman, H. (1974), Computer processing of line-drawing images, *ACM Comput. Surv.*, *6*(1), 57–97.

Fu, K., and J. Mui (1981), A survey on image segmentation, *Pattern Recognition*, *13*(1), 3–16.

Fulton, R., J. P. Breidenbach, D. J. Seo, D. Miller, and T. O'Bannon (1997), The WSR-88D rainfall algorithm, *Weath. Forecasting*, *13*, 377–395.

Gabella, M., and G. Perona (1998), Simulation of the orographic influence on weather radar using a geometric-optics approach, *J. Atmos. Oceanic. Technol.*, *15*, 1485–1494.

Gabella, M., J. Joss, and G. Perona (2000), Optimizing quantitative precipitation estimates using a noncoherent and coherent radar operating on the same area, *J. Geophys. Res.*, *105*(D2), 2237–2245.

Gabella, M., M. Bolliger, U. Germann, and G. Perona (2005), Large sample evaluation of cumulative rainfall amounts in the Alps using a network of three radars, *Atm. Res.*, *77*, 256–268.

Gath, I., and A. B. Geva (1989), Unsupervised optimal fuzzy clustering, *IEEE Trans. Pattern Anal. Mach. Intell.*, *11*(7), 773–781.

Germann, U. (1999), Radome attenuation - a serious limiting factor for quantitative radar measurements?, *Meteorol. Z.*, *8*, 85–90.

Germann, U., and J. Joss (2002), Mesobeta profiles to extrapolate radar

precipitation measurements above the Alps to ground level, *J. Appl. Meteorol.*, *41*, 542–557.

Germann, U., G. Galli, M. Boscacci, and M. Bolliger (2006), Radar precipitation measurement in a mountainous region, *Q. J. R. Meteorol. Soc.*, *132*, 1669–1692.

Germann, U., M. Berenguer, D. Sempere-Torres, and M. Zappa (2009), REAL-Ensemble radar precipitation estimation for hydrology in a mountainous region, *Q. J. R. Meteorol. Soc.*, *135*, 445–456, doi: 10.1002/qj.375.

Giuli, D., M. Gherardelli, A. Freni, T. A. Seliga, and K. Aydin (1991), Rainfall and clutter discrimination by means of dual-linear polarization radar measurements, *J. Atmos. Oceanic. Technol.*, *8*, 777–789.

Goovaerts, P. (2000), Geostatistical approaches for incorporating elevation into the spatial interpolation of rainfall, *J. Hydrol.*, *228*(1-2), 113–129, doi:10.1016/S0022-1694(00)00144-X.

Goudenhoofdt, E., and L. Delobbe (2009), Evaluation of radar-gauge merging methods for quantitative precipitation estimates, *Hydrol. Earth Syst. Sci.*, *13*, 195–203.

Gourley, J. J., and C. M. Calvert (2003), Automated detection of the bright band using WSR-88D data, *Weath. Forecasting*, *18*, 585–599.

Gourley, J. J., D. P. Jorgensen, S. Y. Matrosov, and Z. L. Flamig (2009), Evaluation of incremental improvements to quantitative precipitation estimates in complex terrain, *J. Hydrometeorol.*, *10*, 1507–1520.

Grecu, M., and W. F. Krajewski (2000), An efficient methodology for detection of anomalous propagation echoes in radar reflectivity data using neural networks, *J. Atmos. Oceanic. Technol.*, *17*, 121–129.

Habib, E., W. F. Krajewski, and A. Kruger (2001), Sampling errors of fine resolution tipping-bucket rain gauge measurements, *J. Hydrol. Eng.*, *6*(2), 159–166.

Haddad, Z. S., and D. Rosenfeld (1997), Optimality of empirical Z-R relations, *Q. J. R. Meteorol. Soc.*, *123*, 1283–1293.

Haig, T., and Y. Attikiouzel (1989), An improved algorithm for border following of binary images, in *Circuit Theory and Design, 1989., European Conference on*, pp. 118–122.

Handwerker, J. (2002), Cell tracking with TRACE3D - a new algorithm, *Atm. Res.*, *61*, 15–34.

Harrold, T. W., and P. G. Kitchingman (1975), Measurement of surface rainfall using radar when the beam intersect the melting layer,

Preprint Vol, 16th Radar Meteorology Converence, pp. 473–478, Amer. Meteor. Soc., Boston.

Hazenberg, P., H. Leijnse, and R. Uijlenhoet (2011a), Radar rainfall estimation of stratiform winter precipitation in the Belgian Ardennes, *Water Resour. Res.*, *47*(W02507).

Hazenberg, P., N. Yu, B. Boudevillain, G. Delrieu, and R. Uijlenhoet (2011b), Scaling of raindrop size distributions and classification of radar reflectivity–rain rate relations in intense Mediterranean precipitation, *J. Hydrol.*, *402*(3-4), 179–192.

He, L., Y. Chao, K. Suzuki, and K. Wu (2009), Fast connected-component labeling, *Pattern Recognition*, *42*(9), 1977–1987.

Hitschfeld, W., and J. Bordan (1954), Errors inherent in the radar measurement of rainfall at attenuating wavelengths, *J. Meteorol.*, *11*, 58–67.

Hobbs, P. V., S. Chang, and J. D. Locatelli (1974), The dimensions and aggregation of ice crystals in natural clouds, *J. Geophys. Res.*, *79*(15), 2199–2206.

Holleman, I., A. Huuskonen, M. Kurri, and H. Beekhuis (2010), Operational monitoring of weather radar receiving chain using the sun, *J. Atmos. Oceanic Technol.*, *27*, 159–166.

Hossain, F., E. N. Anagnostou, T. Dinku, and M. Borga (2004), Hydrological model sensitivity to parameter and radar rainfall estimation uncertainty, *Hydrol. Proc.*, *18*, 3277–3291.

Houze Jr., R. A. (1993), *Cloud dynamics*, 573 p. pp., Academic Press.

Houze Jr., R. A. (1997), Stratiform precipitation in regions of convection: A meteorological paradox?, *B. Am. Meteorol. Soc.*, *78*(10), 2179–2196, doi:10.1175/1520-0477(1997)078¡2179:SPIROC¿2.0.CO;2.

Hu, Z., and R. C. Srivastava (1995), Evolution of raindrop size distribution by coalescence, breakup, and evaporation: theory and observations, *J. Atmos. Sci.*, *52*(10), 1761–1783.

Huggel, A., W. Schmid, and A. Waldvogel (1996), Raindrop size distributions and the radar bright band, *J. Appl. Meteorol.*, *35*, 1688–1701.

Iñesta, J. M., M. Buendía, and M. Á. Sarti (1996), Local symmetries of digital contours from their chain codes, *Pattern Recognition*, *29*(10), 1737–1749.

Jaffrain, J., A. Studzinski, and A. Berne (2011), A network of disdrometers to quantify the small-scale variability of the raindrop size distribution, *Water Resour. Res.*, *47*(W00H06), doi:10.1029/2010WR009872.

Jain, A., M. Murty, and P. Flynn (1999), Data clustering: A review, *ACM Computing Survey*, *31*(3), 264–323.

Jameson, A. R., and A. B. Kostinski (2002a), When is rain steady?, *J. Appl. Meteorol.*, *41*, 83–90.

Jameson, A. R., and A. B. Kostinski (2002b), Spurious power-law relations among rainfall and radar parameters, *Q. J. R. Meteorol. Soc.*, *128*, 2045–2058.

Johnson, J. T., P. L. MacKeen, A. Witt, E. DeWayne Mitchell, G. Stumpf, M. D. Eilts, and K. W. Thomas (1998), The storm cell identification and tracking algorithm: An enhanced WSR-88D algorithm, *Weath. Forecasting*, *13*, 263–276.

Jordan, P., A. Seed, and G. Austin (2000), Sampling errors in radar estimates of rainfall, *J. Geophys. Res.*, *105*(D2), 2247–2257.

Jordan, P. W., A. W. Seed, and P. E. Weinmann (2003), A stochastic model of radar measurement errors in rainfall accumulations at catchment scale, *J. Hydrometeorol.*, *4*, 841–855.

Joss, J., and E. G. Gori (1978), Shapes of raindrop size distributions, *J. Appl. Meteorol.*, *17*, 1054–1061.

Joss, J., and R. Lee (1995), The application of radar-gauge comparisons to operational precipitation profile corrections, *J. Appl. Meteorol.*, *34*, 2612–2630.

Joss, J., and A. Pittini (1991), Real-time estimation of the vertical profile of radar reflectivity to improve the measurement of precipitation in an Alpine region, *Meteorol. Atmos. Phys.*, *47*, 61–72.

Joss, J., and A. Waldvogel (1990), Precipitation measurement and hydrology, in *Radar in Meteorology: Battan Memorial and 40th Anniversary Radar Meteorology Conference*, pp. 577–597, American Meteorological Society.

Joss, J., M. Gabella, S. C. Michaelides, and G. Perona (2006), Variation of weather radar sensitivity at ground level and from space: case studies and possible causes, *Meteorol. Z.*, *15*(5), 485–496.

Kirstetter, P. E., H. Andrieu, G. Delrieu, and B. Boudevillain (2010a), Identification of vertical profiles of reflectivity for correction of volumetric radar data using rainfall classification, *J. Appl. Meteorol. Climatol.*, *49*, 2167–2180.

Kirstetter, P. E., G. Delrieu, B. Boudevillain, and C. Obled (2010b), Toward an error model for radar quantitative precipitation estimation in the Cévennes-Vivarais region, France, *J. Hydrol.*, *394*, 28–41.

Kitchen, M., and R. M. Blackall (1992), Representativeness errors in comparisons between radar and gauge measurements of rainfall, *J. Hydrol.*, *134*, 13–33.

Kitchen, M., and P. M. Jackson (1993), Weather radar performance at long range - simulated and observed, *J. Appl. Meteorol.*, *32*, 975–985.

Kitchen, M., R. Brown, and A. G. Davies (1994), Real-time correction of weather radar data for the effects of bright band, range and orographic growth in widespread precipitation, *Q. J. R. Meteorol. Soc.*, *120*, 1231–1254.

Klaassen, W. (1988), Radar observation and simulation of the melting layer of precipitation, *J. Atmos. Sci.*, *45*, 3741–3753.

Klaassen, W. (1989), From snowflake to raindrop, doppler radar observations and simulations of precipitation, Ph.D. thesis, Rijksunversiteit Utrecht.

Krajewski, W. F., E. N. Anagnostou, and G. J. Ciach (1996), Effects of the radar observation process on inferred rainfall statistics, *J. Geophys. Res.*, *101*(D21), 26,493–26,502.

Krajewski, W. F., et al. (2010), Towards better utilization of NEXRAD data in hydrology: an overview of Hydro-NEXRAD, *J. Hydroinf.*, *13*, 255–266.

Lanza, L. G., and E. Vuerich (2009), The WMO field intercomparison of rain intensity gauges, *Atm. Res.*, *94*, 534–543.

Leander, R., A. Buishand, P. Aalders, and M. de Wit (2005), Estimation of extreme floods of the river Meuse using a stochastic weather generator and a rainfall-runoff model, *Hydrol. Sci. J.*, *50*, 1089–1103.

Lee, G. W., and I. Zawadzki (2005), Variability of drop size distributions: Time-scale dependence of the variability and its effects on rain estimation, *J. Appl. Meteorol.*, *44*, 241–255.

Li, L., W. Schmid, and J. Joss (1995), Nowcasting of motion and growth of precipitation with radar over a complex orography, *J. Appl. Meteorol.*, *34*, 1286–1300.

Lin, N. P., C. I. Chang, N. Y. Jan, H. J. Chen, and W. H. Hao (2007), A deflected grid-based algorithm for clustering analysis, *Int. J. Math. Mod. Meth Appl. S.*, *1*, 33–39.

Lindström, G., M. Gardelin, B. Johansson, M. Persson, and S. Bergström (1997), Development and test of the distributed HBV-96 hydrological model, *J. Hydrol.*, *201*, 272–288.

List, R., N. R. Donaldson, and R. E. Stewart (1987), Temporal evolution

of drop spectra to collisional equilibrium in steady and pulsating rain, *J. Atmos. Sci.*, *44*(2), 362–372.

Ma, E., and T. Chow (2004), A new shifting grid clustering algorithm, *Pattern Recognition*, *37*(3), 503–514.

Mandapaka, P. V., G. Villarini, B. C. Seo, and W. F. Krajewski (2010), Effect of radar-rainfall uncertainty on the spatial characterization of rainfall events, *J. Geophys. Res.*, *115*(D17110), doi: 10.1029/2009JD013366.

Marshall, J. S., and W. M. K. Palmer (1948), The distribution of raindrops with size, *J. Meteorol.*, *5*, 165–166.

Marshall, J. S., W. Hitschfeld, and K. L. S. Gunn (1955), Advances in radar weather, *Adv. in Geophys.*, *2*, 1–56.

Martner, B. E., S. E. Yuter, A. B. White, S. Y. Matrosov, D. E. Kingsmill, and F. Martin Ralph (2008), Raindrop size distributions and rain characteristics in California coastal rainfall for periods with and without a radar bright band, *J. Hydrometeorol.*, *9*, 408–425.

Marzoug, M., and P. Amayenc (1994), A class of single- and dual-frequency algorithms for rain-rate profiling from a spaceborne radar. part 1: Principles and tests from numerical simulations, *J. Atmos. Oceanic. Technol.*, *11*, 1480–1506.

McMillan, H., B. Jackson, M. Clark, D. Kavetski, and R. Woods (2011), Rainfall uncertainty in hydrological modelling: An evaluation of multiplicative error models, *J. Hydrol.*, *400*, 83–94.

Menke, W. (1989), Geophysical data analysis: Discrete inverse theory, *Academic Press, Inc.*, p. 260 pp.

Michelson, D. B., and D. Sunhede (2004), Spurious weather radar echo identification and removal using multisource temperature information, *Meteorol. Appl.*, *11*, 1–14.

Molini, A., P. La Barbera, L. G. Lanza, and L. Stagi (2001), Rainfall intermittency and the sampling error of tipping-bucket rain gauges, *Phys. Chem. Earth (C)*, *26*, 737–742.

Mood, A. M., F. A. Graybill, and D. C. Boes (1974), *Introduction to the theory of statistics*, vol. 564pp, 3 ed., McGraw-Hill, Inc.

Morin, E., W. F. Krajewski, D. C. Goodrich, X. Gao, and S. Sorooshian (2003), Estimating rainfall intensities from weather radar data: The scale-dependency problem, *J. Hydrometeorol.*, *4*, 782–796.

Moulin, L., E. Gaume, and C. Obled (2009), Uncerties on mean areal

precipitation: assessment and impact on streamflow simulations, *Hydrol. Earth Syst. Sci.*, *13*, 99–114.

Nash, J. E., and J. V. Sutcliffe (1970), River flow forecasting through conceptual models. Part 1 - A discussion of principles., *J. Hydrol.*, *10*, 282–290.

Neary, V. S., E. Habib, and M. Fleming (2004), Hydrologic modeling with NEXRAD precipitation in middle Tennessee, *J. Hydrol. Eng.*, *9*(5), 2004.

Nguyen, T. T. (2011), A flood routing scheme in a distributed framework: A case study of the Ourthe catchment in Belgium, Master's thesis, Wageningen University, The Netherlands.

Nicotina, L., E. Alessi Celegon, A. Rinaldo, and M. Marani (2008), On the impact of rainfall patterns on the hydrologic response, *Water Resour. Res.*, *44*(W12401), doi:10.1029/2007WR006654.

Obled, C., J. Wendling, and K. J. Beven (1994), The sensitivity of hydrological models to spatial rainfall patterns: an evaluation using observed data, *J. Hydrol.*, *159*, 305–333.

Ogden, F. L., H. O. Sharif, S. U. S. Senarath, J. A. Smith, M. L. Baeck, and J. R. Richardson (2000), Hydrologic analysis of the Fort Collins, Colorado, flash flood of 1997, *J. Hydrol.*, *228*, 82–100.

Overeem, A., I. Holleman, and A. Buishand (2009), Derivation of a 10-year radar-based climatology, *J. Appl. Meteorol. Climatol.*, *48*(7), 1448–1463.

Pauwels, V. R. N., and G. J. M. De Lannoy (2006), Improvement of modeled soil wetness conditions and turbulent fluxes through the assimilation of observed discharge, *J. Hydrometeorol.*, *7*, 458–477, doi: 10.1175/JHM490.1.

Pellarin, T., G. Delrieu, G. M. Saulnier, H. Andrieu, B. Vignal, and J. D. Creutin (2002), Hydrologic visibility of weather radar systems operating in mountainous regions: Case study for the Ardeche catchment (France), *J. Hydrometeorol.*, *3*, 539–555.

Prat, P. O., and A. P. Barros (2009), Exploring the transient behavior of z-r relationships: Implications for radar rainfall estimation, *J. Appl. Meteorol. Climatol.*, *48*, 2127–2143.

Rakovec, O., A. H. Weerts, P. Hazenberg, P. J. J. F. Torfs, and R. Uijlenhoet (2012a), State updating of a distributed hydrological model with Ensemble Kalman Filtering: effects of updating frequency and observation network density on forecast accuracy, *Hydrol. Earth Syst. Sci.*, *16*, 3435–3449.

Rakovec, O., P. Hazenberg, P. J. J. F. Torfs, A. H. Weerts, and R. Uijlenhoet (2012b), Generating spatial precipitation ensembles: impact of temporal correlation structure, *Hydrol. Earth Syst. Sci.*, *16*, 3419–3434.

Ren, M., J. Yang, and H. Sun (2002), Tracing boundary contours in a binary image, *Image and Vision Computing*, *20*(2), 125–131.

Rinehart, R. E., and E. T. Garvey (1978), Three-dimensional storm motion detection by convectional weather radar, *Nature*, *273*, 287–289.

Robson, A. J., P. G. Whitehead, and R. C. Johnson (1993), An application of a physically based semi-distributed model to the Balquhidder catchments, *J. Hydrol.*, *145*, 357–370.

Rogers, R., I. Zawadzki, and E. Gossard (1991), Variation with altitude of the drop-size distribution in steady light rain, *Q. J. R. Meteorol. Soc.*, *117*, 1341–1369.

Rosenfeld, A. (1970), Connectivity in digital pictures, *J. ACM*, *17*, 146–160.

Rosenfeld, A., and A. C. Kak (1982), *Digital Picture Processing*, 2nd ed., Academic Press, Inc., Orlando, FL, USA.

Rosenfeld, A., and J. L. Pfaltz (1966), Sequential operations in digital picture processing, *Journal of The ACM*, *13*, 471–494, doi: 10.1145/321356.321357.

Rosenfeld, D., and C. W. Ulbrich (2003), Cloud microphysical properties, processes, and rainfall estimation opportunities, *Radar and Atmospheric Science: A Collection of Essays in Honor of David Atlas, Meteor. Monogr.*, pp. 237–258.

Rossa, A., K. Liechti, M. Zappa, M. Bruen, U. Germann, G. Haase, C. Keil, and P. Krahe (2011), The COST 731 Action: A review on uncertainty propagation in advanced hydro-meteorological forecast systems, *Atm. Res.*, *100*, 150–167.

Russchenberg, H. W. J. (1992), Ground-based remote sensing of precipitation using a multi-polarized FM-CW Doppler radar, Ph.D. thesis, Delft University of Technology, 206 pp.

Sánchez-Diezma, R., I. Zawadzki, and D. Sempere-Torres (2000), Identification of the bright band through the analysis of volumetric radar data, *J. Geophys. Res.*, *105*(D2), 2225–2236.

Sauvageot, H., and J. Lacaux (1995), The shape of averaged drop size distributions, *J. Atmos. Sci.*, *52*(8), 1070–1083.

Schleiss, M., and A. Berne (2012), Stochastic space–time disaggregation of rainfall into DSD fields, *Journal of Hydrometeorology*, *13*, 1954–1969.

Schleiss, M., A. Berne, and R. Uijlenhoet (2009), Geostatistical simulation of two-dimensional fields of raindrop size distributions at the meso-gamma scale, *Water Resour. Res.*, *45*(W07415).

Segond, M. L., H. S. Wheater, and C. Onof (2007), The significance of spatial rainfall representation for flood runoff estimation: A numerical evaluation based on the Lee catchment, UK, *J. Hydrol.*, *347*, 116–131.

Sekhon, R. S., and R. C. Srivastava (1970), Snow size spectra and radar reflectivity, *J. Atmos. Sci.*, *27*, 299–307.

Sekhon, R. S., and R. C. Srivastava (1971), Doppler radar observations of drop-size distributions in a thunderstorm, *J. Atmos. Sci.*, *28*, 983–994.

Seliga, T. A., and V. N. Bringi (1976), Potential use of radar differential reflectivity measurements at orthogonal polarizations for measuring precipitation, *J. Appl. Meteorol.*, *51*(1), 69–76.

Sempere-Torres, D., J. M. Porrà, and J. D. Creutin (1994), A general formulation for raindrop size distribution, *J. Appl. Meteorol.*, *33*, 1494–1502.

Sempere-Torres, D., J. M. Porrà, and J. D. Creutin (1998), Experimental evidence of a general description for raindrop size distribution properties, *J. Geophys. Res.*, *103*(D2), 1785–1797.

Seo, B. C., and W. F. Krajewski (2011), Investigation of the scale-dependent variability of radar-rainfall and rain gauge error covariance, *Adv. Water Resour.*, *34*, 152–163.

Seo, D. J., and J. P. Breidenbach (2002), Real-time correction of spatially nonuniform bias in radar rainfall data using rain gauge measurements, *J. Hydrometeorol.*, *3*, 93–111.

Seo, D. J., J. Breidenbach, R. Fulton, D. Miller, and T. O'Bannon (2000), Real-time adjustment of range-dependent biases in WSR-88D rainfall estimates due to nonuniform vertical profile of reflectivity, *J. Hydrometeorol.*, *1*, 222–240.

Serrar, S., G. Delrieu, J. D. Creutin, and R. Uijlenhoet (2000), Mountain reference technique: Use of mountain returns to calibrate weather radars operating at attenuating wavelengths, *J. Geophys. Res.*, *105*(D2), 2281–2290, doi:10.1029/1999JD901025.

Sheikholeslami, G., S. Chatterjee, and A. Zhang (2000), Wavecluster:

A wavelet based clustering approach for spatial data in very large databases., *VLDB J.*, *8*(3-4), 289–304.

Shih, F. Y., and W. T. Wong (1999), A one-pass algorithm for local symmetry of contours from chain codes, *Pattern Recognition*, *32*(7), 1203–1210.

Sivaramakrishnan, M. V. (1961), Studies of raindrop size characteristics in different types of tropical rain using a simple recorder, *Indian J. Meteorol. Geophys.*, *12*, 189–217.

Smith, C. J. (1986), The reduction of errors caused by bright bands in quantitative rainfall measurements made using radar, *J. Atmos. Oceanic. Technol.*, *3*, 129–141.

Smith, J. A., and W. F. Krajewski (1991), Estimation of the mean field bias of radar rainfall estimates, *J. Appl. Meteorol.*, *30*, 397–412.

Smith, J. A., and W. F. Krajewski (1993), A modeling study of rainfall rate-reflectivity relationships, *Water Resour. Res.*, *28*(8), 2505–2514.

Smith, J. A., M. L. Baeck, Y. Zhang, and C. A. Doswell III (2001), Extreme rainfall and flooding from supercell thunderstorms, *J. Hydrometeorol.*, *2*, 469–489.

Smith, J. A., M. L. Baeck, K. L. Meierdiercks, A. J. Miller, and W. F. Krajewski (2007), Radar rainfall estimation for flash flood forecasting in small urban watersheds, *Adv. Water Resour.*, *30*, 2087–2097.

Smith, J. A., M. L. Baeck, G. Villarini, C. Welty, A. J. Miller, and W. F. Krajewski (2012), Analysis of a long-term, high-resolution radar rainfall data set for the Baltimore metropolitan region, *Water Resour. Res.*, *48*(W04504), doi:10.1029/2011WR010641.

Smith, P. L. (2003), Raindrop size distributions: Exponential or gamma - does the difference matter?, *J. Appl. Meteorol.*, *42*, 1031–1269.

Smith, P. L., Z. Liu, and J. Joss (1993), A study of sampling-variability effects in raindrop size observations, *J. Appl. Meteorol.*, *32*, 1259–1269.

Smyth, T. J., and A. J. Illingworth (1998), Radar estimates of rainfall rates at the ground in bright band and non-bright band events, *Q. J. R. Meteorol. Soc.*, *124*, 2417–2434.

Steiner, M., and J. A. Smith (1998), Convective versus stratiform rainfall: An ice-microphysical and kinematic conceptual model, *Atm. Res.*, *47-48*, 317–326.

Steiner, M., and J. A. Smith (2000), Reflectivity, rain rate, and kinetic energy flux relationships based on raindrop spectra, *J. Appl. Meteorol.*, *39*, 1923–1940.

Steiner, M., and J. A. Smith (2002), Use of three-dimensional reflectivity structure for automated detection and removal of nonprecipitating echoes in radar data, *J. Atmos. Oceanic. Technol.*, *19*, 673–686.

Steiner, M., and J. A. Smith (2004), Scale dependence of radar-rainfall rates - an assessment based on raindrop spectra, *J. Hydrometeorol.*, *5*, 1171–1180.

Steiner, M., R. A. Houze Jr., and S. E. Yuter (1995), Climatological characterization of three-dimensional storm structure from operational radar and raingauge data, *J. Appl. Meteorol.*, *34*, 1978–2007.

Steiner, M., J. A. Smith, S. J. Burges, C. Alonso, and R. W. Darden (1999), Effect of bias adjustment and rain gauge data quality control on radar rainfall estimation, *Water Resour. Res.*, *8*, 2487–2503.

Steiner, M., J. A. Smith, and R. Uijlenhoet (2004), A microphysical interpretation of radar reflectivity-rain rate relationships, *J. Atmos. Sci.*, *61*, 1114–1131.

Stewart, R. E., J. D. Marwitz, J. C. Pace, and R. E. Carbone (1984), Characteristics through the melting layer of stratiform clouds, *J. Atmos. Sci.*, *41*, 3227–3237.

Suzuki, K., I. Horiba, and N. Sugie (2003), Linear-time connected-component labeling based on sequential local operations, *Computer Vision and Image Understanding*, *89*(1), 1–23.

Tabary, P. (2007), The new French operational radar rainfall product. Part I: Methodology, *Weath. Forecasting*, *22*, 393–408.

Testi, D., C. Zannoni, A. Cappello, and M. Viceconti (2001), Border-tracing algorithm implementation for the femoral geometry reconstruction, *Computer Methods and Programs in Biomedicine*, *65*(3), 175–182, doi:10.1016/S0169-2607(00)00125-5.

Testud, J., S. Oury, R. A. Black, P. Amayenc, and X. Dou (2001), The concept of "normalized" distribution to describe raindrop spectra: A tool for cloud physics and cloud remote sensing, *J. Appl. Meteorol.*, *40*, 1118–1140.

Tokay, A., and D. A. Short (1996), Evidence from tropical raindrop spectra of the origin of rain from stratiform versus convective clouds, *J. Appl. Meteorol.*, *35*, 355–371.

Tokay, A., D. A. Short, C. R. Williams, W. L. Ecklund, and K. S. Gage (1999), Tropical rainfall associated with convective and stratiform clouds: Intercomparison of disdrometer and profiler measurements, *J. Appl. Meteorol.*, *38*, 302–320.

Tuttle, J. D., and G. B. Foote (1990), Determination of the boundary

layer airflow from a single doppler radar, *J. Atmos. Oceanic. Technol.*, *7*, 218–232.

Uijlenhoet, R. (1999), Parameterization of rainfall microstructure for radar meteorology and hydrology, Ph.D. thesis, Wageningen University, The Netherlands.

Uijlenhoet, R. (2008), Precipitation physics and rainfall observation, *Climate and the Hydrological Cycle (Marc Bierkens, Peter Troch, and Han Dolman, editors)*, *IAHS Special Publications 8*, 59–97.

Uijlenhoet, R., and A. Berne (2008), Stochastic simulation experiment to assess radar rainfall retrieval uncertainties associated with attenuation and its correction, *Hydrol. Earth Syst. Sci.*, *12*, 587–601.

Uijlenhoet, R., and D. Sempere-Torres (2006), Measurement and parameterization of rainfall microstructure, *J. Hydrol.*, *328*, 1–7.

Uijlenhoet, R., J. A. Smith, and M. Steiner (2003a), The microphysical structure of extreme precipitation as inferred from ground-based raindrop spectra, *J. Atmos. Sci.*, *60*, 1220–1238.

Uijlenhoet, R., M. Steiner, and J. A. Smith (2003b), Variability of rain drop size distributions in a squall line and implications for radar rainfall estimation, *J. Hydrometeorol.*, *4*, 43–61.

Uijlenhoet, R., J. M. Porrà, D. Sempere-Torres, and J. D. Creutin (2006), Analytical solutions to sampling effects in drop size distribution measurements during stationary rainfall: Estimation of bulk rainfall variables, *J. Hydrol.*, *328*, 65–82.

Ulbrich, C. W. (1983), Natural variations in the analytical form of the raindrop size distribution, *J. Appl. Meteorol.*, *22*, 1764–1775.

Ulbrich, C. W., and D. Atlas (2007), Microphysics of raindrop size spectra: Tropical continental and maritime storms, *J. Appl. Meteorol. Climatol.*, *46*, 1777–1791.

Ulbrich, C. W., and L. G. Lee (1999), Rainfall measurement error by WSR-88D radars due to variations in Z-R law parameters and the radar constant, *J. Atmos. Oceanic. Technol.*, *16*, 1017–1024.

van de Beek, C. Z., H. Leijnse, P. Hazenberg, and R. Uijlenhoet (2013), Close-range radar rainfall estimation and error analysis, *Q. J. R. Meteorol. Soc.*, *in prep.*

Velner, R. G. J. (2000), Rainfall-runoff modeling of the Ourthe Catchment using the HBV model - a study towards increasing the leadtime of flood forecasts on the river Meuse, Master's thesis, Wageningen University.

Vieux, B. E., and P. B. Bedient (1998), Estimation of rainfall for flood prediction from WSR-88D reflectivity: A case study, 17-18 October 1994, *Weath. Forecasting*, *13*, 407–415.

Vignal, B., and W. F. Krajewski (2001), Large-sample evaluation of two methods to correct range-dependent error for WSR-88D rainfall estimates, *J. Hydrometeorol.*, *2*, 490–504.

Vignal, B., H. Andrieu, and J. D. Creutin (1999), Identification of vertical profiles of reflectivity from volume scan radar data, *J. Appl. Meteorol.*, *38*, 1214–1228.

Vignal, B., G. Galli, J. Joss, and U. Germann (2000), Three methods to determine profiles of reflectivity from volumetric radar data to correct precipitation estimates, *J. Appl. Meteorol.*, *39*, 1715–1726.

Villarini, G., and W. F. Krajewski (2010), Review of the different sources of uncertainty in single polarization radar-based estimates of rainfall, *Surv. Geophys.*, *31*, 107–129.

Villarini, G., W. F. Krajewski, G. J. Ciach, and D. L. Zimmerman (2009), Product-error-driven generator of probable rainfall conditioned on WSR-88D precipitation estimates, *Water Resour. Res.*, *45*(W01404), doi:10.1029/2008WR006946.

Vivoni, E. R., D. Entekhabi, R. L. Bras, V. Y. Ivanov, M. P. Van Horne, C. Grassotti, and R. N. Hoffman (2006), Extending the predictability of hydrometeorological flood events using radar rainfall nowcasting, *J. Hydrometeorol.*, *7*, 660–677.

Vivoni, E. R., D. Entekhabi, and R. N. Hoffman (2007), Error propagation of radar rainfall nowcasting fields through a fully distributed flood forecasting model, *J. Appl. Meteorol. Climatol.*, *46*, 932–940.

Wagenknecht, G. (2007), A contour tracing and coding algorithm for generating 2D contour codes from 3D classified objects, *Pattern Recognition*, *40*(4), 1294–1306.

Waldvogel, A. (1974), The The N_0 jump of raindrop spectra, *J. Atmos. Sci.*, *31*, 1067–1078.

Wang, W., J. Yang, and R. R. Muntz (1997), STING: A Statistical Information Grid Approach to Spatial Data Mining, in *Twenty-Third International Conference on Very Large Data Bases*, edited by M. Jarke, M. J. Carey, K. R. Dittrich, F. H. Lochovsky, P. Loucopoulos, and M. A. Jeusfeld, pp. 186–195, Morgan Kaufmann.

Wessels, H. R. A., and J. H. Beekhuis (1994), Stepwise procedure for suppression of anomalous ground clutter, *Cost 75, Report EUR 16013 EN*, pp. 270–277.

Willis, P. T., and A. J. Heymsfield (1989), Structure of the melting layer in mesoscale convective system stratiform precipitation, *J. Atmos. Sci.*, *46*(13), 2008–2025.

Wilson, C. B., J. B. Valdes, and I. Rodriguez-Iturbe (1979), On the influence of the spatial distribution of rainfall on storm runoff, *Water Resour. Res.*, *15*(2), 321–328.

Wong, C., C. Chen, and M. Su (2001), A novel algorithm for data clustering, *Pattern Recognition*, *34*(2), 425–442.

Woods, R., and M. Sivapalan (1999), A synthesis of space-time variability in storm response: Rainfall, runoff generation, and routing, *Water Resour. Res.*, *35*(8), 2469–2485.

Wright, D. B., J. A. Smith, G. Villarini, and M. L. Baeck (2012), Hydroclimatology of flash flooding in Atlanta, *Water Resour. Res.*, *48*(W04524), doi:10.1029/2011WR011371.

Wu, K., E. Otoo, and K. Suzuki (2009), Optimizing two-pass connected-component labeling algorithms, *Pattern Anal. Appl.*, *12*, 117–135, doi:10.1007/s10044-008-0109-y.

Xiao, Y., J. J. Zou, and H. Yan (2001), An adaptive split-and-merge method for binary image contour data compression, *Pattern Recognition Letters*, *22*(3-4), 299–307, doi:10.1016/S0167-8655(00)00138-0.

Younger, P. M., J. Freer, and K. J. Beven (2009), Detecting the effects of spatial variability of rainfall on hydrological modelling within an uncertainty analysis framework, *Hydrol. Process.*, *23*, 1988–2003.

Yuter, S. E., and R. A. Houze Jr. (1995a), Three-dimensional kinematic and microphysical evolution of Florida cumulonimbus. Part 1: Spatial distribution of updrafts, downdrafts, and precipitation, *Mon. Weath. Rev.*, *123*, 1921–1940.

Yuter, S. E., and R. A. Houze Jr. (1995b), Three-dimensional kinematic and microphysical evolution of Florida cumulonimbus. Part 2: Frequency distributions of vertical velocity, reflectivity, and differential reflectivity, *Mon. Weath. Rev.*, *123*, 1941–1963.

Yuter, S. E., and R. A. Houze Jr. (1995c), Three-dimensional kinematic and microphysical evolotion of Florida cumulonimbus. Part 3: Vertical mass transport, mass divergence, and syntesis, *Mon. Weath. Rev.*, *123*, 1964–1983.

Yuter, S. E., and R. A. Houze Jr. (1997), Measurements of raindrop size distributions over the Pacific warm pool and implications for Z-R relations, *J. Appl. Meteorol.*, *36*, 847–867.

Zamperoni, P. (1981), A note on the computation of the enclosed area for contour-coded binary objects, *Signal Processing*, *3*(3), 267–271.

Zawadzki, I. (1975), On radar-raingauge comparison, *J. Appl. Meteorol.*, *14*, 1430–1436.

Zeng, Z., S. E. Yuter, R. A. Houze Jr., and D. E. Kingsmill (2001), Microphysics and rapid development of heave convective precipitation, *Mon. Weath. Rev.*, *129*, 1882–1904.

Zhang, J., K. Howard, and J. J. Gourley (2005), Constructing three-dimensional multiple-radar reflectivity mosaics: Examples of convective storms and stratiform rain echoes, *J. Atmos. Oceanic. Technol.*, *22*, 30–42.

Zhang, J., C. Langston, and K. Howard (2008), Brightband identification on vertical profiles of reflectivity from WSR-88D, *J. Atmos. Oceanic. Technol.*, *25*, 1859–1872.

Zhang, J., et al. (2011), National mosaic and multi-sensor QPE (NMQ) system, *B. Am. Meteorol. Soc.*, *92*(10), 1321–1338.

Zhang, Y., and J. A. Smith (2003), Space-time variability of rainfall and extreme flood response in the Menomonee river basin, Wisconsin, *J. Hydrometeorol.*, *4*, 506–516.

Zucker, S. W. (1976), Region growing: Childhood and adolescence, *Computer Graphics and Image Processing*, *5*(3), 382–399.

List of publications

Peer-reviewed publications

van Huijgevoort, M. H. J., **P. Hazenberg**, H. A. J. van Lanen, A. J. Teuling, and R. Uijlenhoet, et al., 2013: Global multi-model analysis of drought in runoff for the second half of the 20th century, *J. Hydrometeor.*, accepted for publication.

Rakovec O., **P. Hazenberg**, P. J. J. F. Torfs, A. H. Weerts, and R. Uijlenhoet, 2012: Generating spatial precipitation ensembles: impact of temporal correlation structure, *Hydrol. Earth Syst. Sci.*, 16(9), 3419-3434.

Rakovec O., A. H. Weerts, **P. Hazenberg**, P. J. J. F. Torfs, and R. Uijlenhoet, 2012: State updating of a distributed hydrological model with Ensemble Kalman Filtering: effects of updating frequency and observation network density on forecast accuracy, *Hydrol. Earth Syst. Sci.*, 16(9), 3435-3449.

van Huijgevoort, M. H. J., **P. Hazenberg**, H. A. J. van Lanen, and R. Uijlenhoet, 2012: A generic method for hydrological drought identification across different climate regions, *Hydrol. Earth Syst. Sci.*, 16(8), 2437-2451.

Brauer, C. C., A. J. Teuling, A. Overeem, Y. van der Velde, **P. Hazenberg**, P. M. M. Warmerdam, and R. Uijlenhoet, 2011: Anatomy of extraordinary rainfall and flash flood in a Dutch lowland catchment., *Hydrol. Earth Syst. Sci.*, 15, 1991–2005.

Hazenberg, P., H. Leijnse, and R. Uijlenhoet, 2011: Radar rainfall estimation of stratiform winter precipitation in the Belgian Ardennes., *Water Resour. Res.*, 47, W02507.

Hazenberg, P., N. Yu, B. Boudevillain, G. Delrieu, and R. Uijlenhoet, 2011: Scaling of raindrop size distributions and classification of radar reflectivity–rain rate relations in intense Mediterranean precipitation., *J. Hydrol.*, 402, 179–192.

Driessen, T.L.A., R.T.W.L. Hurkmans, W. Terink, **P., Hazenberg**, P.J.J.F. Torfs, and R. Uijlenhoet (2010), The hydrological response of the Ourthe catchment to climate change as modelled by the HBV model, *Hydrol. Earth Syst. Sci.*, 14 (4), 651–664.

Submitted publications

P. Hazenberg, P. J. J. F. Torfs, H. Leijnse, G. Delrieu, and R. Uijlenhoet, 2013: Identification and uncertainty estimation of vertical reflectivity profiles using a Lagrangian approach to support quantitative precipitation measurements by weather radar, *J. Geoph. Res.*, current status: Minor revisions.

P. Hazenberg, H. Leijnse, and R. Uijlenhoet, 2013: Conceptual radar rainfall ensemble generation and its impact on the catchment hydrological response during cold season precipitation, *Water Resour. Res.*, current status: Under review.

Yu, N., G. Delrieu, B. Boudevillain, **P. Hazenberg**, and R. Uijlenhoet, 2012: Unified formulation of single and multi-moment normalizations of the raindrop size distribution based on the gamma probability density function, *J. Appl. Meteor. Clim.*, current status: Major Revisions.

Netherlands Research School for the
Socio-Economic and Natural Sciences of the Environment

C E R T I F I C A T E

The Netherlands Research School for the
Socio-Economic and Natural Sciences of the Environment
(SENSE), declares that

Pieter Hazenberg

born on 11 October 1982 in Leeuwarden, The Netherlands

has successfully fulfilled all requirements of the
Educational Programme of SENSE.

Wageningen, 24 June 2013

the Chairman of the SENSE board	the SENSE Director of Education
Prof. dr. Rik Leemans	Dr. Ad van Dommelen

The SENSE Research School has been accredited by the Royal Netherlands Academy of Arts and Sciences (KNAW)

KONINKLIJKE NEDERLANDSE
AKADEMIE VAN WETENSCHAPPEN

The SENSE Research School declares that **Mr. Pieter Hazenberg** has successfully fulfilled all requirements of the Educational PhD Programme of SENSE with a work load of 60 ECTS, including the following activities:

SENSE PhD Courses

- Environmental Research in Context
- Research Context Activity: Communicating research results to a wider audience and relevant popular media
- Uncertainty Analysis

Other PhD and Advanced MSc Courses

- First Annual Catchment Science Summer School
- Atmospheric Dynamics

Management and Didactic Skills Training

- Co-organizing the Exchange Program of the hydrology research groups at Wageningen University and Gent University
- Supervision of eight MSc theses and four BSc theses
- Lecturer for the of the BSc course *Field Practical Hydrology, Water Quality and Meteorology*
- Practical supervision for the BSc course *Hydraulics and Hydrometry*

External training at a foreign research institute

- Landslide modelling, Universitat Politècnica de Catalunya, January 2011, Spain
- Weather radar modelling, Laboratoire d'étude des Transferts en Hydrologie et Environnement, October 2008 – March 2009, Grenoble, France

Oral Presentations

- *The inter- and intra-event dropsize distribution for the Cévennes-Vivarais region, southern France.* EGU 2009, 19-24 April, 2009, Vienna, Austria
- *Applying volumetric weather radar data for rainfall runoff modeling: The importance of error correction*. EGU 2009, 19-24 April, 2009, Vienna, Austria
- *Variability of raindrop size distributions and radar reflectivity-rain rate relations in extreme Mediterranean*. IPC 2010, 23-25 June, 2010, Coimbra, Portugal

SENSE Coordinator PhD Education

Drs. Serge Stalpers